Author:
Slater, Ben A

Title:
Towards a fully integrated quantum optic circuit

Towards a fully integrated quantum optic circuit

By

BENJAMIN SLATER

Department of Physics
UNIVERSITY OF BRISTOL

A dissertation submitted to the University of Bristol in accordance with the requirements of the degree of DOCTOR OF PHILOSOPHY in the Faculty of Engineering.

MARCH 2021

Word count: 64,076

Abstract

Quantum technologies walk the line between fundamental science and state-of-the-art engineering. Quantum photonics is revolutionising quantum information and communication, providing complex, integrated photonic circuity that can control flying qubits (photons), in parallel computational advancements are realised by processing and controlling quantum systems on large scales. Flying qubits are a qubit that can be freely send from one node to the other. The quantum internet will be a network of quantum devices that exchange information harnessing quantum mechanics. With these new advancements, protocols, tools and machines have provided multiple methods to communicate using fundamental laws [1–3]. The challenge to push the technology further to multiple end-to-end communication users is on the horizon. Few of the engineering feats have been mastered to overcome the large number of devices needed to interconnect and power such a global network.

This thesis reports on progress towards a large-scale fully integrated quantum systems based on integrated quantum photonic devices. We demonstrate the capability to communicate quantum states across three silicon photonic devices using high dimensional (4D) communication protocols in a multi-core fibre optical network. We review the engineering challenges faced to distribute entangled photons, dimensionally separated in space, using active phase stabilisation to provide the quantum computational basis for communications. A three device integrated silicon network is demonstrated for the first time.

With proof of the network, we then address maximising the number of users. Superconducting Nanowire Single Photon Detectors (SNSPDs) provide high detection efficiencies, low dark counts and timing jitter, proving to be ideal choices for quantum communications. SNSPDs require cryogenic temperatures for operation, and housing hundreds of detectors in a single cryogenic station is required to ensure the scalability of quantum communication networks using nodes. This has never been achieved due thermal power constraints caused by number of devices and high speed electrical connections required to control and manipulate the optical circuity as well as direct communication with the detectors and electrical circuits that produce tangible information. We present the engineering feats in operation of such a cryogenic station and SNSPD models that bring us closer to this, as well as using cryogenically operational Field Programmable Gate Arrays (FPGAs) to process qubit readings.

Lastly, we present models of a ring cavity SNSPD optimised for short wave infrared (SWIR) photons. SWIR can be used to reach increased numbers of photons per circuit and therefore increased communication and computations rates. Photon in the SWIR spectrum benefit from a higher transparency in silicon, alongside a reduction of other non-linear undesirable interactions such as two-photon absorption and exploits optical non-linear effects that drive photon pair production, the cornerstone of quantum photonic technologies. The detectors presented here show increased measurement efficiencies and tailor-ability of photons, offering a route to improve the performance of state-of-the-art devices.

Dedication and acknowledgements

This thesis was the culmination of four years of my life and I am grateful to many people, who without them, I believe I could not achieve this.

Firstly my heartiest thanks go to Dondu Sahin and Jorge Barreto who have supervised my projects throughout the entirety of the PhD experience. Providing much guidance, wisdom and scientific expertise. Your great enthusiasm and passion for science is infectious and I believe all these will greatly benefit me in future.

I would also like to thank Mark Thompson and John Rarity who gave me the opportunity to embark on the research. Appreciate you for offering me much freedom to try and dig in many areas I was interested in.

In the detector group of QETLabs I would like to thank the PhDs who have made this journey an adventure and provided much expertise in their fields and areas to enable a high quality production of research. Mack Johnson, Antonio Gentile, Nicola Tyler and Ben Burridge. You guys are great and I strongly believe you will reap the rewards of your hard work. I would especially like to thank Mack for almost being a mentor in a lot of my work, having my back and being utterly dependable. Thanking his knowledge in fabrication and patients. I would like to thank Nicola Tyler, who has not been around for most of my PhD, but being a great source of knowledge to begin and using her work, to produce my own research. I would to to thank Antonio Gentile for his electronics, cryogenics and engineering knowledge to help me hit the ground running in cryogenic electronics.

I would like to thank the Research Associates Andrew Hart, Rob Heath and Gerardo Villarreal. I thank Andrew Hart for being a great friend and making the PhD adventure, showing my much knowledge about digital and RF electronics and being a knowledge collaborator. I thank Rob Heath for being a mentor the darkest of times and providing much motivation, guidance in scientific methods involving SNSPDS and cryogenics as well as programming, that helps me in my future career. I thank Gerardo Villarreal for dependability in cryogenics and patients.

I would like to thank the two PhDs Daniel Llewellyn and Caterina Vilgar who started this journey with me and collaborated with on a large research project. Dan has become a close friend, whose endless scientific knowledge, sensor of humour and chemistry has made this PhD into an adventure. Thanks to his contributions and friendship, I couldn't imagine completing this PhD without him. Caterina has also become a great friend, being completely dependable and supportive in our research efforts and kindness created a productive environment to enable growth of friendships and work.

I would like to thank the masters students, Molly Blake who worked on a research project who pushed and motivated me to become a stronger leader and researcher.

I would also would like to provide special thanks Imad Faruque, Laurence Rosenfeld, Henry Semenko, Stefano Passenai other PhDs, other have contributed in my effort.

Dedicated to my Mum and Dad for you unwavering love and support. I couldn't of done this without you and thank you for believing in me to get here.

Also thanks to everyone else at QET Labs and the friends I have made during this experience. I would like to thank my room mates, friends from swing dancing, Tae Kwon Do friends and any others friends I have made during this process. Thank you all!

AUTHOR'S DECLARATION

I declare that the work in this dissertation was carried out in accordance with the requirements of the University's Regulations and Code of Practice for Research Degree Programmes and that it has not been submitted for any other academic award. Except where indicated by specific reference in the text, the work is the candidate's own work. Work done in collaboration with, or with the assistance of, others, is indicated as such. Any views expressed in the dissertation are those of the author.

SIGNED: ..... DATE: .....

TABLE OF CONTENTS

List of Tables

List of Figures

Figure **Page**

Acronyms

ADC	Analogue to Digital Converter
ASIC	Application Specific Integrated Circuit
AMZI	Asymmetric Mach-Zehnder Interferometer
AV	Anti-Vibration
BS	Beam Splitter
CAD	Computer Aided Design
CPS	Counts per second
CC	Coincident counts
CMOS	Complementary metal-oxide-semiconductor
CPLD	Complex Programmable Logic Device
CW	Continuous Wave
DAC	Digital to Analogue Converter
DC	Direct Current
DCR	Dark Count Rate
DNL	Differential Non-Linearity
DSP	Digital Signal Processor
EBL	Electron Beam Lithography
FDTD	Finite-difference time-domain
FPGA	Field Programmable Gate Array
FSR	Free Spectral Range
FWHM	Full Width Half Maximum
FWM	Four-Wave Mixing
GHZ	Greenberger-Horne-Zeilinger
GM	Gifford-McMahon
HD	High-Dimensional
HOM	Hong-Ou-Mandel
HSQ	Hydrogen Silsesquioxane
INL	Integral Non-Linearity
IQP	Integrated Quantum Photonics
IWD	Integrated Waveguide Detector
LSB	Least Significant Bit
LUT	Look-Up Table
LVDS	Low-Voltage Differential Signalling

MIR	Mid-infrared
MM	Multi-mode
MMI	Multimode interference
MZI	Mach-Zehnder interferometer
MUB	Mutually Unbiased Basis
NIR	Near infrared.
OL	Optical lithography
OSA	Optical Spectrum Analyser
PBS	Polarisation Beam Splitter
PC	Polarisation controller
PCB	Printed circuit board
PMF	Polarisation maintaining fibre
PMT	Photomultiplier Tube
PNRD	Photon Number Resolving Detector
QE	Quantum Efficiency
QIP	Quantum information processing
QKD	Quantum Key Distribution
RCD	Ring Cavity Detector
RF	Radio Frequency
RIE	Reactive Ion Etching
RSFQ	Rapid Single Flux Quantum
RTD	Resistance to Temperature Diode
SDE	System detection efficiency.
SDRAM	Synchronous Dynamic Random Access Memory
SEM	Scanning electron microscope
SFWM	Spontaneous four-wave mixing
SFQ	Single Flux Quantum
SM	Single-mode
SMF	Single-mode fibre
SMU	Small Measurement Unit
SNR	Signal-to-Noise Ratio
SNSPD	Superconducting Nanowire Single Photon Detector
SoC	System on Chip
SOI	Silicon on insulator
SPAD	Single Photon Avalanche Diode
SPD	Single Photon Detector
SPDC	Spontaneous parametric down-conversion
SPM	Self-phase modulation
STD	Standard Deviation
SWIR	Short-wave infrared

TAC	Time-to-Analogue Converter
TDC	Time-to-Digital Converter
TE	Transverse electric
TES	Transition-Edge Sensor
TM	Transverse magnetic
TOPM	Thermo-optic phase modulator
TPA	Two-photon absorption
VGA	V-groove array
VHDL	VHSIC Hardware Description Language
VHSIC	Very High-speed Integrated Circuit
VNA	Vector network analyser
VOA	Variable optical attenuator
WG	Waveguide

CHAPTER 1

INTRODUCTION

The development of quantum mechanics in the 20^{th} century has led to new ways to harness information resources in the 21^{st} century. In today's society, humanity reaps the benefits of the "first quantum revolution". Some of the most important discoveries of this revolution are semiconductors, lasers and integrated photonic circuits on semiconductors, where quantum mechanics describes their working principles [4–6]. These technological developments led to fundamental tools, such as the transistor and light-emitting diodes (LEDs). However, the technologies listed only use quantum mechanics to understand how the device is created and used. The computer and laser have no quantum properties in themselves, such as superposition or entanglement. The first quantum revolution can be considered as the use of these technologies and applications relying on an understanding of quantum mechanics and its uses in the fields of electromagnetism and atomic physics.

Scientific advancements have currently brought us to the "second quantum revolution": where individual quantum entities are generated and manipulated, giving us access to the fundamental quantum properties of the system, for example, quantum entanglement and superposition. Many new technologies and applications spring off from this era: quantum computing [7], quantum communications [8], quantum metrology [9] and quantum simulations [10] are some highlighted examples.

These applications provide an engineering challenge of controlling and validating these quantum devices. Current scientific research is in pursuit of harnessing these quantum technologies by creating stable environments. A wide variety of different approaches and platforms are being investigated: ion trap systems [11], quantum dots [12, 13], superconducting circuits [14], nitrogen-vacancy centres in diamonds [15], quantum photonics [16] are some key selections.

1.1 Quantum Information

A classical computer encodes information in bits (0 or 1), while a quantum computer encodes the data in quantum bits, qubits ($|0\rangle$ or $|1\rangle$). Utilising entanglement for quantum supremacy in quantum information processes surpasses that which is currently achievable by classical information. Quantum supremacy is defined as when a quantum computer exists that surpasses a classical computer at a process. Three technologies are forerunning to achieve quantum supremacy [17]: trapped ions, superconducting circuits and quantum photonic circuits. This thesis focuses on using photons for its technology for qubits due to photons showing very little decoherence and being easily accessible. They are also classed as the only “flying qubit", allowing the qubit to naturally travel in space between other qubits, which ultimately results in computation interactions.

The photon is a key fundamental phenomenon discovered in the early 20^{th} century and has long been used to communicate information. Einstein used the electric field's quantisation to explain the photoelectric effect back in 1905 [18]. He described the phenomena as the electric field carrying discrete packets of energy E, determined on the wavelength λ, the value of Planck's constant h and the speed of light c: $E = h\lambda/c$ labelling the concept as particle-like behaviour. On the way to creating a quantum computer, a currently used technology, quantum communication, exploits many of the same quantum phenomena.

Quantum key distribution (QKD) [1, 19] is one application of quantum technologies. Providing robust security protocols based on physics laws, QKD has increased from a proof of concept to network demonstrations on a commercial level [20]. Even with these incredible advancements, QKD has not been widely adopted due to practical implications that are likely to be overcome with integrated design based devices.

Quantum communications are far more than just [21] QKD. QKD provides a stepping stone to enable technologies such as quantum networks and the quantum internet, providing a fully connected global, robust network.

Integrated photonics provides [22] a stable, compact and robust platform to realise quantum photonic applications described above. Currently, most proof-of-concept demonstrations are performed in quantum optics and rely on bulk optics [23]. They have inefficient, non-deterministic photon sources and low to modest efficiency photon detectors, covering tables, using bulky mirrors, beams splitters, and waveplates, which is not practical in achieving stability and scalability, and complexity needed to realise quantum computers and communications [24].

This thesis will report the experiments completed on the silicon quantum optic platform and technologies required for quantum information realisation.

1.2 Disclaimer

In this thesis, I use the phrase ‘we’ to describe guiding the reader, i.e. you and I, through the content. Later experiments were performed collaboratively and involved other people's work; the

term ‘we’ here also applies to the collective contribution of the group to work. However, in general, the thesis contents, such as diagrams, simulations, and experimental data, were solely performed and created by myself. Exceptions to this are indicated in the acknowledgements section at the end of each chapter.

1.3 Thesis Outline

This work addresses the evolution of large parts of a fully integrated quantum optics communication detection system. The work presented in this thesis is broken into four distinct parts:

- **Chapter 2**: presents an overview of the topics and background behind the different research areas presented. Firstly this introduces quantum information and quantum optics theory to inform what aspects are needed to be understood for a high-dimensional entanglement distribution network. A description of the silicon (Si) photonics platform and individual components make up a fully integrated device. We then go on to cover superconducting nanowire single-photon detectors (SNSPDs) theory and ring resonators in more detail to fully understand the last results chapter. Lastly, introducing digital electronics, time-to-digital converters, Field Programmable Gate Arrays (FPGAs) and cryogenics.

- **Chapter 3**: is concerned with the high dimensional entanglement distribution, demonstrating a High Dimensional Quantum Key Distribution (HD-QKD) network. Presenting separate quantum optics Si integrated devices, with multiple sources, transmitter and two receiver devices, creating a complex network. The source device is used to generate and prepare HD states of entangled photons on a chip, while the receivers projection into Mutually Unbiased Basis (MUBs) shows QKD potential. We used a multi-mode core fibre to transmit 2D and 4D bipartite spatially entangled photon states using an active phase stabilisation system scheme.

- **Chapters 4**: details the quantum node, for controlling SNSPDs for applications in quantum computing/communications. The experimental design and engineering in running a cryogenic station, using cool readout and amplification electronics for embedded SNSPDs in one system. Covering key aspects in the system that are needed to be addressed before tackling the Time-to-Digital-Converter (TDC) covered in chapter 5—dealing with the practical aspects by characterising and minimising the vibrations of the system to allow for compatibility with integrated optic devices. We also cover the characterisation of the SNSPD used, which allows for the TDC’s characterisation by using generated SNSPD electric signals.

- **Chapters 5**: follows on from the previous chapter, explaining the characterisation and design considerations for a cryogenic fully encompassed SNSPD readout system. To ensure

scalability in the future of quantum communications by supporting hundreds of SNSPD in one system. This first deals with choosing an optimal electrical off-the-shelf GaAs RF amplifier, finding a device balancing optimal gain and input power. That is connected in tandem with the SNSPD and TDC. An FPGA is used as a TDC readout system to measure in time the SNSPD signals generation to be read out by a user in the environment. We show that this is possible and the errors expected.

- **Chapter 6**: is concerned with developing a new waveguide integrated cavity SNSPD for Short-Wave Infrared (SWIR). At around 2 μm TPA effect is significantly reduced in Si, but SNSPDs at this wavelength have shown low efficiency, mainly due to under researched design considerations for quantum information applications. We move to mitigate this with a new design for the SWIR SNSPD. Firstly showing the potential of an integrated waveguide detector and then showing the improvement gained in placing the waveguide (WG) integrated SNSPD into a cavity. At the same time, we are considering the practical implications of the path of the SNSPD needed for electrical signal readout, within an Multi Mode Interferometer (MMI) structure at the detection area. We are concluding that competitive efficiencies and jitters comparable to state-of-the-art are achievable.

- **Chapter 7**: Finally, the conclusion of the work is presented here, alongside an outline of shortcomings and future directions research may take to overcome them. The importance of reaching a quantum network to be available to multiple users is discussed. I am touching on why many engineering steps are still to come to achieve this goal. Simultaneously, several have been investigated in this thesis—explaining that a communication system's infrastructure requires communication between multiple integrated devices and that a quantum node, with filtering detectors, is a method to achieve this.

CHAPTER 2

BACKGROUND

This chapter provides an overview of the theory, components, and technology needed for most of the following chapters. Additional background required for an understanding of the following chapters can be found within them. This chapter gives a guide through Quantum information and QKD protocols and execution, Si photonic components and detectors focusing on SNSPDs. This chapter will also cover the technologies needed to achieve these experiments, including new state-of-the-art cryogenic systems and cryogenic read out electronics.

2.1 Quantum Information & Communication

This section will explore quantum theory and how this is used to realise quantum information and communications. Quantum theory is relevant for understanding the motivation behind why the topics researched in this thesis are areas of interest for the progression of technology in our lives. It will allow us to understand how quantum communication uses quantum mechanics to allow us to deliver messages while protected from quantum computers.

Quantum information is the study of information on a state within a quantum system, using techniques to process and manipulate the information by changing states. Quantum information theory includes many key concepts in quantum mechanics such as superposition, entanglement and teleportation to enable the investigation of systems used for computing and communication. Computing and communication are encompassed within quantum information and are methods to utilise quantum information in our world. This section covers the fundamental concepts of quantum mechanics, quantum information, and quantum communications to pave the way for the rest of the theories built on in this thesis.

2.1.1 Quantum Mechanics

Quantum mechanics postulates that quantum states represent all the information of a quantum system and can be represented by a normalised wavefunction that can be denoted by ket $|\Phi\rangle$. This denotes a pure state. However, it is also possible for a system to be in a statistical ensemble of different state vectors (called a mixed state): For example, there may be a 50% probability that the state vector is $|\Phi\rangle_1$ and a 50% chance that the state vector is $|\Phi\rangle_2$. This notation is Dirac notation, where Φ represents the target state under investigation. The vector $|\Phi\rangle$ inhabits within the Hilbert space H, which contains the set of all orthonormal (orthogonal and normalised) vectors that the state could be measured. The vector dual space coincides within the Hilbert space, with the dual vector $|\Phi\rangle^\dagger$ that can be rewritten as a 'bra' in Dirac notation, $\langle\Phi|$. The † operation transforms between the two spaces and is defined as the conjugate transpose $|\Phi\rangle^\dagger \rightarrow |\Phi\rangle^{*T}$. In quantum physics, all that can be known about this pure quantum system is represented by a normalised vector.

The following postulates describe the relationships between the physical world and the mathematical formalism's used to describe them:

States: Quantum state is a complete description of a physical system by the vector $|\Psi\rangle$ in the Hilbert space $\mathscr{H}^d$ in a d-dimensional complex inner product vector space. This class of vectors can be multiplied by a complex scalar so that they are indistinguishable.

Observables: An observable is a property of a physical system that can be measured. A Hermitian operator describes it as a linear transformation on the vector,

$$\hat{A} : |\Psi\rangle \longrightarrow A\,|\Psi\rangle\,, \tag{2.1a}$$

$$\hat{A} : a\,|\Psi_1\rangle + b\,|\Psi_2\rangle \longrightarrow aA\,|\Psi_1\rangle + bA\,|\Psi_2\rangle\,. \tag{2.1b}$$

The observable A has a spectral representation such that its eigenstates form a complete orthogonal basis:

$$\hat{A} = \sum_n \alpha_n\,|\alpha_i\rangle\,\langle\alpha_i| = 1. \tag{2.2}$$

An example of this is the energy operation or a Hamiltonian $\hat{H}$. The time evolution of a quantum system is determined by the Schrödiner equation:

$$i\hbar\frac{d}{dt}\,|\Psi\rangle = \hat{H}\,|\Psi\rangle\,, \tag{2.3}$$

where $\hbar$ is $h/2\pi$, where h is Plancks constant. The eigenvalue E_n and eigenvector $|e_n\rangle$ of the Hamiltonian are the quantum system's eigenenergy and eigenstates. The eigenvalues of the matrix will be the potential energies the system can have. The eigenvectors give us the basis for space and therefore give us a way to represent any state:

$$\hat{H}\,|a_i\rangle = \hat{A}_i\,|a_i\rangle\,. \tag{2.4}$$

Knowing the Hamiltonian allows us to solve the eigenvalues and eigenstates. Mathematically, we can write the Hamiltonian with a matrix representation, allowing us to solve the eigenvalues by diagonalising the matrix. A matrix is diagonalisable if there exists an invertible matrix **P** and a diagonal matrix **D** such that

The Shrödinger picture explains the evolution of a system in the time domain. Using a time independent Hamiltonian H_t the evolution of a state is described by:

$$|\Psi_t\rangle = e^{(-i\frac{H_t}{\hbar}t)}\,|\Psi_0\rangle\,, \tag{2.5}$$

where $|\Psi_0\rangle$ is the initial state of the system and $|\Psi_t\rangle$ is the state of the system after time evolution t, has occurred. We can label this as a unitary $\hat{U}$, with the postulate stating that the evolution of a closed quantum system is described by a unitary transformation, and that the state $|\Psi_0\rangle$ of the system at time t_0 is related to $|\Psi_t\rangle$ of the system at time t_1 by the Unitary operator $\hat{U}$,

$$|\Psi_t\rangle = \hat{U}\,|\Psi_0\rangle\,. \tag{2.6}$$

In quantum information, we are typically more interested in the unitary itself then the states before and after the evolution. Transformations within a quantum information circuit from input to outputs states are essential, and examples of this is shown later on.

2.1.2 Quantum Information

2.1.2.1 Qubits

In information theory, a bit is used to describe a physical system that can exist in two distinguishable states [25–27]. A bit can hold one piece of information. Superposition is key in quantum mechanics and quantum information. A coherent superposition of eigenstates can describe any quantum state,

$$|\Psi\rangle = \sum_n c_n\,|\phi_n\rangle\,. \tag{2.7}$$

That two states can be named as in '1' state or within a '0' state. A qubit is a quantum version of the system, having the same properties. The states are labelled $|0\rangle$ and $|1\rangle$. Where a bit is in one of two states constantly. A qubit can be in a superposition of the states:

$$|\Psi\rangle = \alpha_0\,|0\rangle + \alpha_1\,|1\rangle\,, \tag{2.8}$$

where a_0 and a_1 are complex numbers.

These qubits reside on a two dimensional Hilbert space. The probability of achieving one state when measured must always be one, as $|a_0|^2 + |a_1|^2 = 1$. If we do a measurement of this superposition of states we will get $|0\rangle$ with a probability of $|\, a_0\,|^2$ or $|1\rangle$ with a probability of $|\, a_1\,|^2$. A qubit cannot cannot be cloned according to the no-cloning theorem [28], as it is impossible to create an identical copy of an arbitrary unknown quantum state. We can rewrite Equation 2.8:

$$|\Psi\rangle = cos\frac{\theta}{2}|0\rangle + e^{i\phi}sin\frac{\theta}{2}|1\rangle\,, \tag{2.9}$$

where θ and ϕ define a point on the unit three dimensional Bloch sphere [27]. The Bloch sphere is a representation of the state of a single qubit, where on the x-axis you have the $|\pm\rangle = |0\rangle + |1\rangle/\sqrt{2}$ states, the y the $|\pm i\rangle = |0\rangle + i\,|1\rangle/\sqrt{2}$ states and z-axis $|0\rangle\,, |1\rangle$ as shown in Figure. 2.1.

$|\Psi\rangle$ is a vector in two-dimensions for a qubit. It can be represented in many different forms, as described above. The Dirac notation, wavefunctions, matrix notation, Bloch sphere, and density matrices are some of the most used representations [26]. All of these representations have their advantages and uses in different scenarios. The Dirac notation elegantly presents a quantum system's state evolution, while the wavefunction is typically used to describe the time evolution of the quantum system. Matrix notation is used to perform calculations. The density matrix is an excellent way to present how pure a state is. The Bloch sphere presents an excellent intuitive way to visualise the states.

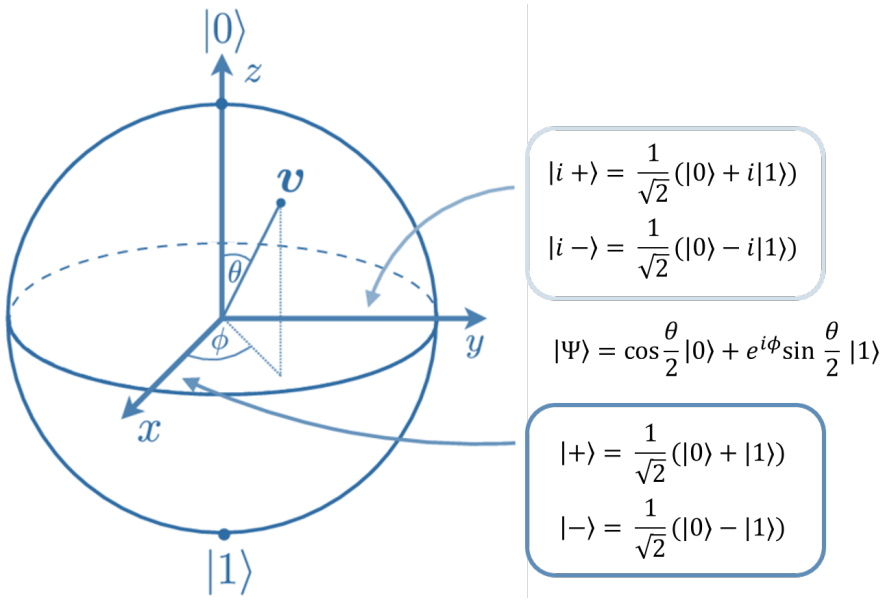

FIGURE 2.1. Bloch sphere representing a qubit state.

The correspondence between Dirac notation and matrix representation of basis states on the Bloch sphere is listed below:

$$
\begin{aligned}
|0\rangle &= \begin{bmatrix} 1 \\ 0 \end{bmatrix}, \quad |+\rangle = \begin{bmatrix} \frac{1}{\sqrt{2}} \\ \frac{1}{\sqrt{2}} \end{bmatrix}, \quad |+i\rangle = \begin{bmatrix} \frac{1}{\sqrt{2}} \\ \frac{i}{\sqrt{2}} \end{bmatrix}, \\
|1\rangle &= \begin{bmatrix} 0 \\ 1 \end{bmatrix}, \quad |-\rangle = \begin{bmatrix} \frac{1}{\sqrt{2}} \\ \frac{-1}{\sqrt{2}} \end{bmatrix}, \quad |-i\rangle = \begin{bmatrix} \frac{1}{\sqrt{2}} \\ \frac{-i}{\sqrt{2}} \end{bmatrix}.
\end{aligned} \tag{2.10}
$$

Physical representations can include the orthogonal polarisations of a photon, paths on an interferometer, electron states via spin or energy levels on an atom and quantum dots.

An ideal system to use for qubit implementation should meet the following requirements: long coherence, universal operations, scale-ability and robustness [26, 27]. A set of universal quantum gates is any set of gates to which any operation possible on a quantum computer can be reduced; that is, any other unitary operation can be expressed as a finite sequence of gates from the set. Trapped ions or atoms with two energy level systems can be used to encode a qubit state, while a laser is used to control the states. An atomic system offers long coherence times. Photons can also represent a qubit system and have infinite decoherence times. Also, the use of photon interference allows for universal operation, allowing it naturally to be used in quantum communication [21], quantum information [27] and metrology [9].

2.1.2.2 Quantum Interference

The second quantisation formalism describes light as an ensemble of quantum harmonic oscillators with a Hamiltonian:

$$
\hat{H} = \sum_k \hat{H_k}, \qquad \hat{H_k} = \hbar\omega_k(\hat{a_k}^\dagger \hat{a_k} + \frac{1}{2}) \tag{2.11}
$$

where $\hat{H_k}$ is a single harmonic oscillator, ω_k is the angular frequency of the kth mode. The ladder operators $\hat{a_k}^\dagger$ and $\hat{a_k}$ are the creator and annihilation operators, respectively, for the excitation in k-modes. k represents each of the system's modes, which can be spacial modes, polarisation, orbital angular momentum, spectral, etc. The modes mainly used and described in this thesis will be spacial modes, represented by occupying different waveguides on-chip.

Photon states can be represented using Fock states with $|n\rangle_k$, with n being the number of photons in mode k. The operators above act on the Fock states as follows:

$$
\hat{a_k}^\dagger |n\rangle_k = \sqrt{n+1}\,|n+1\rangle_k\,, \hat{a_k}\,|n\rangle_k = \sqrt{n}\,|n-1\rangle_k\,. \tag{2.12}
$$

For this photons occupying the same optical mode are indistinguishable. The eigenvalue of this is represented by $E_n = \hbar\omega(n+1/2)$. For this type of quantum mechanical oscillator, the energy difference between nearest neighbours is set at a fixed value of $E_0 = \hbar\omega 1/2$. E_0 is also the ground state and is so named as a vacuum state. The two ladder operators also combine to give another import operator, the number operator $\hat{n} = \hat{a_k}^\dagger \hat{a_k}$. $\hat{n}$ provides the photon number.

2.1.2.3 Encoding qubits and qudits with information

In quantum photonics, qubits are typically encoded onto a photon by using its properties of polarisation, frequency, mode or angular momentum. They are encoded with information via a Fock state of a single photon in two optical modes. These modes can be represented by many multiple degrees of freedom (frequency [29] time, polarisation [30], orbital angular momentum, spatial [7]); here, we use space by the photon path.

The primary encoding we will use is 'dual-rail' or 'path' encoding, where the spatial location of a single photon encodes the information. Here we define two distinct waveguides as 'rails'. A photon in the top rail encodes a $|0\rangle$ and in the bottom rail encodes a $|1\rangle$.

The mapping of logical states from Fock states is as followed:

$$\text{Fock Basis} \Longleftrightarrow \text{Logical Basis}$$

$$|1\rangle_0 |0\rangle_1 \Longleftrightarrow |0\rangle \tag{2.13a}$$

$$|0\rangle_0 |1\rangle_1 \Longleftrightarrow |1\rangle \tag{2.13b}$$

The qubit is in the logical state $|i\rangle$ if the photon is in the i^{th} mode. Therefore, this can be generalised to d-dimensions qudits where a photon can occupy as many dimensions as there are modes. Fock states are indicated using the same bra-ket notation as for logical states of, e.g., qubits. The meaning of the two is, however, different in general and should not be confused. A unitary on two modes is performed with a controlled interference, where more modes require implementing a universal linear system of gates and interference points.

2.1.2.4 Qudits

A qudit is a quantum version of d-ary digits for $d > 2$. Qudit technologies are emerging as an alternative to qubit for quantum information science and quantum computation. This is due to its multi-level nature, qudit provides a larger state space to process and store information and the ability to control multiple operations simultaneously [31].

$$|\Psi\rangle = \alpha_0 |0\rangle + \alpha_1 |1\rangle + \alpha_2 |2\rangle + \alpha_3 |3\rangle + ... \tag{2.14}$$

A three-dimensional version is named a "qutrit," and a four-dimensional is named a "quqart". These are presented mathematically by expanding the matrix and density matrix notations to

capture a qudit system with d base states, with d being the number of dimensions. Photons are naturally unbounded in eigenmodes (orbital angular momentum (OAM), space, etc.), allowing for qudits' implementations. Qudits offer higher information capacity for quantum communications [32], and practical advantages for quantum computing [31].

2.1.2.5 Entanglement

Entanglement is a counter-intuitive idea of the quantum world associated with composite quantum systems. The equation below shows a two-qubit entangled state.

$$|\Psi\rangle = \frac{|00\rangle + |11\rangle}{\sqrt{2}} \tag{2.15}$$

A multiparticle system $|\Psi\rangle$ is described as being entangled if its wavefunction cannot be factorised into a product of the wavefunctions of the individual particles $|a\rangle$ and $|b\rangle$.

In 1935, the EPR paper [33] was published, which coined the term “entanglement" [34, 35]. A source emits a pair of correlated photons: by measuring each photon's polarisation, you can assign the orthogonal polarisation is the values $|0\rangle$ or $|1\rangle$. They are perfectly correlated if both photons' pairs are measured in-state $|0\rangle$ or $|1\rangle$. Quantum non-locality predicts that if one qubit is measured, then the result for the other entangled qubit will be immediately determined, independent of the distance between them. Entanglement is an essential resource for quantum information applications.

To expand entanglement for large scale quantum information there is: multi-parties entanglement and multi-dimension entanglement, as represented mathematically:

$$\begin{aligned} Multi-parties: &\qquad |\Psi\rangle = \tfrac{1}{\sqrt{2}}(|0\rangle^{\otimes N} + |1\rangle^{\otimes N}) \\ Multi-dimensional: &\qquad |\Psi\rangle = \tfrac{1}{\sqrt{N}} \textstyle\sum_1^N |i\rangle\,|i\rangle \end{aligned} \tag{2.16}$$

This is also an example of a Bell state. A Bell state is a two party and two-dimensional entangled state. Their simplicity has allowed them to have been realised in a number of diverse experiments. Their conventional form is:

$$|\Psi^{\pm}\rangle = \frac{1}{\sqrt{2}}\,|0,1\rangle \pm |1,0\rangle \quad |\Phi^{\pm}\rangle = \frac{1}{\sqrt{2}}\,|0,0\rangle \pm |1,1\rangle \tag{2.17a}$$

The Bell states are the common eigenstates of the three operators $\hat{\sigma}_x \otimes \hat{\sigma}_x$, $\hat{\sigma}_y \otimes \hat{\sigma}_y$, $\hat{\sigma}_z \otimes \hat{\sigma}_z$, with eigen values ± 1, corresponding to the spin components being equal or opposite. These are defined further within this chapter.

Einstein stated that "God does not play Dice" in reference to explaining the form of “Hidden variables". He proposed to provide deterministic explanations of quantum mechanical phenomena by introducing un-observable hypothetical entities.

2.1.2.6 Fidelity

Fidelity is a popular measure of distance between density operators. Fidelity measures the distance between pure states. For two states given here by the unit vectors $|\phi\rangle$ and $|\Psi\rangle$ it is $|\langle\phi|\Psi\rangle|$. It can also be used to measure the distance between two mixed states, described by a density matrix. If two density matrices ρ and σ, the expression is:

$$F(\rho,\sigma) = \left(tr\sqrt{\sqrt{\rho}\sigma\sqrt{\rho}}\right)^2. \tag{2.18}$$

2.1.2.7 Qubit Operations

A famous example of a unitary evolution are the Pauli matrices shown here:

$$\hat{X} = \hat{\sigma_x} = \begin{bmatrix} 0 & 1 \\ 1 & 0 \end{bmatrix}, \tag{2.19}$$

$$\hat{Y} = \hat{\sigma_y} = \begin{bmatrix} 0 & -i \\ i & 0 \end{bmatrix}, \tag{2.20}$$

$$\hat{Z} = \hat{\sigma_z} = \begin{bmatrix} 1 & 0 \\ 0 & -1 \end{bmatrix}, \tag{2.21}$$

The $\hat{X}$ is commonly known as the quantum NOT gate, and its operation is referred to as a “bit flip". The bit flip name is so-named as it takes $|0\rangle$ flips it to $|1\rangle$ and $|1\rangle$ flips it to $|0\rangle$. The Z matrix is known as a phase flip, by leaving $|0\rangle$ invariant and taking $|1\rangle$ flipping it to $-|1\rangle$, where the -1 factor represents a change in the phase factor.

Another very well used unitary operation is the Hadamard gate,

$$H = \frac{1}{\sqrt{2}}\begin{bmatrix} 1 & 1 \\ 1 & -1 \end{bmatrix}, \tag{2.22}$$

which results in $H|0\rangle = (|0\rangle + |1\rangle/\sqrt{2})$ and $H|1\rangle = (|0\rangle - |1\rangle/\sqrt{2})$. I differ in this thesis the Hamiltonian $\hat{H}$ and the Hadamard gate with H, by using the hat symbol.

2.1.3 Quantum Information Processing

Here we briefly discuss quantum information processing in a linear optic network, where more than one photon is involved. A prime mechanism of qubit interaction is non-classical interference (quantum interference). An example of this is the famous Hong-Ou-Mandel (HOM) effect [36].

The set up is where two identical photons use two different input port paths to meet at a beam splitter to interfere and exit out of two output ports, which are measured [37].

In the classical world, the two photons could be modelled as evolving individually, and each photon has an equal 50% probability of exiting out of either port leading to four possible outcomes as shown in Figure.2.2. With detectors at each output, there is a coincidence detection event probability of 0.5 that both detectors simultaneously measure a photon.

The quantum story of these events plays out different. Consider two indistinguishable single photons arrive at the Beam Splitter (BS) simultaneously. This two photon state with each mode occupied may be written as $|1\rangle_1|1\rangle_2 = \hat{a}^\dagger_{1,in}\hat{a}^\dagger_{2,in}|0\rangle$. The operator for the beam splitter is written as:

$$U_{BS} = \frac{1}{\sqrt{2}}\begin{pmatrix} 1 & i \\ i & 1 \end{pmatrix}. \tag{2.23}$$

Hence, the evolution of the mode operators is $\hat{a}^\dagger_{out} = U^T_{BS}\hat{a}^\dagger_{in}$

Therefore the outputs state are explicitly described as

$$\frac{1}{2}(\hat{a}^\dagger_{1,out} + i\hat{a}^\dagger_{2,out})(\hat{a}^\dagger_{2,out} + i\hat{a}^\dagger_{1,out})|0\rangle \tag{2.24}$$

$$\frac{1}{2}[i(\hat{a}^\dagger_{1,out})^2 + i(\hat{a}^\dagger_{2,out})^2 + \hat{a}^\dagger_{1,out}\hat{a}^\dagger_{2,out} - \hat{a}^\dagger_{1,out}\hat{a}^\dagger_{2,out}]|0\rangle \tag{2.25}$$

$$\frac{i}{\sqrt{2}}(|2\rangle_1|0\rangle_2 + |0\rangle_1|2\rangle_2). \tag{2.26}$$

This describes the situations only where the two photons are collected together into the same output mode, leading to a probability of coincidences of the detectors 0. The HOM effect is a very important tool used in quantum information processing. This is also describes as a NOON state [38]. This is a NOON state where N = 2. A general NOON state is described by:

$$|\Psi_{NOON}\rangle = \frac{|N\rangle_{k1}|0\rangle_{k2} + e^{iN\theta}|0\rangle_{k1}|N\rangle_{k2}}{\sqrt{2}} \tag{2.27}$$

with N in this case representing a superposition of N particles. More than two photons and NOON stables are commonly used in quantum metrology, and quantum sensing [39].

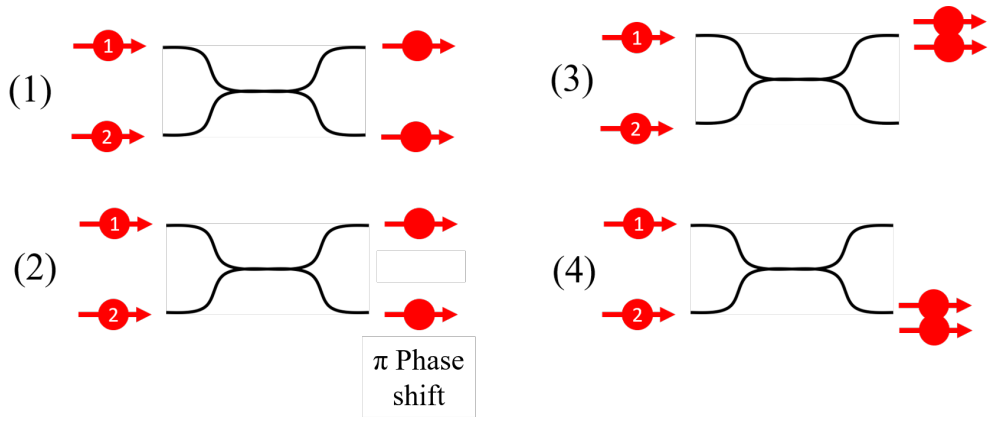

Figure 2.2: The schematics represent each of the possible outcomes when the photon pair interact on a BS. HOM possible results with all four of the circumstances equally possible in the classical world, but in the quantum regime with indistinguishable particles, results (1) and (2) are identical, except for the sign change, therefore cancel each other out and do not occur.

2.1.4 Mutually unbiased bases

A complete set of MUBs allows for an efficient quantum tomography to be measured as this discloses the complete information about an arbitrary state of the system. Intuitively, we expect the average entanglement over all states account for the complete set of MUBs to be fixed concerning measurement, independent of the bases' choice. The measure of entanglement is a function of the linear entropy of a reduced density operator. The idea of this proof is to use the property of a complete set of MUBs. [40]. The entanglement averaged over a complete set of MUBs is the same as the entanglement averaged over all pure quantum states. It has been proven that the maximum number of the MUBs in a Hilbert space of dimension n is $n + 1$, where n is an integer power of a prime number. Mathematically, complementary observables are described by noncommuting Hermitian operators whose sets of eigenstates form different bases in the Hilbert space that are MUBs. This refers to the fact that the inner product of any pair of states belonging to different bases is the same.

Let A and B operators in a d-dimensional Hilbert space, whose eigenbases form an orthonormal set $|a_i\rangle, |b_i\rangle$. These bases are said to be mutually unbiased if:

$$|\langle a_i|b_j\rangle|^2 = \frac{1}{d} \tag{2.28}$$

Given any eigenstate of one, the outcome resulting from a measurement of the other is entirely undetermined.

Thus comes the obvious question of how many MUBs exist for a d-dimensional Hilbert space.(d+1) MUBs exist. For a 4D system, the following bases form an MUB set:

$$\hat{I}_4 = \frac{1}{2}\begin{bmatrix} 1 & 0 & 0 & 0 \\ 0 & 1 & 0 & 0 \\ 0 & 0 & 1 & 0 \\ 0 & 0 & 0 & 1 \end{bmatrix}, \qquad \hat{H}_4 = \frac{1}{2}\begin{bmatrix} 1 & 1 & 1 & 1 \\ 1 & 1 & -1 & -1 \\ 1 & -1 & -1 & 1 \\ 1 & -1 & 1 & -1 \end{bmatrix} \tag{2.29}$$

$$\hat{M}_2 = \frac{1}{2}\begin{bmatrix} 1 & -1 & -i & -i \\ 1 & -1 & i & i \\ 1 & 1 & i & -i \\ 1 & 1 & -i & i \end{bmatrix}, \qquad \hat{M}_3 = \frac{1}{2}\begin{bmatrix} 1 & -i & -i & -1 \\ 1 & -i & i & 1 \\ 1 & i & i & -1 \\ 1 & i & -i & 1 \end{bmatrix}, \qquad \hat{M}_4 = \frac{1}{2}\begin{bmatrix} 1 & -i & -1 & -i \\ 1 & -i & 1 & i \\ 1 & i & 1 & -i \\ 1 & i & -1 & i \end{bmatrix} \tag{2.30}$$

2.1.5 Quantum Communications

2.1.5.1 Cryptography

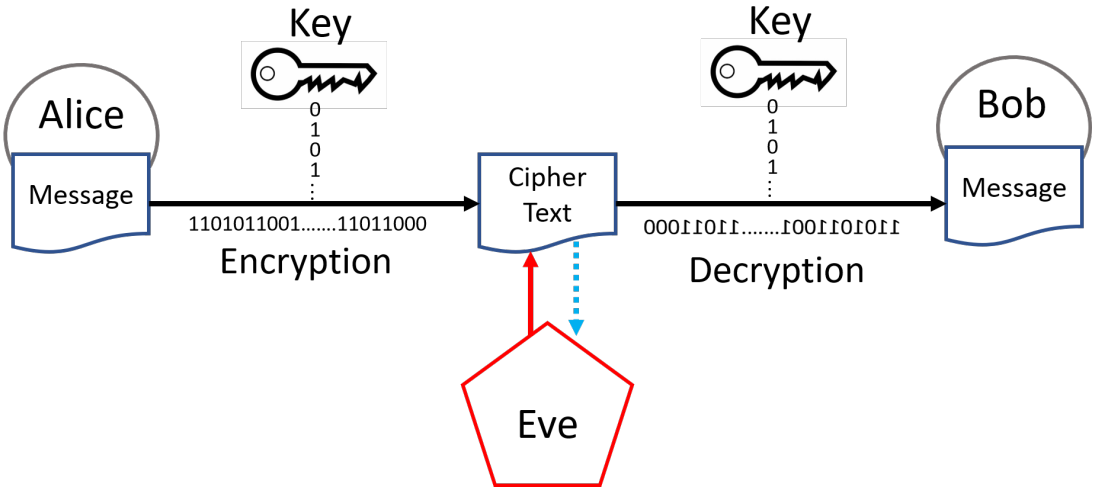

Figure 2.3: Two parties, named "Alice" and "Bob", communicate over a public channel by encrypting their message using a shared key, making the message a cipher text and not understandable by any outside party (Eve) and decrypting using a key.

Throughout the history of written communication methods, there have been methods in restricting and disguising the information of the actual message to others besides the recipients. The field of cryptography provides privacy, authentication, and confidentiality for the users, as cryptography is the practice of obscuring the message's information without decoding it. In cryptography, the terminology is used to help bring clarity in communication schemes: the two parties involved in the communications are called “Alice" (the sender) and “Bob" (the receiver), which are the two parties communicating their message. A third party is known as “Eve" is an eavesdropper, acting as an antagonist attempting to extract information from the message. In

some circumstances, we have a 3rd party in the receipts, named “Charlie", who provides resources to enable communications between Alice and Bob or to be communicated to as well. The diagram below Figure.2.3 represents how the encryption communication between the two occurs.

2.1.5.2 Cipher

A mathematical description of a cipher can be presented as the following. Representing the plain text space is $\mathscr{M}$, the set of all ciphertext space is $\mathscr{C}$ and a set of all keyspace as $\mathscr{K}$. The family of encryption functions $\mathscr{E}_{\mathscr{K}}$ described mapping plain text to ciphertext, and the family of decryption functions $\mathscr{D}_{\mathscr{K}}$ describe the mapping of cipher text to plain text.

$$\begin{aligned} &\mathscr{E}_{\mathscr{K}} : \mathscr{M} \to \mathscr{C}, \\ &\mathscr{D}_{\mathscr{K}} : \mathscr{C} \to \mathscr{M}, \\ &\mathscr{D}_{\mathscr{K}}(\mathscr{E}_{\mathscr{K}}(\mathscr{M})) \end{aligned} \tag{2.31}$$

Alice and Bob agree on a secret key over a secure channel. They can then send their ciphertext over an insecure channel. There are different examples of encryption systems used throughout history, such as early ones (Caesar Cipher), growing more involved. A notable encryption invention is the One-time Pad (OTP) that uses a symmetrical randomly generated shared key between Alice and Bob. The key is the same length as the message, resulting in an unbreakable cipher. As the key is entirely random, an attempt to replicate is entirely random unless you know how the key is generated. Therefore generating an utterly random key is a current point of research. Quantum Random Number Generators (QRNG) use quantum mechanical laws to generate completely random numbers that cannot be reversed engineered. This area of research is not covered in this thesis.

Rivest, Shamir and Adelman (RSA) [41] provide us with a widespread public-key cryptography protocol, which generates a public and private key that uses two prime numbers, currently used in much of today’s communications, including banking and military purposes. The protocol is not fully described here [41]. However, the idea is that multiplying two prime numbers to generate the key while decomposing into the two source prime numbers to crack the key is difficult. However, As computers become more powerful, the security of this technique weakens. RSA is used instead of the OTP, as OTP is resource-intensive, as the key must be as long as the message. Therefore non-OTP cryptography systems have a lifetime, as it is only a matter of time to break with a computer.

2.1.5.3 Quantum Key Distribution

In this section, we will move from quantum mechanics generally to cover the area of Quantum Key Distribution (QKD) [42], and the fundamental mechanisms underpinned by quantum mechanic laws.

Quantum computing motivating quantum cryptography

Quantum computers will be able to factor large integer numbers more efficiently than classical computers. Shor's algorithm [43] would allow quantum computers to crack many currently used cryptography protocols in polynomial time decrease. Breaking these would have dramatic ramifications in the information privacy in our current world. Quantum cryptography provides a solution, as the system's quantum nature provides us with the **no-cloning theorem** tool [28]. The no-cloning theorem states that it is impossible to create an identical copy of an unknown and arbitrary quantum state. A statement that has great implications in the field of quantum computing. A mathematical proof of these systems follows.

Suppose we have a quantum device, where we have our *target slot*, which is an our unknown pure state $|\Psi_1\rangle$, which is the state we wish to copy, into our *cloned slot* that starts out as a random pure state $|?\rangle$. We can use some unitary for cloning our target state called U_C, which performs:

$$|\Psi_1\rangle \otimes |?\rangle \rightarrow U_C(|\Psi_1\rangle \otimes |?\rangle) = |\Psi_1\rangle \otimes |\Psi_1\rangle \tag{2.32}$$

Assuming we can apply this copying unitary to another specific pure state $|\Psi_2\rangle$. If we then take the inner product of these two equations:

$$\langle\Psi_1\rangle\,\Psi_2 = (\langle\Psi_1\rangle\,\Psi_2)^2 \tag{2.33}$$

This leaves only two possible solutions: either these states $|\Psi_1\rangle$ and $|\Psi_2\rangle$ are the same, or they are orthogonal to one another. Therefore a potential cloning device cannot distinguish between these two. QKD protocols deal with Mutually Unbiased Basis (MUB), and therefore cannot determine the state from the measurement. MUB in $\mathscr{H}$ is two orthonormal bases, such that the square of the magnitude of the inner product between any basis states equals the inverse of the dimension d. If a system is prepared in a state belonging to one of the bases, then all outcomes of the measurement with respect to the other basis are predicted to occur with equal probability.

This leads to motivation in using pure quantum states to communicate information, as an eavesdropper will have to measure the state to discover the key that Alice and Bob are exchanging. The information intercepted by Eve will not be used in producing the key as that information is lost. If Eve wishes to replace/clone the state they measured, they cannot, due to the cloning theorem just stated. Key exchange is a solution that offers good performance for relatively low transfer rates. This method is more feasible than a "True" quantum communication, where the message itself is transferred from the quantum channel. Using both a quantum channel and a classical channel, exchanging only the key to decrypt the message on the quantum channel and sending the message itself via the classical channels works around the low transfer rate.

Quantum entangled states enable a method to generate randomness between two parties. During the quantum measurement, the probability of obtaining specific results depends on the

basis the user has chosen to measure. As the entanglement distribution for communication purposes between two parties depends on each user choosing their basis to measure incoming quantum states. When both pairs of quantum entangled states are measured on the same basis, there is a statistically higher probability of correlation between measurements. For example, if Alice chose to measure in the computational basis $\hat{\sigma_z}$, both users simultaneously choosing to measure their results on this basis would be perfectly correlated.

Similarly, if they had both chosen to measure in the Hadamard basis ($\hat{\sigma_x}$), perfectly correlated measurements would be the result. However, if Alice or Bob choose different bases, for example, one chose $\hat{\sigma_z}$ and the other $\hat{\sigma_x}$, the measurements would be uncorrelated, resulting in the production of a flat probability distribution. The circumstances just described provide the backbone for QKD: after their measurements have been collected publicly, each member publicly announces the basis they have measured in to correlate their same basic measurements, this allows for the key generated between them to remain secret.

2.1.5.4 BB84

Bennett and Brassard in 1984 (BB84) [44] developed one of the most popular QKD protocols. The scheme exploits quantum mechanics uncertainty principles in Eve to gather enough information to compromise the key.

The protocol:

- Alice prepares each qubit she is going to send and for each one, she randomly generates one of two bases: the Z basis ($|0\rangle$, $|1\rangle$) or the X basis ($|+\rangle, |-\rangle$). These bases are chosen as they are orthogonal to one another. Therefore any states measured on either basis will provide no information about the other basis.

- Alice generates a qubit state in the randomly chosen basis. The options are a 0 ($|0\rangle$ in the Z basis or $|+\rangle$ in the X basis) or a 1 ($|1\rangle$ in the Z basis or $|-\rangle$ in the X basis).

- This now qubit is encoded into a photon using one of its degrees of freedom. Examples can be polarisation, phase, frequency, time and space. For this example, we will use polarisation, as its two natural orthogonal polarisation modes allow for a fluent understanding.

- The qubit is sent to Bob via a secure communication channel. Bob has randomly generated a basis between the same two that Alice used to measure his incoming qubit.

- If Bob measures a qubit in the same basis as Alice measure her qubit, then Bob will measure the same bit as Alice originally sent. This is assuming that the qubit was not altered during transit between the two parties. An example: If Alice sent a 0 bit in the X basis ($|+\rangle$), Bob would also measure a 0 bit ($|+\rangle$ in this case) if he chose the same (X) basis. If Bob had chosen the Z basis, he would measure a 0 or a 1 with equal probability. Therefore no information on the key is added for that qubit measurement.

- After all of the qubits are sent, Alice and Bob both publicly announce which basis they chose for each qubit sent. They look for coincidences between their bases and discard any measurements/results where the bases do not match. Then, assuming no errors using the remaining qubits measured, generate a shared key between both parties, which is identical.

- Eve can hack the communication channel between Alice & Bob and measure the flying qubits in the same way Bob measures them by randomly choosing a basis. Nevertheless, Eve and Bob independently randomly choose a basis that will not always coincide. Therefore half of the time, she will not measure the same basis as Bob. Also, Bob will receive no detection event unless Eve replaces the missing qubit. Not knowing what state to replace the qubit with, Bob will receive a state not entangled with Alice's state.

A threshold limit on the error is typically applied to QKD protocols that must be met to use the key. A number of the generated states are lost during transfer, or other errors may reduce the number of qubits received and measured. The error rate for practical QKD using BB84 was calculated to be 27.6% [45]. To help distinguish between just loss or fluctuations of information, which may be natural in an optical fibre communication channel. The channel is compromised and the qubits leaked to Eve. If they do not meet this threshold, they throw away the key they have generated and look to generate a new key.

2.1.5.5 MDI-QKD

MDI-QKD is a novel quantum communication protocol that allows two users Alice and Bob, to communicate with one another even if the hardware they are using has been tampered with and thus is not trusted. This is achieved by measuring correlations between Alice and Bob's signals rather than the actual signals themselves. There are proven research methods of attacking the channel [46], with no countermeasures. Measurement Device Independent (MDI) [3][47] QKD removes these potential side channels which could be exploited via hacking. This assumes that both Alice and Bob both have their own devices and use a third party. This third party (named "Charlie") will measure the states sent from Alice and Bob and announce successful events. Knowing these successful events, only Alice and Bob can determine their key by knowing the basis they sent their qubit in. This allows Charlie to be un-trusted (it can even be Eve).

An example of an MDI-QKD protocol is as follows: Alice and Bob independently prepare phase randomised weak coherent pulses (WPCs) in different BB84 polarisation states. At Charlie's end, photons from Alice and Bob interfere on a 50:50 BS that has on each end a polarising BS (PBS) projecting the input photons into either of the BB84 basis horizontal. In Figure.2.4a schematic of the following description of MDI-QKD can be found. (H) or vertical (V) polarisation states. Using single photon detectors at the four outputs after the two PBS, the photons are measured, and the results are publicly announced. The results are only announced if a successful Bell state measurement occurs, by opposite polarisation's detection coincidences events. A click in Detector

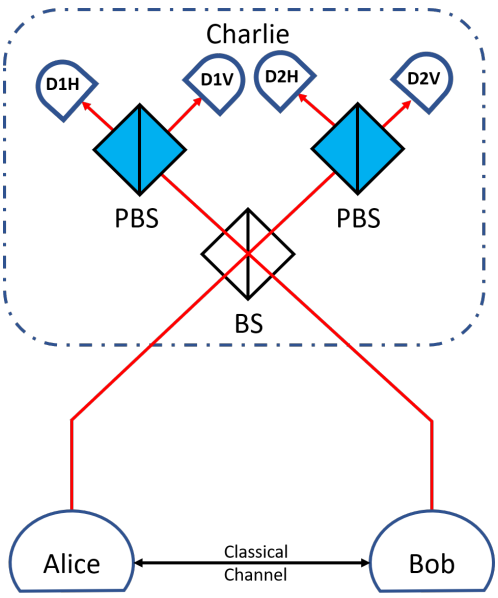

FIGURE 2.4. MDI-QKD set up representation. With Alice and Bob sending their polarisation encoded prepared states to the Beam Splitter (BS), that sends the photons to two possible polarising beam splitters (PBS), that then send to one of the four single photons detectors.

1 on the Horizontal (D1H) & D2V, or in D1V & D2H, indicates a projection into the Bell state $|\Psi^+\rangle = \frac{1}{\sqrt{2}}(|HV\rangle - |VH\rangle)$, while a click in D1H & D1V, or in D2H & D2V, indicates a projection into the Bell state $|\Psi^-\rangle = \frac{1}{\sqrt{2}}(|HV\rangle + |VH\rangle)$.

Compared to standard security proofs, it has a key advantage of removing all detector side channels, and it doubles the transmission distance covered over conventional QKD schemes. Furthermore, it has a particularly high key generation rate which is comparable to that of standard security proofs. Its key generation rate is orders of magnitude higher than the previous approach of full device independent QKD. In view of its excellent security, performance and simple implementation.

2.2 Integrated Quantum Photonics

Here, we provide an introduction to integrated quantum photonics. We are discussing the components and the overall technology. We expand by saying how they are used to realise the last section giving the user the highest control of quantum photonics information states yet developed. This is relevant as it allows us to know the platform we expect the following chapters to operate in and how operations and experiments are performed.

2.2.1 Introduction

To realise the potential of quantum photonics to encode hundreds of qubits with information, integrated photonics is a promising platform. Many proofs of concept ideas such as the first two-qubit experiments and BB84 protocol [44] was shown in bulk optics, using free space lenses to manipulate scales poorly with the number of qubits and dimensions. Free space also provides turbulence, changes in path length, phase and polarisation, in a partly chaotic medium. Alternatively, fibre-based quantum optics allows for the containment of the qubits and transfer of qubits of hundreds of kilometres [48]. However, this platform still scales poorly in size with the number of components and qubits.

2.2.2 Linear and Non-Linear effects in Si

The dielectric response of a medium is determined by the electric polarisation **P**, which is defined as the electric dipole moment per unit volume. The electric displacement **D** is related to the electric field **E** and **P** through:

$$\mathbf{D} = \epsilon_0 \mathbf{E} + \mathbf{P} \tag{2.34}$$

In an isotropic medium, the microscopic dipoles align along the direction of the applied electric field, so that we can write:

$$\mathbf{P} = \epsilon_0 \chi \mathbf{E} \tag{2.35}$$

where ϵ_0 is the electric permittivity of free space and χ is the electric susceptibility of the medium.

High power coherent light sources can interact with a material in a non-linear phenomenon, described by:

$$P = \epsilon_0 \chi^{(1)} E + \epsilon_0 \chi^{(2)} E^2 + \epsilon_0 \chi^{(3)} E^3 + ... \tag{2.36}$$

The first term in Equation 2.36 is the same as in Equation 2.35 describing the linear response of the medium. The order ith of the superscript for 1 represents linear susceptibility and two or more nonlinear susceptibility. In "weak" fields, we only consider the first term. Si is a centrosymmetric crystal material. Therefore, it lacks nonlinear processes that require $\chi^{(2)}$, such as spontaneous parametric down-conversion [49]. Third-order nonlinearities are significant in silicon as they exhibit a wide variety of phenomena [49]. This can be seen from Si relatively refractive index value, that has a directly proportional relationship $\chi^{(3)} \propto (n-1)^4$ [49].

Band Gap: A band gap is the distance in energy between the valence band of electrons and the conduction band. Silicon has four electrons in its valence band. In a silicon crystal, the electrons form covalent bonds with other electrons in the valence band of neighbouring atoms.

Hence, at absolute zero, there are no electrons free for conduction. The density of silicon states and all semiconductors contains a bandgap between the conduction and valence band. As the bandgap of semiconductors is relatively small compared to insulators, interactions by thermal excitations at increasing temperature excite electrons into the conduction band, increasing conductivity. The band gap defines the wavelengths that are optically transparent through a material and wavelengths that are absorbed.

Therefore, a semiconductor's bandgap determines how much energy is needed to excite an electron to the conductive state. Band gaps where no phonon assistance is required are called direct band gaps. In some cases, the assistance of a phonon is also required to achieve excitation. Some materials conduction band has a different momentum than the minimum energy state in the valence band. In these materials, the crystal lattice vibrations are required for momentum conservation, an indirect bandgap. At room temperature, silicon has an indirect bandgap of 1.12 eV and a direct bandgap of 3.4 eV [50]. The injection of impurities named dopants can change the conductivity of silicon. Introducing nitrogen atoms, which have five electrons in the valence band, results in a spare electron after bonding to silicon, and therefore the conductivity of silicon has been increased. Doping with electron donors creates n-type semiconductors. The same can be done by introducing impurities with fewer valence electrons than silicon, such as boron with three in the valence band. This leads to the creation of absences of electrons or 'holes'. Doping with electron acceptors creates p-type semiconductors.

2.2.3 Quantum Photonics

Two Photon Absorption (TPA): TPA is the nonlinear optical phenomenon that occurs when a material simultaneously absorbs two photons. In an insulator or semiconductor, TPA can generally occur only if the photons' energy is at least half the bandgap energy. If the energy of a single photon of a particular wavelength cannot promote the electron into a free carrier, but the energy from two photons can, this qualifies as TPA. The photon's energy E depends on its wavelength λ and can be calculated using $E = hc/\lambda$. Here, h represents Planck's Constant and c is the speed of light. These free carriers change the refractive index and optical properties of the medium. This is a nonlinear effect. The higher the photon flux, the stronger the effect becomes. This limits potential power through a medium providing diminishing returns in power transmitted to the input power. We will use the example of Si to illustrate.

In Figure.2.5 a) we illustrate the TPA absorption in the degenerate and non-degenerate case. Two photons are absorption promoting the electron from the Ground level E_g to the valence band E_v. In the non-degenerate case, two photons of different wavelengths ω_1 & ω_2 are absorbed. In the degenerate case ω_1 is equal to ω_2.

In silicon photonics, the C-band (4 - 8 GHz) is used in many applications. The energy of a 1.55 μm photon is 0.8 eV, and the energy of a 2.2 μm photon has is 0.56 eV. The bandgap of Si is 1.12 eV. Less photon absorption occurs at 2.2 μm as higher phonon energies are required to also close

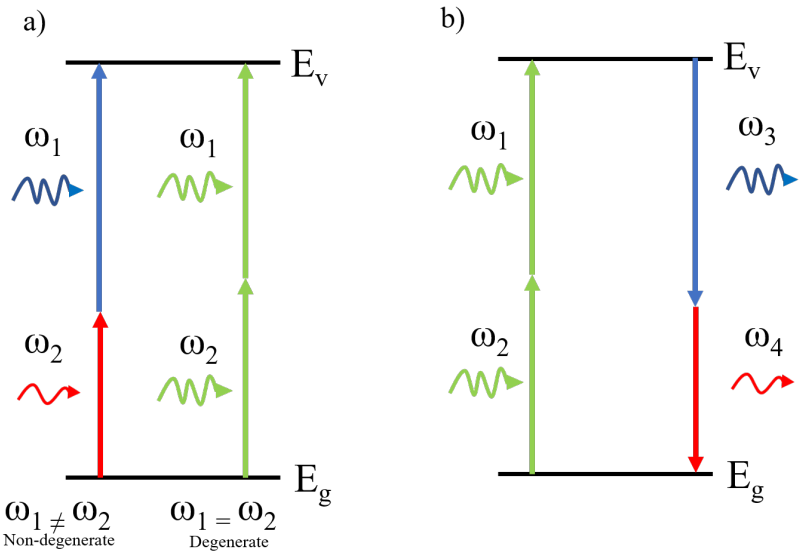

FIGURE 2.5. a) Degenerate and Non-degenerate TPA mechanism, with ω the angular frequency of the photons, and colour representing the energy. b) Spontaneous Four Wave mixing with absorption of coherent photons and emission of two photons of different wavelengths.

the band gap. A single photon cannot excite a carrier from valance to the conduction band, but if two 1.55 μm photons combine and are absorbed, it can create a free carrier. If the two photons' combined energy is lower energy than hc/λ, the effect becomes unattainable, as the two photons combining energies are insufficient to overcome the bandgap. There is three-photon absorption, but this effect is orders of magnitude lower and negligible.

Spontaneous Four-Wave-Mixing (SFWM): This is a nonlinear process where two photons with angular frequency ω_1 and ω_2 are converted into two photons with angular frequency ω_3 and ω_4. This conversion occurs by the absorption of the initial two photons to promote a carrier, which is down-converted into two photons of different wavelengths. Energy is conserved therefore ω_1 + ω_2 = ω_3 + ω_4 as shown in Figure. 2.5 b).

Coherence Length: Two photon sources are coherent if they produce photons with the same frequency, waveform and a constant phase difference. The coherence length is the distance at which a wave propagates over, in which it is considered to maintain coherence. The interference between the two photons is strong when the paths mismatch by less than the coherence length. Coherence length L can be calculated for a Gaussian emission spectrum by $L = \sqrt{\frac{2ln2}{\pi}} \frac{\lambda^2}{n\Delta\lambda}$. λ is the wavelength of the photon and $\Delta\lambda$ is the bandwidth of the photon source and n is the refractive index of the material.

2.2.4 NIR and SWIR

Silicon is considered to be an ideal material to choose as a platform for quantum photonics [50]. In silicon photonics, the C-band is used in many applications. This wavelength band typically used within quantum photonics [51], as used in classical communications channels because of its transmission properties in optical fibres. Any quantum communications systems designed with this wavelength may use the current classical optical fibre networks already established globally. Due to its prevalence, integrated optics fabrication foundries in Si for optic devices fabricate components for that are optimised for 1550 nm, which lies within the C-band and is the high transmission in Si. It is also the atmospheric transparency window allowing for use in LiDar systems [52]. This wavelength's capabilities and infrastructure around it have been heavily invested in [51].

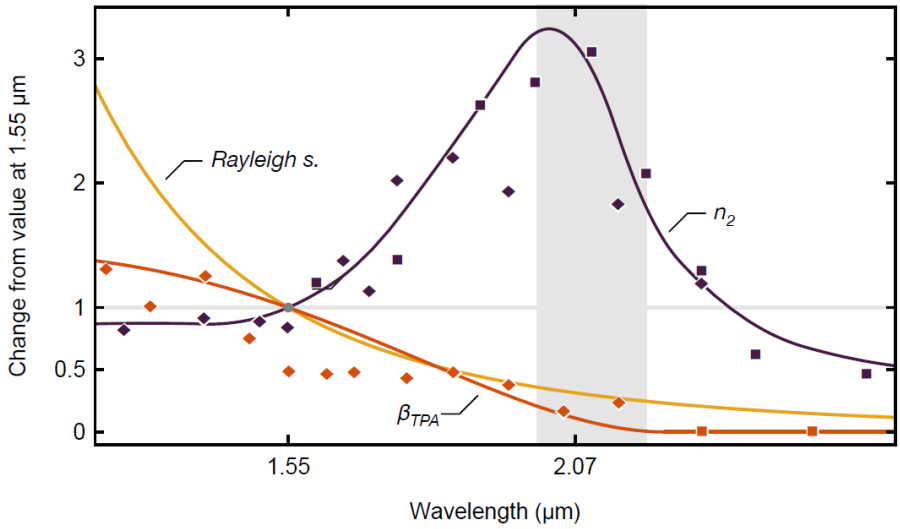

FIGURE 2.6. Values are relative change from the phenomena at 1550 nm in Si. The lines represent Dispersion of nonlinear refraction n_2, a nonlinear two-photon absorption model $_{TPA}$ and Rayleigh scattering. This figure is reproduced from [53].

There is also current research at longer wavelengths than 1550 nm, due to the advantages they have and the draw backs 1550 nm has as shown in Figure.2.6. At this wavelength you have nearly eliminated TPA and amplified nonlinear optical properties that are used to generate and manipulate photons. [16, 53] show that using longer wavelength photons in the SWIR is currently under research as an alternative to 1550 nm.

2.2.4.1 Other platforms

There are several candidates that can fulfil the role of the medium for photon manipulation. The properties that are needed are: a higher refractive index than the environment; large enough band gap to minimise photon absorption; high values of χ^2/ or χ^3 for photon control; mature foundry methods to allow for the fabrication of devices; and compatibility with CMOS to enable both active control of electronics and photons on the device. Some examples of other platforms are SiN[54], glass [55], Germanium [56] and InGaAs [57].

2.2.5 Integration of passive SOI components

We now describe the set of integrated optical components that become the engineering tool box to achieve many of the measurements achieved in this thesis. Silicon is a growing optical material which has allowed it to be at the forefront of quantum photonics. In recent years there has been the uprising of reprogrammable [58] optical information processors [59], which are the first steps to the ultimate goal of a fully integrated, universal quantum computer device.

Waveguides can be fabricated in semiconductor materials such as Ge, GeSN, InGaAs, etc as well as dielectrics such as glass. We focus on using Si. A waveguide uses its refractive index to trap the light and guide it. Waveguides are the building blocks of quantum photonics in Si.

2.2.5.1 Waveguides

A waveguide is a component that allows for the confinement of waves. These can be sound waves or radio frequency waves, but this will focus and cover light confinement. The light is confined from total internal reflection. The waveguide has a higher refractive index than the material surrounding. When light interacts with this boundary, total internal reflection can be performed. This occurs if the light interacts at the interface with an angle smaller than that of the critical angle $\theta_c = arcsin(n_2/n_1)$, with n_2 being the material with a lower refractive index than n_1, as light is trapped and can obtain different dimensions and different modes depending on the wavelength of the light and the properties of the waveguide (geometry and refractive index).

Modes are defined by the properties of coherence and orthogonality: modes are orthogonal solutions of the wave equation, they do not interfere. Only the light within one and the same mode is coherent and does interfere. Two types of modes are distinguished: spatial modes transverse to the direction of propagation (crosssection and divergence), and temporal modes in the direction of propagation (time and frequency). If the light is propagating down the z-axis, the x and y dimensions of the waveguide are normally smaller to guide the light in one direction at a time. The Figure 2.7 shows multiple different forms a waveguide can take with varying success in light confinement. The Rib waveguide allows the mode to travel in the central part, while the evanescent trails travel in the sides of the rib. In the slit waveguide, the light is confined between the two Si waveguides.

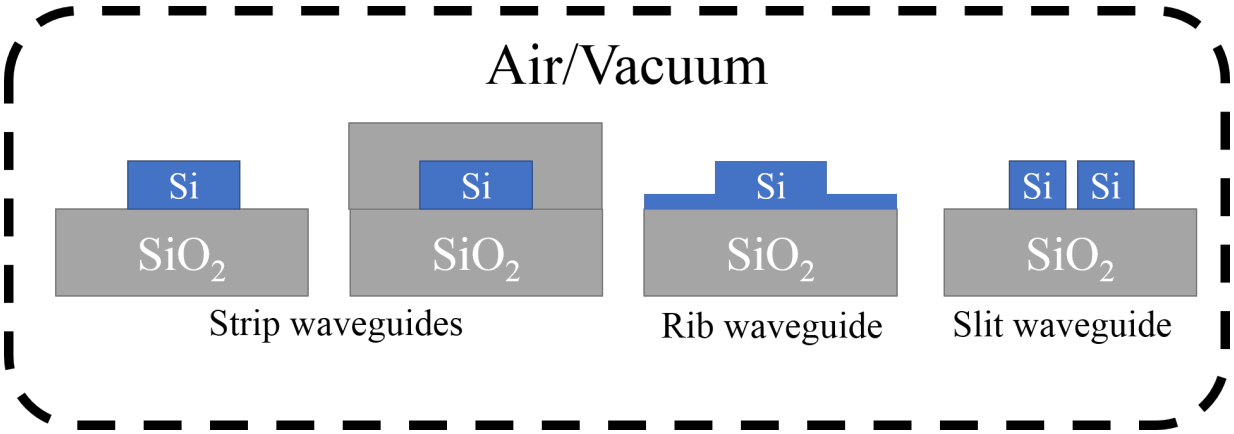

FIGURE 2.7. Diagram of the cross-section from different waveguide geometries. SiO_2 and Air has a lower refractive index, than that of Si.

This thesis will only concentrate on strip waveguides. When the dimensions of the waveguide begin to be the same magnitude of the wavelength of light propagating through it, two of the surfaces begin to shape the light. If a waveguide can support only a single mode of light it is called a single mode waveguide, whereas if it can support multiple modes its called a multi mode waveguide.

These modes can be be derived from Maxwell's equations. If we take a rectangular waveguide, with light propagating in the Z-direction we get the following results:

$$\frac{\partial^2 E_z}{\partial x^2} + \frac{\partial^2 E_z}{\partial y^2} = [\beta^2 - \frac{\omega^2}{c} n^2(x,y)]E_z \tag{2.37}$$

$$\frac{\partial^2 M_z}{\partial x^2} + \frac{\partial^2 M_z}{\partial y^2} = [\beta^2 - \frac{\omega^2}{c} n^2(x,y)]M_z \tag{2.38}$$

where n is refractive index, $\beta = n_{eff}\omega/c$ is the propagation constant, E_z is the z component of the electric field and M_z the z component of the magnetic field. When the polarisation of the electric field oscillates in the y direction, convention calls this the transverse electric (TE) mode. Alternatively, when the magnetic field oscillates in the y direction, conventions name this the transverse magnetic (TM) mode. The geometries of the waveguide are tailored for the TE mode and was the great transmission for this mode compared to the TM mode.

The following experiments use strip Si waveguides with a buried oxide (SiO_2) cladding base. Cladding is one or more layers of materials of lower refractive index than the mode propagating core, in intimate contact with the core material which has a higher refractive index. The cladding causes light to be confined to the core of the fibre by total internal reflection at the boundary between the two. Air and Hydrogen Silsesquioxane (HSQ) are common cladding mediums. When

a Si waveguide is fabricated, the side walls and top wall of the waveguide can be cladded with air or HSQ in a lot of cases. HSQ has similar refractive index properties as glass [60].

Losses in Waveguides Losses are an important part of consideration for Si photonics [61–64]. Losses can occur in waveguides through the fabrication process. These are scattering losses from the high contrast between the core and the cladding. The index contrast scales cubic ally with the difference in refractive indices [65]. We have already covered some of the losses that occur in Si in the last section, from non-linear affects such as TPA, SFWM and waveguide bends.

2.2.5.2 Grating couplers

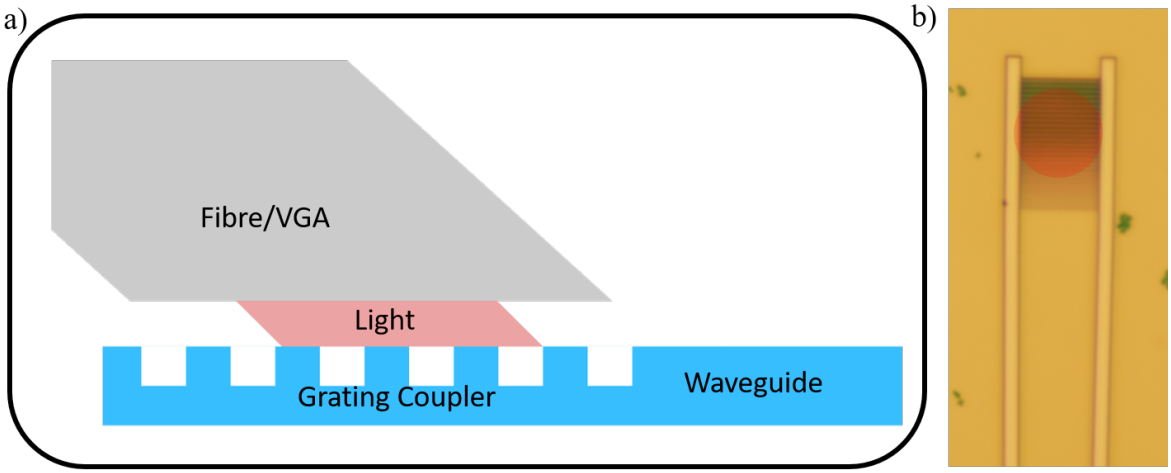

FIGURE 2.8. a) Schematic diagram of a fibre array projecting light onto a grating coupler, to confine into the connected waveguide. b) A microscope image of a Si grating coupler with a red laser spot shadow on the grating, without a VGA or fibre.

Optical coupling is the method of transmitting light between two different confinements. A common practice in photonics is coupling light from an optical fibre into waveguides: matching or converting your mode in your fibre, to one that is compatible with the waveguides, or vice-versa. One method of coupling is interfacing your fibre directly to the side of the device, where the waveguide ends. This is named 'butt coupling' or 'side coupling'. Side coupling can be an ineffective way to couple the light with large losses, due to mode mismatch. Mode mismatch is where the two coupling materials do not support the same optical modes as one another. One way to compensate for that is to have waveguides of dimensions or material closer to the patch cable, which then change dimensions or material gradually to the waveguide of use, within the rest of the medium. This allows the light to travel in the TE mode reducing reflections, scatter

and losses. These are called 'spot-size converters' [66]. Unfortunately they can be centimetres long, taking up valuable real estate on a device for other components.

An alternative method is 'top coupling', where light can be projected from the top of the device and coupled into the waveguide, allowing for another dimension to be utilised for design. These designs tend to be smaller relative to side coupling for their coupling efficiency, making them desirable components. The top couplers are named grating couplers (GC) [67], as they act as a grating array to diffract the light from one plane into the waveguide plane, while also converting the mode, as seen in Figure.2.8. A GC can be described using the following equation:

$$ma = \frac{\lambda}{n_{eff} - n_1 sin\theta} \tag{2.39}$$

where m is the number of the gratings, a is the period or distance between the grating and θ is the angle from the normal to the coupler. n_{eff} is the effective index of the medium, while n_1 is of the cladding around the grating coupler (this could be air/vacuum). These variables can be visualised in Figure.2.9. Using this design grating couplers with different mediums, sizes and angle of incident, for different wavelengths, with varying percentages of optical power transmitted can be designed.

To improve upon the efficiency, you can place the grating couplers into cavities or use other fabrication methods to improve coupling. Scattered light from these could lose light, decreasing counts needed for quantum optical experiments. The scattered light can also scatter into the chip, creating background noise in the form of scattered light. One solution to this issue is using a mirror on the underside of the GC to reflect any light that passes through back into the GC [68]. Alternative solutions include using the depth of the grating couplers that is different to the waveguide height, to allow for greater diffraction efficiency. We can also taper the height of the gratings to allow for greater mode matching.

Beam Splitters Beam splitters are one of the fundamental building blocks of linear optics. In integrated optics there two two main approaches to implement it: directional couplers [69] and multi mode interferometers [70]. An ideal beam splitter can by described using the following unitary matrix:

$$\hat{U}_{BS} = \begin{pmatrix} \sqrt{\eta} & i\sqrt{1-\eta} \\ i\sqrt{1-\eta} & \sqrt{\eta} \end{pmatrix}, \tag{2.40}$$

where η is the beam splitter reflectively.

Directional Couplers

Directional Couplers are a near lossless method of coupling light between two waveguides, brought together via waveguide bends over an interaction length L_c. A schematic and simulation is shown in Figure. 2.10 a) & b). If the distance δx between the two waveguides in the interaction region is on the sub-micron scale enough for the fields for the photons modes evanescent to

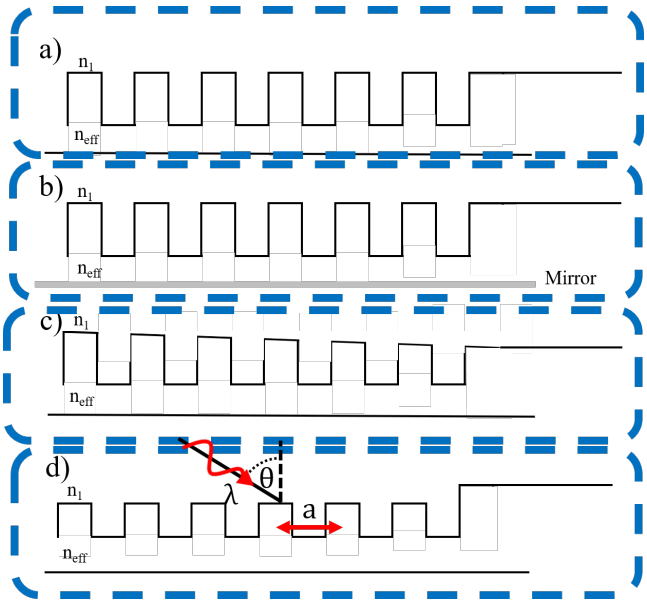

FIGURE 2.9. A side view of different grating coupler designs that are available to increase coupling efficiency into the waveguide. a) Illustration of a standard grating coupler design with the light propagating from left to right into the waveguide. b) Has a mirror on the under side to reflect any un-diffracted light, with the aim of diffracting into the waveguide. c) The gratings have a tapered height/depth to allow the mode mismatch to be more gradual to reduce loss. d) The depth of the gratings don't match the depth of the waveguides, which can also reduce scatter. This also show the incident of light of the photons.

overlap with the adjacent waveguide's. Evanescent being a field or wave which extends into a region where it cannot propagate and whose amplitude therefore decreases with distance. Two modes are excited: the symmetric and the anti-symmetric supermode of the waveguide pair. The difference between these super-modes is that they have slightly different effective indices from one another $\Delta n = n_{eff,odd} - n_{eff,even}$. This leads to a slight difference in phase velocities $v_p = \lambda/T$, which induces beating between them. Where T is the time period of the wave. The light injected into on of the waveguide oscillates between the two waveguides. A coupling coefficient determines the power splitting between the two waveguides, defined by [71]:

$$\eta_{DC} = cos^2\left(\frac{\pi \Delta n z}{\lambda}\right) \tag{2.41}$$

Δn is proportional to the spacing between the two waveguides $\Delta n \propto e^{-\delta x}$. The linear differential solution to this equation can be written using the beam splitter matrix as [72]:

$$\hat{U}_{DC} = \begin{pmatrix} \cos(\pi z \Delta n/\lambda) & i\sin(\pi z \Delta n/\lambda) \\ i\sin(\pi z \Delta n/\lambda) & \cos(\pi z \Delta n/\lambda) \end{pmatrix}. \tag{2.42}$$

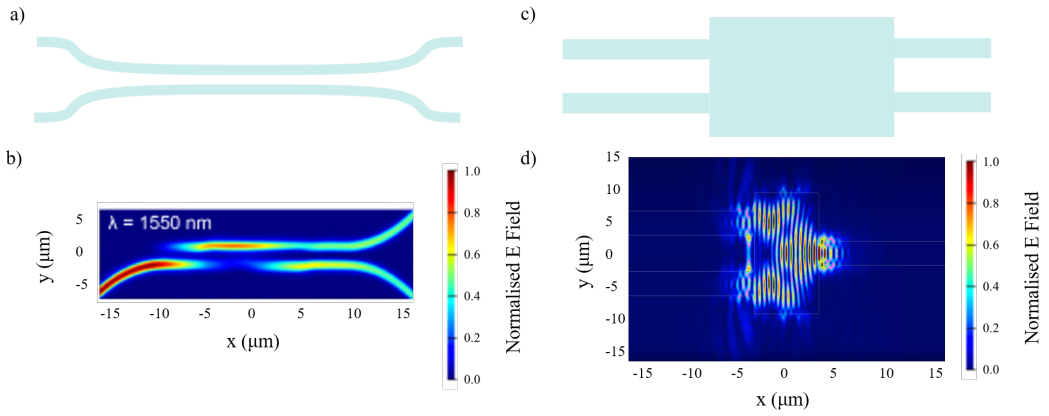

FIGURE 2.10. Directional Coupler and MMI Schematics with Simulations a) Schematic of a directional coupler design. b) A numerical simulation made using FDTD simulations showing that the E field transfer between waveguides successfully with light injected from the bottom left port. c) A simplified schematic of an MMI with two input and two output ports. d) A numerical simulation of a 50:50 MMI made using FDTD showing the the E field splits in half, coupling into each waveguide equally.

For a 50:50 beam splitter you have an interaction length $L_{50:50} = \lambda/2\Delta n$. For a realistic coupler however there is a non-zero coupling contribution from the bending region before and after the interaction length. Finite-difference time-domain (FDTD) simulations of a directional coupler with an interaction length of zero will provide estimates of the effective index difference in the bends, that contributes to the coupling. This gives a final length for the coupling region of interaction length = $z - L_{bend}$, where L_{bend} is the length of the bend region.

Directional couplers are prone to fabrication variations, due to their nanoscale gap size between waveguides. Deviations in this, change the directional couplers reflectively. Typical losses from a directional coupler are 0.05dB for fabricated devices in Si, depending on tolerances and waveguide quality. Directional couplers always have a slight loss and mis-balance to them due to fabrications.

Multimode interference (MMI) coupler

An MMI coupler has the benefit of being a more fabrication robust beam splitter, but typically comes with a higher insertion loss. A schematic for an MMI can be found in Figure 2.10 c) and numerical simulation in d). Multiple waveguides can come in and out of the MMI region, where multiple modes co-propagate simultaneously. Two input and two output ports create a beam splitter MMI. The typical loss observed of devices fabricated in Si are ≈0.1 dB. The multiple modes propagate with different group velocities inside the multi-mode waveguide, they accumulate different phases giving rise to interference patterns within the MMI. Beating from interference, repeated images are formed over periodic lengths within the MMI. By tailoring the length of the multi-mode waveguide, light can be collected through both ports evenly. The transformation

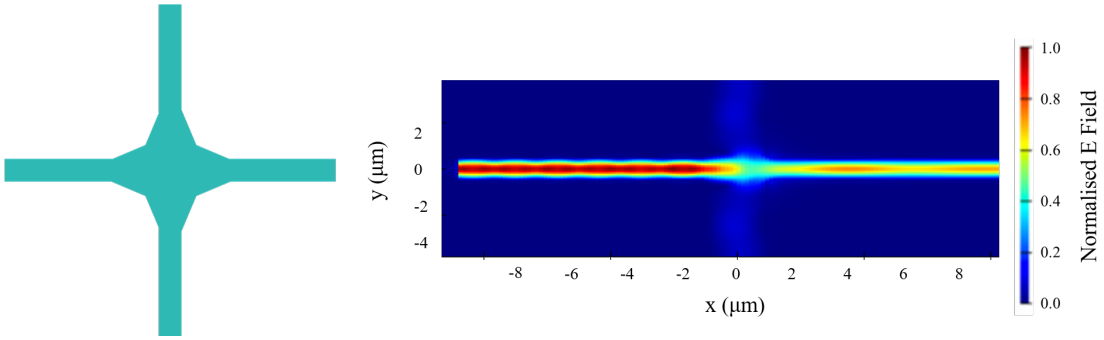

FIGURE 2.11. Crosser Schematics with Simulations Results. a) Schematic of a waveguide crosser coupler design. b) A numerical simulation made using FDTD simulations showing that the E field propagated across the waveguide, with relatively small E field leakage into crossing waveguides. Cross talk for devices have been reports to be as low as -50 dB [73]

given by the MMI of an exactly balanced beams-splitter is given by the matrix:

$$\hat{U}_{MMI} = \frac{1}{\sqrt{2}} \begin{pmatrix} 1 & i \\ i & 1 \end{pmatrix}. \tag{2.43}$$

To keep the fundamental TE mode from single to mutlimode MMI an adiabatic transition of the mode confinement is needed. The angle at which the taper from single mode to multimode is defined by:

$$\theta < \frac{\lambda_0}{2W n_{eff}} \tag{2.44}$$

where θ is the local half angle of the taper, λ_0 is the wavelength in a vacuum, and W is the local full width of the taper at the MMI waveguide.

2.2.5.3 Crossers

In a 2D Si photonics circuit, the mode paths of the photons may need to pass over one another to different parts of the chips, while crossing other photons' paths as shown in Figre.2.11 a). This means there must be intersections, where one waveguide meets another. The paths should be perpendicular to one another and the single mode must be disrupted as little as possible [74]. The waveguide crossing allows a larger density of components to be built on chip due to its small (typically 50 μm x 50 μm) footprint. It can circumvent problems associated with routing waveguides around other structures on chip such as leakage due to evanescent field coupling with another waveguide when their separation is small. The effective index depends

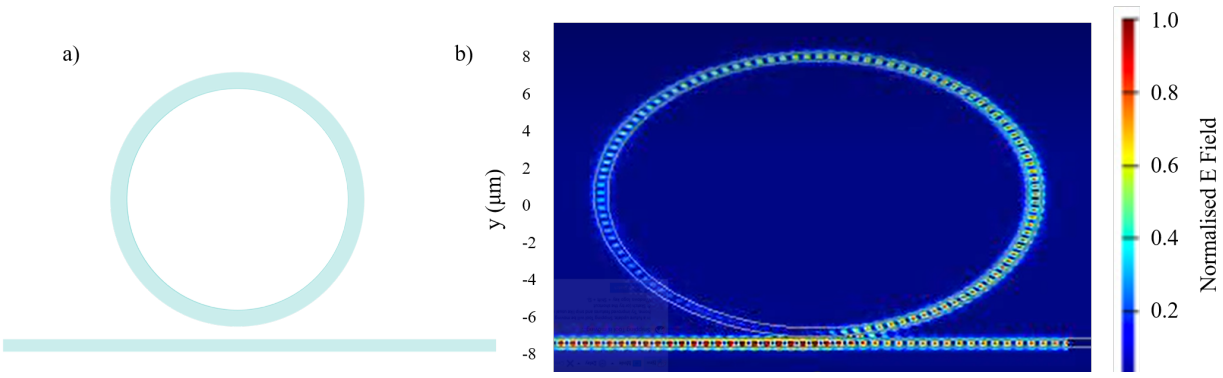

FIGURE 2.12. Micro Ring Resonator Schematics with Simulations a) A simplified Schematic of a Micro Ring Resonator design. b) A numerical simulation made using FDTD simulations showing that the E field propagated coupling into the Micro ring resonator and propagating around before part of the E field couples out.

on the geometry of the medium confining the light. Abrupt changes disrupt the mode, causing scattering and losses [74]. Various designs for waveguide crossings have been demonstrated such as direct right-angle crossings [75], multi-mode interference crossings [76] and sub-wavelength [77] structures. Crosstalk is the power difference between the target port and the ports running perpendicular to the path in the structure. So if the light is injected into the left, with the output target the right, the top and bottom ports power measured and their difference would be the crosstalk. Best crosstalk achieved is $< -70dB$. Mutlimode photons have scatter less with change in effective index, this happens at crossing intersection points. Simulations of light injected into the crosser component showing the magnitude of the E-field.

2.2.5.4 Ring Resonators

In 1969 Macrcatili [78] published one of the first papers on an integrated ring resonator for a band-pass filter. Two straight waveguides known as the bus and port waveguides couple either by directional couplers via the evanescent field or MMI into the ring resonator, creating a unidirectional coupling between the ring of radius R and the waveguide.

The silicon looped waveguide operates at critical coupling where both phase and momentum is conserved through the input of light (E_{i2}) into the cavity, matching the total output (E_{t2}) and losses (α). Critical coupling depends on the wavelength of the light, the interaction (coupling) length between the bus waveguide and the ring, as well as the width of the gap between the ring's waveguide and the bus. This is shown in Figure. 2.12 and described through:

$$\begin{pmatrix} E_{t1} \\ E_{t2} \end{pmatrix} = \begin{pmatrix} r & \kappa \\ -\kappa^* & r^* \end{pmatrix} \begin{pmatrix} E_{i1} \\ E_{i2} \end{pmatrix}. \tag{2.45}$$

The complex mode amplitudes E are normalised, so that their squared magnitude corresponds to the modal power (modal power being the power measured in that particular mode). The coupling parameter's reflection(r) and transitivity(κ) depend on the coupling length L_c and coupling width W_c. The * denotes the conjugated complex value of r and κ, respectively. The matrix is symmetric because the network is reciprocal, therefore: $|r^2| + |k^2| = 1$. Light is trapped in the ring through matching bus ring coupling to losses in the cavity, enabling multiple round trips. The output of the ring is related to the input and the absorption within the ring. The round trip in the ring is given by

$$E_{i2} = \alpha e^{\theta} E_{t2} \tag{2.46}$$

where $\theta = \omega L/c$, with ω the angular frequency, L is length of the ring and c the phase velocity. Ring resonators can be described by certain figures of merit depending on their intend use cases. Micro Ring Resonators (MRR) are used for optical filtering, and as a source to generate photons [79]. One important metric the FSR is defined by is the distance between the resonant peaks which is called the Free Spectral range (FSR), which is the difference between the vacuum wavelengths corresponding to two resonant conditions.

$$FSR = \frac{\lambda^2}{n_g L} \tag{2.47}$$

The wavelength dependence of the effective index is not neglected and is incorporated via the group index n_g, which is defined as:

$$n_g = n_{eff} - \lambda \frac{\delta n_{eff}}{\delta \lambda} \tag{2.48}$$

Another parameter of importance is the resonance width, which is defined as the Full Width Half Maximum (FWHM), where 3dB of the bandwidth of the line shape is cut. The final parameter to consider is the quality (Q) factor, which can be defined as the energy stored divided by the power lost per cycle. This Q factor is proportional to the ratio of FSR and FWHM:

$$Q = n_{eff} \frac{FSR}{FWHM} \frac{L}{2\pi\lambda} \tag{2.49}$$

Ring resonators for their applications should be designed to couple in as much light as possible. When the field at the through port waveguide is at a minimum, critical coupling occurs. There is also under coupling and over coupling that are all achieved under the following conditions:

$$\text{Under Coupling: } \sqrt{\eta_{DC}} > \alpha \tag{2.50a}$$

$$\text{Critical Coupling: } \sqrt{\eta_{DC}} = \alpha \tag{2.50b}$$

$$\text{Over Coupling: } \sqrt{\eta_{DC}} < \alpha \tag{2.50c}$$

2.2.6 Integration of active optical components

2.2.6.1 Phase shifters

The phase of a periodic function, a real variable T (such as time) is an angle representing the number of periods spanned by that variable. It is denoted ϕ and expressed in such a scale that it varies by one full turn as the variable T goes through each period. The phase shifter alters the refractive index of the modes path. If the path length in space is the same between two photons, but their n_{eff} is the difference, the phase between them will increase in magnitude. As their speed of travel will be different, by passing through different refractive indices spaces. This will cause any light wave travelling through, to change in refractive index. This can be used in an Mach Zehnder Interferometer (MZI), to by changing the path length a photon experience. This allows the photons to interfere at this point in a destructive manner. Phase shifting in Si photonics is commonly achieved by the two following methods.

Thermal phase shifters: heat up the waveguide and the surrounding material, in turn increasing the refractive index of the Si [80]. Thermal phase shifters can operate at kHz rates and have relatively low loss compared to PN junction phases shifters discussed next. This is normally achieved by a metal restive material film, placed above the waveguide and the ohmic heating affect by current, changing the refractive index. The thermo-optic effect [81] changes in the effective index from temperature giving the following phase-shift:

$$\Delta\phi = \frac{2\pi L}{\lambda}\frac{dn_{eff}}{dT}\Delta T \tag{2.51}$$

PN junction Phase shifters: changes the free carrier density within the material [82]. The change in the number of charge carriers in turn changes the refractive index. This can be of a relatively higher rate of MHz compared to thermal phase shifters, which provides capabilities for integrated QKD applications. These components tend to have higher loss and the extinction ratio between switches is low. The phase difference between two optical arms in both cases can also be described by the unitary:

$$\hat{U}_{\phi} = \begin{pmatrix} 1 & 0 \\ 0 & e^{i\phi} \end{pmatrix} \tag{2.52}$$

2.2.6.2 Mach-Zehnder Interferometer (MZI)

An MZI is built from two beam splitters with an optical phase shifter inbetween them on one of the optical arms. In integrated Si photonics this can be achieved using two MMI and a thermal optic phase shifter, as shown in the simple schematic at Figure .2.13 a). An MZI transformation matrix is built in the following way:

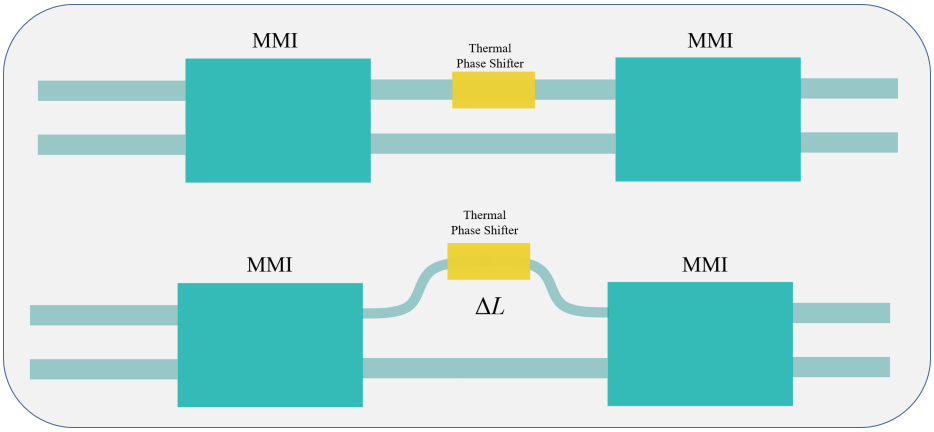

FIGURE 2.13. a) A simplified schematic of a MZI built from two MMI, with a optical thermal phase shifter on one arm. b) An AMZI, that have the same components as the MZI, but with one of the arms is ΔL longer.

$$\hat{U}_{MZI} = \hat{U}_{BS}\hat{U}_{\phi}\hat{U}_{BS} = \frac{1}{\sqrt{2}}\begin{pmatrix}1 & i\\ i & 1\end{pmatrix}\begin{pmatrix}1 & 0\\ 0 & e^{i\phi}\end{pmatrix}\frac{1}{\sqrt{2}}\begin{pmatrix}1 & i\\ i & 1\end{pmatrix} = ie^{i\phi}\begin{pmatrix}sin(\phi/2) & cos(\phi/2)\\ cos(\phi/2) & -sin(\phi/2)\end{pmatrix} \tag{2.53}$$

They are used to separate photons of different frequencies, changing mode paths and filtering off bright pump light after photon generation. An MZI is an important, frequently used component in linear optics and quantum information processing. The above transformation matrix can be used to create a classical interference pattern in the optical intensity at each output port; allowing us to divide optical power equally between output ports, when one port is injected with light.

2.2.6.3 Asymmetric Mach-Zehnder Interferometer (AMZI)

An AMZI is the same as an MZI, with the key difference of having one of the optical arms longer than the other, as shown in Figure.2.13. The difference between the two arms ΔL gives the intrinsic phase difference between the two paths defined by:

$$\Delta\phi = 2\pi\frac{\omega\Delta L}{v_g} \tag{2.54}$$

where v_g is the group velocity. The phase is linearly dependent on the frequency, separating photons whose frequency differ by $\Delta\omega$. With a path difference of $\Delta = v_g/\Delta\omega$ constructive interference is obtained in the top port of the MZI and the destructive interference will exit from the bottom port, assuming the top port is injected light with zero phase. Therefore such a structure can be used for different wavelengths of light to leave different ports of the AMZI. This feature allows the AMZI to be utilised as on-chip filters. The overall goal is that signal and idler photon pairs at wavelengths λ_s and λ_i can be spatially de-multiplexed with high probability.

2.3 Single Photon Detectors

We provide a background and introduction to single photon detectors, with a focus on a specific technology at the end. These devices are a fundamental building block in quantum photonics and it is important to understand their physics to provide motivation in the developments found in the majority of the result chapters.

2.3.1 Photomultipler tubes (PMT)

First utilised in 1935 [83], PMT uses the photoelectric effect by absorbing a photon that has higher energy than the work function to eject an electron. This electron is then accelerated by an electric field, to another plate releasing more electrons, causing a cascade effect. This amplifies the signal into a readable detection. PMT are used frequently because their large spectral range, but not used as efficient single photon detectors, due to their poor detection efficiency [83].

There are also Microchannel plate PMTs that have lower jitter at 30ps full-width at half-maximum. The jitter is the error in time of recording the detection event. This is achieved by reducing the path of the initial electron. PMTs are physically fragile, require high voltages (kVs) and are expensive [83]. They are also importantly not scalable to Si photonic applications. They are not integrable into nanophotonic structures, which prevents them being part of an enclosed system.

2.3.2 Single photon avalanche diodes (SPADs)

SPADs in Si were found to be single photon detectors in 1980 [84]. They operate the diode in the Geiger-mode which is biasing the diode at a higher voltage than the diodes breakdown voltage (Zeeman Effect) [85]. This is caused by a release of free electrons, that is then amplified by the avalanche, which causes a breakdown in the PN junction. Afterwards they are reset through quenching. Si SPADs have a spectral range of 400 to 1000 nm, a peak efficiency at 650 nm of 65% and FWHM timing jitter of 20ps [86].InGaAS SPADs are used in telecommunications as their band gap (1.7 μm) allows them to detect 1550nm photons with reported up to 20% efficiencies.

2.3.3 Superconducting Detectors

For measuring single photons many superconducting detectors are available, that use their property of superconductivity and the breaking of superconductivity to signal the arrival of the photon. We cover some of the technologies available.

Figure.2.14 shows metrics that are considered and choosing a detector.

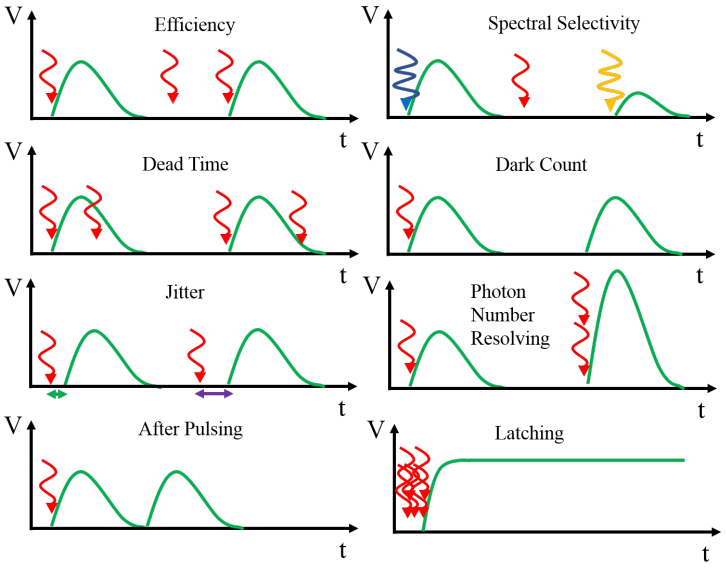

FIGURE 2.14. Detection efficiency is the probability of the creation of a detection signal when a photon arrives. Some detectors exhibit different behaviour depending on the wavelength of the photon to be detected. Dead time represents the time the detector requires to recover from photon detection until it is ready for a new photon. Dark counts are detection signals that arise without the arrival of a single photon. Jitter is the variation in time difference between photon arrival and signal generation. Some detectors have the ability to resolve the number of photons arriving. Detectors may after pulse, where the detector emits another pulse from the energy and noise of the system included from a previous detection event. Latching is a state achieved where the detector remains in the non detective state possibly induced from heat, current or number of photons detected.

2.3.3.1 Superconductivity

The classical mode of resistance versus temperature is they are proportional to one another. As you increase temperature you increase resistance, due to the number of collisions with the travelling electrons increasing, because to increased vibrations. But it has been noted that as some materials began to reach the 0 K regime, their resistive behaviour didn't follow trends.

In 1911, by the cooling of liquid Helium, Mercury was the first material to have be measured to having a zero resistance [87]. This phenomenon was named superconductivity. The theory of superconductivity became fully described by Bardeen, Cooper and Schrieffer (BCS) in 1957 [88]. They built upon the theory from Landau of the electron-electron interaction via phonons. Just above the Fermi surface, electrons pair up using phonons, binding them into pairs. These are so named Cooper Pairs. The pair of electrons behave as bosons by their exchange of symmetry. If all other states are below the Fermi surface (that can be realised at lower energy levels) and adding two electrons, their centre of total momentum, will behave to show no centre of mass.

These Cooper pairs allow for superconductivity.

Superconductors can break their superconducting states by the current driven through them surpassing a certain threshold value. Once the current is above this value the material returns to the restive state. This threshold value is called the critical current (I_c). The critical current density (J_c) is the critical current within a certain surface area. Critical current density is geometrically independent and a property of the material, while critical current is normally a property measured and labelled to a superconducting device.

When choosing a superconducting material there are a limited number of superconductors available, due to the large number of detector parameters that have to be optimised: optical absorption across a range of wavelengths, operating temperature, material stability under thermal cycling, fabrication yield, resistance to dark counts, and output signal amplitude.

Superconductors also have a specific temperature, which is they are not below at a specific pressure will loose their superconductive state. This is called the Curie Temperature T_c.

2.3.3.2 Superconducting Tunnel Junctions (STJ)

STJ were first used to detect X-Ray photons, but later were extended to detect optical photons. They were the first superconducting single photon detector. They consisted of two superconducting films that were separated by a buffer layer on the order on 1 nm in thickness. Applying a voltage through the two films allows for an incident photon to be absorbed by the top layer to create quasipartciles that tunnel through the buffer layer, leading to a voltage peak. These require very low temperatures of mK, making them difficult for wide-spread use, as the higher temperatures can cause thermal tunnel. Their jitter was respectively high at μs scales. They have very small Dark Count Rates (DCR) and detection efficiency η with count rates of 10s of kHz.

2.3.3.3 Superconducting transition-edge sensors (TES)

Superconducting transition-edge sensors (TES) [89] use the superconductivities temperature dependence. The thin film is cooled to below T_C, and when a photon of sufficient energy is incident , it pushes the temperature above the T_C causing a voltage peak. This is measured using a superconducting quantum interference device (SQUID). The size of the voltage peak is dependent on the energy of the photon. These can have efficiencies as high as 95%, and dead times of 100 ns, but their large jitter of around 100 ns. TES are used as the first superconducting detector integrated on a waveguide [90]. TES have also been used as bolometers [91] that have enabled large detector arrays for several applications, including Cosmic Microwave Background (CMB) measurements.

2.3.3.4 SNSPDs Mechansim

The SNSPD is a thin film of a few nm in thickness, to 100s of nm in width and the length varies from 1-1000μm, depending on the detector design. The superconducting nanowire is biased

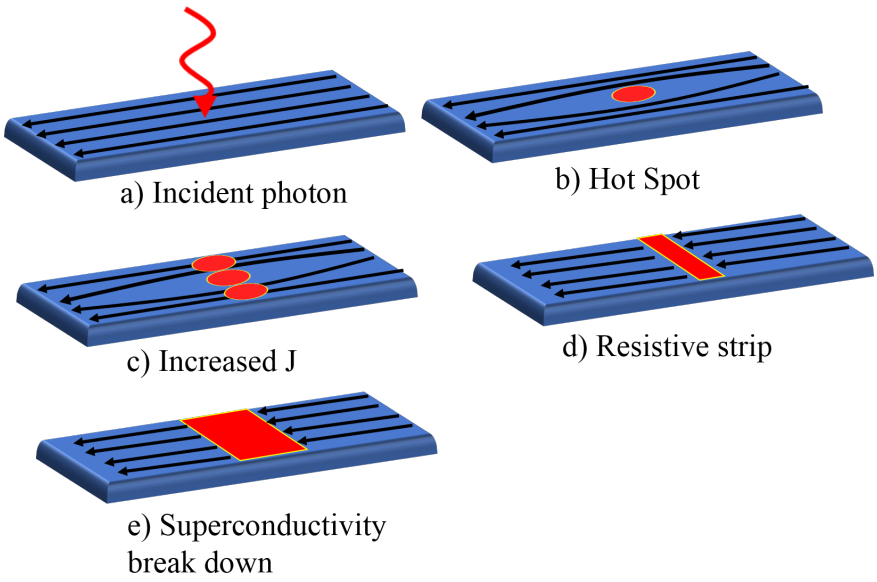

FIGURE 2.15. Diagram of the SNSPD triggering method, based on an illustration in the initial paper by Gol'tsman[92]. a) A photon is incident on the current carrying detector releasing energy into the nanowire; b) a "hotspot" is formed pushing the supercurrent around the resistive region; c) if the bias is sufficiently high, 'sidewalks' of the detector are pushed past the critical current threshold, transitioning to the resistive state: d) a fully-resistive spot forms spanning the detector; e) the resistive region then entirely spreads along the wire via Joule heating, increasing the measured resistance.

just under its I_c. When a photon is incident on the surface, it is absorbed by the material. The mechanism of the detection in an SNSPD is shown in Figure. 2.15. The energy from the photon is sufficient to break the Cooper pairs within the material, eliminating superconductivity there. This creates a hot spot and resistive area, forcing the current around the hot spot. The current density therefore increases towards the edges, pushing it over the critical current density (J_c). Therefore a whole strip become resistive, breaking the superconductivity. These results can be measured as a voltage spike. This can then relax if the temperature and I_c to return below their thresholds. The voltage spike is the measurement of a photon, impinging on the surface and being absorbed. Therefore using a voltage sensor a threshold value can be set and if the voltage measured surpasses this point a detection event "click" is recorded.

2.3.4 Current Research

Integrated Waveguide Detectors (IWDs) have been shown to exist on the same device with other passive photonic components (ring resonators[93], grating couplers[67] and directional couplers[50]). In [93] they demonstrate high detection efficiency of 91% and how the length of the nanowire can directly affect photon absorption, further showing that the width of the nanowires

can directly affect the dark counts. Reducing the width reduces DCR, while length increases efficiency and DCR.

Thermal conductivity measurements can use SNSPDs [94] in thick-films. They are used to show that the thermal conductivity of thin SiO_2, which are used in optical cavities, compared to SiO_2, which is used in bulk as cladding, is smaller than the bulk. By fabricating WSi wires in parallel one is used as a Joule heater, causing a hot spot and a temperature gradient across the film. The nanowires running parallel at consistent pitches will have different I_c. Being at different temperatures forms, surrounding the substrate and mapping the temperature.

Crystalline and amorphous superconductors each have their own strengths as SNSPD material candidates. Crystalline has been shown to give better jitter, dead time, higher T_C and DCR, while amorphous has superior efficiency and fabrication yield. This paper [95] uses the proximity effect in superconducting metals to allow for pinning of the electrons to share properties. The proximity effect between metals and superconductors is when a normal metal is introduced close to a superconducting material and the normal electrons diffuse into the superconductor, suppressing the T_C. There is also a counter-effect where superconducting electrons diffuse into the normal metal, but this is less common in photo detector technology. 2 nm of WSi on top of 2 nm of NbN on top of SiO_2 in an optical cavity, display properties of 96% efficiency, 52 ps Jitter, <5 ns reset time. With a T_C of 2.6 K, that lies between the two materials T_C in thin-films [96].

In 2016 A. Vetter [97] released a paper critiquing an SNSPD cavity system using photonic crystals and a nanowire of only 1 μm long, to reduce kinetic inductance, speeding up the detectors. The periodic crystal structure increases the efficiency ten-fold and produces sub nanosecond results of 120 ps decay time, 510 ps recovery time and 32 ps timing jitter.

E. Schmidt in 2017 [98] published the use of an Al-N buffer layer for NbN on GaAs, demonstrating a higher critical temperature, critical current density and lower residual resistivity in comparison to films deposited onto bare substrates. This also demonstrated three orders of magnitude lower dark count rates and about ten times higher detection efficiency at 900 nm being measured at 90% of the critical current. The system timing jitter of SNSPDs on buffered substrates is 72 ps which is 36 ps lower than those on bare substrate.

SNSPDs have been integrated with new state-of-the-art photonics sources, to characterise them within a photonic circuit. In [99] single walled carbon nanotubes (SWCNT) are placed inside a waveguide structure and electrical stimulation of the SWCNT causes photonic emissions down waveguides. SNSPDs are placed along these waveguides to characterise the the emissions from the SWCNT.

SNSPDs have also shown to be the detectors used in QKD experimental, because of their high detection efficiency and low dead times [1, 100, 101].

2.4 Error Reduction

All measurements in science come with errors, this experiment is no different. The system's fundamental measurements measure the arrival times of photons with high precision to find the correlation between these events. Photons are challenging to measure due to their low interference with the matter. Photons are also a particle quickly produced and abundant in the environment. Filtering out photons from the environment and ones used to construct complex entangled quantum states provides a challenge. Therefore we aim here to minimise the errors to find only the photons we want to measure.

The system challenges described are a source of errors and do not represent the system, and can be filtered out to show the statistical ensemble produced from the system and its projection more accurately. One of these is dark counts that occur when no laser stimulated emission occurs and are photons from other sources within the detector system. These low values can be measured and subtracted from the counts.

2.4.1 Detection efficiency

The system efficiency of the SNSPD can be defined as the photon detection's efficiency once it enters the system the SNSPD is housed in, defined by:

$$\eta_{SDE} = \frac{R_{detected}}{R_{input}} \tag{2.55}$$

This equation is also considered as a black box efficiency. Here $R_{detected}$ is the rate of photons detected, and R_{input} is the rate of photons injected into the system. Equation 2.56 defines the system detection efficiency (SDE) broken into three contributing factors. The coupling coefficient $\eta_{coupling}$ represents the probability of the photon coupling into the detection region.

$$\eta_{SDE} = \eta_{coupling}\dot{\eta}_{absorption}\dot{\eta}_{trigger} \tag{2.56}$$

The absorption coefficient $\eta_{absorption}$ represents the probability of the coupled photon being successfully absorbed into the thin film. The triggers coefficient $\eta_{trigger}$ represents the probability of the device registering the measurement through a voltage pulse. The light emitted from an optical fibre diverges with distance, therefore maintaining a minimum distance between the optical fibre end and grating coupler maximises coupling efficiency. As the centre of these miss align, the optical power decreases ($1/r^2$) with distance from the grating coupler's centre. Waveguide integrated SNSPDs require the focal point of the lens to fall onto the focal point (centre) of the grating couplers.

2.4.2 Post-Processing

Another source of signal and idler photons created besides the rings within the devices are the silicon waveguides, but not within the ring resonators. These photons pairs may be created at different times. They are named accidentals due to their probability of coincidental measuring with other detection events. These events are not the target generated quantum states. Hence we ensure their filtering from final counts. This is also measured and subtracted from the final measurement by repeating the measurement detection with the ring resonators out of the critical coupling regime, allowing for only pairs generated within the waveguide and therefore measured.

DWDM filters out the signal and idler photons but do not provide perfect extinction; therefore pump and other wavelength photons also reach the detector. The number of these is also measured by counting the number of coincident events at different delay times. Using a coincident window offset from the determined arrival time of the target entangled pair, we can determine the background number of photons. The coincident window is ten times larger than the 1 ns window used, to the average of events, to remove local maxima and minima. This provides a background number of photons throughout the system besides dark counts and stimulated emission. These counts are also subtracted from the end measurement to provide a close approximation to the system's statistical representation.

2.5 Low Temperature Physics

In this section we cover the physics, technology and equipment used, to allow us to enable SNSPD operations. This is relevant as Chapter.4 explores the uses of an SNSPD and the technologies surrounding it.

2.5.0.1 Flow Regimes and conductance

There are three different flow regimes to consider. These regimes describe the behaviour of the molecules inside the vacuum. The viscous flow regime is where most gas molecules collisions are exclusively with each other. The Knudsen flow regime [102] is where particles have an equal chance of colliding with each other as well as the boundaries (the wall). Lastly the molecule flow regime, which is where particles are most likely to have collisions with the wall. Details about the regimes are shown in the Table. 2.1.

Conductance is the measure of "pumping power" on a system. For this to be as high as possible, the pumping out system uses a pipe and when pipes are connected in parallel the conductance is additive, but when in series its the reciprocal. Therefore the shortest pipe possible will give the best flow regime.

The different flow regimes can be described by Knudsen number, which is defined as:

Flow Type	Viscous	Knudsen	Molecular
Knudsen number	<0.01	0.01<0.5	>0.5
General Pressure/mbar	few mbar to 10^{-1}	10^{-3} to 10^{-1}	10^{-3} to 10^{-7}

Table 2.1: Flow Regimes by Knudsen number.

$$K_n = \frac{k_B T}{\sqrt{2}\pi p d_m^2 d_{flow}} \tag{2.57}$$

where k_B is the Boltzmann constant, T is temperature, p is pressure, d_m is the molecular diameter and d_{flow} is the flow channel diameter. Further the conductance can be defined as:

$$L_{cond} = \frac{d(V_{vol}p)}{dt}\frac{1}{\Delta p}. \tag{2.58}$$

2.5.1 Cryogenic Liquids

As stated in the previous sections SNSPDs require cryogenic temperatures to function. This also means that the integrated photonics on the same chip is required to be at cryogenic temperatures. Over a century of research has gone into making dewars and cryostats as cold as possible, researching down to μK temperatures. In this section we give an introduction to the physics of achieving these low temperatures. The most common method of achieving temperatures close to 0 K is by using cryogenic liquids. There are several metrics to consider when choosing a cryogenic liquid.

- Firstly the boiling point, indicating at what temperature and pressure a medium phases between the liquid state and the gaseous state.
- The latent heat, which is the energy required to change the material between different state phases. Higher latent heats are desirable for cooling as we can extract more heat from an object before changing state, over a lower latent heat. The latent heat of consideration for cooling at cryogenic temperatures is the enthalpy of vapour.
- Specific heat capacity, the amount of energy required to heat 1 kg of material by 1 K. A high heat capacity will provide a stable temperature.
- Lastly, thermal conductivity can be defined as the rate at which heat is transferred by conduction through a unit cross-section area of a material, when a temperature gradient exits perpendicular to the area.

Two common cryogenic liquids used are Helium $^4He_2$ and Nitrogen N_2, which having boiling points at standard pressures (1 Atm) of 4.2 K and 77 K respectively.

^4He is extracted from natural gas. The low boiling point is stated and ^4He hasn't been known to exist as a solid at standard pressure, but can exist as a superfluid [103]. As a super fluid, which occurs at 2.2 K under standard pressure. A superfluid has no viscosity of such, so experiences no friction in this state, has a high thermal conductivity and vaporisation of this fluid can only occur at the surface. These properties means it provides great temperature homogeneity and flows towards warmer areas to increase the evaporation rate.

2.5.2 Cryogenic Systems

This section outlines how different cryogenic systems function and how their designs allow for different temperatures to be reached. All cryogenic systems consist of the following design engineer considerations. Isolating the cold environments from the hotter ones: this is achieved using vacuum isolation or a cold jacket. A cold jacket is where a intermediate cryogenic liquid separates the warmer environment from the colder one, such as a Helium system covered in liquefied Nitrogen. An alternative method is by using vacuum isolation. Minimising the existence of a medium for heat conduction and convection to travel through. Materials have different expansion coefficients, therefore matching them to ensure vacuum or mitigating damage through compression is crucial. Lastly it is import to monitor the pressure within the systems, so pressure gauges are attached, as turning liquids to gas can lead to high pressures quickly which can be dangerous.

2.5.2.1 Helium Dewar

This is the simplest and lowest vibration method of cooling, by dipping the test item in a dewar filled with pre-liquefied ^4He. However liquid He is increasingly becoming a rare resource and this provides an inefficient and costly method to operate SNSPDs as to use SNSPDs constantly would require the constant boil off of ^4He as the ^4He is lost to the environment. It is pumped from the system as the expansion of gas in these dewars are not typically contained for sustainable periods. It is becoming an increasing rare resource, which increases the price. An additional factor is the operational complexity of limited cooling times. A 4.2 K temperature is sufficient to cool NbN based SNSPDs, but other SNSPDs in research as WSi require lower temperatures.

2.5.2.2 Closed-cycle refrigeration

The temperature of a liquid cryogenic can be reduced below its boiling point by reducing the pressure. This is done by connecting a vacuum pump to where the cryogenic liquid is contained and pumping the vapour, extracting heat via evaporation and thereby cooling the liquid. There can be multiple regimes where this occurs in cryostats. This can be performed as a continuous

operation, where the flow of liquid ^4He matches the vaporisation rate, or single-shot, where the vaporisation is greater then the flow of liquid ^4He in. Single shots are usually used to obtain a lower temperature for a limited time until the ^4He in the volume runs out.

This cooling process by evaporation can be described by the combination of the Clausius-Clapeyron and the Ideal Gas equation [104]:

$$\frac{dP}{dT} = \frac{LP}{\Delta R T^2} \tag{2.59}$$

where P is the pressure, R is the ideal gas constant, T is temperature, and L is the latent heat. It can be shown that the cooling power $\dot{Q}$ of the bath being pumped on is related to the rate the number of particles being transfer from the liquid to the vapour phase state [104].

$$\dot{Q} \propto exp(-\frac{L}{RT}) \tag{2.60}$$

Cooling power exponentially reduces with temperature as well as the superfliud state of ^{4}He having a higher evaporation rate, requires increasing higher vacuum pump power.

Closed cycle cryostats use cold heads, which are closed refrigeration systems using ^4He to provide the cooling power. A Gifford-McMahon (GM) [105] cryostat is used to cool systems. A schematic describing the functionality of the the cryo-cooler is presented in Figure. 2.16. The GM cycle builds upon the reverse Stirling cycle [106] which is based on the Carnot cycle by introducing a rotary element between the cold and hot sides of the system alternating connection between high- and low-pressure lines. The GM cycle suffers vibrational noise, and their mechanical parts are prone to failure. A pulse tube offers a solution with no moving parts in the cold head. Pulse tubes come in two general types: Stirling-type, operates at 60 Hz and has high efficiency, but has a higher base temperature. The GM type, which operate at 1 Hz to 2 Hz, are less efficient but have low vibration, and can reach temperatures below 4 K.

Instead of ^{4}He, we can use the rarer isotope ^{3}He, can be used to reach temperatures down to 0.3 K, due to its larger vapour pressure. We can also reach lower temperatures by having a mixture of both isotopes [104].

2.5.2.3 Cryopumping

For isolation, high vacuum is a must. This is typically achieved using rotary or turbo-molecular pumps, but in cryostats, where the walls of the cryostat around a few Kelvin, a more power pumping method can be achieved if already at a rough vacuum ($< 10^3 Pa$). This is cryopumping, where the remaining molecules will condense onto the cold walls inducing a higher vacuum, beyond the capabilities and speed of a turbo pump. Cryopumping requires sources to the other pumps to be closed, due to its pumping power, and can cause higher vacuums in the other connected pumps drawing through oil in the pumps, that can then also condense onto the walls and contaminate the cryostat.

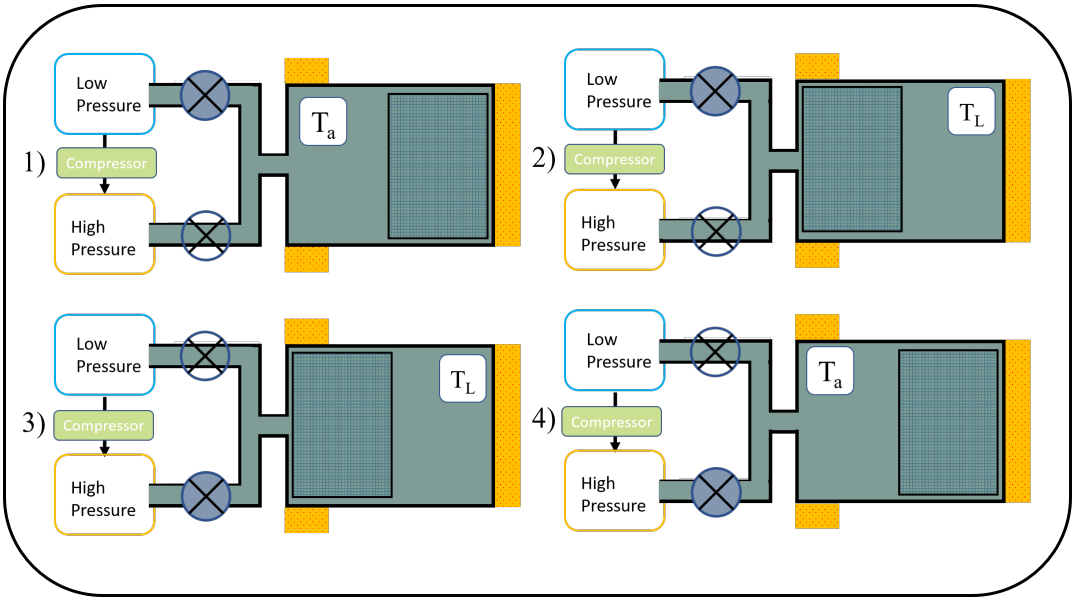

Figure 2.16: Gifford-McMahon cooler's cooling cycle in four-stages: The environment is connected to two different pressure environments controlled by valves and a regenerator moving between left and right. (Orange: heat exchangers, circle-cross: Values {filled = shut, unfilled = empty}. 1) $\rightarrow$ 2): The dark green displacer moves from right to left, while open to high pressure environment. Gas passes through the regenerator, while exchanging heat to the regenerator, $T_a \rightarrow T_L$. 2) $\rightarrow$ 3): While open to the low pressure environment, the gas flows through the regenerator (unmoved) and the gas expands isothermally. This step generates the cooling power. 3) $\rightarrow$ 4): Regenerator moves from left to right, forcing cold gas to flow through taking up heat, $T_L \rightarrow T_a$. 4) $\rightarrow$ 1): The system is open to the high pressure environment compressing the gas at T_a, causing heat to be released to the heat exchangers.

2.6 Amplifiers

In the next three following sections electronics around SNSPD readout is explained. This is relevant to understand the SNSPD readout technology presented later thesis in Chapter 5.

When an SNSPD is triggered a sharp voltage pulse occurs, with a exponentially trailing edge, returning the voltage to zero (excluding noise). The amplitude of these pulses are on the scale of μV. As the pulses travel along Radio Frequency RF signal sustaining medium, the pulse further decays over length of travel. Many of the devices used to count the number of voltage pulses from an SNSPD detector measured at mV levels. Amplifiers are commonly used to amplify (increasing the amplitude) of the SNSPD pulse to $mV - V$ magnitudes.

Transistors: At the heart of an amplifier is a transistor. A transistor is a semiconductor device that is used to amplify or switch electronic signals. It is commonly used in digital circuits as a switch for the ON or OFF state. It is the foundation to build up logic gates. Applying a small electrical current to the device can allow larger current source to flow through to amplify the input signal, therefore having a dual purpose.

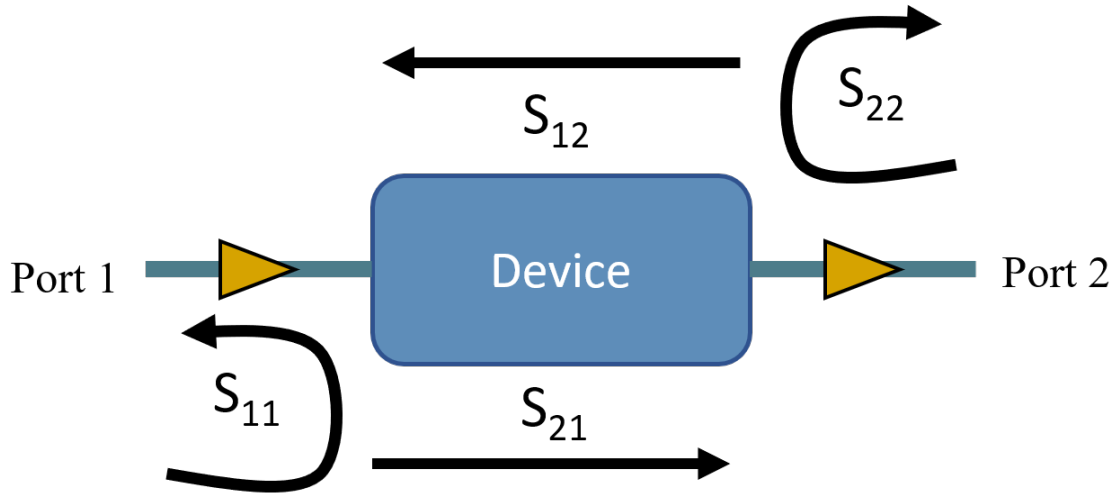

Figure 2.17: A diagram schematic representing the scattering parameters, where a electrical RF signal is injected into a device. S_{11} - Reflection coefficient at port 1, when the signal is sent from port 1 and received at port 1. S_{12} - Reverse Transmission, when the signal is sent from port 2 and received at port 1. S_{21} - Forward Transmission, when the signal is sent from port 1 and received at port 2. S_{22} - Reflection coefficient at port 2, when the signal is sent from port 2 and received at port 2.

A Low-Noise Amplifier (LNA) is an electronic device that amplifies a low-power electrical signal (signals close to the noise-floor) increasing the ratio of the Signal-to-Noise. The amplifier will introduce some additional noise, but the difference between the amplified noise and the signal provides no hindrance to the SNR.

2.6.1 Scatter Parameters

Scattering Parameters, known as S-parameters are mathematical representations of the energy propagation within a multi-port electronic network. They are used within electronic engineering to characterise electrical linear networks for communication systems, mainly for RF and microwave engineering. This is expressed through complex matrices, consisting S parameters. They give a full combination of the transmission and reflection parameters in the network as shown in Figure. 2.17. Here below a 2 port network is shown.

$$\begin{pmatrix} b_1 \\ b_2 \end{pmatrix} = \begin{bmatrix} S_{11} & S_{12} \\ S_{21} & S_{22} \end{bmatrix} \begin{pmatrix} a_1 \\ a_2 \end{pmatrix} \tag{2.61}$$

$S_{nm} = b_n/a_m$, where b_n is the outgoing signal amplitude and a_m amplitude is the incoming signal. Where $a_m = V_m^+/\sqrt{Z_m}$ and $b_m = V_n^-/\sqrt{Z_n}$. V are the positive and negative voltages depending on the direction and Z_m is the factor of impedance. These parameters are used to characterise the gain through an amplifier circuit.

2.7 Field Programmable Gate Arrays (FPGA)

SNSPDs can have detection rates at MHz frequencies. A device that measures and logs the arrival time of these events is named a time tagger. Time taggers can be designed to host input signals from multiple SNSPDs. In quantum photonic experiments, millions of photons can be measured on an SNSPD in each second, with quantum information experiments increasingly using more SNSPDs [35]. The experiments also require us to know the precise arrival time of the photons (ps), to be able to measure coincidences between detection events (detection events that occur simultaneously). Many entanglement based experiments require these measurements. A logic device to tag every incoming channel requires high precision and for it to host multiple detection events.

An FPGA is essentially built up from many interacting transistors [107]. An FPGA provides design with flexibility and parts providing almost any digital function [108, 109]. An FPGA is a programmable logic device, made of semiconductors and is a subset of programmable logic devices. In 1969 Programmable Read-only Memory (PROM) devices were available with the ability to erase them coming in 1971. In 1975 Programmable Logic Arrays (PLA) were finally released. Complex Programmable Logic Device CPLDs are multi PLA with input and output connections between devices and the whole system itself [110].

In an FPGA is a programmable device consists of only, wires, logic gates and register/flip-flop. They contain an array of programmable logic blocks, in a hierarchical design which allows for the reconfiguration of the inter-connectors between the blocks, metaphorically wiring them together as the user sees fit. This allows for complex functions of logic to be executed. It is configured using a Hardware Description language (HDL). They are typically programmed by using Very High-Speed Integrated Circuit (VHSIC) Hardware Description Language (VHDL) or Verilog [111]. Many FPGAs can also have memory stores in the way of flip-flops. Flip-Flops can store a single bit of data each. They are electrical circuits that can change state by applying one or more inputs, which then give one or two outputs. This is the basic storage for logic.

FPGA logic use Look Up Tables (LUTs) routing between each other. LUTs have different sizes depending on the number of inputs, [109]. If m is the LUT size we need m^2 inputs to configure this. Each input requires a memory location. Larger LUTs require greater amount of memory location, but small LUTs compute less logic and need more routing between them, creating more complex systems. LUTs can be combined to make Adders that are used to add. Adders are logic devices built up to add numbers together. Therefore you can count and multiply with enough Adders. Here we have the beginning of a Central Processing Unit (CPU). Each Adder can be thought of as controlling a BIT (switch between 0 or 1, On or off state). Four, 1 BIT Adders can create a 4 BIT Adder. The connection and configuration of these LUTs (collection, communications) is designed by the manufacturer, but how different LUTs communicate is implemented by the end user. An example of the fabric of an FPGA is shown in Figure.2.18

Electrical pulses are a foundation in timing and communicating within an FPGA, where

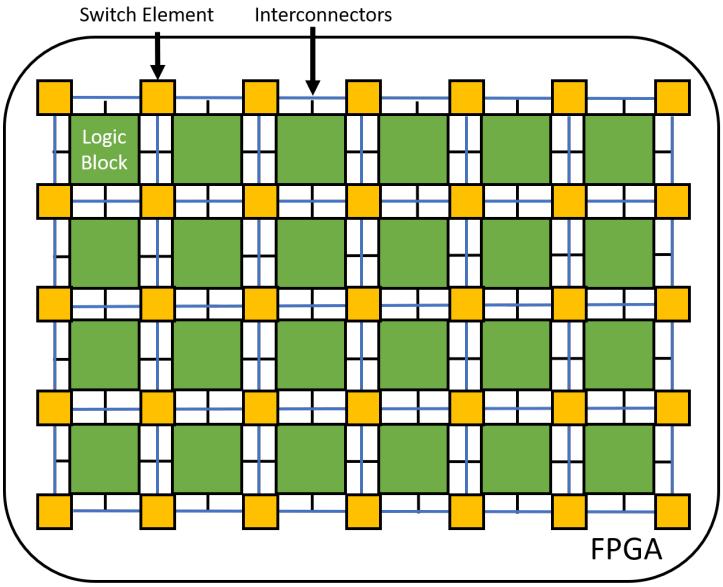

FIGURE 2.18. Cartoon illustration of the fabric inside an FPGA, with the switches and logic blocks connected with inter-connectors between them.

operations can start on the rising edge or a falling edge of the electrical pulse signal. We therefore will refer to these as X edge, where X is the signal reason/origin, such as a clock pulse signal.

The main performance advantage of an FPGA comes from its concurrent nature, providing very fast operational speeds down to its logic-based circuity compared to commercial general CPUs and GPU used in computers. Also, utilisation of asynchronous logic elements implementations over other options make them desirable for fine time measurements due to the ability to exploit the physical nature of the semiconductor device to gain ps resolution in timing.

The drawback of FPGAs compared to Application-Specific Integrated Circuits (ASIC), which are similar to FPGAs but customised for the needs of the application, is logic utilisation [112]. Non-utilise logic blocks in an FPGA consume power needlessly. Research shows that the average logic area taken up by an FPGA is 35 times that of an ASIC counter-part leading to a 14 times greater dynamic power consumption.

ASIC: These typically achieve better timing resolutions than FPGAs, however this is reflected in their cost. Roughly 100'000 units of ASIC become more cost-efficient than the FPGAs at the same number of units [112]. Therefore unless ASICs are widely mass manufactured for the purpose, FPGAs are considerable a plausible tool for timing measurements.

J-Tag: is a common hardware interface that provides a communication interface between hardware and a PC. [108]. Four dedicated pins called TDI, TDO, TMS and TCK deliver 3 inputs and 1 output from the FPGA, to deliver the programming code. The TCK is the clock, TMS is the signal that controls the TAP controller (a state machine), and the TDI, TDO with the TDI shifting bits to the FPGA and the TDO shifting the same bits out.

Critical paths are slowed with LUTs and Adders depend on previous LUT or Adder, therefore carry chain logic flows through to initialise other logic throughout the FPGA. These are built up from a system of connected AND and OR logic gates, with mutli dimensional inputs and outputs. PROM have AND logic gates going to OR gates and then out putting while PLAs have vice versa. FPGAs are enabling many key products such as self-driving cars, the Internet of Things, Robotics, Machine Learning, Smart Diagnostics etc.

FPGA Criteria When choosing and evaluating an FPGA for specific task there are a number of criteria to judge the performance:

- The number of logic gates the FPGA has.
- The cost per a logic gate and the cost of the overall FPGA.
- The speed that they run at, measured by the maximum clock frequency input,
- The power consumption: low power consumption provides less heating and more efficient logic. Considerations during static and dynamic power states.
- On board storage both power on and off (SRAM and Flash).
- The number of I/O available.
- Timing is deterministic.
- Reliability.
- Range of temperatures to function at.
- Life time and endurance of the flash memory and the FPGA.

2.8 Time-to-Digital-Converter (TDC)

2.8.1 Coincident Counting

An application of TDCs is in the counting of photons [113]. Many quantum computing applications require the measuring of the coincidence of two or more photons being detections simultaneously: meaning being a photon triggering a detect the same time as another. This is required because many applications utilise the entanglement property between photons for operations, where metrics of entanglement can be gathered via coincident measurements. A statistic ensemble is gathered over many measurements from photon pair generation being correlated with time. The count rate of the “signal" photons C_s and the “idler" photons C_i can be determined using the rate of photons incident on the detector R_s, R_i and the efficiency to measure each photon η_s, η_i, is described with $C_{i,s} = \eta_{i,s}R$. Therefore the net count rate is a combination of the efficiencies of both detectors used and the rate of photons incident.

The rate photons are incident do not always match. N_n is the net coincidence count (CC) rate described by $N_n = N_t - N_a$, with N_t total number of photons measured and N_a being the accidental photons measured. Accidental photons make measuring CC more complicated as their sources can be from DCR in the detector, non-linearity generating more photons in waveguides, pump photons leaking into space and noise from other sources. This rate of photons is further encapsulated by greater description of the models as shown in [114]. Affects such as DCR can be measured prior to CC measurements of entangled photons to characterise the system and subtracted, to give a true CC rate.

Ultimately the efficiency of measuring the pair of the photons can be given by:

$$\eta_{CC} = (1-(1-\eta_s)^n)(1-(1-\eta_i)^n), \tag{2.62}$$

where n in this case is the number of photon pairs produced at the source and to reach the detector. The formation of this equation can be understood as $(1-\eta_s)$ is the probability of the "signal" photon not making it to the detector, therefore $1-(1-\eta_s)$ is the probability of NOT the photon not making it to the detector.

2.8.2 Introduction to TDCs

FPGAs are digital devices and the voltage pulse from an SNSPD is an analogue signal, holding the timing of the detection event. Engineering to transform and extract the time of the signal into a digital signal that can be interpreted by the user is required. A TDC is a device that has be engineered to perform this operation.

TDCs are precise time measurement devices commonly used in many different science and engineering applications [115]. They have popularly been used in Time-of-Flight (ToF) applications such as: LiDAR systems [116], PET scanners, QKD [117] detection systems and Phased-Locked Loops (PLLs). TDCs are closely related to Analogue-to-Digital-Converters (ADCs), so much so that some TDCs implementations use ADCs [118].

TDCs convert an analogue pulse that occurs at a specific time into a digital signal that can be interrupted into a time stamp to record the time the signal was detected. It measures the difference time between the START and STOPS signals. Mostly modern day TDC implementations occur on FPGAs, ASIC and other circuitry, using the most fundamental logic components as the resolution of the TDC. The resolution is presented by the Least Significant Bit (LSB) of the time stamp. In an FPGA the STOP signal is a clock edge and the START is T_{in}, which is measured relative to the clock.

2.8.3 Coarse TDC

The most basic form of TDC is the coarse counter. Using a START signal, a counter starts counting the number of clock edges that occur until the insertion of a STOP signal. The time between the

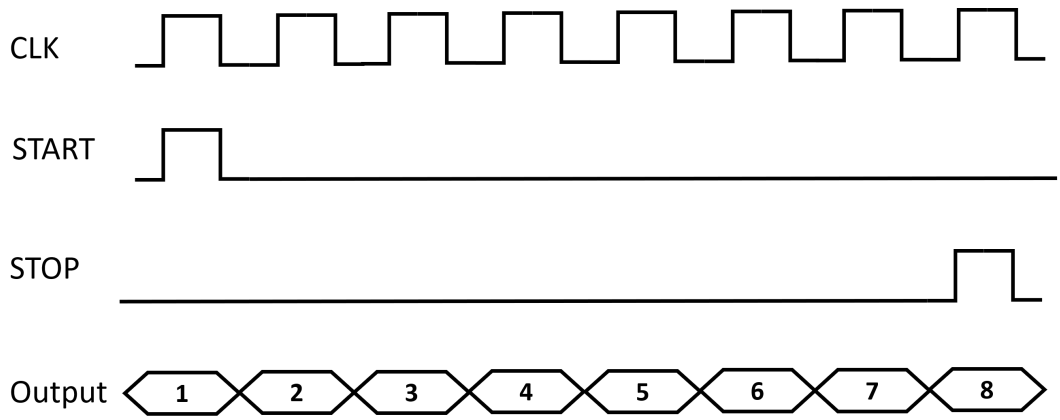

FIGURE 2.19. Illustration of a coarse counter TDC and its waveforms. With the clock signal at the stop setting the resolution and the START and STOP signals beginning the counting of the number of clock periods that is outputted as the value in the bottom row.

START and STOP signals is quantised by the clock edges. The waveforms of the time difference between the START and STOP signals while counting the clock edges can be seen in Figure.2.19

The advantage of this method is its simplicity, using less logic as it only requires registering the counter values as the counter increments. Therefore the limitation is the resolution being limited to the clock frequency. Increasing the resolution means increasing the clock frequency.

A variation on the coarse counter is the Multi-Phase Clock, which uses multiple phase-shifted clocks to generate different counters. This increases resolutions, at the cost of reasonably high logic utilisation.

The Multi-Phase Counter is different to the Multi-Phase Clock by using the total number of clock edges and the number of clock periods passed. The passed phases $\Delta\phi$ implements fine timing element. The time difference is a combination of both measurements, as shown:

$$\Delta T = nT_{clk} + \Delta\phi \tag{2.63}$$

2.8.4 Fine TDC

Fine TDCs [119, 120] are defined as schemes that perform beyond the limitations of the clock period. The coarse time quantisation is overcome and still implemented on FPGAs and ASICs. In this sub-section some fine TDC concepts and schemes are presented.

Time-to-Analogue Converters: One method is Time-to-Analogue converters (TACs) [121–123], essentially converting the time signal to an analogue one and then the analogue signal to the digital value. First, time is converted to a voltage, and then the voltage to digital with the use of ADC. The time between the START and STOP signals is linked to the electrical charge stored

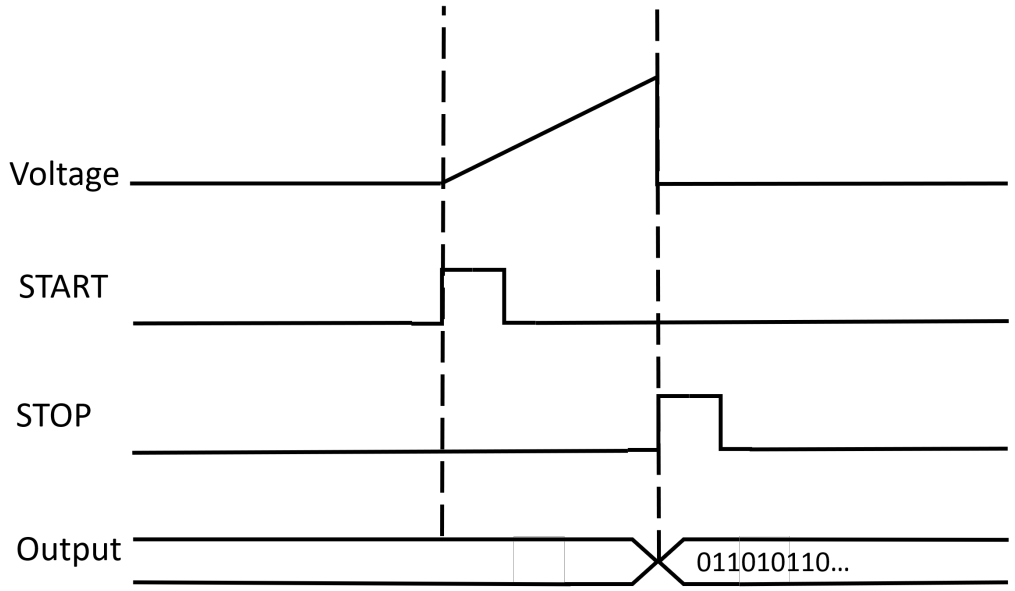

FIGURE 2.20. Waveforms of TAC based on a TDC, with the analogue voltage increase controlled by the START and STOP input lines. This measured voltage is converted into the binary code representing the time.

in a capacitor, with the START signal beginning the charge and the STOP signal discharging and using the ADC.

An integrator op-amp is used to achieve this, integrating the input voltage over time between the START and STOP events. This then passes to the ADC. The waveforms of how the time difference between the START and STOP signals are converted into the output code can be seen in Figure. 2.20.

This is a generally older TDC method and cannot be implemented on the FPGA [124] due to its non-digital elements. Resolutions of 10 ps were achieved in 1988 [125], but their main limitation is their large dead time on the scale of μs. The source of this large dead time is two fold. The double-conversion of time to analogue and then analogue to digital have two separate dead times. The second reason is that the capacitor requires a full discharge before another measurement.

Tapped Delay Lines: More popular and fully digital are Tapped Delay Lines (TDLs). TDLs consist of equal length delay elements chained together to subdivide time intervals into equally sized bins. The START signal propagates through the delay line until the STOP signal is asserted and the delay line stated captured. The STOP signal is usually replaced with the CLK edge. The triggers relative time compared to the clock edge is captured in the delay line.

The resolution of the TDL is dependent on the delay elements, which is the smallest bin size. In FPGAs, D-type flip-flops are used as this element. The D-type flip-flops ensures that inputs Signal (S) and Reset (R) are never equal to one at the same time. The D-type flip flops

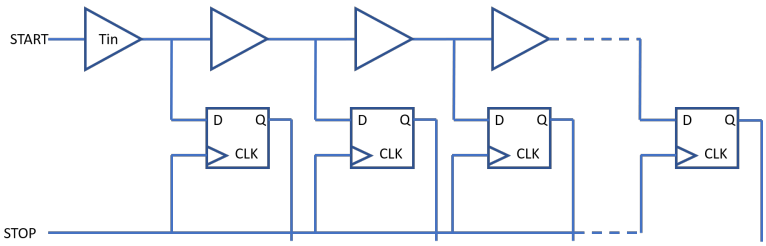

Figure 2.21: Circuit diagram of a TDC implemented on an FPGA backed on delay lines using a carry chain structure.

are constructed from a gated SR flip-flop with an inverter added between the S and the R inputs to allow for a single D (Data) input, which linked together form a trialling list of '1's and '0's. To increase the number of bits represented by the fine code, the logic consumption increases exponentially. A breakdown of the TDL can be seen in Figure. 2.21. The TDL length in time is usually equal to the clock period, to provide maximum capture of input signal. Therefore the time event of the signal can be described.

A differential TDC is a TDC variation which aims to improve the signal integrity of a TDC by operating in differential mode between elements by alternating the propagating signal by '1' and '0'. This method was reported to improve the metastability by in-trade of an increase in the logic utilisation of about four times [126]. The time of the event can be described by

$$T_E = \frac{T_{STOP}}{N_T} N_i + \epsilon, \tag{2.64}$$

where T_{STOP} is the clock period, N_T is the total number of delay elements, N_i is the number of delay elements triggered and ϵ is the quantisation error. Quantisation errors arise when it is necessary to convert a continuous analogue variable into a digital code using a limited number of significant figures.

Other fine TDCs: Area Vernier delay line. A Vernier delay line utilises two delay lines: a fast and slow delay line and measuring the difference between their propagation in delays. The thermometer code is captured when the START and STOP signals catch one another. Thermometer code resembles the output produced by a thermometer. In thermometer code, a value representing number N has the lowermost N bits as '1'; others as '0'. So, to move from N to $N+1$, just change the rightmost '0' to '1'. The START signal trigger one delay line, while the STOP the other. The time difference is between the fast and slow delay elements, going past the quanisation of the delay element size. These are usually formed into a Vernier Ring that loops the signals to optimise logic utilisation.

Another form is a Pulse Shrinking TDC, where the pulse of the time between the START and STOP signal is attenuated, down until there is no longer a pulse. The number of times the pulse

is shrunk is counted, therefore not limited to the delay line size element. This optimisation on logic saving is much higher than a TDL, the resolutions lower due to the signal conversion.

2.8.4.1 Hybrid Counter

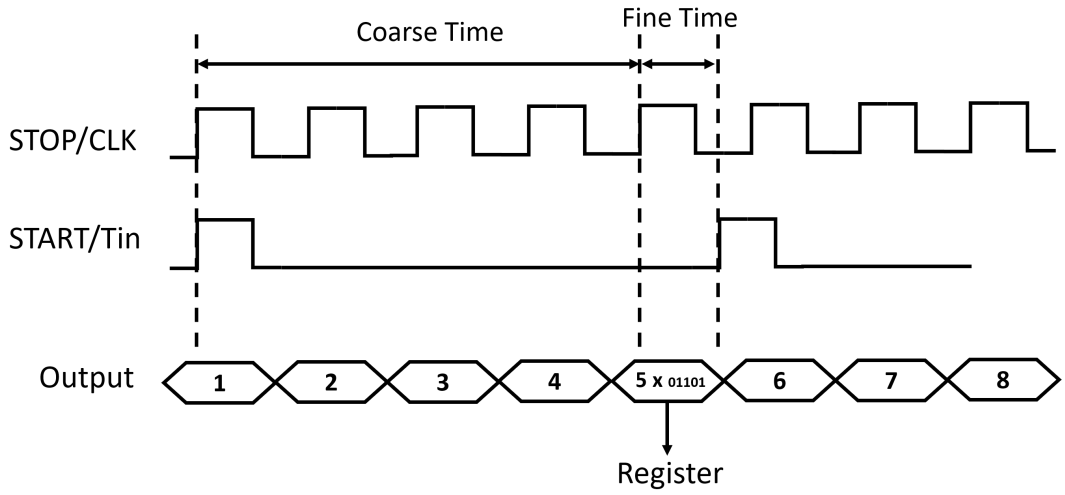

Figure 2.22: Time evolution of signals in a delay line based TDC implemented in an FPGA employing the carry chain structure. The squares are flip-flops, where the Q output triggers if the D input is high. W

Also called the Nutt Interpolation scheme [127], a hybrid counter is a method of combining fine and coarse interpolation schemes to provide TDC architectures which can count longer ranges with higher precision. These work by measuring time intervals greater than the clock period with a coarse counter, while the fine TDC measures the intervals shorter than the clock period, described by,

$$T_E = nT_{CLK} + \frac{T_{STOP}}{N_T} N_i + \epsilon. \tag{2.65}$$

Where T_{CLK} is the clock period and n is the number of clock periods. The waveforms for this scheme can be viewed in Figure.2.22.

2.8.4.2 Carry Chain

For fine time measurements, such as the ones implemented here, we use asynchronous logic circuits such as the carry chain, which subdivides the clock period into smaller bins.

Carry Chains are features within FPGAs, providing efficient arithmetic operations (such as adders and counters). Each logic element can implement a one count of a counter bit. Logic elements can communicate to other logic elements and parts of the FPGA with general-purpose

routing structures. These are relatively slow, signal routes therefore most FPGAs have an extra routing signal connecting logic element to one another as can be visualised in Figure.2.23. They are heavily optimised for speed along the carry chain path, allowing hundreds of MHz counting speeds. The shorter the carry chain the faster the counter must be clocked, so as to restart the carry chain in-time with its finish.

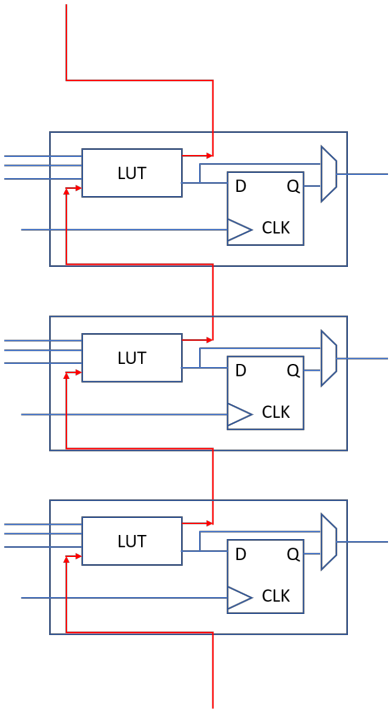

Figure 2.23: Illustration of a carry chain used to subdivide the clock period into the smaller bins, made up of multiple LUTS.

Within some FPGAs a dedicated fast look-ahead carry logic is provided called CARRY4, which provides performance fast arithmetic addition and subtraction in a slice. These carry chain blocks are cascade-able to form wider add/subtract logic. They consist of four bits per a slice, using carry multiplexers and dedicated XOR gates. These logic blocks elements form block to form large logic operations similar to the illustration in Figure. 2.23.

2.8.5 Errors and Precision in a TDC

As a TDC is a device used in measuring timing events, understanding and calibrating the timing errors in the device is vital to allow the user to calculate that exact time of the event they are measuring. The concept of measurement errors in TDCs reflects the measured sinusoidal input and spectrum of the output signals, which is obtained by applying the Fourier Transform to the input to transfer it to the frequency domain. It takes multiple measurements to form the spectrum, and a process of constructing this spectrum is called the single-shot experiment. Taking

a single shot measurement for a fixed time interval and measuring for multiple instances while characterising the measurement ranges and errors affecting these measurements, can present multiple errors such as: TDCs non-linearity, quantisation errors [128], metasability [129, 130] and offset & gain errors. The quantisation of time and digitising presents inevitable measurement errors affecting the precision of the measurement. In this section some of the errors affecting TDCs are discussed.

To measure the time precision error margin, repeating measurements at a fixed time interval and recording will produce a histogram with a Gaussian distribution of the probability of hitting the desired time bin. This error in time precision is a symptom of jitter and noise affecting the measurements. Using the standard deviation σ, single-shot precision's (SSPs) (also known as RMS time-resolution) and FWHM to quantify this. An SSP is defined as $\sigma/\sqrt{2}$.

In an ideal TDC the relationship between input and output code should be linear. Therefore every bin should be equal. However due to temperature, power fluctuations, fabrication tolerances and routing TDCs suffer non-linearities. TDCs can be calibrated to reduce the effects of the non-linearity on a bin by bin basis. These bin sizes can be measured by using an out of sync, random time difference between the START and STOP triggers, over a large number of hits. The probability of filling each bin is linked to the bins size: the more counts, the larger the bin size. A visualisation of the differences is shown in Figure.2.24.

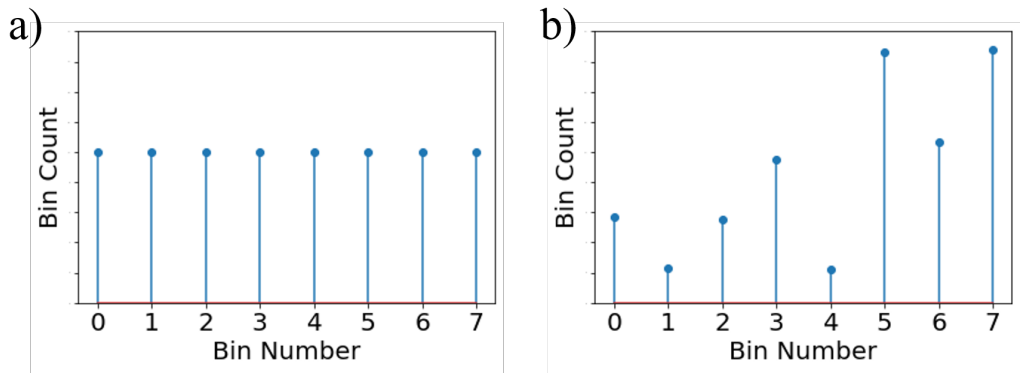

Figure 2.24: Illustration of ideal and non-ideal delay line bin.

The offset error is an error in the measured code that is the intended time shifted along the time axis, registering as a longer time than intended. The non-linearity of the TDC is a typical occurrence of this error. The offset and gain errors can be quantified by the DNL and INL respectively.

2.8.5.1 Differential/Integral Non-linearity

Differential Non-Linearity (DNL) describes the deviation between how analogue values and digital values correspond with one another. It is used as a specification of measuring the error

in DACs and ADCs [115]. The Least Significant Bit (LSB) is the smallest unit bit position in a binary integer, also thought of as the lowest order bit or right most bit. To increment this by one a specific voltage step is assigned to it V_{LSB}. An example is increasing 0.2V each time increase the LSB by 1 each 0.2V. Ideally, any two adjacent digital codes have one LSB difference. The ADC can give an increase of two LSB for one V_{LSB} giving a DNL value of +1, and vice-versa. This leads to "missing code" where bit strings are skipped over or remitted for the same or different voltage values, respectively. A DNL step value can be defined by:

$$DNL_i = \frac{V_{out}(i+1) - V_{out}(i)}{LSB}, \tag{2.66}$$

where $V_{out}(i)$ is the voltage at that bit, DNL_i is the DNL at the i_{th} bit and the LSB is a single bit step. Integral Non-Linearity (INL) is the maximum deviation from the actual output from the ideal. The INL at the i_{th} bit is defined by

$$INL_i = \sum_{i=0}^{n} DNL_i. \tag{2.67}$$

This gives the error of the entire carry chain. A graphic representation of how this works can be found in Figure.2.25

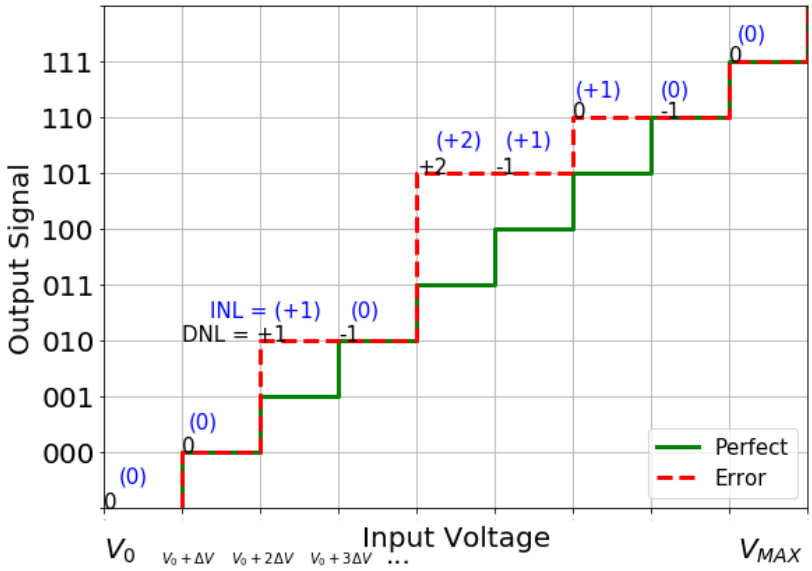

FIGURE 2.25. Missing code examples, for mis-registering LSB values. With the example of how the arbitrary input voltage values provide LSB changes and the DNL and INL values obtained from the missing code values.

As mentioned DNL and INL are parameters used to measured quantities of an ADC or DAC precision. The input analogue signal will trigger the step up or step down of LSB, by measuring

the voltage without skipping any levels or without holding at the same level in an ideal case. The DNL is the maximum deviation from LSB between two adjacent levels. 1 LSB is the ideal distance between bits, smaller than this would mean the bin is smaller and larger than this would mean the bin is larger. If the DNL is two or greater, then missing steps(code) can occur. INL is essentially the cumulative sum of all the DNL values for each bit up to that point being measured, giving the total offset of the system.

Another phenomenon affecting the linearity of the TDC is the number of missing bins. These bins do not collect any Hits and cannot be used in the time quantisation. Therefore minimising the number of missing bins to activate bins ratio improves the linear trend. There are a few methods to tackle this: adding more activate bins to the line, selecting a line where the missing to activate bins ratio is lower, or averaging over multiple lines by paralleling the input signal sent to all of them.

2.8.5.2 Quantisation Errors

Quantisation errors are the errors the between occurrence of the actual event and the measurement of the event. In practical occurrence the quantisation values change half up and down with respect to the event. Since quantisation errors have equal probability of occurring in any measurement, the error can be expressed as a uniform distribution.

The standard deviation in a uniform distribution can be shown by $\sigma = u/\sqrt{3}$, where u is the uncertainty In this case the uncertainty is the quantisation step in time of the code T_{code}. There are usually two signals for the TDC: the START and STOP signal, each with their quantisation error in measurement therefore doubling the error for each time recording. Therefore the error can be described as:

$$\sigma_{error} = \sqrt{\frac{T_{code}^2}{12} + \frac{T_{code}^2}{12}} = 0.408 T_{code} \tag{2.68}$$

where T_{code} is the time event code recorded. Aspects that can change the quantisation errors are power and temperatures, affecting all events evenly.

2.8.5.3 Metastability

Metastability occurs from setup (initialising the state) and hold (maintaining the state) violations in flip-flops becoming a unpredictable state. This is a typical occurrence in asynchronous TDCs. The flip-flop takes a time T to process the trigger readout the event and store. There is also the time of the event t. A critical window is made up from the setup time and the hold time of the flip-flop. The setup time is just before the clock and an input signal is asserted, while the hold time is the time after the flip-flop receives the trigger and is registering the reading. If these times occur in the critical window of the flip-flop, the result is unpredictable.

Metastability can be reduced in a number of ways, such as: increasing the dead-time, allowing more time for stabilisation; adding the number of delay elements (flip-flops) (but these also increases the dead-time, so requires a trade off); or lastly characterising the device by finding the metastability occurrence times, and adding any code falling to this window as white noise.

2.8.5.4 Digital Signal Processors (DSP)

When choosing an FPGA as a TDC, engineers fabricating them tailor their characteristics to be optimised for specific use cases. A unit called DSP are tailored to be optimised for TDC implementation on FPGAs. DSP are specialised microprocessor chips, with architecture designed with optimising for the measuring, filtering and compressing of analog signals. FPGAs also have dedicated DSP blocks, with logic designed to behave as a DSP. DSPs are advantageous from their ability to work in real time and provide light power efficiencies. For a TDC it is necessary to have a higher enough bandwidth DSP for the signals to be time tagged. A low bandwidth increases the precision measured on the rising edge of the pulse. For an FPGA to be used as a TDC the number of DSP slices must be greater than or equal to the number of analogue signal input channels.

2.8.6 Experimental Methods

2.8.6.1 TDC calibration and linearisation

The bins in a TDC implemented on an FPGA, depend on the fabrication of each logic unit used as the smallest time resolution. For variance in the fabrication, bins have different sizes and be vary between one another in the same clock cycle. Bins variance is persistent between clock cycles. Bins may also capture no hits as they are considered dead and cannot register a STOP signal. A typically bin size is on the cycle of several ps, with the variance between bins being at the same magnitude. We discuss following methods to overcome fabrication in-perfections to improve precision and mitigate error nous bins.

Two methods can be used two reduce the affect of errors and improve the precision. These are linearisation and calibrations. The linearisation is a compensation that is implemented to minimise the DNL error. While the calibration improves the INL by not changing, but post-processing the steps bin-by-bin afterwards. In this sub section a few methods of calibration and linearisation techniques are discussed.

2.8.6.2 Direct Calibration

The simplest method is a direct calibration [131] where once the TDC is set up, finding the time period width of each bin. By changing the delay time between the START and STOP triggers, at step sizes smaller than the resolution of the bins. Increasing the delay slowly and measuring the time taken over each bin. This is resource intensive as takes exhaustively longer times for

high-resolution TDCs and long delay lines. Also requires a delay generator capable of input delays smaller than the LSB.

2.8.6.3 Code Density Testing Calibration

This standard approach involves un-synced START and STOP signals triggers asserted into the TDC for a statistically significant high number of counts [115]. Therefore providing the bins to have equal chance to capture the same counts. But the different bin period sizes, amount to different count totals. As larger bins are statistically more likely to get hit. The bin widths in time is described with:

$$Bin_{Time} = T_{clk} \frac{N_i}{N_T}, \tag{2.69}$$

with T_{CLK} is the clock period, N_i, is the number of counts for that bin and N_T is the total number of bits summed from all the bins counts. Summing all these counts the INL can be corrected to remove the error.

To calculate the number of total counts required to give a confidence limit a Gaussian distribution can be used. With A is the number of bits in the time code, z_i, is the area under the Gaussian and β is the tolerance level. The total number of counts required is described with:

$$M = \frac{z_a(2^A - 1)}{2\beta} \tag{2.70}$$

2.8.6.4 Equivalent/Averaging Coding Line TDC Technique

This method is to mitigate the effects of non-linearity by employing multiple delay lines. Both the Equivalent Coding Lines (ECL) and the averaging use multiple delay lines, but the processing is different. In both methods you would calibrate each delay line, with a previous calibration technique mentioned above. Routing the input signal and trigger on the parallel lines and either averaging the result afterwards, or summing up and using their transfer functions. Both increase the resolution and mitigate non-linearity's. They are also more resource intensive taking up another delay line, for each level of precision increased by.

2.8.7 Universal Asynchronous Receiver/Transmitter (UART)

FPGAs communicate their output logic to another device for storage. Many FPGAs can be implemented to communicate using a UART communication protocol. UART protocol transmit data asynchronously, which means there is no clock signal to synchronise the output of bits from the transmitting side to the sampling of bits by the receiving end. In-place of a clock signal, the transmitting UART protocol adds start and stop bits to the data packet being transferred. These

bits symbolise the beginning and end of the data packet so the receiver knows when to start and stop reading the bits. Also a parity bit is used, to check for errors encase of any bit flips. The bit length of the data packet is between seven and ten bits, plus the 3-4 bits for start, end and parity bits as shown in Figure. 2.26. Here Tx and Rx are the transmission ports and receiver ports for the electrical signals, respectively. Both sides are required to have these parts to start and stop sending communication signals between themselves.

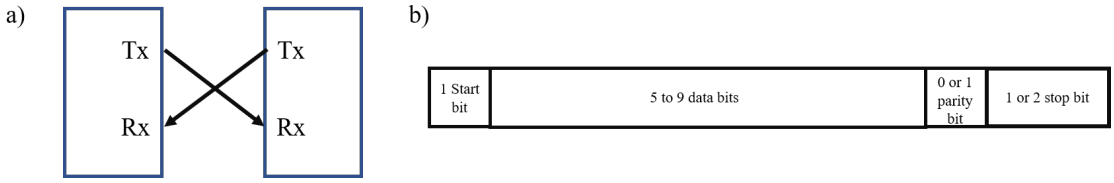

FIGURE 2.26. a) Data flows from the Tx pin on the transmitting UART to the Rx pin of the receiving UART and vice versa is possible. b) The structure of the data package around the transmitting data frame.

When the receiver collects a start bit, it begins to read the arriving bits at a particular frequency known as the baud rate. The baud rate is a measure of the speed of data transfer, expressed in bits per second (bps). Both transmitter and receiver must operate at about the same baud rate. The baud rate between the transmitter and receiver can only differ by about 10% before the timing of bits gets misaligned to far and a corrupt signal is communicated.

2.9 Summary

In this background chapter we have discussed the relevant material for a foundation knowledge for the reminder of this thesis:

- Quantum Theory - Introducing quantum postulates that define quantum theory and how they lead to quantum information and our ability to utilise quantum physics in this technology area.
- Integrated Photonics - Introducing background material on technologies that allow for the realisation of quantum information applications. Including optical components building blocks widely used in silicon.
- SNSPDs - Discussing research and physically mechanisms of these devices. We also explained the low temperature physics and technologies required to operate the devices
- Time Taggers - Introduced the electronics background of using amplifiers and FPGAs to build time taggers for SNSPD applications.

Quantum information systems are set to utilise these techniques to become part of a quantum future. The rest of this thesis concerns developing the integrated platform for quantum key distribution and quantum information.

CHAPTER 3

HIGH-DIMENSIONAL ENTANGLEMENT VERIFICATION OVER MULTIPLE INTEGRATED CHIPS

We have described in the previous chapters how quantum optics enables quantum information tasks to be performed in an integrated photonic components approach. The experiments reported in this chapter demonstrate some of these capabilities. Here, we investigate silicon photonics as a platform to create a network of multiple integrated quantum devices to perform scaled-up experiments. The experiment's focus is to develop and control large numbers of complex interferometers for the generation and processing of high-dimensional (qudits) entangled states of photons across multiple devices. The experiments' particular result is proving the potential of silicon photonics as a platform for a high dimensional Quantum Key Distribution (QKD) protocol between two users using the third device. This third device hosts part of the communication protocol to divide resources, increase security and allows a network of many users to be established. The third device is also a proof-of-concept for a many user network, with the third device connecting to many devices, to act as a node within a network.

Multiple experiments have previously been carried out demonstrating distributing high dimensional entanglement across multiple devices [132–136]. The encoding of qudits has been demonstrated in many different degrees of freedom [35, 135–138]. However, the approaches listed here have not demonstrated a network of 3 separate integrated quantum optic devices controlling, generating and measuring qudits. One of the verified routes to obtaining high dimensional entangled states in integrated photonics is by utilising spatial modes to path encode. This allows highly coherent and high fidelity measurements [35]. In this experiment, we describe an approach to phase stabilisation, amongst other advances that allow us to overcome the challenges encountered during scaling. A third device is a technical challenge, primarily due to the loss of information between devices. The third device increases security by outsourcing

the receiver/communications parties. Allowing no user increased control over the system than another party.

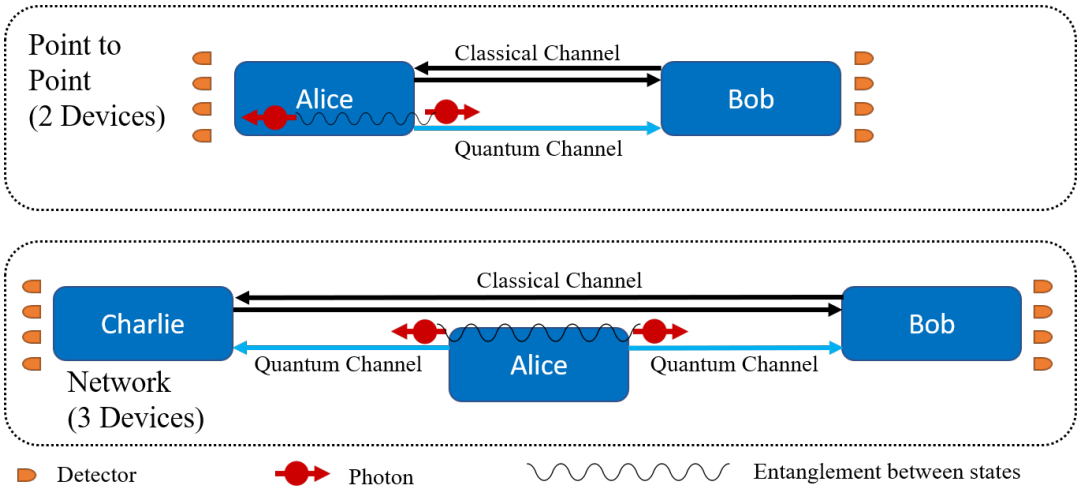

FIGURE 3.1. Diagram of 2 devices (top) and three devices (bottom) QKD set-up. Alice and Bob are generating a shared key at the top, while at the bottom, Charlie and Bob are generating a shared key. In both set-ups Alice prepares an entangled pair of photons (shown in red, with the entanglement between shown by the black wavy line) and sends one of the pair to Bob. The difference is that in the two device set-up, Alice measures one of the pair of bipartite photons she generates, while in the three device set-up, she transmits that photon to Charlie.

Figure. 3.1 shows how two device and three device set-ups can work in QKD. Three devices (Alice, Bob and Charlie) over two devices (Alice and Bob) provide an increased technical challenge in dealing with the system's higher loss and complexity. The system, on the other hand, provides an increase in distance between the two parties. They are allowing for the transmitter device to be in-between the two communicating parties. The third device also reduces the complexity needed by the communication parties as no generation and preparation of states is required. This also allows a single transmitter device to be connected and used between multiple mixtures of parties, showing that many parties (>2) with receiver devices can connect, and communicate through the transmitter device.

Following this train of thought, we can see how this transmitter device can become a node in a network — allowing for multiple parties to generate keys between multiple other parties. This localisation of the laser's resources, along with complex state preparation electronics and photon sources, allows for QKD to become more accessible. A star network, as shown in Figure.3.2 can be formed with the node in the centre. This reduces the number of total connections, as every user does not require a quantum channel, just the central node that transmits the states. In the University of Bristol there is a bulk optics version, where a trusted node-free eight-user metropolitan quantum communication network exists [139]. This reduction in the total number of

connections provides an increase in the communication system's security, providing fewer points to access the in-between network users.

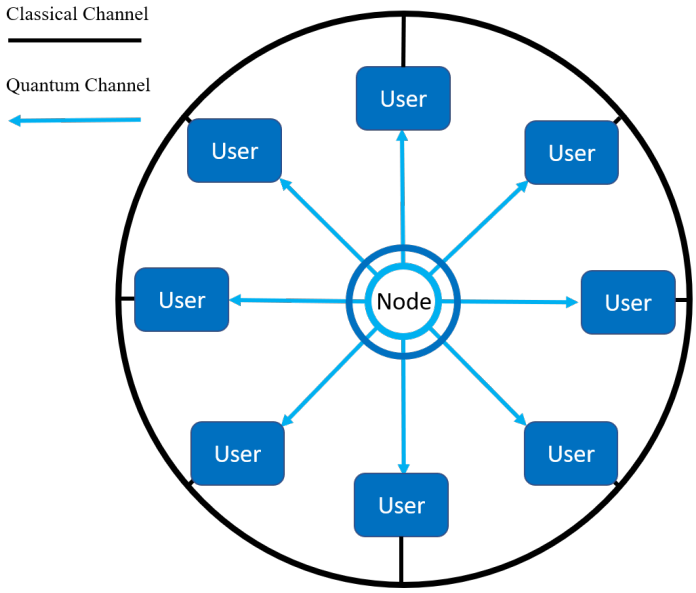

FIGURE 3.2. Star Network of QKD System. The central node generates entangled pairs, transmitting each one of the pair to users to generate a key between them while using the classical channel to set up a protocol.

This chapter begins with a description of the integrated silicon photon device network and the set-up used. We report on the device's characterisation and set-up to overcome environmental challenges faced in maintaining entanglement of qudits across devices by showing basis measurement projection results. We demonstrate quantum information processing results on a single device, followed by chip-to-chip results for two devices, to overcome phase drift using the stabilisation method later described. Finally, we demonstrate High Dimensional (HD) QKD protocols working across three different devices.

3.0.1 State of the art hyper-dimensional quantum information experiments

Qubits transmitted in optical systems travel at light speeds like any optical based communications in general and therefore are a natural candidate for quantum communication systems over large distances (>200 km). The number of available quantum states on a single device relative to the size of the device grows exponentially for n number of photons in a d dimensional space according to d^n [35, 136, 137]. This provides us with the opportunity to increase the information density per device. Increasing n for current integrated linear optical systems has proved to be a challenging problem due to these photons' source, which depends on parametric single-photon sources. The ability to generate these n photons also becomes exponentially difficult with n. Therefore to overcome this, we chose the second path of increasing the number of dimensions the state exists

in. This has already been demonstrated in [35] by producing a smaller number of high-quality states through a larger linear optical device.

Semiconductor fabrication have increased the number of optical components on a single device, providing large bandwidth external control sources and allowing cohabitation of single-photon detectors, on these devices allow for qudits to be realised. The drawback of this is that the device's footprint and complexity increases and becomes a more considerable concern with increasing d as mentioned in [140]. In the paper, path encoding is used, which allows highly coherent and high fidelity measurements, showing two-photon states in up to 15 dimensions. An alternative method to avoid a large footprint is to frequency encode the photons instead of spatial encoding, as demonstrated in [137]. This again comes with its technical challenges of providing high-speed electronics for realisation, and the fidelities achieved via this method are significantly lower than [140].

A particular use case comes under the realm of quantum communications. Here high dimensional systems have been demonstrated to simultaneously provide an increase in information density while increasing noise tolerance [141**?**].

Increasing the information encoded through quantum information into multiple dimensions is a path to dealing with the low key-rates sometimes achieved in QKD [142, 143]. When the key generation rate is limited by the rate at which Alice generates photons or by the rate at which Bob can detect photons because of the detector dead time, the key generation rate can be improved using high-dimensional photon encoding. Each photon can encode as much as $log_2 d > 1$ bits of information. High-dimensional QKD was recently demonstrated in silicon photonics by utilising weak coherent pulses [132]. The key issue to overcome and solve is the lack of phase stability between the two chips [133, 144, 145].

The approach in [32, 132, 146] connects two silicon optical devices with a multi-core fibre (MCF), intending to minimise phase drift between different modes and maintain a similar path length to maintain the generated quantum states. This allows for interference between states on the receiver devices. Despite the use of advanced MCF, they still report phase instability in their system. Another drawback of the above implementation is the limitation of using weak coherent pulses, which generally carry many high-order photon number terms limiting the technology.

3.0.1.1 Photon generation of high-dimensional entangled states

The linear optics scheme used in the source device (Alice) allows for the generation and manipulation of high-dimensional quantum states. The scheme shown in Figure.3.3 can be used to generate and manipulate bipartite states in up to four dimensions entangled in space. Qudits are multi-dimension qubits, while a qutrit refers to three dimensions and ququart four dimensions. The end goal of this chapter is to show ququart entangled over three devices. To produce entangled qudits, the problem can be considered in the same way. For this example, it generates entangled path-encoded qudits on-chip by coherently pumping at least two sources. A pair of

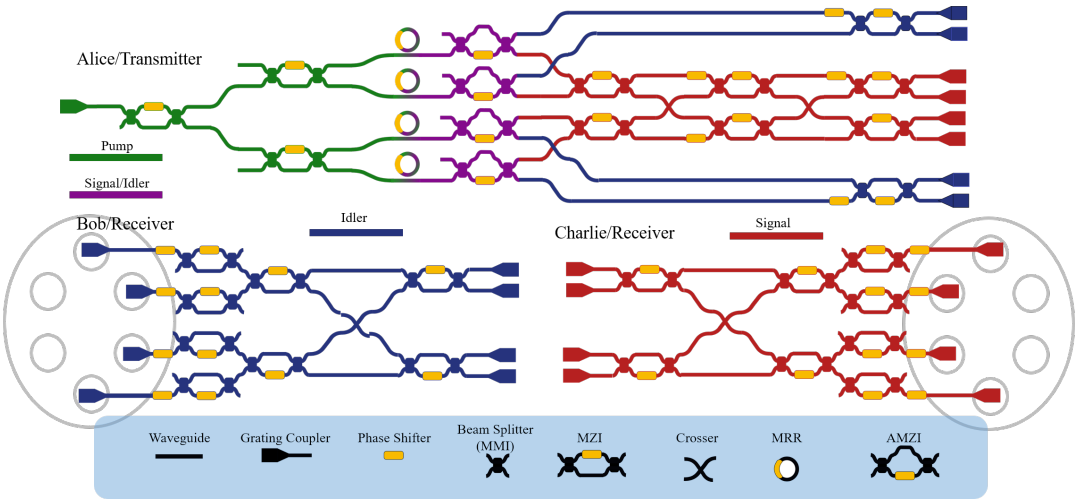

FIGURE 3.3. Schematics of the Transmitter and Receiver devices; Alice, Bob and Charlie. Alice is designed to be highly configurable, performing quantum information measurements and supplying receiver devices with on-chip entangled photon pairs. The red (blue) paths represent the main paths of the Signal (Idler) photons generated, while the purple is the coexistence of before pairs. Green represents the presence of only the pump. Below is a list of main components that build up the devices' complexity, with the lines representing Si waveguides and yellow rectangles the thermal phase shifters. The grey shadows represent where the MCF coupler interfaces. For the operational detail of the components, see Chapter. 2 and further in-detail operations of the devices is discussed further on.

entangled d-dimensional qudits are obtained by pumping d photon sources.

Pump light is injected into the source device and coherently splits into four sources via a network of MZIs. MZIs are reconfigured to redistribute and balance the pumping power arriving at each source, allowing for control of photon generation rates. The pump source is a CW laser operated in the low squeezing regime to provide a close to single pair of photons generated at a time. Signal and idler photons must originate from the same source and the states generated can be described by $\sum_{k=0}^{d-1} c_k |1\rangle_{s,k} |1\rangle_{i,k}$, where $|1\rangle_{s,k}$ ($|1\rangle_{i,k}$) represents the Fock state of the signal (idler) photon being in the k-th spacial mode. We ignore higher order photon terms, as they probability of production is determined by number of incoming photons, that we keep low enough to ensure these are small. The coefficients of c_k represent the normalised complex amplitudes applied to each of the different modes. We can remap the Fock state into a high-dimensional system, as shown in section 2.3.4. So the Fock state labels the photon in the k-th optical mode, therefore producing a general high-dimensional bipartite entangled state: $|\Psi_d\rangle = \sum_{k=0}^{d-1} c_k |k\rangle_s |k\rangle_i$.

To perform this, SFWM is achieved by taking the classical pump laser light and driving the pump between d sources, creating a superposition of the emitted photons. Amplitudes c_k are tuned by a combination of arbitrary configuring pump power delivered to the MRR and resonant frequency of each ring to ensure the equal probability of SFWM and number of photons produced

in each ring. This is performed by the MZIs reconfiguring the input and thermal phase shifts on the ring resonators themselves, shifting their FSR spectra. This gives complete control of the level of entanglement, and equal distribution using all coefficients equally, providing a maximally entangled state of two qudits: $|\Psi_{d,max}\rangle = \frac{1}{\sqrt{d}} \sum_{k=0}^{d-1} |k\rangle_s |k\rangle_i$.

3.1 Set-up and Design

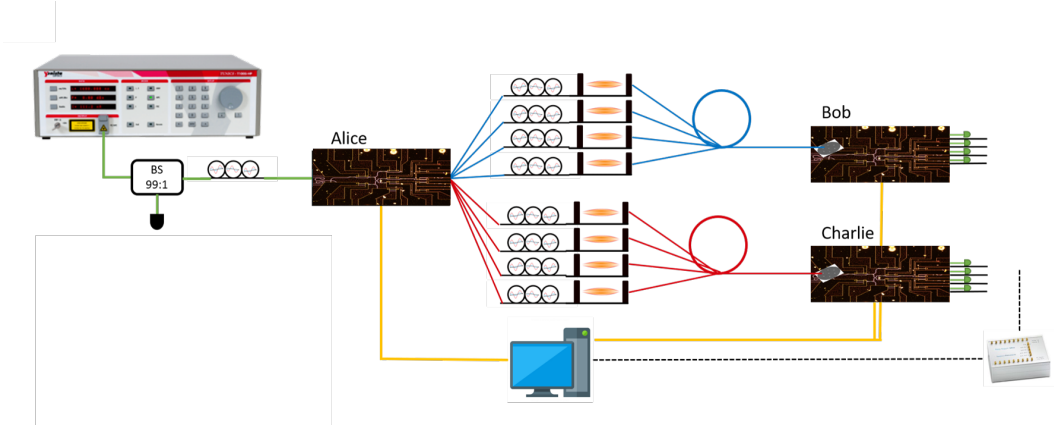

FIGURE 3.4. High dimensional entanglement distribution experimental set-up. A CW laser into a polarisation controller, to DWDM filter, to a 99:1 beam splitter to the Alice Device. Bob and Charlie devices connected with polarisation controlers and positional optical delay-lines, and at the end SNSPDs, all controlled by (PC).

The experimental set-up schematic for the experiment is shown in Figure. 3.4. A CW laser is injected into Alice through a V-Groove Array (VGA) after passing through a polarisation controller, 1.4 nm DWDM filter, and 99:1 beam splitter to measure input power. Generated and pump photons evacuate from Alice and are injected into the corresponding Bob and Charlie devices, depending on their signal or idler photon paths. Both paths consist of polarisation controlers and positional optical delay-lines to match path length. The injection apparatus for the receivers is a 5 m long MCF. Photons are evacuated from receiver devices using an VGA and pass through 0.7 nm de-multiplexing wave division (DWDM) filter, where finally detected by SNSPDs. The control operator (PC) manages on-chip phase shifters via analogue voltage controllers, time tagger device, chips temperature and CW laser.

The general structure of the schemes used to generate and process entangled qudits is illustrated in Figure. 3.3. The silicon devices were designed in Bristol, fabricated by Yunhong Ding and supplied by Davide Bacco's group in Denmarks Technical University (DTU). The integrated Silicon quantum optic chips will generally be referred to as devices. The device with Micro Ring Resonator (MRR), which generates the entangled photons, is referred to as the

transmitter or Alice. The devices measuring the quantum states coupled with MCF are the receiver devices named Bob and Charlie.

The device is designed and fabricated on SOI using electron-beam lithography. The silicon waveguides have a cross-section of 450 nm × 250 nm. The beam splitters are based on multi-mode interferometers (MMIs), described in the chapter. 2. They are combined with thermal phase shifters based on metal Ti heaters to create the Mach-Zehnder Interferometers (MZIs). The insertion loss of the MZIs on each chip is measured to be on average 0.5 dB on the source chip and 1 dB on the receiver chips. The typical extinction ratio in the interference of the filters in the MZIs is approximately 30 dB, therefore close to a 50:50 balance of the MMIs can be assumed. These components are used to create Asymmetrical-MZIs (AMZIs), where the length of one is the arms is longer than the other. Here they are used for filtering by separating idler and signal photons of different wavelengths. The MMI fabrication tolerance limits their extinction ratio.

Light is coupled in and out of the devices using Braggs interference with photonic crystal fibre grating couplers. The width of the crystal structure is approximately 345 nm. The source chip utilises a silver mirror on the underside of the grating couplers' as a back reflector to increase Alice's coupling efficiency [147]. We measured these coupling efficiencies and attenuation loss, by measuring the output power from the fibres and the power measured at the other side of the device. By knowing the length of the device and the average loss of the components and testing this for different device lengths we can calculate the loss. Knowing the difference in lengths and the difference in attenuation losses to find the waveguide loss. This waveguide loss is summed up and subtracted from the total loss, to give us the grating coupler loss. The receivers GC do not have mirror technology. At wavelengths close to 1550 nm, the coupling loss is 0.8 dB. The propagation loss in the waveguides is estimated to be on average 2.4 dB/cm. Each device's total insertion loss is around 10/14 dB for Alice (path dependent) and 18 dB for receivers. The coupling loss on the receivers grating couplers is estimated to be higher from the mismatch between the MCF shape with the grating couplers lead to the higher loss measured. This is estimated to be around 2 dB.

Two photons are generated in a superposition between the four-ring sources. An overview of the pump and generated photons path can be viewed in Figure. 3.4. Continuous Wave (CW) laser is injected into Alice at a wavelength of λ_p 1549.3 nm (pump wavelength) to generate the photon pairs, signal and idlers, via non-degenerate SFWM. Each is post-selected with signal photons at λ_s = 1539.77 and idler photons at λ_i = 1558.98 using the on-chip AMZI filters. The wavelengths chosen are in separate wavelength channels, hence we can filter each individually. These wavelengths are also used as these are resonant wavelengths for both the MMR and the AMZI filters, to allow for selection of photons for each mode. Each is then sent through a network of mechanical free-space delay lines, polarisation controllers and MCF before reaching their corresponding receiver device (Bob or Charlie). Off-chip filters are used to remove the pump light after the receivers, leaving the signal and idler to make their way to the detection system.

The photons are collected out of the device using fibre arrays. Photonspot supplied SNSPDs with an average detection of 85% efficiency measure the occurrence of incoming photons. This average detection efficiency is the detection efficiency quoted by the manufacture and also verified from measurements, by counting the single photons produced between detectors to determine efficiency. Meanwhile, the pump light is sent to ThorLabs optical power meters to be used in phase stabilisation, and device configuration discussed later in the chapter in sections 3.2 and 3.4.

To actively control the device, thermal phase shifters are used. Electrical pads on the chip are wire-bonded to a Printed Circuit Board (PCB) that connects to a computer-interface electronic controller. We developed a Python interface to actively configure the devices by controlling both the phase shifters and the data readout. We use Jupyter notebooks as the interface and loop through the systems so they synchronise. The python interface controls, reads and outputs the devices settings. Separate programmes are used to interface with the voltage controller, reconfiguring the devices. Running simultaneously are several other programs for: "Time Tagger Ultra" made by Swabian, collecting the number of counts at the detectors; phase stabilisation, measuring the pump power and phase shifting to compensate; and hardware activation of lasers and stepper motors for precise coupling. This allows for whole chip management, data collection, and data processing to reconfigure the devices at kHz rates. The limiting factor is the response of the thermal optic phase shifters [148]. The reaction rate of changing the device's refractive index, using heat under these dimensions and materials with this technology, is limited at kHz rates.

3.1.1 Optical Set-up

All of the experiments in this chapter share a common experimental foundation. The assembly rig for the source chip (Alice) and the two receiver devices (Bob and Charlie) are shown in Figure. 3.5. The major constituents highlighted in this set-up are as follows:

1. Nanomax stage from Thorlabs, the clamps at an 12° angle holding brackets that position the optical fibre array above the device to couple light in and out. This allows for sub-micron precision on the scale of the grating couples focal points to couple with 6 axes lateral and rotation to maximise the alignment between vertical grating couplers and the V-groove array.

2. The device holder three axes of linear movement to position the chip and alignment with the VGA. On top of the chip, the holder is a European thermodynamics Peltier, which thermal controls the surrounding temperature, providing temperature stabilisation for the device. A constant temperature is required to keep thermo-optic phase shifter calibrations relative throughout time. The Peltier is in thermal contact with the PCB of the device. We and DTU designed the PCBs' to provide a connection interface between the voltage driver

and the electrical connection on the silicon devices themselves. The chip is held in place with thermally conductive epoxy manufactured by Electrolube.

3. A 7-Cored MCF acts as a conduit between devices, with the proximity of the modes limiting the phase drift, with the loss in each mode 0.7 ± 0.2 dB for a 5-meter distance. We measure this by injecting light into each of the cores and measuring the optical power with a Thorlabs power meter. The fibre couples are at a 12° angle to the receiver devices, as the focal point of the grating coupler is optimised to couple light with the smallest loss at this incident angle.

4. Optical, mechanical delay lines span 20 cm, approximately 300 ps in delay time, with micron precision, and have 0.5 ± 0.1 dB of loss. They are physically separated by adjusting a screw mechanism using distance in free space to add delay to ensure interference over coherence length of the photons. Six delay lines are used, with three assigned to each device and enclosed in environmentally shielding housings to aid in phase drift dampening.

5. Qcontrol voltage control boards, driving voltage for all phase shifters on a device, through the connection via USB to a PC. We can individually and continuously drive current through each shifter with kHz frequency. These are connected to the devices using ribbon cables to the PCB. The PCB connections connect to the on-board heaters via gold wire 25 μm thick ball bonds.

6. The time tagger is a device that counts the electrical signal pulses produced from the SNSPDs during detection events. We use a Swabian Ultra Time tagger with 9 ps RMS jitter, 22 ps FWHM jitter and 1 ps digital resolution. The time tagger has a 2 ns dead time and 70 M tags per a second transfer rate. SMA cables take radio frequency signals from the cryogenic housing station of the SNSPDs to the time tagger, which use a USB 3.0 optical extender to transfer counts at the high rates required from the eight channels used in the experiment to the PC.

7. SNSPDs are supplied by Photonspot and provide on average 85% detection efficiency at 1550 nm.

Delay lines are required to match length to allow coherence lengths to overlap to enable interference, with coherence length represented by $L_c = c/\Delta\omega$, where $\Delta\omega$ is the spectral frequency width of the light. Fine spectral width provides a longer coherence length: the CW laser produces around 30 cm L_c nominally, and the rings with the FSR produce around 10 cm L_c calculated from their bandwidth, which is small by design. A pulsed laser with a large spectral width is used as a fine calibration of delay lines to increase the precision of full overlap of photons during experiment.

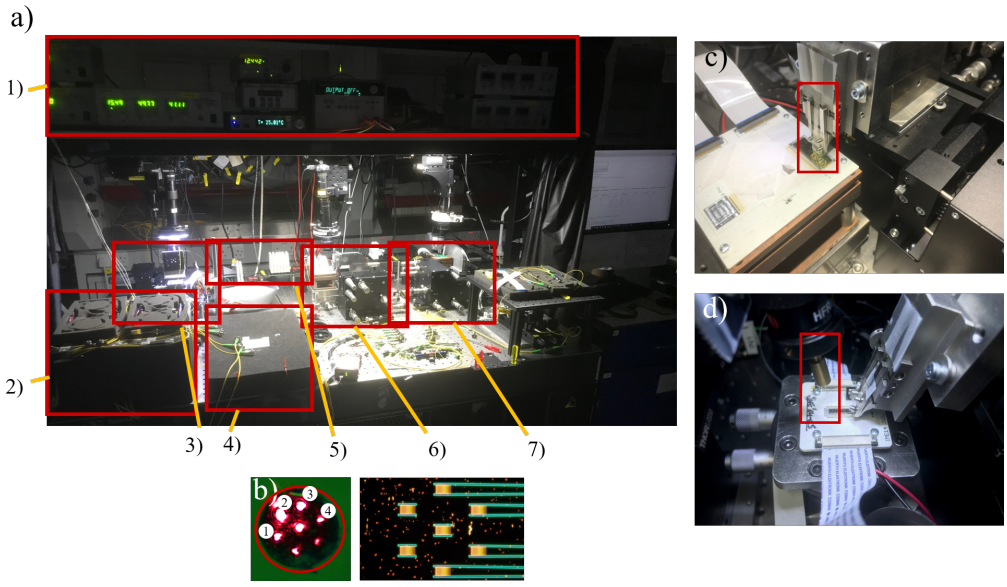

FIGURE 3.5. Experimental Set-up Photos. a) Photo of the overall set-up, with highlighted boxes showing: 1) the experimental hardware control, VGA motor control current supply to control boards and temperature PID controllers; 2) self-contained area of four free space delay-lines with polarisation controllers atop; 3) mount for receiver device Bob; 4) host for the MCF coil; 5) thermal phase shifter voltage control boards; 6) mount for transmitter Alice device; and 7) the mount for the receiver device Charlie. b) Cross-section of MCF, where four cores highlighted are used and matching fabricated grating couplers on the device and the grating coupler arrangement on the device using to couple to the MCF. c) Close up of the coupled transmitter device. d) Close up of receiver device Bob coupled with MCF on the left and the VG on the right, with Charlie set up in a near-identical configuration.

3.2 Characterisation

3.2.1 Characterising on-chip phase modulators

A Tunics T100S-HP CW 13 dBm with a 40 pm bandwidth laser is injected at the pump wavelength into the chip via vertical grating couplers at the pump frequency to characterise the on-chip phase modulator across all silicon integrated photons devices. The thermo-optic phase heater's voltage is swept over a range below its threshold limit (0 V to 3 V). At the same time, we measure the current to produce an IV curve. The curve is fitted with a polynomial fit, and this function is used to determine the voltage to deliver to the heater. The pump light is measured at a connected output mode at the end of the device, along the same path as the component being calibrated. As the voltage is swept, interference between the two arms occurs. We see this by the sinusoidal power change in the monitored output arm. Fitting the results of the square of the voltage to fit non-linear order terms against optical power measured in linear units, we obtain

a phase-voltage relationship for that component. The obtained relationship is referenced when configuring the device to project and prepare states. The intention is to always produce an MZI, with the thermo-optic phase shift along one of the arms of the MZI.

3.2.2 Unitary Configurations

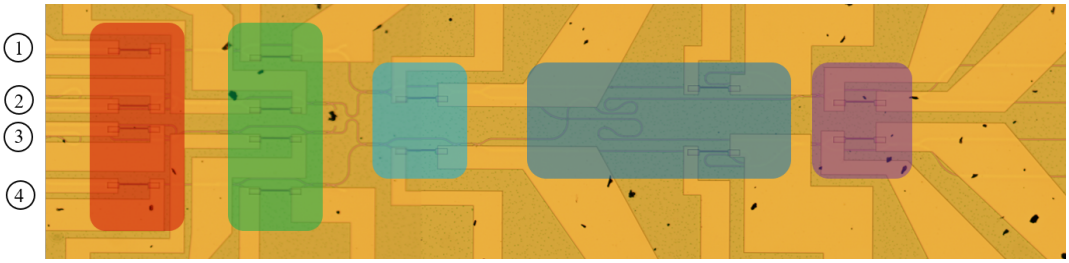

FIGURE 3.6. Photo of the receiver chip under an optical microscope. The Au strips connect to electrical thermal-optic phase shifters. Highlighted are the different optical unitary stages throughout the device. (Red) $\hat{\Phi}_4$ Four phase shifters on the device input, used to stabilise the incoming modes: (Green) $\hat{P}_4$ Attenuators to balance power between the modes, to allow for equal interference; (Light Blue) $\hat{U}_{MZI_4}$ Two MZIs; (Dark Blue) $\hat{S}_4\hat{\Phi}_2$ Swap between modes 2 & 3 and phase shifters on Modes 1 & 4; and (Purple) $\hat{U}_{MZI_4}$ Two MZIs. The numbers on the left hand-side represent the number channel input ports into the device.

Chip-to-chip coupling efficiencies should be kept as high as possible, to minimise loss. Reducing the number of active components (< 0.5 dB introduced by each component) will ensure integrated linear optics provide the smallest concern of loss.

The receiver is shown in Figure. 3.6 and the components that make up the 4D unitary are highlighted.The devices are designed to provide arbitrary projective measurements in four dimensions. The full transformation matrix that describes $(\hat{U})_4^{\dagger}$ (as shown below) can be derived by looking at the on-chip state evolution for an arbitrary heater configuration. When combined with the swapping of waveguide modes via the integrated waveguide crossers, the circuit should allow for the projection of all combinations of complex superposition amplitudes, i.e. all possible 4-dimensional qudit eigenstates. All of the unitaries described here are also applicable to Alice. If though the details are different, we can perform the same projections and measurements for the experiments described. Working from the output side of the device the $\hat{U}_{MZI_4}$ is made up of two $\hat{U}_{MZI_2}$ and described as:

$$\hat{U}_{MZI_2} = \begin{bmatrix} ie^{i\phi_{Aj}} sin(\theta_{Aj}/2) & ie^{i\phi_{Aj}} cos(\theta_{Aj}/2) \\ ie^{i\phi_{Aj}} cos(\theta_{Aj}/2) & -ie^{i\phi_{A}j} sin(\theta_{Aj}/2) \end{bmatrix} \tag{3.1}$$

$$\hat{U}_{MZI_4} = \begin{bmatrix} \hat{U}_{MZI_2} & 0 \\ 0 & \hat{U}_{MZI_2} \end{bmatrix} \tag{3.2}$$

A description of the matrix that forms an MZI is covered in Section. 2.3.4. Here $A_j = A_{1,2,3,4}$, representing the position of the MZI in the device. Using Figure. 3.6, 1) is top right MZI, 2) bottom right, 3) top left and 4) bottom left.

Optical modes 1 & 2 do not interfere with optical modes 3 & 4 unless swapping occurs in this device. Before this, the swapping between modes 2 & 3 occurs, with phase shifts on modes 1 & 4. This is described by the unitary below:

$$\hat{S}_4\hat{\Phi}_2 = \begin{bmatrix} e^{i\phi_C} & 0 & 0 & 0 \\ 0 & 0 & 1 & 0 \\ 0 & 1 & 0 & 0 \\ 0 & 0 & 0 & e^{i\phi_D} \end{bmatrix} \tag{3.3}$$

Where $e^{i\phi_{C/D}}$ is the top or bottom path on the device. There are two more MZIs similar to those described above. Combining these into a single unitary is thus described by $\hat{U}_4 = \hat{U}_{MZI_4}\hat{S}_4\hat{\Phi}_2\hat{U}_{MZI_4}$ and fully described as:

$\hat{U_4^\dagger} =$

(3.4)

$$\begin{bmatrix} \Phi_a sin(\theta_{A3}/2)sin(\theta_{A1}/2) & \Phi_a sin(\theta_{A3}/2)cos(\theta_{A1}/2) & \Phi_b cos(\theta_{A3}/2)sin(\theta_{A2}/2) & \Phi_b cos(\theta_{A3}/2)cos(\theta_{A2}/2) \\ \Phi_a cos(\theta_{A3}/2)sin(\theta_{A1}/2) & \Phi_a cos(\theta_{A3}/2)cos(\theta_{A1}/2) & -\Phi_b sin(\theta_{A3}/2)sin(\theta_{A2}/2) & -\Phi_b sin(\theta_{A3}/2)cos(\theta_{A2}/2) \\ \Phi_c sin(\theta_{A4}/2)cos(\theta_{A1}/2) & -\Phi_c sin(\theta_{A4}/2)sin(\theta_{A1}/2) & \Phi_d cos(\theta_{A4}/2)cos(\theta_{A2}/2) & -\Phi_d cos(\theta_{A4}/2)sin(\theta_{A2}/2) \\ \Phi_c cos(\theta_{A4}/2)cos(\theta_{A1}/2) & -\Phi_c cos(\theta_{A4}/2)sin(\theta_{A1}/2) & -\Phi_d sin(\theta_{A4}/2)cos(\theta_{A2}/2) & \Phi_d sin(\theta_{A4}/2)sin(\theta_{A2}/2) \end{bmatrix}$$

where $\Phi_a = e^{i(\phi_{A1}+\phi_{A3}+\phi_C)}$, $\Phi_b = e^{i(\phi_{A2}+\phi_{A3})}$, $\Phi_c = e^{i(\phi_{A1}+\phi_{A4})}$, $\Phi_d = e^{i(\phi_{A2}+\phi_{A4}+\phi_D)}$

Therefore the above can be defined by breaking it down and just finding the real parameters that can be set. This set of parameters is then used to define the configurations required to project into basis $\phi_{A1}, \phi_{A2}, \phi_{A3}, \phi_{A4}, \phi_C, \phi_D, \theta_{A1}, \theta_{A2}, \theta_{A3}, \theta_{A4}$. At the input of the device are phase shifters, which each change the phase of the incoming mode and can be described by the following unitary:

$$\hat{\Phi}_4 = \begin{bmatrix} e^{i\phi_1} & 0 & 0 & 0 \\ 0 & e^{i\phi_2} & 0 & 0 \\ 0 & 0 & e^{i\phi_3} & 0 \\ 0 & 0 & 0 & e^{i\phi_4}. \end{bmatrix} \tag{3.5}$$

Their phase is only essential relative to one another and is added to the above equation but not fully shown.

All of the unitary components are highlighted in Figure. 3.6. By utilising the above method, arbitrary four-dimensional bases can be measured on the chip by projecting into each of the eigenvectors in turn, where the associated measurement probability that the generated state is found in the measured eigenvector.

In this experiment we simultaneously measure the relative probabilities of the multiple eigenvectors. By finding the orthonormal basis $\hat{M}$ set we can map to the optical modes using $\hat{U_4^\dagger}\hat{M} = \hat{I}_4$. The four states can be constructed using the above parameters using the resulting four vectors to construct a complete set of orthonormal basis vectors in 4D. The basis $\hat{M}$ is a unitary matrix that is easily found, as it is formed from its orthonormal set of vectors, which are obtained when configuring the device to $\hat{M}^\dagger$. As $\hat{M}^\dagger M \hat{=} \hat{I}_4$. Therefore this can be used to measure any 4D basis efficiently.

The approach described, simultaneously measuring the eigenvector for the 4D product bases, speeds up measurement collection 16-fold for two ququarts. This then requires the use of eight SNSPDs over just two when projecting into the 16 eigenvectors separately.

3.2.3 Ring Resonator Source Characterisation

Four Micro-Resonator Rings (MRRs) on Alice SOI device are designed to be identical in properties. Figure. 3.7 b) is the FSR of the four MRRs embedded into Alice, with an FWHM of roughly 0.2 nm and FSR of 3.20 ± 0.4 nm. This is measured by sweeping the wavelength from a CW laser and measuring the optical power output at the ports. The dips show the resonating frequency, where light couples into the device. The resulting spectrum should, therefore, directly correspond to the optical resonances inside the MRR cavity. This same operation is repeated for all four MRRs.

3.3 Time Tagger

On the Swabian, the counts from each channel are measured. The Swabian time tagger has an input threshold dependent on the SNSPD pulse amplitude from each detector. The detectors are biased with a current between 8 and 13 μA, providing a pulse amplitude between 100 and 200 mV. The bias current drives the amplitude of the output pulse. The largest current possible is used before the critical current is reached and the detector latches. A current just below this is chosen, as this provides the greatest detection efficiency. The system is non-linear and the critical current value changes, dependent on the restive or superconducting state. More information on the detector system can be found in Chapter.4.

The input threshold is set between 80 and 120 mV on the Swabian: a value over three standard deviations above the noise floor and over three standard deviations below the average pulse peak value. The time tagger provides counter channels for each input, allowing for every pulse to be counted and tagged with measurement time. Virtual channels are created that count coincidences if two photons are counted in two other channels within a specific time window

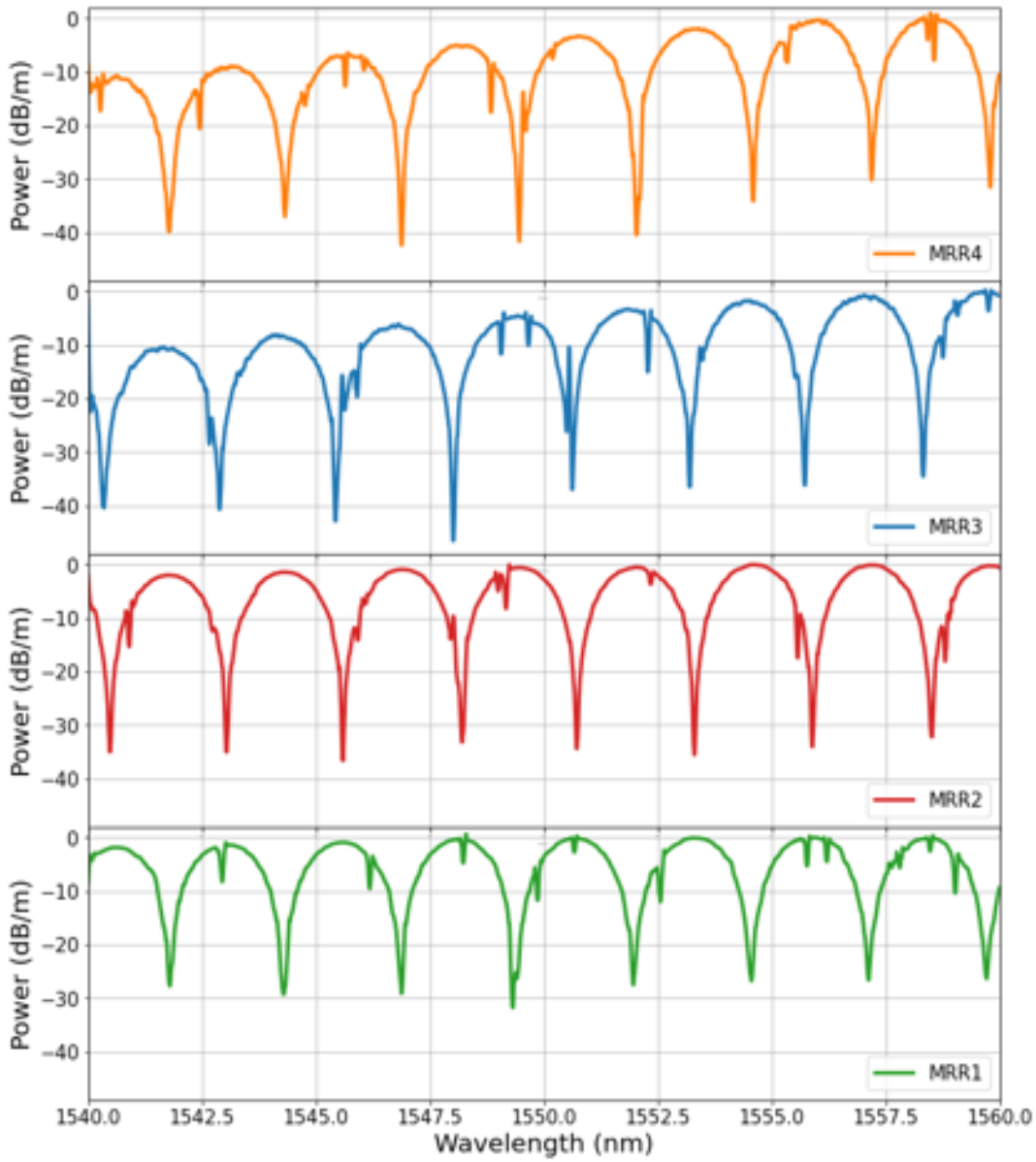

FIGURE 3.7. Measured spectrum of four MRR on Alice with radius 27 μm.

a 1-2 ns. In this experiment, virtual coincidence channels are created between all the possible signal and idler permutations, leading to 16 virtual coincident channels. The coincident channels count when two input pulses are measured within a time window. The bin width chosen in these experiments is 1 ns. The photons' path after projection may differ; therefore, artificial delay times are added to their arrival times to simulate simultaneous arrival times in all channels. This allows entangled pairs of photons to be detected simultaneously, showing that statistically more counts are measured between these channels.

The measurements on each of the virtual channels are integrated for 5 minutes with a

bin-width time of 1 s, and the sum of the bins of this time are summed.

3.3.0.1 Power Balance

Figure. 3.8 shows the coupling efficiency of the grating couplers in all three devices. The spectrum of the receiver devices coupling is tuned to have a minimal loss at both the signal and idler wavelengths. Alice has two peaks towards the signal and idler wavelengths shown in the figure. This is to optimise the probability of entangled photon pairs reaching their receiver devices. Alice's average coupling efficiency is a maximum of 0.8 dB, while receiver devices maximum coupling is around 2 dB, with a 3 dB width loss at between 30-40 nm in wavelength.

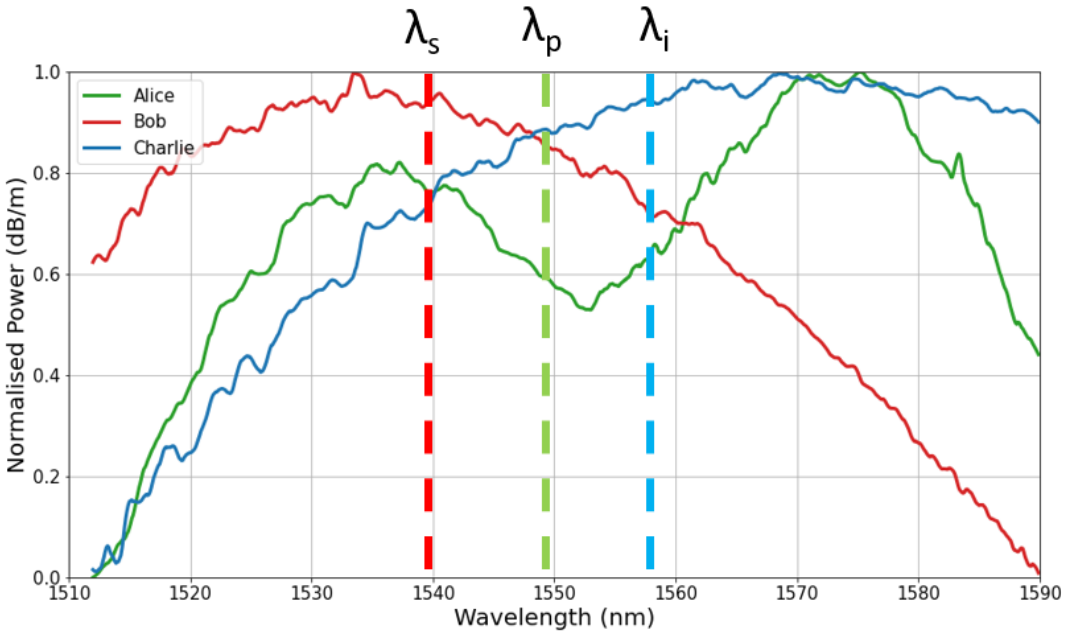

FIGURE 3.8. Measured spectrum of fully etched 1D grating couplers in silicon of the source chip (Alice) and the two receiver devices (Bob and Charlie), with the wavelengths of the photons used shown. b)

All of the channels between devices have different optical powers, and further losses that come into play. This can include different coupling alignment, the efficiency of the grating couplers, the components of delay lines and PC having other losses, and the power going through the teleportation chip as different modes have different numbers of MZI travelling through.

Different powers in the line will lead to reduced visibility of any interference between modes on-chip, which needs to occur to perform a measurement basis such as the Hadamard basis. Also, the number of counts at the detector will vary, and these can be compensated by reading the output powers.

3.4 Stabilisation

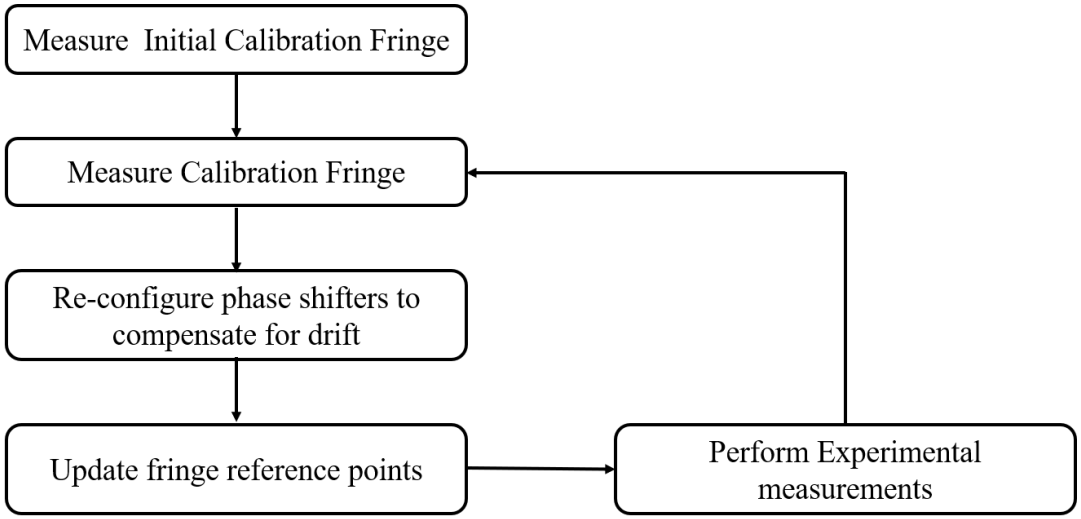

FIGURE 3.9. Phase stabilisation System flow chart

The phase delay between the incoming modes varies between chips, because their environmental surroundings fluctuates. Changes in temperature, vibration, and humidity will change the medium the photons travels through. The phase must be the same when leaving the source chip and entering the receiver chip to preserve entanglement. Otherwise, interference in the MZIs will not occur as expected, not allowing a correct projection into the measurement basis to be applied to them.

In this section, we demonstrate phase stabilisation. The high dimensional states between transmitter and receivers must remain coherent. Ensuring initially identical superposition states remain in their identical states during transfer between devices allows for repeatable and consistent interference on the receiver device between modes.

Phase stabilisation for high dimensional systems, where the method is spatial modes, must have the same effect across all the photonic states. Each optical path is stabilised to be indistinguishable under the same unitary transformation at the receiver(s). One of the MCF properties is to minimise the phase difference between modes that occurs, maintaining states by providing the same environment across all modes. The MCF is the dominating environment transit between devices. Transmitter chip delay-lines and polarisation controlers provide the dominating noise during transmission.

The polarisation of the four modes drifts over time, on timescales of few to several seconds. The phase drifts are long enough that negligible difference can be measured compared to the time for measurements. The fluctuations in the single photons' arrival time for each optical mode occurs randomly and are stabilised where measurements involving interference between paths occur. We measure the results from projecting into the computational basis, that do not require

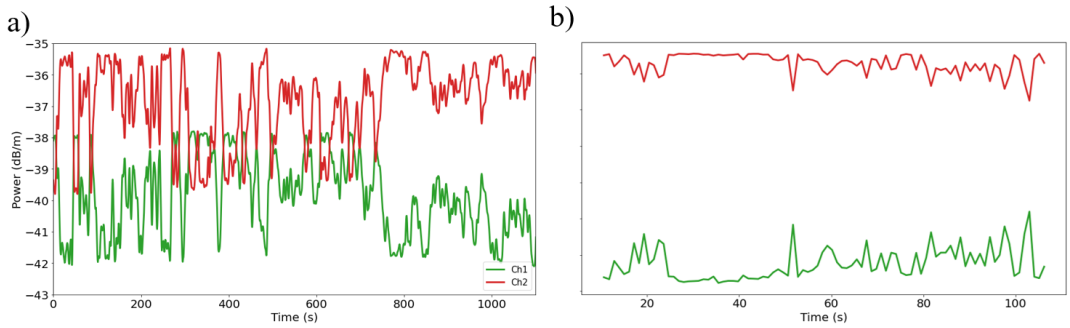

FIGURE 3.10. a) The phase drift between two modes, showing temporally dependent overlap leading to the motivation of phase stabilisation as shown in the right hand figure. b) Optical power output across two chips using the phase stabilisation where the fluctuation in power is significantly decreased.

phase stabilisation and projections into the Hadamard, that requires phase stabilisation, as an MZI is set up across the two devices in this configuration. The path difference between the photons is time-independent. Fabrication imperfection differences and transmitter chip designs are taken care of with mechanical, optical delay lines that adjust to allow for interference.

To maximise interference on the receiver chip, a CW laser is used due to its small bandwidth, therefore producing photos with coherence lengths of $\approx 300\ ps$. Long coherence lengths allow for increase overlap between modes ensuring maximum interference, reducing the effect of change in path length. Phase drift is measured to oscillate on the order of several seconds, as seen in Figure. 3.10 a). The on-chip activate thermal phase shifters operate at kHz frequencies, therefore provide adequate response time.

The pump laser is already emitted and transmitted between devices, creating an interferometer between the two devices. By setting, both transmitter and receivers between two modes equally interfere (AMZI to $\pi/2$). A reproducible standard to measure the phase between the two paths can be performed by measuring the optical power in a single arm. The power in the arm would determine the phase difference between another. Selecting a single mode to be the reference arm allows other modes phase change relative to the difference between the modes to be measured and mitigated. The measured phase drift can be seen in Figure.3.10 a).

We illustrate the algorithm we used to achieved phase stabilisation in Figure. 3.9. The system is initially calibrated by sweeping over a phase of 2π to obtain an interference fringe. The sinusoidal curve fit, and standard deviation away from the measurement data is calculated and kept below a certain threshold to ensure a high-quality calibration fringe. This is done using the classical channels and the beam splitters. Fluctuations are on a scale longer than the phase shifters allowing the thermal phase shifters to compensate for the fluctuations. Two different fringes are measured: a calibration fringe and subsequent measurement fringes, with the calibration fringes done over a longer period and repeated until a full fringe is taken. Their

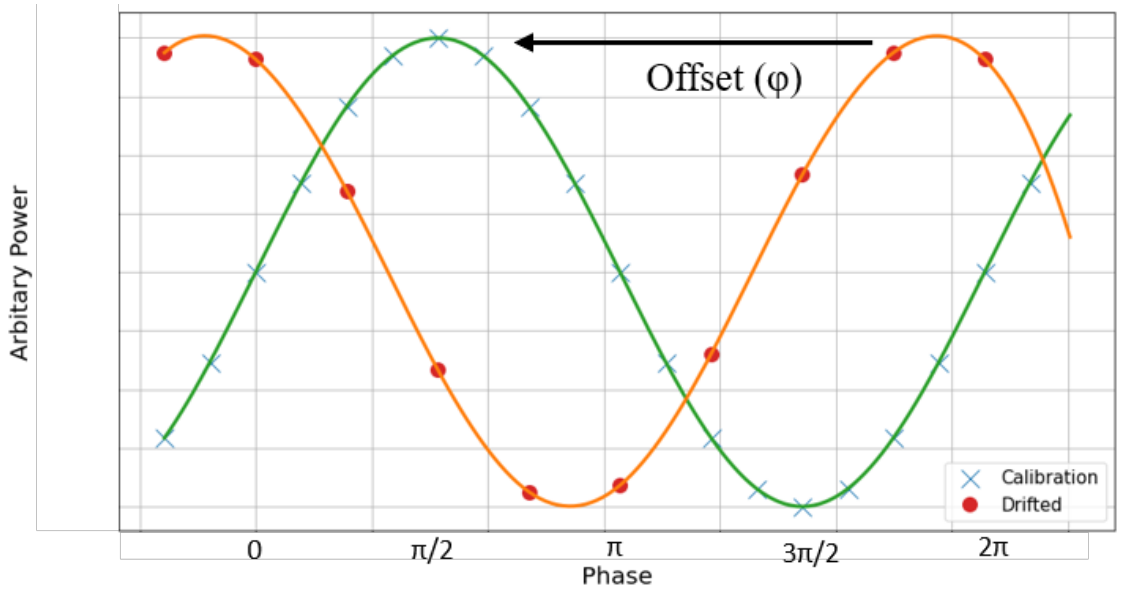

FIGURE 3.11. Model diagram of an application of phase stabilisation interference between two spatial modes, with measurement of a calibration interference fringe (green) and subsequent fridges (orange), with mismatch phase offset and correction of the wave to match previous interference.

parameters are determined, including the phase of the calibration ϕ_{cal} and difference ϕ_{diff} fringes. The subsequent fringes are measured in under a second. Figure. 3.11 simulates the measuring of a calibration fringe and then correction fringe, and then the changing that occurs to correct this. The phase offsets $\Delta\phi$ and correction phases ϕ_{set} can be described by:

$$\phi_{set} = \phi_{target} + \Delta\phi, \tag{3.6}$$

$$\Delta\phi = \phi_{cal} - \phi_{diff}, \tag{3.7}$$

The unitary configured onto the device determines ϕ_{target}. Sweeps using the thermal phase shifters will form another fringe. Both are fitted with sinusoids. The two fringes will be similar, with the significant difference in the relative phase difference between them calculated after measuring the second. This phase offset value is added to on-chip phase shifters on the receiver chip to match the phase cancelling out the phase drifts.

After this, the phase-matched measurements can be taken with the target unitary configured until the modes drift apart again. The switching between chip-to-chip interference and measurements unitaries on the chip occurs until enough counts are collected. Immediately after the stabilisation it will slowly decay; therefore, pulses less than the drift ($\approx 1s$) in data measurement

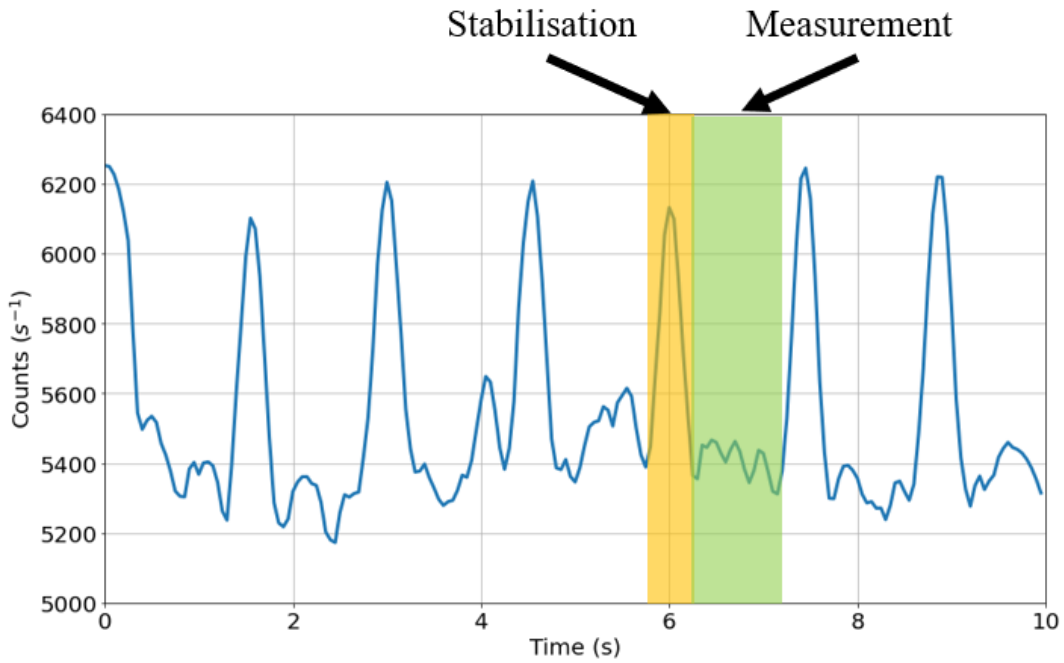

FIGURE 3.12. Measurements of single-photon count in a single spatial mode. The peaks represent the phase sweep to collect an interference fringe and the stabilisation (highlighted green), while the subsequent measurement period (highlighted yellow) occurs with a short one-second burst afterwards.

are required. We measured the single counts at the SNSPDs during the phase stabilisation and measurement process and show the fluctuations in the counts in Figure. 3.12. In the figure, we can see the peaks in yellow that the system is stabilising and after this point in green a 1 s interval, where measurements can be taken as the phase has been corrected. This result shows the the number of counts remain constant with an 8% change in counts during these measurement phases.

The subsequent classical power stabilised compared to the non stabilised light can be compared with one another using Figure 3.10 a & b. In b) we can see that the power on each arm fluctuates 1 dB compared to the 5 dB before.

3.4.1 Quantum state communication

The following experiments are to test the success of chip-to-chip phase stabilisation performed when distributing qubits between device. We generate a bipartite entangled state of $|00\rangle + |11\rangle$, and interfering these states: the first state from each composite state, on one beam splitter and the second on another beam splitter. The difference between classical and the quantum interference is witnessed by the interference pattern produced. Photon pairs are produced, undergoing a global phase shift. They will produce a double interference pattern compared to the classical

interference described by:

$$|\Psi\rangle \rightarrow e^{i\theta} \frac{|s,i\rangle_0 + |s,i\rangle_1}{\sqrt{2}}, \tag{3.8}$$

$$|\Psi\rangle \rightarrow e^{i\theta} |s\rangle_{0A} |i\rangle_{0B} + |s\rangle_{1A} |i\rangle_{1B} \tag{3.9}$$

Where s (i) represents the signal (idler) photon. The following results demonstrate quantum interference results of classical and quantum relative to three different scenarios. The number 0,1 represent the rings the state originated from and the letters A & B the modes they occupy at the end. Single device interference: Figure.3.13 a) presents the schematic set-up used on the transmitter device. This phase-dependent measurement verifies phase stabilisation is adequate for following mode measurements. When transferring the qubits between devices, a maximally entangled Bell state is prepared, where the signal photon is measured on the transmitter and photon 1 the receiver device. Here we measure in the basis $\hat{\sigma_x} \otimes (cos(\theta)\hat{\sigma_x} + sin(\theta)\hat{\sigma_y})$. This basis is chosen to obtain pure states with expectation values oscillating from 1 and -1, while in a maximally mixed state it obtains zero. The plot of the expectation values against the classic power is also measured, while sweeping the θ parameters between 0 and 2π is viewed in Figure.3.13 b).

The expected fit is a cosine function. When $\theta = 0$ ($\theta = \pi$), the expected measurement is 1 (-1) as $\hat{\sigma_x} \otimes \hat{\sigma_x}$ ($\hat{\sigma_x} \otimes -\hat{\sigma_x}$.). While when $\theta = \pi/2, 3\pi/2$ the two qubits are measured in mutually unbiased bases $\hat{\sigma_x} \otimes \pm\hat{\sigma_y}$, we expect zero correlation between positive and negative eigen values.

3.5 Single Device 4D Quantum Measurements

3.5.1 Introduction

In the experiment we focused on measuring high dimensional entanglement across three devices, showing that this is possible and can be exploited for QKD purposes. We build up results by performing quantum information measurements, by projecting quantum states into different bases with the increasing number of devices.

In this section and the next, we use the Alice device to project into 4D $\hat{I_4}$, two 2D $\hat{H_2}$ and two 2D $\hat{\sigma_y}$. The Bob device is connected over MCF, where CST has already been proven using two operational modes at a time, so measuring 2 $\hat{H_2}$ and a $\hat{H_4}$. Next, the third device, Charlie, is connected as the final receiver and shows that 2D QKD is possible using $\hat{I_2}$ and $\hat{H_2}$. Lastly, we expand to 4D and measure $\hat{I_4}$ across four devices. The path-dependent high dimensional entanglement measurements are made possible using the phase stabilisation methods previous described, ensuring that the quantum state between generator device and measurement device (receiver) remains coherent.

The following results are completed on a single device. These measurements of the device's calibration provides an understanding of the errors of the device providing a bench mark for results

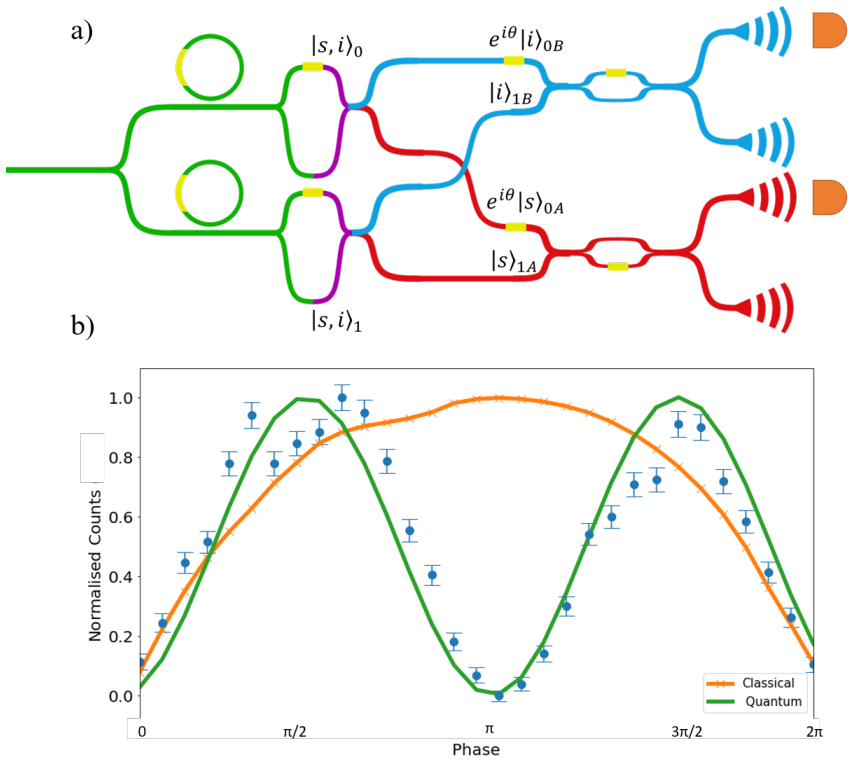

FIGURE 3.13. Quantum interference set-up and measurement results. a) A simplified schematic diagram of the chip diagram for the quantum interference measurement set-up. b) Visibility of the Chip-to-chip interference fringe. Datapoint with error bars showing chip-to-chip quantum interference fringe between modes 0A(0B) and 1A(1B). The coincidence counts are taken from the 0A & 0B modes, i.e. the positive eigenvalue. The classical fringe is recorded by output mode 1B. Each set of results fits to a sinusoidal curve using a fit function in python (scipy package).

between devices. As it provides all of of the unitaries necessary to simulate all of the following projection measurements. The limited nature of the device presents a handful of measurements that have been performed. We prepare two different states. The first state is a 4D entangled state that we project into the computational basis. We also project 2 2D state simultaneously into the Hadamard and Y basis. We go on to measure to project into the computational basis and the Hadamard basis in 2D.

3.5.2 Configurations

All four of the sources are pumped with the CW laser, generating an entangled pair at four possible sites. This provides eight possible paths to go down, therefore eight SNSPDs are used in all experiments that measure 4D and four SNSPDs for 2D.

A simplified schematic of the device and the minimum amount of components required the perform all of the aforementioned measurements can be found in Figure. 3.14. For all of the

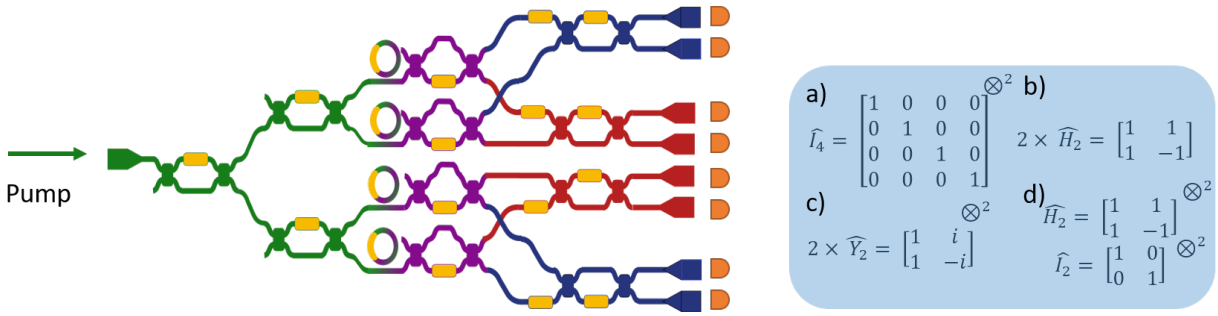

FIGURE 3.14. Simplified schematic of a device and the detectors at the end of the device used to perform the measurements with the measurement basis of each described in the blue box.

measurements the set up is the same with pump light split equally between all of the modes and the ring resonances balanced, to produced equal number of pairs photons each. This ensures maximum interference. The pairs are split into their idler and signal modes by the AMZI shown in purple in Figure. 3.14.

In the computational basis all of the MZIs are set to identity. This preserves the spatial modes, and no interference between the modes occurs. With the coincident measured at the end between pairing detectors. In the 2D Hadamard state all of the MZIs, past the AMZIs are set to 50:50 beam splitters, to equally interfere the modes, and allow equal probability that the photons can choose either path. This set up is the same when measuring into the Y-basis. The difference here, is that the mode is now phase shifted by π before the beam splitter. The last measurement, sees the ilders projected into the computational and the signals projected into the Hadamard. Therefore the MZIs in the signal path are set to identify and the Idlers set to 50:50.

3.5.3 Results

During this experiment, a few different bases are measured. Firstly the $\hat{I}_4$ basis is measured as seen in Figure. 3.15 a), which has a fidelity of 88±1%. Two 2D $\hat{H}_2$ basis are measured and are shown in 3.15 b), with a fidelity of 89±1%. We measured the computational and Hadamard basis in 2D on the same chip; essentially splitting the chip in two and running experiments in parallel, projecting two 2D modes into the computational basis on the signals and projecting the idler into the computational, where the results from this can be seen in 3.16. In Figure. 3.17 is when two 2D photon pairs states are projected into the Y-basis. The on the chip configuration of this is represented by a $\pi/2$ shift before the beam splitters. The fidelity of the Y-basis is 73%.

Fidelity's below 50% can be achieved with a classical system [136]. Results measuring these basis have been quoted to be 96% [136] for 4D states. The results here are above what is achievable by a classical state, but not as high as previous reported results. In this result they used spiral sources instead of MRRs.

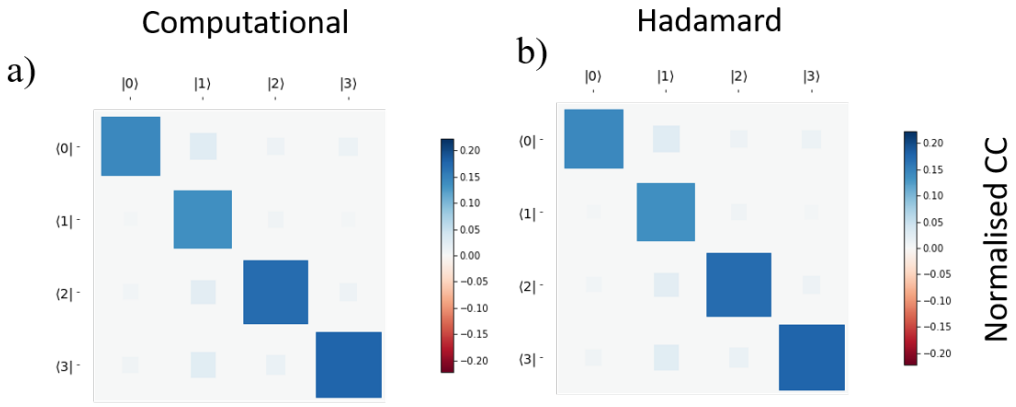

FIGURE 3.15. Single device high dimensional results. a) Computational basis projector measurements, probability matrix of a 4D entangled state. Both are representing the probability of detection of the combination of coincidences (qudits). The results are normalised and scaled with the single counts in each mode. b) The results are two 2D measurements on the same device between modes 1 & 2 and modes 3 & 4. Hadamard basis is measured on each $\hat{H}_2$.

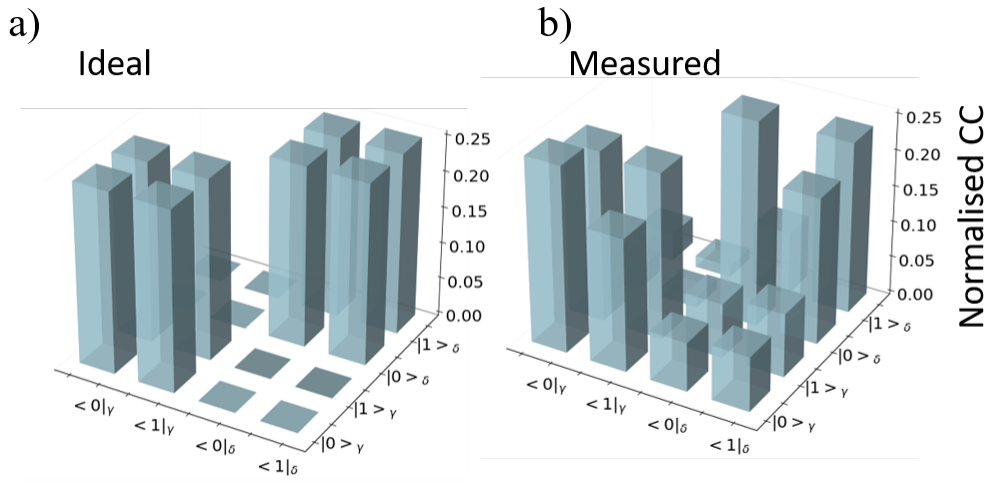

FIGURE 3.16. Single device high dimensional results. Modes 1 & 2 idler channels projected into the computational basis while the signals of mode 1 & 2 are projected into the Hadamard. a) is the ideal scenario and b) the measured results for this projection

3.6 High dimensional Entanglement Distribution

Previous results taken between Alice and the receiver device Bob by Dr. Daniel Llewellyn included a state decomposition in 4D, and a compressed sensing tomography [149]. This includes 1600

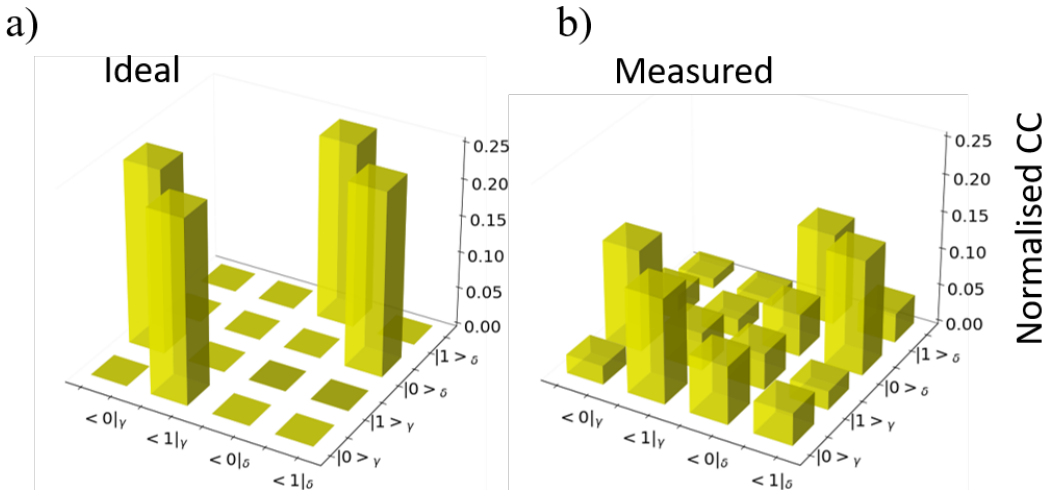

FIGURE 3.17. Single device high dimensional results. Two 2D Y-bias measurements on a single device with the bottom measurements of the two pairs of modes measuring the computational and Hadamard basis, therefore no correlation between modes. a) is the Ideal circumstance and b) the measured CC counts.

total measurement basis settings performed, leading to a 16D density matrix reconstruction and showing that a fidelity of 87% is achievable [150]. The following results build upon this by explaining and presenting how more complex measurements involving multiple mode stabilisations are performed during measurements.

3.6.1 Two device 4D

3.6.1.1 Configurations

In this section the devices Alice and Bob are used: Alice as the transmitter and Bob as the receiver. Alice and Bob measure the same basis for both measurements. A 4D compressed sensing tomography between the two devices has already been reported on by Daniel Llewellyn [150], therefore the measurement of these capabilities to project and measure into quantum states has been proven. Our aim here is to test the phase stabilisation and possible results achieved, using the current phase stabilisation methods. Both devices project their received quantum states into Hadamard basis. The first experiment projects into the $\hat{H}_2$, but completes this on two modes simultaneously. Therefore the interaction is only between two modes each. This allows us to only measure and stabilise two modes each relative to their partner pair; i.e. stabilise Ch 2 relative to Ch 1 and stabilise Ch 4 relative to Ch 3. This reduces the time to stabilise the full system, allowing for short phase drifts to occur. The simplified schematic of the minimal number of components needed to preform this measurement and the matrices to describe the basis are shown in Figure. 3.18.

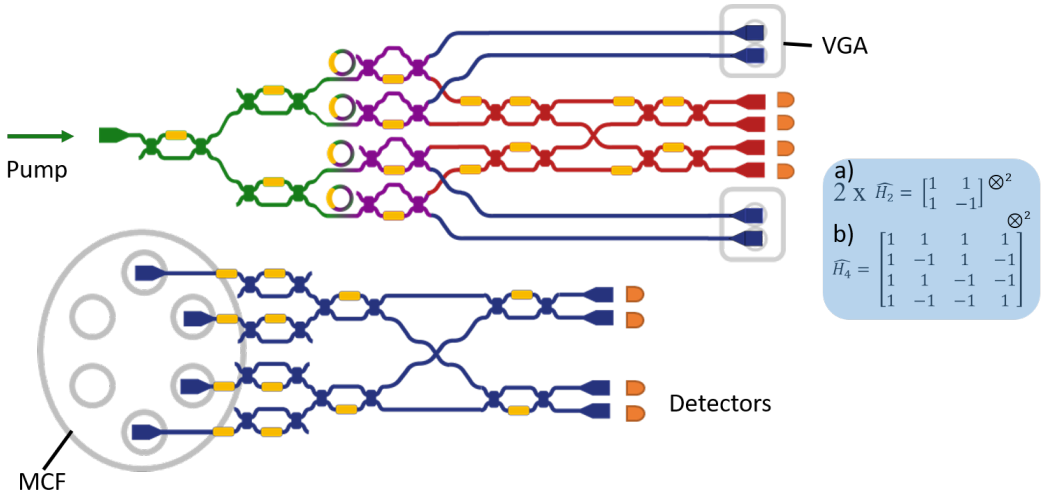

FIGURE 3.18. The simplified schematic of the minimum structure needed to perform this measurement between the two devices, with the same measurements on each performed.

The next of these results projects all four of the modes into a $\hat{H}_4$. We require all of the modes to interfere with each other on a single device. For this configuration to work, three of the modes must be phase stable compared to one. Therefore in this scenario, we use mode 1 as the target phase and require the other three modes (2, 3 & 4) phases to match mode 1. The process flow chosen is interfering modes 1 & 3 together on the receiver device at MZIa2 or MZIa4. Once they are phase-matched, we simultaneously measure the phase differences between modes 1 & 2 as well as modes 3 & 4, similarly to what we have done previously, interfered in MZIa1 and MZIa3 respectively. While measuring the phase shifts between the two pairs of mode, the phase matching stabilisation would decay with time, therefore deteriorating the receiver device's quantum states. The time of the phase stabilisation is minimised to ensure maximum entanglement is preserved.

3.6.1.2 Results

Photon coincident counting (CC) statistics are collected and are shown in Figure. 3.19, where the two 2D Hadamards projected are in Figure. 3.19. With spatial modes 1 & 2 projecting into the 2D Hadamard basis while modes 3 & 4 on the devices do the same. The statistical probability of measuring the coincident between the modes is presented, showing a high correlation in the pairing signal and idler modes for $\hat{H}_2$ two 2D. In the same Figure. 3.19 counting statistics for the 4D Hadamard are represented. As expected, the joint counting statistics show a strong correlation in the cases where the same bases are measured and low correlation when different bases are measured. The fidelity's of each of these are 83% and 73%, respectively. We present both these results next to the ideal in the same figure. The ideal statistics for both measurement results is the same. The different results are labelled in the figure.

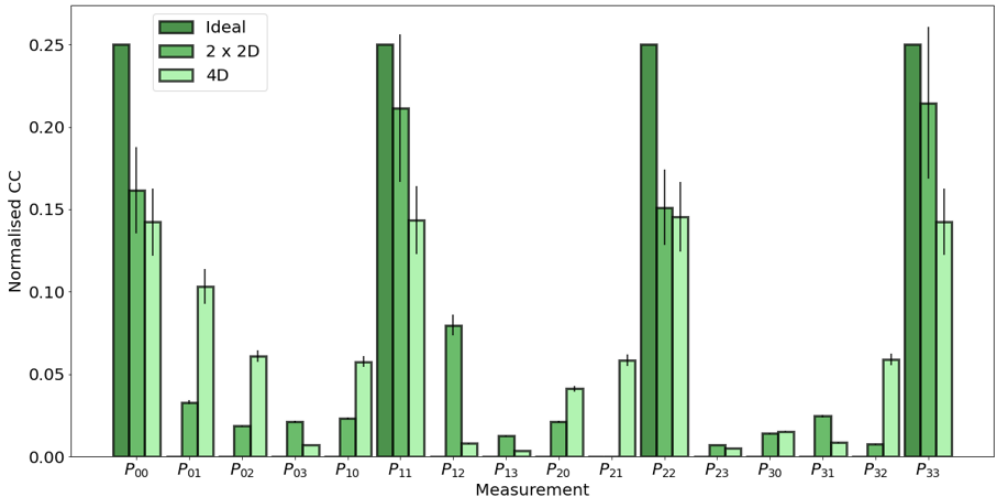

FIGURE 3.19. Transceiver and receiver Hadamard results.2 $\hat{H}_2$ measurements performed simultaneously, Essentially all four modes are projecting into the two 2D Hadamard basis The configuration set-up is the same on both the receiver and transceiver devices. Probability of coincidences while projecting all four modes into the $\hat{H}_4$ measured across the two devices is shown. Phase stabilisation occurring between all of the modes. The ideal state is also shown and the error bars are the normailsied square root of the number of counts taken.

The fidelity of the two 2D Hadamard state has a higher fidelity, as fewer phase stabilisation steps are needed and therefore less phase drift has occurred during measurement. Also fewer components are need and less error between the components forms.

The results for the two measurements made between the two devices, are close in comparison to the CST tomography results taken between 2 modes at a time. This decrease in fidelity, is from the longer phase drift experienced while correcting for the increased number of modes. [132] achieved 97% fidelity for their QKD measurements between two integrated Si devices using MCF.

3.6.2 QKD

3.6.2.1 Configurations

We demonstrate the step-by-step construction of a chip-to-chip measurement. Performing quantum measurements on a particular device cannot provide a platform for practical QKD protocols, as the goal is for each user to have a device, choose their configurations for their device, and project into their chosen measurement basis. At least two devices are required — one for Alice and one for Bob. High dimension entanglement distribution requires the generation of entangled states, which is achieved highly efficiently with integrated photonic sources on chips. An example here is in the form of MRRs. These are embedded in Alice device, allowing her to generate the qudit and measure them, while also sending the entangled pairing photon for measurement to

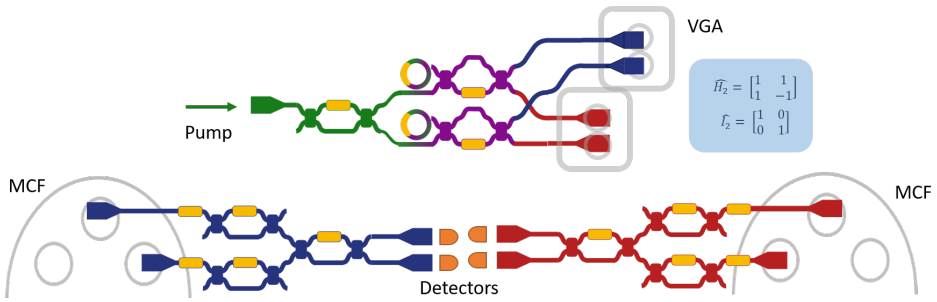

FIGURE 3.20. Simplified schematic of the three devices used to perform the measurements and the basis each is projected into for QKD.

the other user. The generator of the states can manipulate the states beforehand, causing a bias in communication. One of them must have the resources to generate the states.

An alternative is having a third party to generate entangled qudit states and distribute them among other users. The Alice, Bob and Charlie model described here makes Alice the generator and sender of the entangled states, while Bob and Charlie are the receivers. This removes the need for the receiver to host resources and biases in the communication. The simplified schematic of the minimal number of components needed to perform this measurement and the matrices to describe the basis are shown in Figure. 3.20.

As mentioned previously in this chapter, phase stabilisation is required for most measurement bases because of the requirement for all dimensions to have the same phase when projected, otherwise leading to uncorrelated measurements. Using the phase stabilisation method above has drawbacks in computational resource cost as well as time costs. Deteriorating the quality of the phase stabilisation hence deteriorates the fidelity of the quantum states.

This section builds up complexity in phase stabilisation through stabilising multiple modes and using up to three devices.

Dr. Daniel Llewellyn showed the phase stabilisation between two modes while performing QKD measurements [150] between two devices measuring in the basis:

$$\hat{M}_0 = \begin{pmatrix} (|0\rangle + |1\rangle)/\sqrt{2} \\ (|0\rangle - |1\rangle)/\sqrt{2} \\ (|2\rangle + |3\rangle)/\sqrt{2} \\ (|2\rangle - |3\rangle)/\sqrt{2} \end{pmatrix}, \qquad \hat{M}_1 = \begin{pmatrix} (|0\rangle + |2\rangle)/\sqrt{2} \\ (|0\rangle - |2\rangle)/\sqrt{2} \\ (|1\rangle + |3\rangle)/\sqrt{2} \\ (|1\rangle - |3\rangle)/\sqrt{2} \end{pmatrix}. \tag{3.10}$$

The average projector fidelity was 91%, with an average quantum error rate of 8.8%. We measured the loss increase of each device, the connecting fibres and the entirety of the network. We measured the loss in each of these be injecting a CW laser of 13 dBm, into the input port and measuring the power using Thorlabs power meter at the end. The devices included the VGAs loss, but this is nominally minimal compared to the loss within the devices. We measured the

connecting network through polarisation controllers, delay-lines and MCF again separating it from the network and injecting light into one end. All three of the components are measured at once. We used a free/space device to measure the output of the MCF.

After these measurements we connect the whole system together, inject light into Alice and measure the power outputted from Bob and Charlies outputs. We are able to find the loss of each component and the loss of the entirety of the network, allowing for an estimation in the number of counts a second we receive as well as the length of integration time needed, to visually represent the projected states.

The challenge of including a third device is the loss through the system. The transmitter device is measured to have a loss of around ≈15 dB. At the same time, a receiver device has a loss of around ≈20 dB. The network between them has a loss of ≈5 dB on each of the modes between the devices from the components and coupling. Many of the bases being projected require balanced power (number of photons) to project unbiased into the basis configured. The difference in the losses is measured at the receiver side of the chip by the interfere of photons on MZIs.

Adding the complexity of a second receiver, also having around 20 dB loss, further increases the attenuation in the number of photons detected, contributing to a total loss of around 65 dB (not including the loss to the SNSPDs and their efficiencies). This reduced number of photons, bringing it close to the noise floor and the dark count rates measured by the SNSPDs. Overcoming this is an engineering challenge, and explanations of methods used to overcome this are set out previously in Chapter 2. These hurdles must be overcome to provide a photon count high enough to produce a sufficient key rate for QKD. Reducing the number of modes to two allows double the pump power to the sources. Increasing the number of photons generated, therefore increasing the count rate. The complexity of ensuring optical power between all modes increases polynomially with increased dimensions (d). The increased power reduces the noise in the interference pattern, giving more precise offset phase shifts required for stabilisation.

With the reduced number of channels the phase stabilisation is for only active on two modes relative to their partner, much less resource intensive than 4D. Reducing the phase drift time and improving results accuracy.

Because of the reduced power from coupling to a third device, we increase the integration time as the count rate of the states decreases. We increase the integration time to one hour, with still 1 second measurement intervals and sum the results.

3.6.2.2 Results

We build upon this result, expanding to a network from two integrated devices to three. In the above, the states' sender also measured on the same device, while here, we demonstrate two receiver devices after the transmitter. The number of dimensions is lower to reduce the experiment's complexity and resource intensity, only coherently pumping two of the four sources on the device. This also reduces the complexity in phase stabilisation, stabilising just one pair of

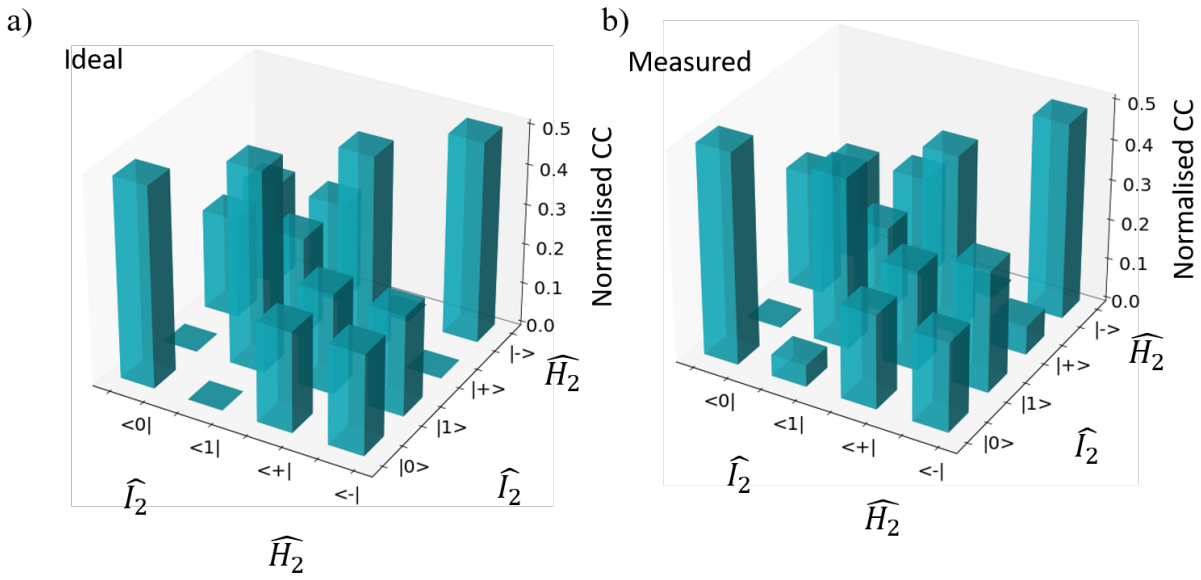

FIGURE 3.21. 2D QKD measurements. The entangled state is measured between 2D mutually unbiased bases, $\hat{I}_2$ and $\hat{H}_2$, as shown in the equations 2.20. a) The ideal simulated measurements, while the statistically collected measurements in b).

modes for each chip.

To verify the correlations in the measured counts between the qubits, all of the combinations of measurements were measured. Figure. 3.21 shows the eigenvectors in the bases that are predicted a), and that were actually measured b). The key outcomes that should be taken away are that when the users' measure on the same basis highly correlated measurements are found, allowing for a key to be established. In contrast, when the users chose a different basis, a close to equal probability distribution is measured in all outcomes. The measured results show a strong correlation when both of the same bases are measured on each receiver device and low correlations when the bases are different (mutually unbiased). The average state fidelity for this measurement is approximately 96%, close to other previously measured experiments. In contrast, the average bit error rate is calculated to be 6.4%, well below the 11% BB84 limit set [**?**].

The fidelity reported here is between 3 intergrated devices and is 96%, on par with two device measurements from [132]. The limit of other QKD measurements in literature between two integrated devices is quoted to be 98%, which we have very closely achieved between the three devices presented in this thesis.

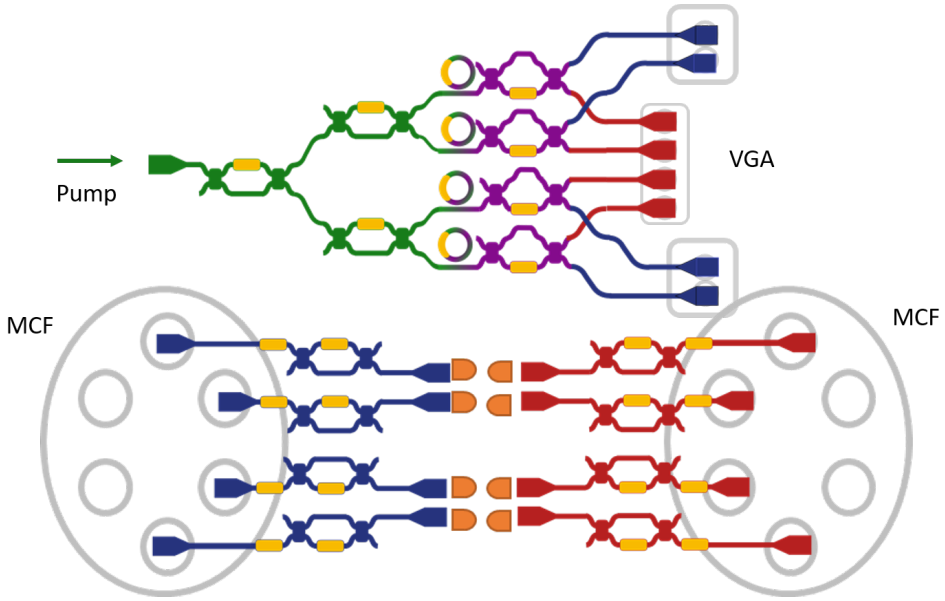

FIGURE 3.22. The simplified schematic used to perform the 4D measurements of detecting modes spatial modes across three devices.

3.6.3 Three Chip 4D

3.6.3.1 Configurations

High dimensional QKD has multiple key benefits, exploiting high dimensional quantum states generated and shared between users. High dimensional states have been shown to be more noise resilient, reducing the noise in the communications channels. The number of photons received by the receiver generally decreases with distance as there is an exponential decay in the transmission. The rate to generate the key also decreases with distance. High dimensional states overcome this by increasing the information density per single photon, allowing for a faster key rate generation.

Therefore, in this section, we increase the number of dimensional back-ups to four as we send the computational basis, which can be used in a high dimensional QKD protocol. Using Alice as the transmitter and Bob and Charlie devices like the receivers, set to project into the computational basis, no phase stabilisation is required as there is no interference between modes on the receiver side. The simplified schematic of the minimal number of components needed to preform this measurement and the matrices to describe the basis are shown in Figure. 3.22.

3.6.3.2 Results

For QKD the proposed measurement bases used are the computational $\hat{I}_2$ basis and the Hadamard $\hat{H}_2$ basis. These two are mutually unbiased and can be appropriately measured when using eight detectors, four at each receiver's output. The benefit of the basis I_4 basis and H_4 basis over

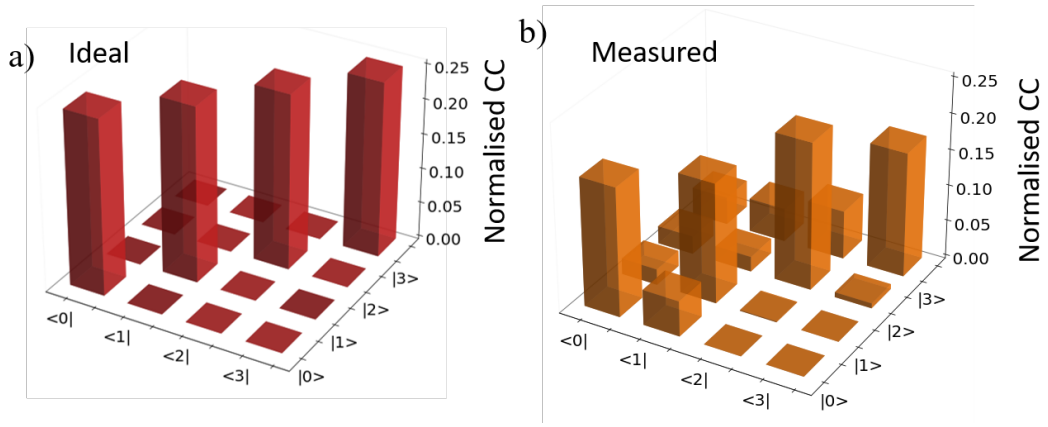

FIGURE 3.23. Computational Basis measurements across three devices. a) The simulated ideal probability matrix of a 4D coincidence measurement between the four modes across the two receiver devices. b) The statistically actual measurement probability of coincidences between all of the modes measured between the receiver devices, receiving signal and idler photons in each.

the 4D basis used $\hat{M}_0$&$\hat{M}_1$ previously is that this only measures two of the modes sent to each receiver at a time. Therefore, a minimum of two detectors are needed for this measurement and it only requires phase stabilisation one mode at a time to the other. This reduces the number of resources and complexity needed to balance the powers but dramatically increases the key rate generation, because the number of measurements taken increases.

Measuring in the $\hat{I}_4$ and $\hat{H}_4$ and using eight detectors increases the key rate generation fourfold. $\hat{I}_4$ is chosen, as the quantum states are projected into a basis not requiring phase stabilisation. The following experiment shows the first measurement of high dimensional entangled states distributed through multi-core fibre between three separate Si devices. Figure. 3.23, presents the simulations results from a) and measured results b) when projecting the 4D quantum states into the computational basis. As expected, there is a clear correlation in the photon statistics between the same modes, showing entanglement between the generated photons. Here the fidelity is measured at 85%, roughly on par with other communication protocols currently used [32, 132, 134, 136, 151]. A result that an be improved upon with improved phase stabilisation, but well above the quantum threshold.

3.7 Summary & Conclusion

This chapter has reported on chip-to-chip experiments in silicon quantum photonics, involving qubits and ququarts logical states. These are transmitted between integrated devices successfully. We have demonstrated that a 85% fidelity of 4D computational basis between three separate integrated devices is achievable. Two significant engineering aspects causing difficulty overcome

were the high loss rates experienced on each mode through the three devices and the coincidence measured at lower rates because of the phase drift between the multiple modes. The phase stabilisation protocol utilised a full fringe sweep to find the offsets and allowed up to four modes to stabilise, allowing for a phase-sensitive measurement, projecting a quantum state into the Hadamard basis producing a 73% fidelity, on par with previous results. We have shown that a spatial measurement basis for QKD across three integrated devices is possible.

3.8 Outlook

3.8.1 Phase Stabilisation

The limiting factors highlighted in this chapter is the capability to provide phase stabilisation between several modes on two different devices simultaneously. In this section of the outlook, we briefly look to cover different phase stabilisation protocols that can be applied and programming methods.

Firstly programming restrictions allowed only the phase-shifting and measurement of one modes at a time as these ran sequentially. Therefore stabilising four modes on both receiver devices is sequential. The method described for phase stabilisation of one receiver would require six additional stabilisations to occur. Therefore, by completing the last stabilisation and changing back to the measurement basis, the first two pairs of modes stabilised would have drifted apart from one another and the quantum states prolong sufficiently entangled for high fidelity measurements.

Reducing the phase drift rate is one approach to reduce this error. Using two multi-core grating couplers on the transmitter device would allow an MCF to be used along the entire communication path, reducing the difference in path length and temperature fluctuates each mode is exposed to.

Another approach is to use a parallel programming method by multi-threading processors controlling voltage boards to control each phase shifter independently. We would be controlling both devices at the same time and performing phase stabilisation measurements simultaneously, cutting the stabilisation phase in half. Stabilising a pair of two sequential modes on each device can be done simultaneously, meaning that the time to perform six measurements would be the same as the time to perform two.

In the experiments mentioned above that require phase stabilisation, the receiver devices' unitary configuration is the same configuration required to check the stabilisation of the phase. Changing the phase stabilisation configuration and the measurement configuration would also add time to increase the phase drift. When measuring the 4D Hadamard, this occurs once when measuring the phase difference between modes 1 & 3.

The methods described here all address and improve the phase stabilisation, using methods to reduce the phase drift rate or speed up the stabilisation process. An alternative method is to use

another laser. Injecting a second laser light into the system, whose path runs in opposition to the path of generated photons, allows for the phase difference between modes to be measured while measurements are being made. Phase stabilisation and the measurement phase can therefore occur at the same time. This uses an activate phase stabilisation, which only looks at measuring the power difference between the modes and not sweeping an entire fringe to find the magnitude and the direction of the phase drift.

3.8.2 QKD and CST

The ultimate goal is to show that high dimensional entanglement based QKD can occur between three separate quantum optics integrated devices. This requires the ability to measure at least two different mutually unbiased bases on the receiver devices. The computational bases are shown to be measured with fidelity of 85%. Another basis, such as the Hadamard basis, once measured on these devices can be used to show that QKD is possible, similarly to the method shown in the 2D QKD experiment reported. Once the basis has successfully projected in with high fidelity, completing a CST of the quantum state on the three devices will show that it is possible to use multiple basis between devices.

3.9 Acknowledgements

The author's contributions consisted of mounting and characterising the device and the experimental set-up, designing and performing the experiments, and analysing the data. Dr Daniel Llewellyn contributed to the experiment realisation, theoretical support and precursor results. Molly Thomas provided support in phase stabilisation calibration, optimising the stabilisation, which enabled the final results presented. The device was designed by Dr JianWei Wang and fabricated by Dr Yunhong Ding at the Technical University of Denmark. Dr Jorge Barreto supervised the work.

3.10 Code

The code for the project can be found at this Github Repository: https://github.com/ben-slater-121/Quantum-Control—Phase-Stabilisation

CHAPTER 4

QUANTUM OPTICS DETECTION SYSTEM PART I: DETECTION

4.1 The NODE

In the last chapter, a quantum photonic integrated communications network of three devices was demonstrated [152–154]. Our existing telecommunications network is complex, vast, all-encompassing and part of our everyday lives. To upgrade this system into a quantum internet [2], the system's engineering must be seamless to the end-users. Currently, encrypted communications largely consist of nodes [155, 156], in the form of servers, to communicate with one another. This is for everything from emails to bank transfers to simulation network clusters for big data. In this paradigm, a central resource is shared by end-users and managed as a service for them. Currently, quantum technologies cannot replace this architecture, but research is, as of 2021, striving for a solution. Testbed networks have been demonstrated in:

- Vienna (2008) A 200 km standard optical fibre between 6 locations [152].
- Tokyo (2010) A 6 node network [153].
- UK (Currently ongoing) Possibly a 3 node network.
- China (2018) A cross country network including ground to satellite QKD [154].

This chapter addresses the experimental practicalities to overcome this to provide a closed system capable of hosting users at scale. The system here is targeted at using MDI-QKD protocols, where these nodes would behave as Charlie in the MDI-QKD [47] scenario addressed in Chapter.2. However, it would behave as Charlie to multiple Alices and Bobs simultaneously, creating a network and behaving as a node between users, and therefore the concept is coined as a Quantum Network Operation Device Receiver (q-NODE).

These networks improve the capability and push the distance that QKD signals can be sent [48, 157], but how to serve a large number (hundreds) of users in a remote location is immature. As an inter-city communication system would require many users and the capacity to handle the traffic, it is important to showcase this functionality before widespread adoption is possible. Therefore, in the next two chapters, we address some of the practical necessities to overcome when developing for many users.

With near-unity system detection efficiency, 15 ps timing jitter [158], and 10s of GHz count rates [101], SNSPDs are an obvious choice when selecting single-photon detectors for quantum information applications. Their efficiency at single-photon detection is unmatched at over 98% [159] and they are still being researched to push their efficiency higher. SNSPDs are now commercially available with efficiencies above 95% as a standard by ID Quantique [160], Single Quantum [161] and PhotoSpot [162] to list a few.

SNSPDs are commonly used in QKD [1, 139, 153], because of their high detection efficiency and low timing jitter. SNSPDs are currently required to be housed inside a cryostat [92] in order to reach their T_c the critical temperature to become single-photon detectors. To house hundreds of SNSPDs in one cryostat requires new considerations compared to current SNSPD readout systems.

The contents of this chapter will be built on in Chapter.5, which will list the equipment, experiments and results that are prerequisites to building such a system. We begin by explaining how the cryogenic station functions and its capabilities to provide the cooling power and user bandwidth needed. After this, we will explain how to overcome the system's vibrations that come with engineering a high power cooling system. Lastly, we will describe the characterisation of the SNSPD used as a testing tool for the later mentioned photon counter system.

4.1.1 Cryogenic system

Superconducting detectors require appropriately low temperatures to operate (typically <2 K). To reach these temperatures efficiently, a closed-cycle cryostat can be used, the definition of which can be found in Chapter 2, section 2.5. The Innovative Cryogenic Engineering (ICE) Oxford company designs and manufactures the system [163]. This system offers the cooling capacity and space for components required to construct a q-NODE.

The ICE Oxford DRYICE1K in Figure. 4.1 is a closed-cycle cryostat that utilises an unusual dual cold head design in tandem with a high-power vacuum pump to liquefy and evaporate helium at low pressure. This gives the system a base temperature of around 1 K. The whole system is thermally isolated from room temperature by a vacuum can. To achieve this, the cryostat has nested radiation shields that effectively separate the vacuum chamber into thermal zones, each with a separate sample stage. It consists of a vacuum container space with four stages, with 3 being sample plates stages for mounting equipment and devices, and the other stage hosting access to electrical and optical connections and a connection to the He pot.

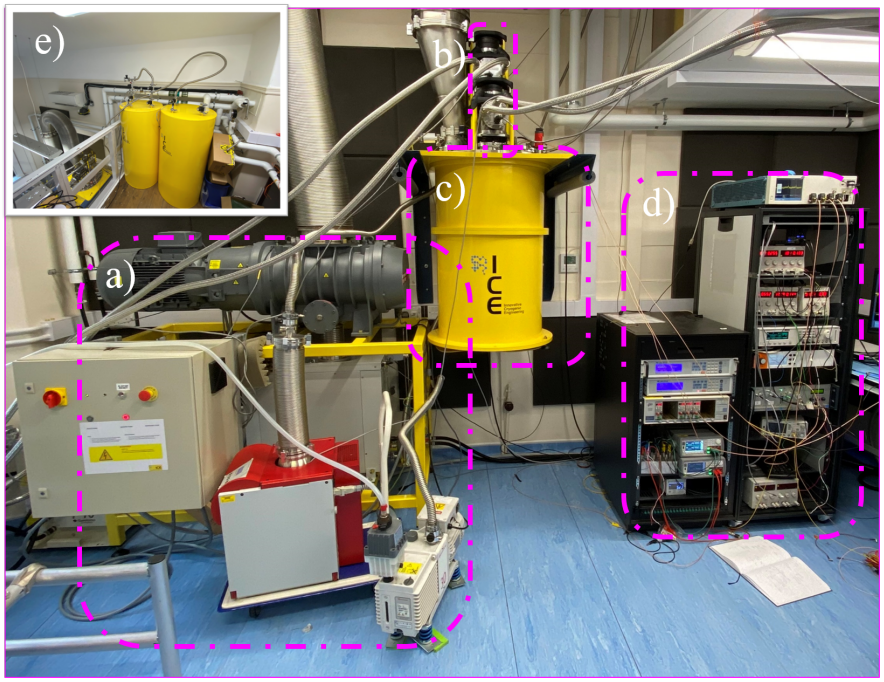

FIGURE 4.1. Photograph of the DRYICE1K experimental set-up. a): Four vacuum pumps with the turbo and roughing pumps used to pump the sample area to vacuum, while the roots and backing pump flow low pressure around the helium network. b): two cold heads. c): The vacuum sample space. d): The equipment racking, hosting temperature sensor readouts, small measurement unit devices, pressure readouts, power supplies, frequency counters, oscilloscopes, arbitrary waveform generators, and position controllers. e): Two 300 L helium resevior dumps.

The He pot is a reservoir to collect liquid He between the pumps and the two-stage cold head. The three stages are named 50 K, 4 K and 1 K, in representation of their nominal temperature as shown in Figure.4.2. Between the 4 K and 1 K stage, is the fourth stage containing the *He* pot. Each of the three sample stages has an individual radiation shield, reducing heating effects from other warmer stages. A vacuum "can" around the outside, as seen in Figure. 4.1, is used to keep the whole system in a vacuum and isolated from the environment. The system is cooled by two GM cold heads and a separate helium gas network system.

The following instrument components are built into the system:

- **RDK-500B Sumitomo Cryocooler**: A single-stage cold head, 60 Hz operating frequency providing 94 W of cooling power at 30 K. This penetrates the cryostat system down to the 50 K sample plate stage, thereby cooling this stage and pre-cools low-pressure helium. This is installed with grated copper heat exchangers along the shaft to maximise heat transfer with helium.

- **RDK-415D2 Sumitomo Cryocooler**: A two-stage cold head with 60 Hz operating frequency provides cooling power of 45 W at 50 K at the first stage and 1.5 W at 4.2 K at the second stage. This passes through the 50 K sample stage, level to the 4 K sample stage, thereby cooling this stage and cooling the helium until liquefaction. This is again installed with copper heat exchangers along the shaft to maximise heat transfer with helium.

- **F-70 Water-cooler Sumitomo compressor**: Each cold head is attached to a separate He compressor, which liquifies helium as a heat transfer mechanism which is then cooled by the water inside the cooler.

- **Edwards GX600 L Dry Pump**: Backing pump flows helium through the system and providing cooling power via lowering the pressure inside the He pot. We measured a pressure of of 7e-4 mbar inside the sample area, using the Edwards GX600 L Dry Pump is in use.

- **Edwards EH4200 Mechanical Booster roots pump**: Increasing the vacuum on the He pot and, therefore, the cooling power of the system. This pump can be used as a single-shot or continuous cooling operation.

Two 300 L dewars supply 99.999% purity helium at 950 mBar that cools the sample space inside DRYICE1K. Helium flows from the dewars around the two cold heads: Sumitomo RDK-500B Cryocooler and the Sumitomo RDK-415D2 Cryocooler [164], in turn. They are mounted on flexible bellows to provide a vibration-damping buffer between the cold heads and the rest of the system. The helium flows over copper heat exchangers that are mounted on the cold heads, cooling and condensing the helium into the He pot that sits at the 1K plate. The Liquid He (LHe) is pumped in a closed loop by the backing and roots pumps between the dewars and the He pot in the cryostat. A computer-driven needle valve limits the flow rate between the pumps and the He pot, controlling the flow rate of the He through the system.

There are three separate helium flow circuits. Two of the lines provide high-pressure helium for the cold heads. The compressors are pumping helium to and from the cold heads and compressors. The third is the low-pressure line that flows through the 300 L dewars and in and around the cooling network within the cryostat. This helium line provides a thermal heat transfer between the cryostat and the heat exchanges on the cold heads. It evapourates into the He pot to provide cooling via evaporation. The two cold heads operate on the similar principle as a domestic refrigerator. Water-cooled compressors cycle high-purity helium at high pressure (200-400 PSI) through heat exchangers within the He line. Thermal energy from the low-pressure Helium exchanges with the cooler higher-pressure helium. This is then pumped out of the cryocooler, where the compressor increases the pressure, increasing the temperature and allowing the excess heat to be transferred to refrigerated cooling water, before the gas is then cycled back through.

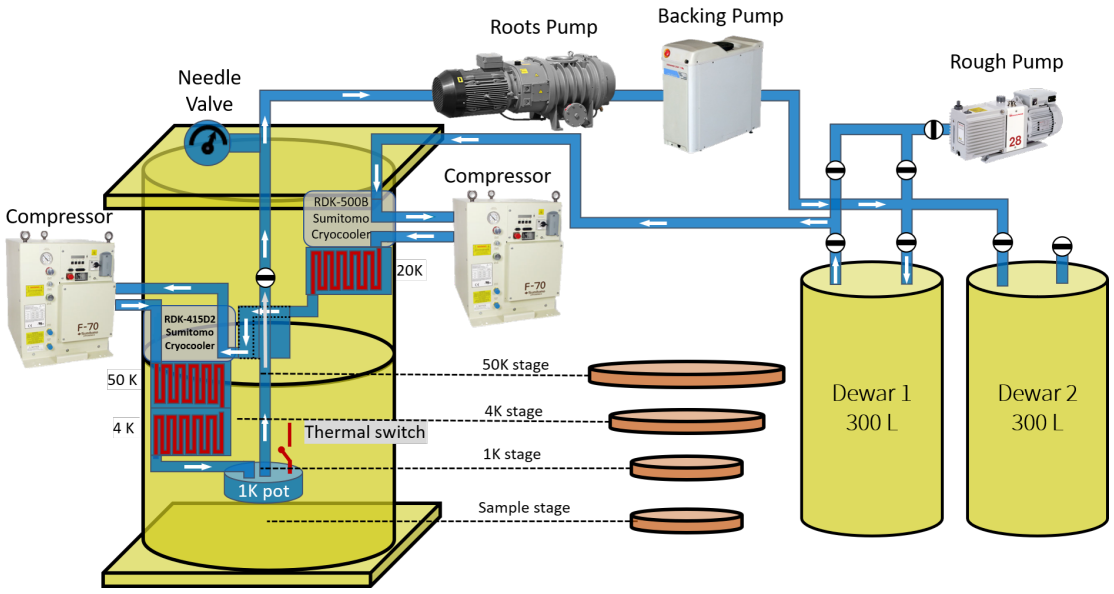

FIGURE 4.2. Schematic of the helium network for the DRYICE1K system with the blue line representing the path of the helium. The line is a low vacuum. Once the dumps are open to the line, the helium flows around the system, where the pumps then pass the helium back to the dumps completing the cycle. The helium passes over the heat exchangers of both cold heads, cooling the helium in the system. Once at 4.2 K, liquid helium is collected in the He pot.

The system requires only electricity and cold water ($< 18°C$), as the helium itself is contained internally, thus running for long uninterrupted periods and requiring no external handling of cryogens.

The DRYICE1K operates in either continuous or single-shot cooling modes. A base temperature of 1.3 K is used in continuous mode, the needle valve providing a 2 mbar pressure environment. To perform a single shot measurement, all of the He for the dumps is condensed into the He pot. When an equilibrium in pressure occurs, between the pot and dumps, no more He is condensed into the Pot. This provides the longest time duration (3 hours) for a single-shot. As the He condensation becomes to main cooling mechanism. During single-shot operation, with the roots pump active, a base temperature of 0.9 K can be reached. The specific base temperatures are dependent on the heat load and vary with the experiment. The pumps return the helium to the dewars, forming a closed system.

The system provides 64 electrical connections between the 1 K stage and the outside environment. 16 of the connections are made of semi-rigid cabling suitable for RF signals up to 6 GHz. 48 of the connection are DC rated lines that are un-shielded and support low-frequency electrical signals. Eight single-mode fibre 9/125 μm connections also provide an optical path between the 1 K stage and the outside environment. All the connections allow for driving voltages, SNSPDs readout, and detector efficiency equipment to be accessed. Extra ports are available for additional

bespoke connections.

Good thermal conduction is required inside the cryostat. The sample stages are made of oxygen-free and high thermal conductivity copper. Sample mounts are also typically made from copper. However, they are usually coated with a protective layer of gold to improve reflectively, in-turn reducing the absorption of black-body radiation from higher temperature stages. The gold layer also does not oxidise over time, unlike copper, which reduces in thermal conductivity. Copper has a thermal conductivity of 385 $Wm^{-1}K^{-1}$ [165] and gold 314 $Wm^{-1}K^{-1}$ [165], both a relatively high thermal conductivity for available metals. However, the copper oxide that can oxidise on the surface has a much lower thermal conductivity of 33 $Wm^{-1}K^{-1}$ [165]. In respect of the rest of the system, the can and flanges are made of steel for strength and have a relatively low thermal conductivity of 30-70 $Wm^{-1}K^{-1}$ [165] depending on the steel carbon content. The the sample and cooling stages are not in thermal contact with the vacuum can, as the vacuum insulates between the two. During the cool down, a heat switch in the form of Cu braids that can be placed in thermal contact with the sample pot stage from the 4 K stage allows for an increased cooling rate and reduces cycle times.

When operating the DRYICE1K from a typical starting state, the helium network would be at 20 mBar pressure, with 600 L of 99.999% pure helium contained in dewars, and the vacuum can and radiation shields removed to expose the sample stages for loading test samples. The three radiation shields and the vaccum can (Order: 1 K, 4 K, 50 K, vacuum can) are attached in order to close up the system. The turbo and rough pump are used in tandem to create a 1e-5 mBar vacuum in the sample space. The sample space is isolated from the pumps as the system begins the cooling cycle.

The two water-cooled compressors are activated, in turn initialising the cold heads to begin cooling the cryostat. Simultaneously, helium from the dewars is released to flow around the helium network, assisted by the activation of a backing pump. The cold heads then begin to cool the helium in the helium network and the system. The system requires 36 hours to reach the base temperature of 1.3 K.

4.1.2 Vibration Damping

The compressors, cold heads and vacuum pumps, while active, cause mechanical vibrations. In a system designed to host integrated quantum optics, vibration in the system has to be minimised. Vibrations are naturally caused by GM cryocoolers, which are the optimal choice when frequent cooling cycles and cooling power is required in the environment.

The GM coolers naturally provide a source of vibrations, which when coupled with integrated quantum photonics devices provides high losses. There are methods to reduce vibrations [166–169], but many come at a cost to cooling power. Therefore maintaining cooling power and dampening vibrations externally is a suggested way forward.

The DRYICE1K system has been designed to allow integrated waveguide SNSPDs to be

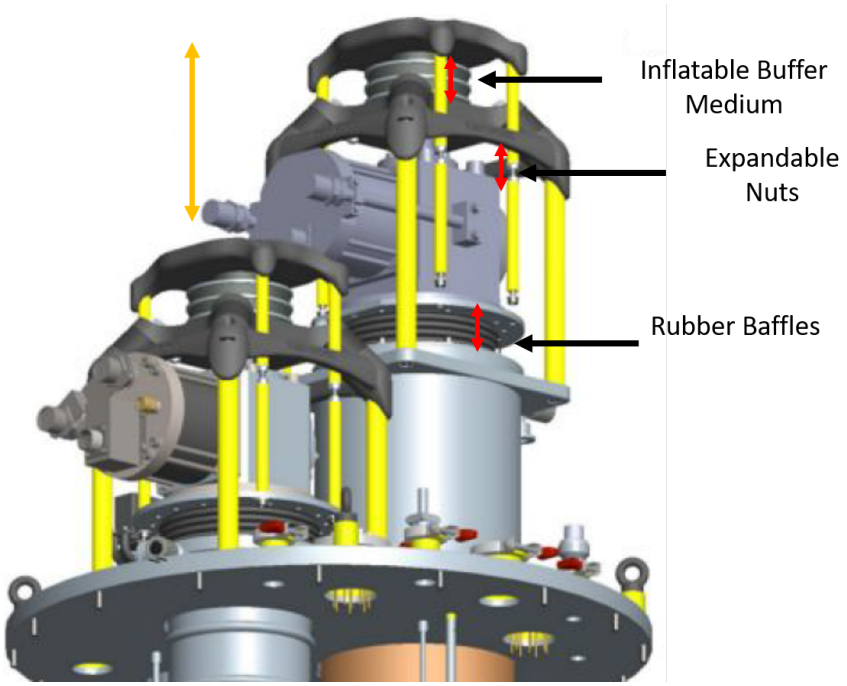

Figure 4.3: Technical drawings supplied by ICE oxford of the GM cold heads, with AV frames. The orange and red arrows for the adjustable components in the AV frame structure.

coupled optically through grating couplers. This requires photons to pass between fibres and optical devices using a free standing fibre V-groove array (VGA) and grating couplers. The grating couplers and fibre apertures on the scale of microns. Misalignment between fibre arrays and grating couplers leads to loss of photons and reduced system detection efficiencies.

The AV frame used is shown in Figure. 4.3. With the adjustable mechanical nuts and the inflatable buffer providing lift to the cold head. The cold head is lifted to minimise weight through the rubber baffles so the weight is hanging by the inflatable buffer. The rubber baffles only expand to accommodate the gap between the cryostat top plates and the GM cold head flanges. This is expanded through the adjustment of the inflatable buffer and adjustable nuts.

An adafruit is a micro-controller with an in-built 3-axis accelerometer is used to measure the vibrations [170] and is bolted to the 1 K sample stage. The accelerometer is located at the same location as the optical device during operations. This location will provide a approximation measurement of the vibrations that an optical device would experience. Measurements are collected during a cooling cycle: before the freeze-out causes, the accelerometer to stop.

Presented here are measurements of the vibration sources that show how damping of vibrations is performed to allow for acceptable vibration values. 5 μm vibration tolerance is deemed acceptable, as on this scale the fibre and grating couplers still overlap to provide coupling.

Multiple vibration sources are identified throughout the system. These are the turbo pump, the backing pump, the roots pump and the coldheads/compressors. This is done by powering each

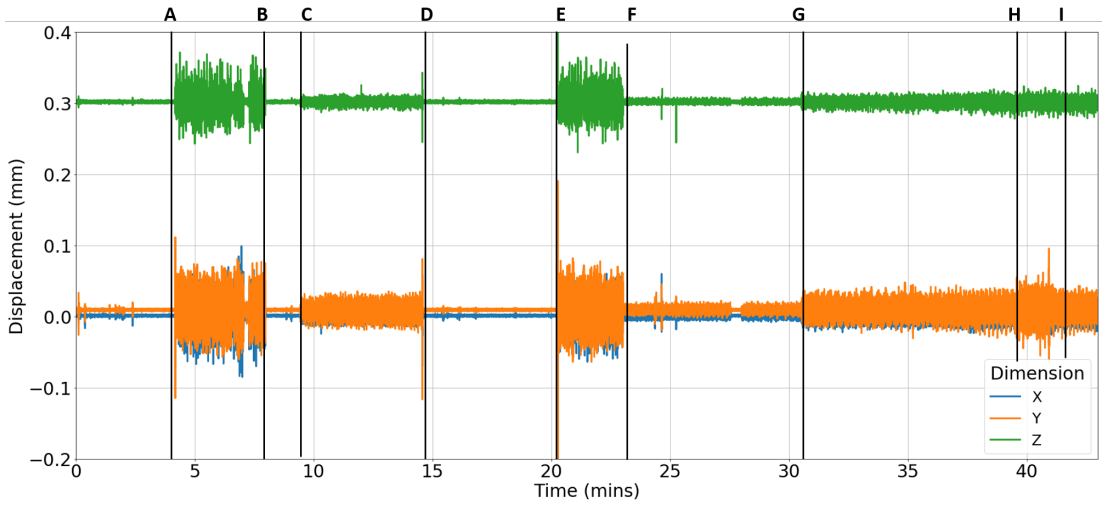

Figure 4.4: Measured displacement with time for different sources being activated and deactivated. Several sources are identified: roots pump, backing pump, turbo-pump, cold head and the beating between the two cold heads. The figure measures base vibrations. (A-D): Both cold heads are turned on and then switched off at B; just the 4 K cold head is switched on and then off. (E-F) The cold heads and the backing & roots pumps are switched on, and then at F the cold heads are switched off. (G-I): The 4 K compressor is switched on followed by both cold heads at H, which is then switched off at I.

asset in isolation over a testing cycle, as shown in Figure.4.4 which represents a vibration test cycle timeline with vibrations measured of different components of the cryostat, with isolated and combined vibrations, to map, outsources, and interactions between sources. The timeline in Figure.4.4 shows the maximum displacement of X calculated, while the accelerometer measured acceleration a. By knowing the frequency f of the vibrations measured, we can assume that follows sinusoidal vibrations, and we can use the formula:

$$X = \frac{a}{2\pi^2 f^2}. \tag{4.1}$$

The Z-axis has a constant acceleration measurement due to gravity. This result is left purposely displaced as the z-axis vibrations differ in magnitude from the XY plane.

Figure. 4.5 is the RMS values for each of the sources of vibrations. AS we can see the roots pump provides 18 μm of vibration, but the dominating source of vibrations is the compressors, above 60 μm RMS of vibrations. In this figure we also see the vibration from the compressors when the AV frame shown in Figure. 4.3 is engaged.

The turbopump for the sample space was also tested. Negligible vibrations from the base are measured. The turbopump operations are not used at base temperatures; therefore, they are omitted from further investigation and consider unnecessary to damp.

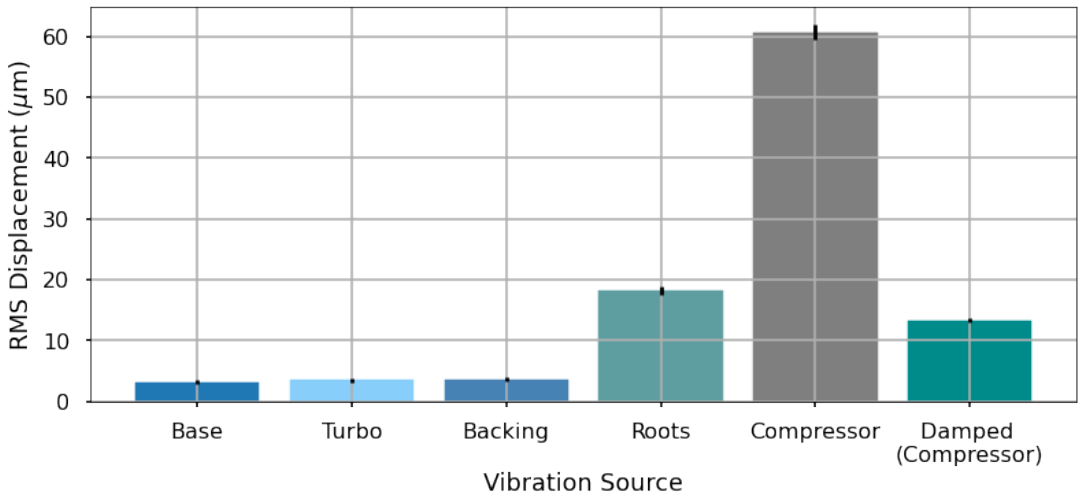

Figure 4.5: Chart of the vibration displacement of all three axis RMS, for each asset, with error bars.

Vibration Source	FWHM Axis-X (μm)	FWHM Axis-Y (μm)	FWHM Axis-Z (μm)
Base	1.49 (±0.2)	1.41 (±0.2)	2.44 (±0.2)
Turbo Pump	1.71 (±0.2)	1.90 (±0.2)	2.31 (±0.2)
Backing Pump	1.92 (±0.2)	2.01 (±0.2)	2.33 (±0.2)
Roots Pump	13.10 (±0.4)	12.28 (±0.4)	3.04 (±0.2)
Compressors	35.27 (±0.7)	43.61 (±0.8)	23.1 (±0.5)
(Damped) Compressors	8.50 (±0.2)	9.11 (±0.3)	4.69 (±0.2)

Table 4.1: FWHM of the histograms of the displacement calculated from the acceleratometer in contact with the 1 K sample plate during activation of different vibration sources required for DRYICE1K operation.

From the timeline we can see that the colds head being active simultaneously provides the largest vibration source, on average 0.06 mm displacement, dominating the vibrations over the line vacuum pumps. Individually, each of the cold heads provides the largest vibration source, but when their activation and vibrations are combined, the vibrations' sum varies. A beating is created by the timing phase between the two cold heads' pulses. Their phase determines their combined vibrations' amplitude. This is difficult to measure due to the start-up nature being performed manually. The timing between pulses is around 1 second; therefore the time between pulses is difficult to measure accurately, but different vibrations' amplitudes are measured. The displacement measured at the sample stages is visualised in Figures.4.6 and 4.7. The magnitude of vibrations is larger in the XY plane than the Z-axis, as the beating causes a "rocking" motion within the cryostat.

The cold head pulses are the dominant source of vibrations in the system. Therefore the aim is to reduce the contact and force the mechanical vibrations exerts on the rest of the cryostat system via damping. Anti-vibration (AV) [171] frames are bolted to the cold heads, floating in the

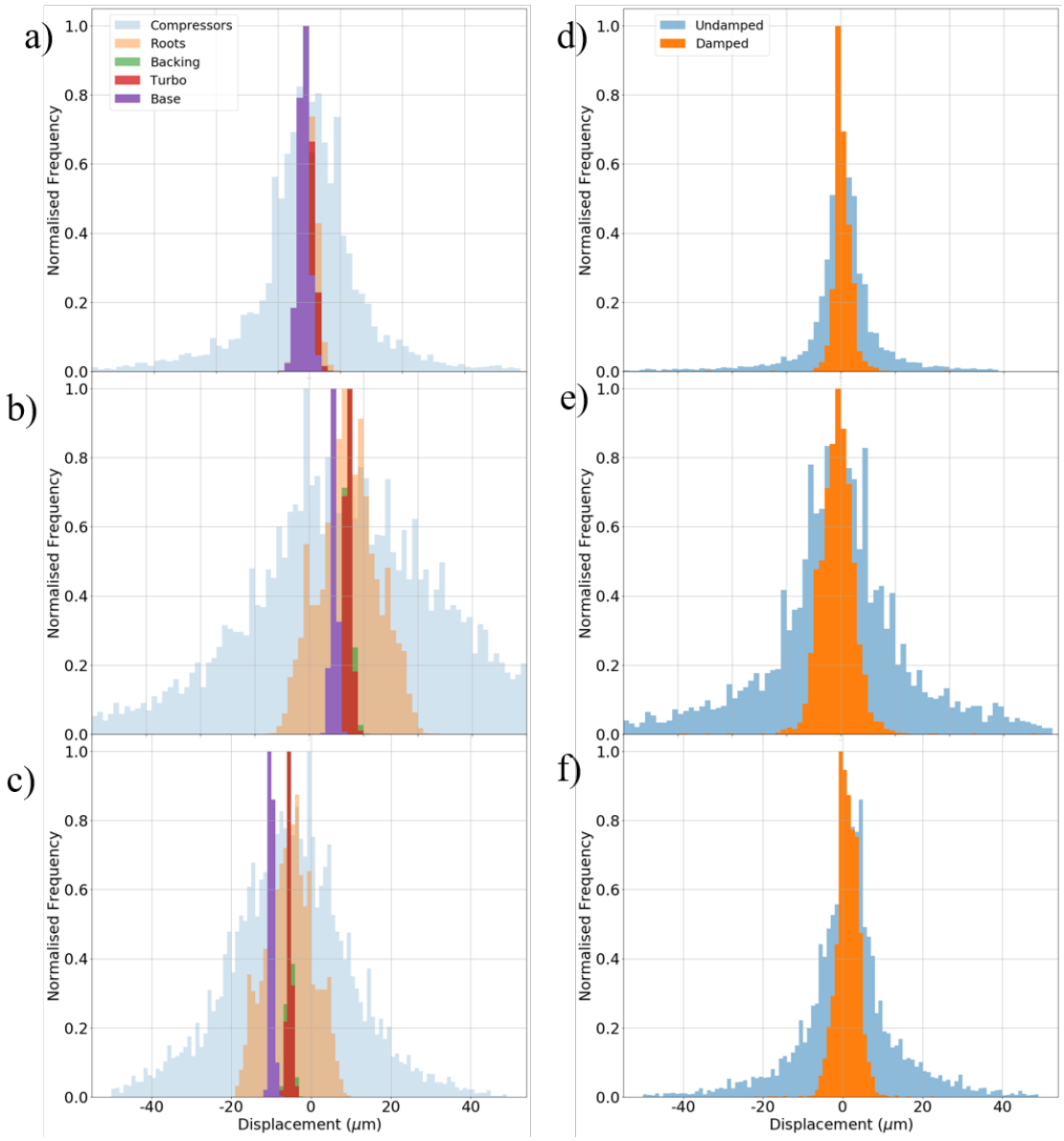

Figure 4.6: Histogram of vibrations measured for 5 minutes with each source normalised. Vibration displacements in the a) Z-axis, b) Y-axis, and c) X-axis. The Z's off zero values are due to the acceleration from gravity, which is compensated for, and the offset in the XY measurements due to the un-flush connection between accelerometer and the sample mount, leading to a tilt, therefore measuring acceleration due to gravity. d), e) and f) represent the same axis measurements and show the difference in the compressor's vibrations before and after the AV frame is used.

cryostat, meaning that the only two sources of contact both between the cryostat & cold heads are rubber baffles and an air cushion between the AV frame & cold head. When the air cushion is inflated this simultaneously lifts the cold head and damps the vibrations. The differences in vibrations throughout are shown in Figures.4.6 & 4.7.

The figures show that the vibration difference between the roots pump and the compressors become dominating displacement sources at 40 Hz. The accelerometer measures the vibrations at different resonant frequencies and the acceleration was largest around this frequency. The displacement is calculated from the acceleration measured from the adafruit 3-axis accelerometer. In Figure.4.6 a) the vibrations from the compressors have a much smaller FWHM than in the XY plane. The offset from the accelerometer's systematic error can be seen in the results with the shift from the centre. Figures.4.6 d)-f) are vibration measurements before and after the AV frames are engaged.

Heat maps of the histograms of each vibration source in the XY plane for Figures.4.6 a-c) are visualised in Figures.4.7, while Figures.4.7 e) & f) are visualised in Figures.4.7 d)-f). These figures show that the spread of points varies between different vibration sources. Figure.4.7 e) & f) also shows that the AV frame's damping significantly reduces the displacement. The low resolution of some of the graphs in the figures is from small FWHM, as the accelerometer's resolution limit is reached.

The FWHM of the vibration displacements from Figure.4.6 are shown in Table.4.1. The main vibrations sources are the roots pump and the compressors. The roots pump is not used unless achieving temperatures below 1.3 K or single-shot measurements, which is not required for SNSPDs to be superconductive. Single-shot operation can reduce the temperature of the system to 0.9 K where some commercial SNSPDs operate at. The AV frame provides an average decrease of 75 % in vibrations in the XY plane, close to the tolerance of vibrations to achieve top-down optical coupling.

4.1.2.1 Summary

Vibration damping was also attempted with removable legs for the cantilever frame. Two adjustable steel rods are expanded to fit between the floor and the cryostat frame arms. These are rubberised at either end and can be removed to allow access to the vacuum cans during sample changes. When the accelerometer is replaced, and the same measurements performed as previously mentioned, no difference in the magnitude of the acceleration is measured. Another method is using the lifting table used to remove the vacuum cans as an artificial floor. A rubber plate is glued to the bottom of the can to provide a large contact surface area between the table and the can. The lifting table can be expanded between this gap to take the weight of the cryostat. When the vibrations are measured during this dampening method, the vibration measured was larger than without the table. Therefore the table is not used.

The damping has significantly reduced vibrations but is not within tolerance defined by

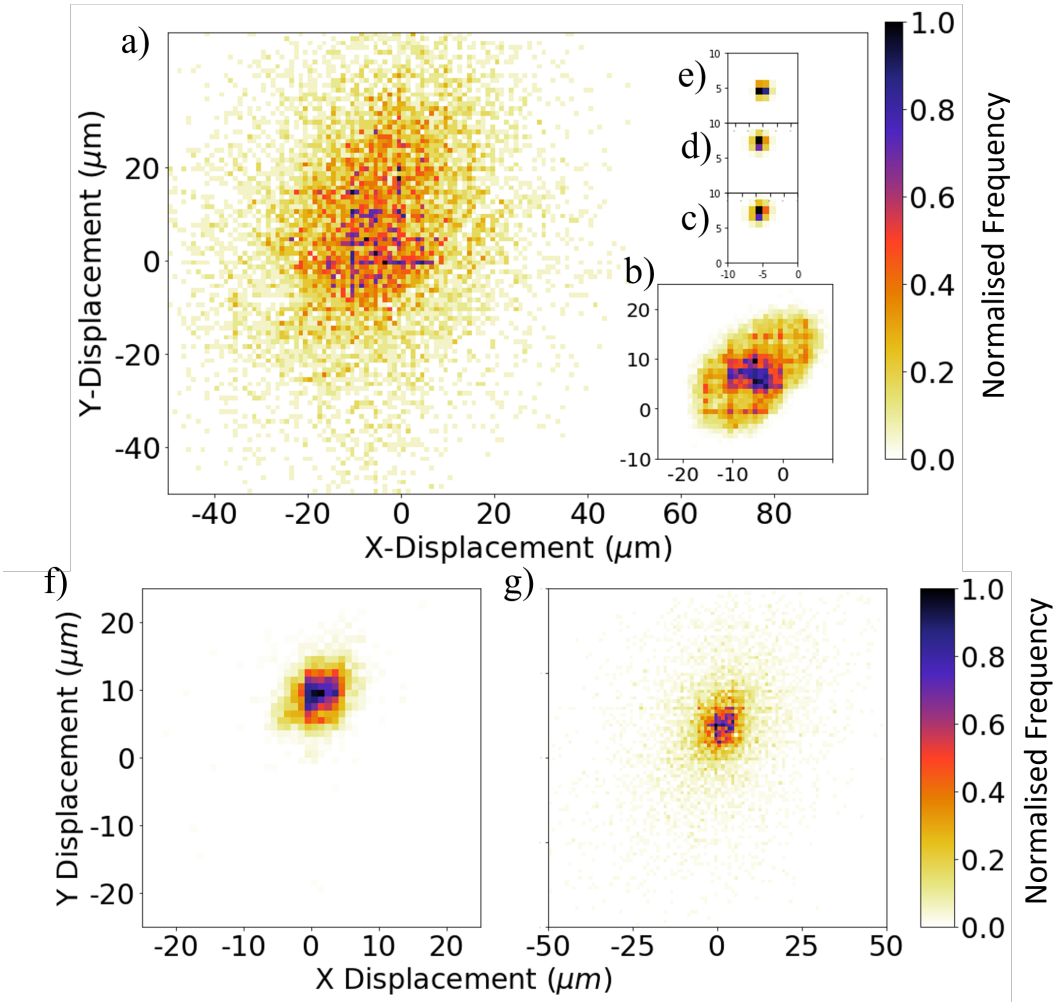

Figure 4.7: Normalised heat map histogram of displacement in the XY plane during: a) both cold heads active, b) roots pumps, c) the backing pump, d) turbo pump and e) base vibrations. The pixels on the figures illustrates the resolution limit of the accelerometer. Normalised heat map histogram of the vibrations from the cold head, when: f) the AV frame is used to damp by lifting the cold head, and g) the AV frame is not utilised.

the focal area of a grating coupler that is on the scale of tens of microns. It is dropping to 9.11 μm displacement in the XY plane. We can compensate for the vibrations with a single shot measurement without the cold heads activated, using the liquefied helium collected in the He pot. Further testing can also be done using two accelerometers, measuring the difference in displacements between the VGA and the device by mounting the accelerometers onto the components.

4.1.3 Temperature Calibration

The DRYICE1K has four Lakeshore RTD cernox temperature sensors, mounted on the He pot plate, the 4 K plate, the He inlet valve after the first stage cold head, and the last sensor on the inlet after the second stage 4 K cold head. These sensors are used to measure the operating performance of the DRYICE1K and not used to measure sample temperatures accurately.

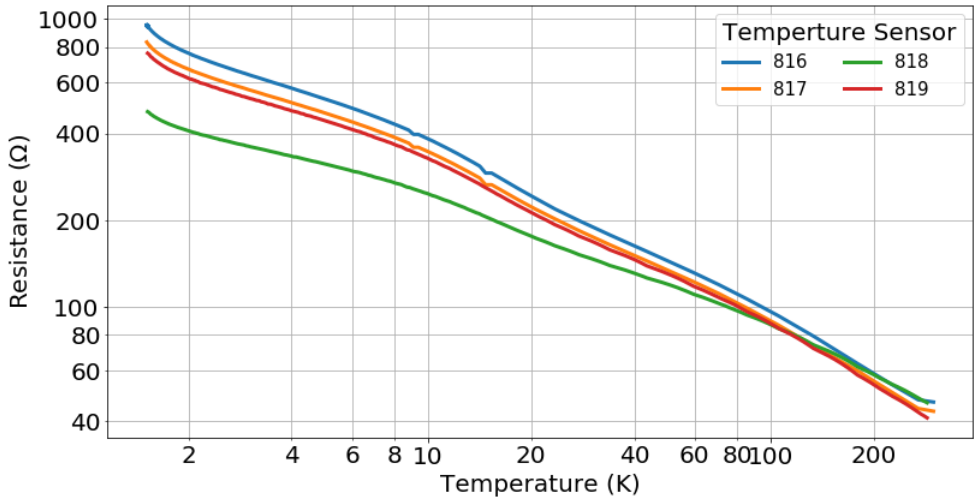

FIGURE 4.8. Temperature sensor calibration, using a Lakeshore calibrated provided cernox RTD sensor, with the samples in thermal contact with the 1 K sample plate plate. Labels refer to unique part of sensors' serial numbers.

Another four cernox RTD CX-SD temperature sensors are used throughout the DRYICE1K operation, one for mounting onto sample holders for proximity to FPGA, amplifiers and SNSPDs. The four sensors require calibration; therefore, another pre-calibrated sensor is in thermal contact with the other four during calibrations. These sensors are mounted in thermal contact with an encapsulated heater pot in thermal contact with the 1 K stage through a Lamitex glass epoxy rod, providing insulation between the heater pot and the sample plate. The heater pot consists of a resistive copper alloy wire, allowing precise and steady temperature variations at the pot to give accurate temperature or resistance measurements for all four sensors during calibration.

The temperature sensors are connected through the DC connection on the cryostat with quad-twist 36 AWG manganin wire. The wire has a low relative thermal conduction, and therefore four-

wire measurements are used to calculate each sensor's resistance. The low thermal conduction materials also have a low electrical conductivity, increasing resistance. To isolate the resistance of the sensor, four-wire measurements are used. The resistance is measured every second as the sample area is heated and cooled using a combination of the installed heater and the DRYICE1K cooling power. The temperature vs. resistances measurements of the calibrations is shown in Figure.4.8 with a logging every instance every second, which is then smoothed with a Savitzky-Golay Filter [172]. These calibration files are loaded onto a Lakeshore Model 336 to reuse the temperature sensors in all of the following experiments and set-up. The sensors are calibrated to the system's base temperature during a single-shot operation of 0.9 K. The system is measured in two different stages to reach sensitivity and precision for lower temperatures as the resistance is logarithmic with temperature. Between 20 K and 300 K, the system is measured during a warm upcycle, while < 20 K the heater provides increasing thermal energy while the system is at base temperature. The sensors are calibrated below the SNSPD operation temperatures used.

The Temperatures sensors provide consistent, continuous data and the calibrations are to high enough resolution to be used as temperature sensors in the rest of the experiments and monitoring of the system. These sensors will be attached to the SNSPD mounts and other components test in Chapter. 5

4.2 SNSPD Characterisation

An SNSPD provided from the University of Moscow by the research group lead by Gregory. N. Gol'tsman is shown in Figure.4.9. The SNSPD was used to test the characterisation setup and extract key metrics. The SNSPD is made for NbN, designed for photon arrival direction perpendicular to the wire's plane. The nanowire has a 100 nm wire width and 100 nm spacing between nanowires. This section explains the performance of the SNSPD, providing critical currents, Dark Count Rates (DCRs) [173], detection efficiencies [174] and other characteristics [175] in support of the results presented in the next chapter.

4.2.1 Setup

The device is mounted on a 16-channel sample mount and attached with 25 cm long Sub-Miniature Push (SMP) RF connectors as shown in Figure. 4.10. These connect to the outside through with Sub-Miniature version A (SMA) cables to the rigid RF cabling in the DRYICE1K. SMAs are the most common and standard connector interface between RF compatible cabling. The coaxial design and screw connector ensure good signal transfer. SMPs behave much the same and are used in some cases due to their smaller size, allowing for increased density of connectors. The device is bolted to the 1 K sample stage as shown in Figure.4.10 a), and thermal conductive grease (Apiezon) forms a heat transfer connection between the gold plated sample mounting plate and the sample stage.

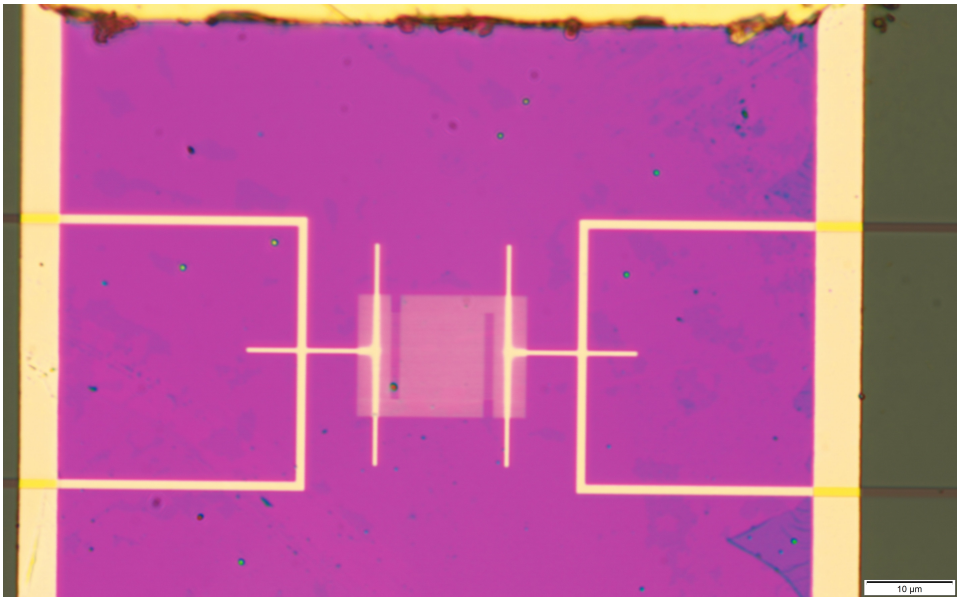

FIGURE 4.9. An optical microscope image of a parallel-wire SNSPD provided by Dr G. N. Gol'tsman, University of Moscow. With the gold lines being the electrical connections between the SNSPD and the eternal connections, and the gold fine mesh in the middle being the NbN nanowire detection spot. The pink area is resist after Au has been removed and is an insulator.

The photos of the electronics testing cages is shown in Figure. 4.10c) with a close up in d). The sample mount for the device comprises a copper mount with gold plating to avoid oxidation. In contact with the sample, the mount is a PCB consisting of 16 gold-coated electrical connections connected to the SMPs and four grounding pads. 25 μm wide gold wire bonds are used to connect the SNSPD to the PCB electrically. The device is adhered to the mount using VGE-7031 varnish. VGE-7031 varnish is used as, once baked, it does not out-gas and can be used in vacuum environments. Out-gas, it gas trapped inside the medium being emitted at low pressures, increasing the pressure of the system and limiting the base pressure achievable. The varnish also provides good thermal conductivity between the sample and mounting.

The device is cooled to a base temperature of 1.3 K during characterisations unless otherwise stated.

The circuit diagram used to characterise the SNSPD can be seen in Figure. 4.11. For the simple characterisation (resistance vs temperature, current vs voltage), only the Source Measurement Unit (SMU), SNSPD, and 50Ω resistor are used. The Keysight B2962A SMU operates in a two-wire resistance mode, with a shunt resistor connected to a T-piece outside the cryostat. We also connect a Agilent 53230A universal frequency counter the measure the number of counts the SNSPD produces. A Tektronix DPO73304SZX (33GHz, 100GS/sec), to measure the SNSPD pulse waveforms. This is also the same setup used in Chapter. 5. The Instrument titled FPGA is not used in this chapter. The waveform generator is also not used and is described in the next

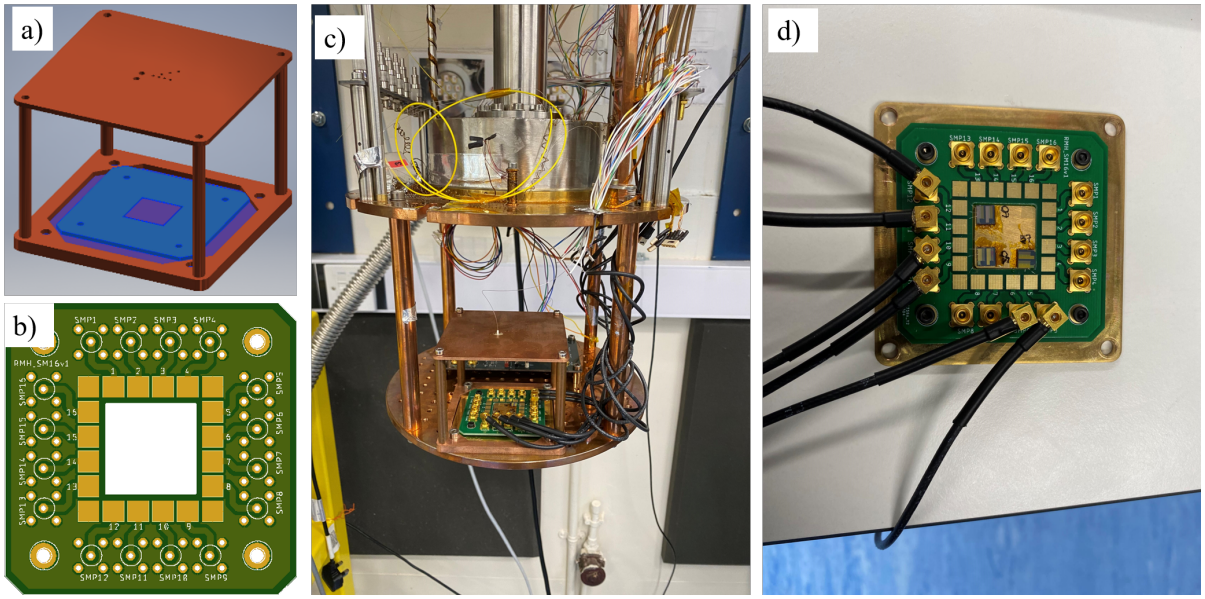

FIGURE 4.10. Sample mounts and set-up equipment a) CAD model of the wire bonding sample mount, with b) as the PCB place into The top copper plate in a) has mounts for fibres to guide light onto the sample. c) is the sample set-up of the 1 K pot and the 1 K sample plate, with the grey He pot in contact with the same plate as optical, RF and DC lines breakouts. d) is a close up of the "cage" design used to optical couple a fibre to an optics device. Images in a) and b) are provided with permission of R. M. Heath.

chapter.

For SNSPD signal readouts, we use a Minicircuits ZX85-12G-S+ bias tee, with a frequency range of 200 kHz to 12 GHz. The bias tee allows DC flow from the SMU to the SNSPD and RF signals to flow from the SNSPD to the amplifiers, as shown in Figure. 4.11. The amplifiers used to amplify the RF signal are adjusted depending on the measurement. LNA 580T/1000 Si amplifiers are used housed outside the cryostat ontop of the system connected to the SNSPDs through the RF channels. They have a bandwidth up to 580 MHz & 1000 MHz respectively and 23dB & 33dB gain.

4.2.2 R vs. T measurements

We start by measuring the room temperature resistance measurements by scaling to an area calculated by squaring the width of the device known as "square resistance" This is to allow the device to be comparable to other devices. No broken or shorting connections have formed during fabrication or use. Devices with too high a square resistances, suggest an incomplete circuit, or too low a square resistance, suggest shorting.

The critical current is the current at which the superconductivity breaks and the restive

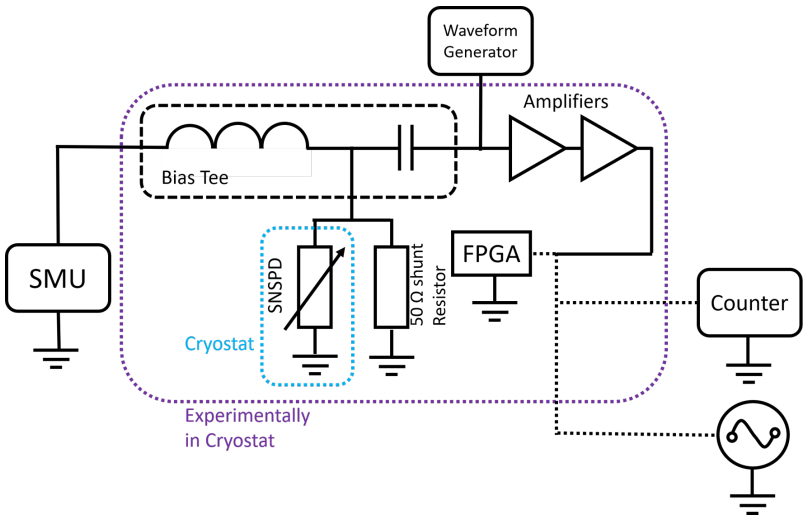

FIGURE 4.11. Electrical circuit diagram for the SNSPD characterisation and operation. The SMU stands for a Source Measurement Unit providing voltage, current and resistance measurements of the SNSPD. Blue box: components that have to be in the cryostat for function, while the purple are components tested within the cryostat. The black dotted lines represent where only one item is connected at a time for different experiments.

state of the SNSPD is reached. SNSPDs' critical temperatures (T_c) and critical current (I_c) are different from the sheet resistance for NbN caused by the 2D geometry of the wire [176, 177]. Therefore, the critical current of the SNSPD and the potential efficiency of the SNSPD will change with temperature and distance from the T_c. Also, heating effects from the amplifiers and TDC cause the system to run at non-base temperature, therefore investigating and understanding the T_c point of the SNSPD is essential for operational performance. The device is cooled from 300 K to 1.3 K, as shown in Figure. 4.12. The SMU provides a small amount of current that is far below the critical current at base temperatures, while varying and measuring the voltage-driven to the device. The SNSPD can be driven in two modes, voltage-driven or current-driven. For voltage-driven, the voltage is kept constant, and the current changes to keep the voltage constant, and vice versa for the other mode; allowing for the exploration of different characteristics.

An I-V curve (short for 'current-voltage characteristic curve') is a graphical representation of the relationship between the voltage applied across an electrical device and the current flowing. At the same time, voltage-driven can find IV curves and resistances in the superconducting and resistive state. The resistance increases with colder temperatures as expected. The zoomed inset does show a transition period that can be confirmed with I-V curves. We measure the resistance both directly and through an IV curve.

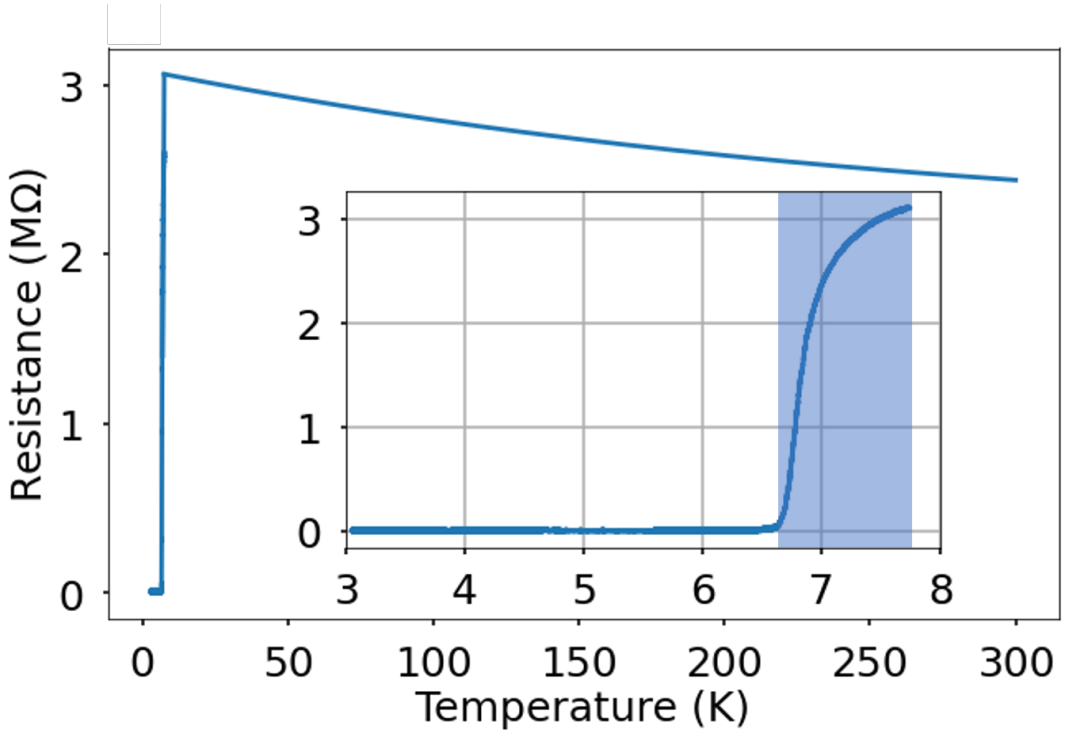

FIGURE 4.12. Resistance measurements of the NbN SNSPD from room temperature down to base temperature. The inset shows zoomed in results close to base temperature, where the resistance of the SNSPD rapidly drops showing that the superconducting transition region (shaded on the graph) is reached between 6.5 K and 8 K.

4.2.3 I-V measurements

A key property of any superconductor is critical current I_C, which is the current that the device can support before transits from the superconducting regime to the resistive—measured using the components shown in Figure.4.11, specifically the SMU and resistors. Ultimately the system is connected to a computer system for automated measurements and alternating-charging batteries used as a voltage source to ensure noise-free [178] and steady output. To operate the SNSPD as a single photon detector [179], it is set up to be in parallel with a 50 Ω “shunt" resistor as shown in Figure.4.11. When the device triggers, the resistance of the SNSPD becomes much higher than 50 Ω. Therefore, most of the current is redirected through the shunt, allowing the heat in the device to dissipate as the device is no longer heated by current flow. An IV curve is related only to the thermal balance of the Joule heating due to the current flowing in the superconducting nanowire and the hotspot inside the nanowire and the phonon-cooling through the substrate and the electron diffusion culling through the electric contacts[180].

SNSPDs are typically operated with a shunt resistor in parallel to the device, as shown in Figure 4.11, and as mentioned in the previous paragraph. Typically, a resistor of 50 Ω is used

as it is sufficient to allow the resistive device regime to "shunt" the current to the resistor path to reduce the self-heating detector's self-heating effect. This prevents the latching of the device, allowing the device to superconduct once again.

The 50 Ω parallel resistor, that are typically reported in the read-out schemes, represents the input resistance of the RF readout electronics. In RF applications both passive (coax cable, filter and attenuators) and active components (i.e. amplifiers) are matched to the nominal value of 50 Ω in order to reduce reflections and losses in the signal transmissions.

The shunt resistor has a resistance higher than the SNSPD during the superconductive state, but a lower resistance than SNSPD in the resistive state. As the majority of the current flows through the path of least resistance, the magnitude of the current flowing through the SNSPD is reduced, to allow the SNSPD to return to the superconducting state. We choose 50 Ω as it is several order of magnitudes in resistance above the superconductive state and several orders below the resistive state, to allows for the current to switch almost entirely between paths.

In turn, the device returns to the superconducting regime. I-V measurements are taken by sweeping the current from zero past the I_C down to -I_C and back up to zero repeatedly. While measuring the current and voltage drawn by the device at below 6.5 K, a transition from the superconducting to resistive state occurs at the critical current value of 6 μA. By measuring the gradient of the I-V curve in Figure. 4.13 for the superconducting regime and the resistive regime we found resistances of 290 Ω and 2.9 MΩ respectively. By taking the gradient of the fitted green lines ($R = V/I$), we can determine the resistance. This is quite a high resistance compared to other SNSPDs [85, 99], indicating that the device has a poor superconducting film. The data within the superconducting region indicates the current of the plateau where the stable hotspot grows with the voltage. The slope in Figure. 4.13 b) is from the internal wiring of the system. [181] describes that the slope of an I-V curve is determined by the resistance in the high voltage regions. While in the low voltage regions the frequency oscillations of hotspot generations determines the gradient. The resistance of the wiring within the cryostat is around 15 Ω, therefore not the main contribution. The cryostat resistance is measured using an SMU unit.

Using the 290 Ω resistance calculated from Figure. 4.13 for the SNSPD in parallel with the 50 Ω resistor, we can use the potential divider equations of (R_{SNSPD} + R_{shunt}) / R_{shunt} to show an increase in the critical current limit of 6.8 times to 41 μA. The I-V measurements have increased noise but show a transition edge at 40 μA.

The I_C changes with temperature. Therefore sweeping the current while measuring the voltage at a different temperature provides a critical current measurement map. In Figure. 4.14, we map the voltage difference in colour over a range of temperatures and currents that go past the critical current. The spikes in the data at the top and bottom of the current range appear to hysteresis effects caused by the device self-heating as there is no shunt resistor during this measurement. The T_C of the devices appear to be around 8K. The values shown agree with the I-V curve critical current and the T-vs-R graph T_C value.

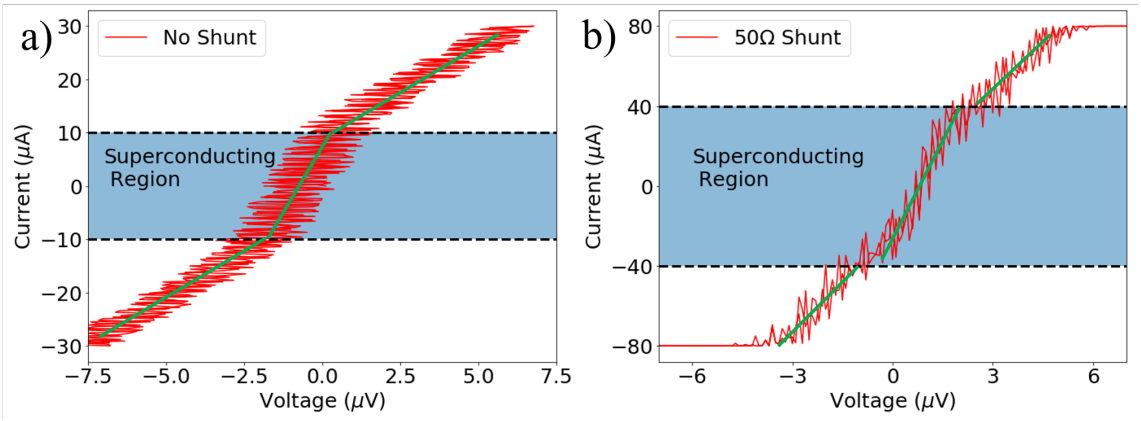

FIGURE 4.13. I-V measurements' characteristics at 1.3 K with a) no shunt resistor and b) a 50 Ω shunt resistor connected in parallel.

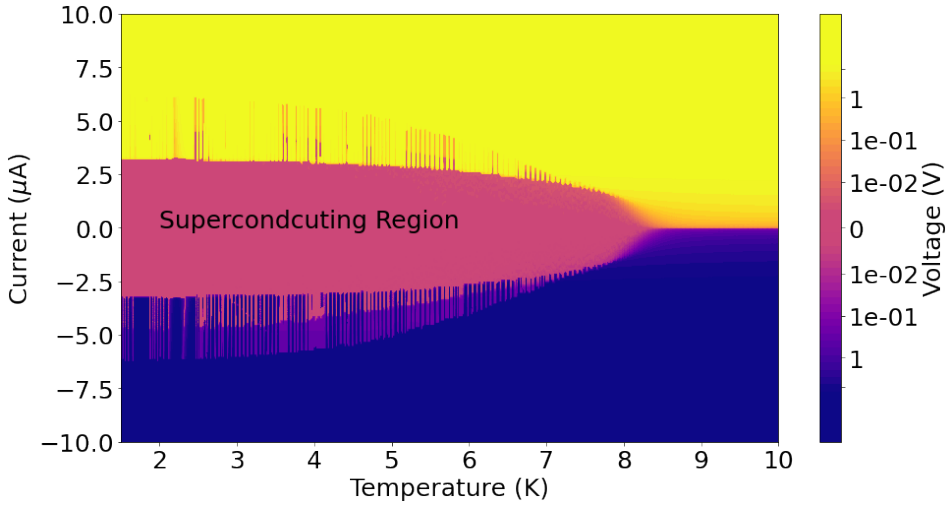

FIGURE 4.14. I-V-T heat map of the SNSPD operations, created by scanning the current and measuring the voltage while varying the temperature of the SNSPD. The superconducting region illustrated by the turquoise region, where the voltage is close to zero, between the positive and negative I_C values and below the T_C value. This is without a 50Ω shunt resistor in parallel. Measurements collected and figure designed with R. Heath.

4.2.4 Dark Count Rate

The dark count rate is the number of counts that the SNSPD produces in the absence of photons. Dark count event can happen due to fluctuations in the 2D superconductor, like vortex antivortex pair unbinding, vortex entering, etc. The dark count rate level changes with the bias current applied to the SNSPD. The photon energy also determines the efficiency of the SNSPD. Larger photon energies create large hot-spots and have an increased probability of breaking the super-

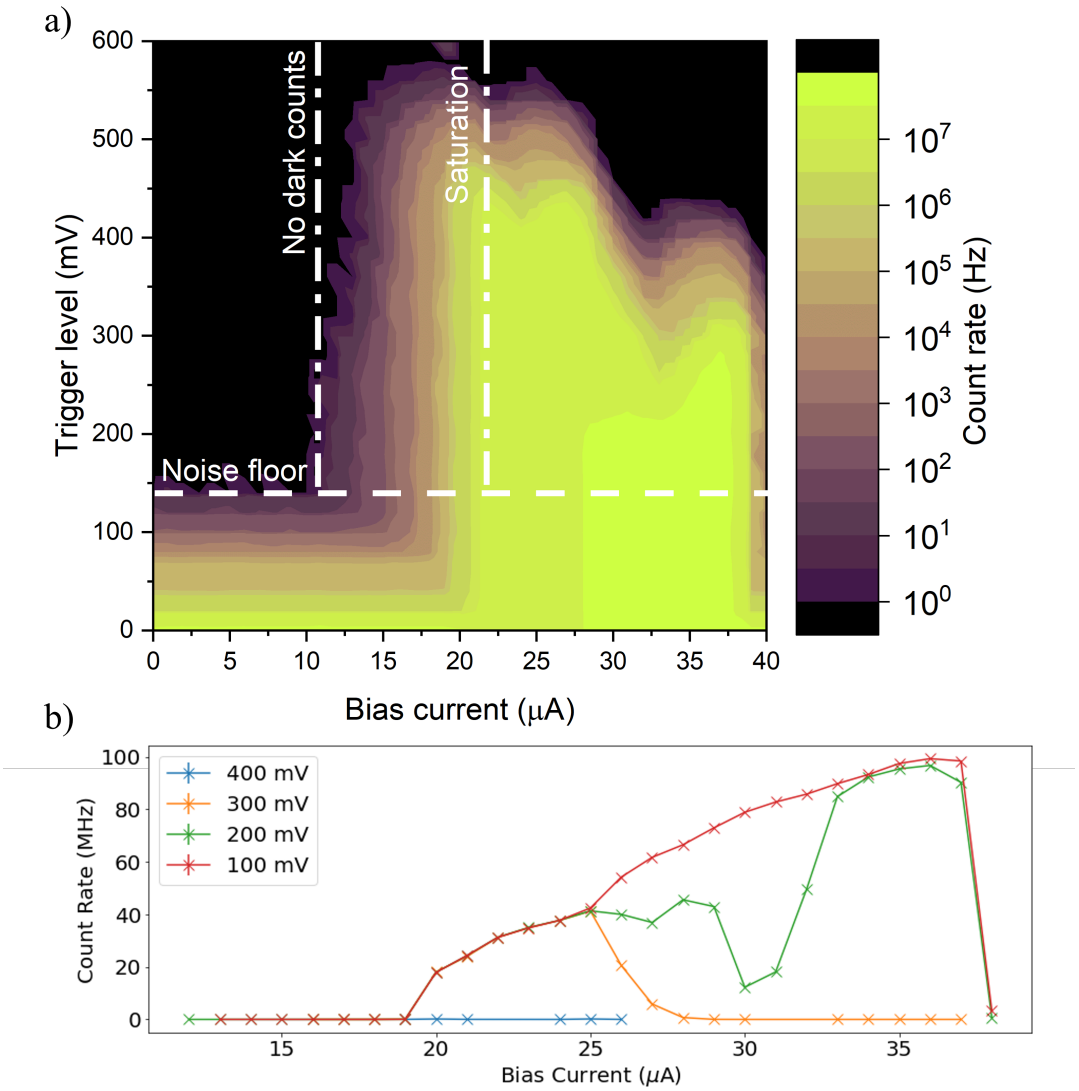

FIGURE 4.15. a) Dark count rate heat map measured on an SNSPD under normal operation ($T = 1.4K$) with changing bias current for different trigger threshold values on the frequency counter. b) Dark count rate dependent on the current at different trigger levels taken from a).

conductivity than a lower energy photon, assuming the same location of incidence. Characterising the dark count rate can allow for the tuning of the count rate to characterise a time tagger's capture efficiency.

The SNSPD is connected to an Agilent 53230A universal frequency counter that integrates for one-second intervals on the falling edge, varying the bias current input and the voltage trigger level to form a count map of the different detection regimes where dark counts occur. The SNSPD pulse signal is amplified with an LNA 580 and LNA 1000 in tandem. Figure.4.15 is the map

of counts from the SNSPD with a maximum count rate of 60 MHz. The circuit used for the measurement is shown in Figure.4.11 with the counter attachment and the "shunt" resistor connected.

The noise floor is when the trigger level is low enough to not distinguish between SNSPD pulse and background noise. Below 10 μA the input current is too low to provide counts and past 21 μA saturation is reached as the pulse height begins to drop as the detector triggers, before completely resetting. After 40 μA, counts drop to zero as the I_C is supplied to the SNSPD.

The amplitude of the SNSPD pulse is measured to be 500±50 mV. If the threshold voltage is set above this value, the number of counts measured rapidly drops off with voltage. Therefore, during operation a value 3 standard deviations below the average is usually chosen. The optimal bias current to drive the device is around 21 μA. The largest count rate for the highest voltage trigger occurs at this point. After this, the voltage trigger drops off. Due to the SNSPD pulses, this may be merged into one, and the SNSPD does not have enough time to relax and reach the noise floor between pulses. At 40 μA there is a sudden drop off in counts as the critical current is reached, therefore no more SNSPD pulses are produced from the device.

4.2.5 Pulse shape

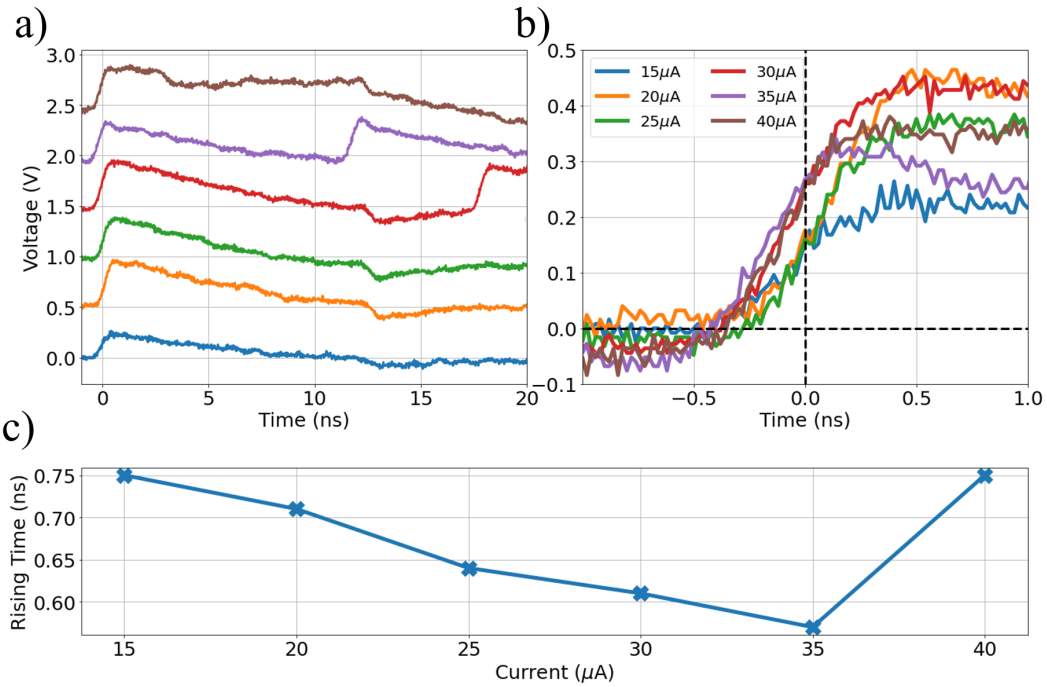

FIGURE 4.16. The pulse shapes of dark counts with no injected laser light during shunted operation measured with a Tekronix DPO73304SZX (33GHz, 100GS/sec) oscilloscope, with a) showing the full pulse shape and b) showing the measured negative rising edge. c) is the rise time of the pulse

Using the same experimental set-up as used to perform the DCR measurement, except replacing the frequency counter for a Tektronix DPO73304SZX (33GHz, 100GS/sec) oscilloscope, the pulse shapes of dark counts were captured for a range of frequencies as shown in Figure.4.16. Pulses were recorded between 15 μA and 40 μA, providing rising times from 0.6 ns to 1.0 ns and a reset times between 10 ns to 20 ns and 400 mV pulse height after 56dB amplification. At higher currents past 25 μA pulse becomes distorted until 40 μA, where pulses no longer occur.

Using the DCR results as a base, we swept the bias current from 15 μA to 40 μA while measuring the oscilloscope's voltage response. We found a negative SNSPD pulse shape with a sharp rising edge and trailing decay. Higher bias currents shortens the time between pulses, until 40 μA where the pulse begins to deform as the pulses merge into each other and cannot relax before the next pulse is initiated and therefore cannot reach the voltage trigger. The rising edge is sharper for larger bias currents as shown in Figure.4.16 c), with the decrease in rise time until the detectors is close to its critical current and the trend breaks down. The reset time is measured by the time is takes for the voltage to decrease from the peak back down to the noise floor. The detector average reset time is 15 ns; this translates to a maximum count frequency of 66 MHz, which is supported by the maximum dark counts measured.

4.2.6 Detection efficiency

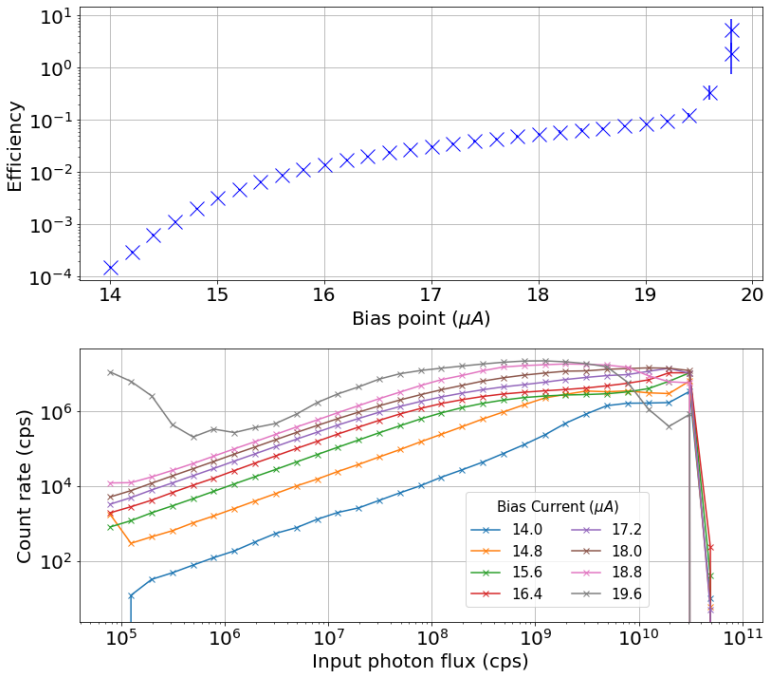

FIGURE 4.17. a) Average efficiency b) Photo-detection efficiency

A 1.25 mm fibre ferrule with 13010 BHP optical fibre is spliced into a connector and passes

through the top sample plate. The position of the fibre outputs is offset to allow the sample itself to attenuate the number of photons. The photodetection efficiency shown in Figure. 4.17 a) suggests that the detector operates at between 1% and 10% efficiency over much of the dynamic range. Figure. 4.17 b) is the number of photodetection per input flux, accounting for the coupling efficiency. Note how the higher currents towards 19 μA begin to form irregular shapes; therefore, the efficiencies above 19 μA cannot be trusted. The DCR in this region for the previous figure suggest only 100 cps. The detector can now be used to measure the readout system's capture rate later presented in the chapter by comparing input flux and expected counts to the total count recorded by the cryogenic time tagger.

4.3 Conclusion

The device becomes superconducting below 6.5 K, while operated with a 50 Ω "shunt" resistor with a critical current of 40 μA. However, it is optimally operated at 21 μA. The device has a dead time of up to 20 ns at this current, and can operate at a maximum of 66 MHZ. The SNSPD pulse can be amplified and adjusted in potential, dead time, shape and frequency, by varying the temperature and current and tailoring the number of counts needed to test a time tagger's properties.

4.4 Acknowledgements

The author's contributions consisted of mounting and characterising the device and the experimental set-up, designing and performing the experiments, and analysing the data. Dr Rob Heath contributed to the experiment realisation, theoretical support and precursor results. R.Heath also supported providing a lot of the coding infrastructure to collect the results and measuring the detection efficiency. He also advised and help provide some of the figures, where noted. Dr Antonio Andreas Gentile provide assistance in the vibration measurements, by programming and operating the Audrino. The technical specifications of the DRYICE1K is supplied by ICE Oxford Company.

CHAPTER 5

QUANTUM OPTICS DETECTION SYSTEM PART II: READOUT

In the previous chapter, we presented key engineering achievements to produce an SNSPD hub to contain many (> 10) detectors. The concept of providing quantum communication networks by concentrating resource-demanding technologies into one area would accelerate quantum communications accessibility to end-users [2]. This would provide a node in the network where end-users can connect to and produce their keys with other end-users. A protocol used for this type of structure is MDI-QKD [47, 182], which is explained in Chapter 2. SNSPDs are already commonly used in QKD because of their detection efficiency [1]. SNSPDs are expensive to build and maintain [92, 183], due to their sensitive fabrication procedure, affecting their yield [184], as well as the cryogenic temperatures required for operation. Combining many SNSPDs into one location minimises the number of cryostats, reducing the resources needed for a communication network.

One of the problems with hosting a large number of SNSPDs (hundreds) is that currently, each requires a Radio Frequency (RF) electrical connection to the outside environment [92]. This connection to the environment provides a thermal link requiring a greater cooling power with a cryostat to maintain base temperature for SNSPD operation ($< 10K$). Limiting the number of connections is a solution that we present here. For quantum photonic applications, coincidences between photons are a key concept [16, 140], to realising many quantum applications. Time taggers mark the photons' arrival time and can check if simultaneous detection events occur between channels [185]. Time taggers can read-in from over 20 RF connections currently. Hence placing the time taggers into the same cryostat as the SNSPDs would limit the electrical connections required to the environment outside the cryostat.

SNSPD's pulses attenuate over the length of an electrical connection, and the connections needed in the larger cryostats between the environment and device are made longer from the size.

Minimising the distance with time taggers next to the qubit readout provides another advantage alongside minimising the number of connections. Moreover, to avoid time and energy consumption over cool cycles, the micro-architectures should support reconfigurable program-ability. Thus FPGAs or Complex Programmable Logic Devices (CPLDs) are an obvious choice. FPGAs are already currently used as time taggers.

The experiments presented in this chapter present a solution to the time tagging of SNSPD signals needed for a fully integrated quantum optics system. The experiments' focus is to show that SNSPD signals can be marked by the time tagger in the same cryogenic system as the SNSPDs. SNSPDs are widely used in integrated quantum photonics, which gives capabilities for quantum computing, communications and simulations.

In quantum photonics, to store quantum information, we need to store the light itself without measuring it [186]. The same properties that make light the ideal medium for transporting quantum information make it difficult to store it. Quantum memory is for the storage and retrieval of quantum information, analogous to a normal computer's memory. Optical quantum memory is the interface between light and matter that allows. Nevertheless, the power of quantum computation relies on maintaining a superposition of quantum states. Immediately after the state is measured, the superposition is destroyed. Hence, it is crucial that a successful quantum memory faithfully reproduces the state so that a measurement can never be made of the system while it is stored. Hence the aim is to measure the quantum states at rates that match their generation not to lose any information. Hosting the number of SNSPDs required for a quantum computer to achieve quantum supremacy [14] and storing their resultant states is the challenge.

The aim of the experiments presents in this chapter is to explore GaAs based off-the-shelf amplifiers that can be used to increase SNSPD signal for the time tagger to trigger and to show a readout. The readout a system uses a commercially available FPGA and amplifiers at cryogenic temperatures of 4.2 K are maintained. These components (FPGAs and amplifiers) are not designed for cryogenic temperatures and are pushed far beyond their specified operating temperatures. We then explore the performance difference of two FPGAs and how, when placed at cryogenic temperatures, their performance characteristics improve or degrade. Lastly, the chapter presents different calibration and linearisation methods that can be used to improve the accuracy and precision of the FPGA as a time tagger.

5.1 Background

Electrical readout systems for low temperature environments have many areas of application, such as in single-photon detection [187], astronomy [188], particle physics [189], quantum computations [190], quantum communication [1], and in [191, 192]. In most of the configurations mentioned (single-photon detectors, quantum computers and quantum communications), the electronics are at room temperature, separate from the cryogenics system. This is usually to

provide access to the electronics, as the electronics would not function at the temperatures within a cryogenic system. The heat expelled from the electronics would decrease the system's performance. Highly complicated systems that require a large number of wiring connections, a large amount of bandwidth, low latency measurements or high power, with separation between the room temperature electronics and the cryogenically cooled devices, provide a challenge that affects performance.

The alternative to this is having the readout electronics wired through to the cryogenic system via connections. Again, to minimise the heat transfer from the outside environment, these cables should have as little heat conduction as possible. The Wiedemann-Franz law dictates that these wires must inherently have a high electrical loss when heat conduction is low, decreasing the potential bandwidth and power transmitted, determined by electrical conductivity σ_c. The Wiedemann-Franz law is described by the following:

$$\frac{\kappa}{\sigma_c} = LT, \tag{5.1}$$

where κ is the thermal conductivity, T the temperature and L Lorenz number. L has a constant value of $2.44 \times 10^{-8} W\Omega K^{-2}$, making κ and σ_c directly proportional to one another for a constant temperature.

Integrating the electronics system within a vacuum dry cryogenics system addresses some of these problems. Research has already addressed this issue by using amplification and multiplexing circuits to boost the signal strength over long high loss wires [101]. Minimising total wiring and connectors by using cryogenically compatible circuits, such as superconducting wiring and logic circuits, can greatly reduce heat through the connections between the outside environment and the cryostat [193].

Readout electronics for quantum computational devices at cryogenic temperatures is heavily researched [194, 195] by all quantum computing streams (Optical [196], spin [197] and superconducting [190]). All these technologies depend on cryogenic temperatures [190, 196, 197] for qubit coherence time and fidelity. Maximising the number of qubits on one device to allow for interactions between qubits is essential to realising a fully integrated quantum computer.

Ideally, TDCs are implemented on an Application Specific Integrated Circuit (ASIC) to tailor their performance to the exact requirements, giving the highest sampling rate for the lowest power consumption. Using an FPGA as a TDC can prove challenging due to the FPGA being fully digital circuitry. As a TDC is a specialised use case for an ADC, the FPGA needs to interrupt analogue signals to assign a timestamp to their arrival. Our colleague at Bristol, Andrew Hart, designed an architecture that fully implements the FPGA to interface with analogue signals to make an ADC. Other TDCs have been implemented on FPGAs [198] for cryogenic temperatures [194], but none for SNSPD readout.

In December of 2019, Intel introduced "Horse Ridge" [199]: a highly integrated, mixed-signal cryogenic system-on-chip (SOC) on a 4 x 4 mm^2 silicon CMOS technology. This in-house fabricated

spin qubit control chip allows them to design, test and optimise their quantum computers. It integrates SRAM and digital core RF circuity into one system. They have four RF channels per device and use signal multiplexing to control up to 128 qubits. They can also host 32 digital signals with a high precision of 200 Hz and 96 RF connections, controlling silicon spin qubits. This commercial system provides a great step in scale-ability but is a similar system for optics has not yer been realised.

Eduardo Charbon with Bishnu Patra published work in 2018 on cryo-CMOS circuits for quantum computing systems [200], demonstrating 4 K Low Noise Amplifier (LNA) reading 150, 1-MHz channels, with a power consumption of 108 mW. They exploit standard circuit techniques adopted for cryo-CMOS to increase speed and lower thermal noise while meeting a dilution fridge's tight power consumption budget. Cryo-CMOS has also been demonstrated with other LNA and in space missions [201, 202].

Clinton Cahall in 2018 presents a low-cost cryogenic readout circuit for amorphous SNSPDs, demonstrating the capabilities potential of off-the-shelf GaAs amplifiers [203]. This demonstrates 35 ps timing resolution and 2 $\times 10^7$ counts per second, with 3 mW power consumption. This was not achieved by integrating the time tagger within the system but only by amplifying the signal.

I.D Conway Lamb in 2015 demonstrates a cryogenic instrumentation platform involving an available commercial Artix-7, Spartan-6, and Spartan-3 FPGAs designed for quantum computing devices [204], presenting the FPGA as capable of signal routing, multiplexing and digital signal processing all at around 4 K. This was achieved with custom design RF cable PCB and FPGA housing. Boasting comparable power consumptions and boosted performance speeds.

Harald Homulle in 2017 demonstrated another cryogenic FPGA TDC readout for qubits, operating at 4K [195]. With logic, speeds have a less than 5 % change between 4 K and RT and all other components are stable over their complete range. This showed that TDC are feasible with good design practices and calibrations techniques, but not in conjunction with an off-the-shelf amplifier for quantum photonics applications such as SNSPDs.

Ekin Arabul *et al.* in 2020 published a high precision FPGA-based multi-channel coincidence counting system for quantum photonics at room temperature [198], using a Spartan-6 Xilinx FPGA, counted 320 MCPS over eight channels with 8.9 ps RMS resolution. This demonstrated a reverse-HOM dip effect using the TDC while measuring the photon coincidences events on the FPGA.

In the literature, [198, 205] they implement coincidence counters. A coincidence counter based on a TDC is implemented on an Altera Cyclone III FPGA for Time of Flight (ToF) Positron Emission Tomography (PET) cameras with a resolution of 69.8 ps, and 72 MCPS [116]. This implementation used a separate 12 channel TDC board to achieve the coincidence counting, which hindered the operation's count-rate.

Integrating large amounts of readout electronics in a high-vacuum cryostat adds its own challenges. Cryogenic amplifiers are commonly used to boost weak electrical signals over long

transmission cables that undergo a large change in temperature gradient. Operating logic, memory systems, digital-to-analogue converters, and analogue-to-digital converters allows for digital signal processing within the cryostat. This also opens the door for using superconducting cables and inter-connectors to reduce the cables' thermal conductivity. Amplification would allow superconducting circuits to multiplex many data lines onto one, thereby reducing thermal transfer to outside.

Rapid Single Flux Quantum (r-SFQ) circuits use superconducting material to form a circuit with high-speed readout logic fabricated on-chip for cryogenic temperatures that can transfer signals through a cryostat. This alternative has been used as a logic circuit instead of a time tagger to measure counts. However, r-SFQ circuits are currently limited on bandwidth from the critical current limit of superconducting circuits. [193] used r-SFQ electronics as a readout system to calculate an average count rate of a set of SNSPDs through multiplexing.

The majority of the TDC architectures in the current literature use technologies such as FPGAs, ASICs and analogue circuits. These are preferable over integrated circuits such as CPU, GPU and digital signal processors (DSP) because the systems clock does not limit them. FPGAs are also more flexible and less expensive than ASICs, so after reviewing the literature for this experiment we decide to use an FPGA. This comes at the cost of high dead times; however, the fast asynchronous and concurrent logic designs possible in an analogue circuit, FPGA, and ASIC implementations outweigh these systems' drawbacks which have proven [206] measure timings comparable to the clock speed. The reconfigurable nature of FPGAs and their much-reduced cost meant allow for rapid, incremental design schedule for implementations. FPGAs were chosen as our platform of choice.

FPGAs have already been shown to work at cryogenic temperatures and have been proposed as an error-correcting control loop. In [197, 204], Spartan 3, Spartan 6 and Artix 7 FPGAs by Xilinx were shown to operate at 4 K. However, as only a few devices have been tested, device performance variations from fabrication differences could not be determined. In this thesis, Artix 7 is chosen over others because of its low-power design and proven cryogenic compatibility.

FPGAs can discriminate signals in the range of (0 - 10) Volts. Typically SNSPD outputs are 10^6 smaller than the input threshold of an FPGA, and therefore need to be amplified. Recent demonstrations have been made with low-noise [207], low power cryogenic amplifiers [188, 208, 209] built from custom made components and commercial transistors. Amplifiers close to the SNSPDs provide two critical advantages. Firstly the thermal noise [207] of the amplifier can be reduced dramatically with very low operating temperatures close to SNSPD cryogenic stage, improving the signal-to-noise ratio (SNR) for a given amplification power. Potentially lowering the required number of amplification stages. Secondly, a reduced cable length between the detector and the amplifier minimises the signal's attenuation prior to amplification, further increasing the signal to noise ratio for a given amplification power. These mechanisms increase the ability to discriminate between an SNSPD detection and background noise which minimises

jitter while maintaining the count-rates [2]. The count rates significantly impact the speed and fidelity of the quantum communication protocols.

5.2 SNSPD pulse simulation

An SNSPD pulse is an electrical signal that results from the breaking and reforming of superconductivity within the nanowire. As a photon incident occurs on the nanowire and the energy is absorbed within, the heat causes the superconductivity to break. The circuit diagram for the SNSPD testing is shown in Figure.4.11. This causes a voltage pulse across the SNSPD only if there is an on-going current below I_c level, and a relatively high resistance R_{nw} within the nanowire. The current flowing through the nanowire is then shunted onto a “shunt" resistor R_{shunt} in parallel. The shunt resistor is typically much lower than the SNSPD in the resistive state, around 50Ω. Therefore negligible current flows to the SNSPD, allowing for the SNSPD to return to the superconducting state.

The mechanism described above can be described using the following equations and Figure.5.1:

$$\begin{aligned} V_R &= V_0 e^{\frac{t}{\tau_{rise}}}, \\ V_{SC} &= V_0 e^{-\frac{t}{\tau_{fall}}}, \\ \tau_{rise} &= \frac{L_k}{R_{shunt}+R_{nw}}, \\ \tau_{fall} &= \frac{L_k}{R_{shunt}}, \end{aligned} \tag{5.2}$$

τ_{rise} and τ_{fall} are the time constant that is characteristic with a capacitor. τ_{rise}, as seen from the equation, is when the SNSPD is in the resistive state, therefore the voltage across the SNSPD raises exponentially depending on the inductance, given by the equation V_R. t is the time since the detection event. L_k is the inductance of the SNSPD and it is an intrinsic property of an electrical circuit to tailor the SNSPD pulse response and to allow for relaxation. This is usually in the form of a longer meandering wire [187, 210, 211], after the SNSPD region. V_{SC} describes the exponential decay of the voltage pulse, after the SNSPD has returned to the superconducting state. Therefore choosing a shunt resistor here will help define the decay rate.

The dead time of an SNSPD, and therefore the frequency, can be tuned with the speed of the decay. A faster decay, for the voltage to be on the scale of the noise floor, will allow for another time defined detection event. Hence, selecting a high resistance shunt, below the resistance of the nanowire in the resistive state, will provide this increased decay with the added bonus of increasing the critical current of the SNSPD system.

The values used in the simulations are measured from the SNSPD described in the results chapters of this thesis. We are able to measure the resistance of the SNSPD and we can choose our shunt resistor. Knowing these and using an oscilloscope (which measures the timing decay of the SNSPD pulse, therefore measuring the inductance of the SNSPD) we can create an accurate model for the SNSPD pulse simulation.

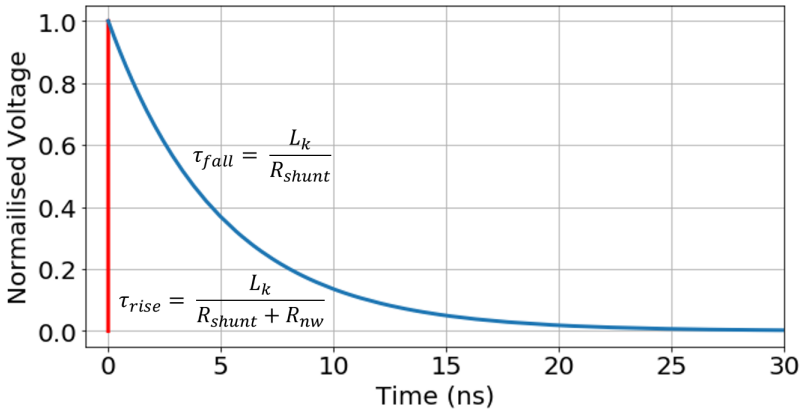

FIGURE 5.1. Modelled SNSPD pulse. The red line showing the rise and the blue line showing the decay.

This simulation pulse was heavily used in the experiments described in Chapter. 5.

5.3 Amplifiers characterisation for SNSPD pulses at cryogenic temperatures

5.3.1 Background

Several works have addressed the operational capabilities of commercially available operational amplifiers at cryogenic temperatures at 77 K, and 4 K. In [212, 213] operation of all devices continued down to 77 K with a reported increase in performance and power consumption. In 2008 the first 4.2 K operation of amplifiers was attempted [214] using an Analogue Devices AD8605 and an AD8651. [215] reported that silicon devices would not work at 4.2 K, but with self-heating and higher voltage drivers, they can overcome this.

SNSPD eight-fold amplification has been achieved with superconducting nanowire avalanche single-photon detectors [216]. However, this does not lead to scaling with many detectors for multiple qubits and still requires further amplification. RSFQ applications have been used to provide readout circuitry for a four-pixel detector array system. However, this still requires external amplification [217].

The amplifiers for SNSPD amplification are typically hosted outside of the cryostat as the heat generated from the amplifiers can limit the temperature achievable of the detector system. Currently the number of SNSPDs in a detection system has been small enough for this not to be an issue.

SNSPD signals are on the scale of μV. The signal must be amplified to the input voltage threshold of the TDC. The SNSPD signal must be amplified to this voltage to trigger the counter on a TDC. Typically cryostats cooling power for SNSPD operation temperatures are below 8 K. If

the amplifiers are placed near the SNSPDs, the amplifier's heat quenches the SNSPD by raising the temperature to over the T_c.

5.3.2 Experimental Setup

The amplifiers, when in use, are placed on a warmer stage than the base stage of a cryostat. The temperature is chosen for operational practicalities as the temperature and cooling power are sufficient. The temperature at this stage reaches 4 K with 3 W of cooling power. Each amplifier experimented on has power well below 1 W, allowing the system to maintain 4 K.

The DRYICE1K electrical Input/Outputs (I/O) consists of 16 RF lines from the environment, breaking out on the He pot stage. We measure the performance of the amplifiers, by the attenuation across frequency ranges. I/O lines are calibrated, allowing us to isolate the amplifier's performance from the resultant signals. This is measured by using a short loop connection between two RF lines. The attenuation is half this for a path. The lines are used in the following experiments to inject and readout SNSPD pulse, clock pulse, and the UART time tags from the readout electronics.

The RF lines have a less than 0.1 dB change in transmission between RT to 1 K. The measured attenuation of the RF I/O lines is between 0.2 MHz to 6 GHz and is roughly 0.1 dB/GHz. This is measured using a field fox spectrum analyser, injecting electrical signals over the frequency range and measuring the difference in return voltage returned at each frequency. The range 0.2 MHz to 6 GHz is chosen as the frequency range of the measurement device. The majority of dominating frequencies in an SNSPD pulse fall within this range. The SNSPD pulse signal passes through the lines without loss of readout shape. The attenuation is deemed to be acceptable and negligible—the setup used for the test of the amplifiers is shown in Figure. 5.2. The faded RF lines represent the changing of device-dependent on measurement. For the measurements of the amplifiers' gain, the RF lines are measured at each temperature and calibrated to remove the effect of the cable on amplifier performance.

The Small Measurement Unit (SMU) uses four-wire measurements to maintain power at a constant voltage for pulse amplification. The oscilloscope, spectrum analyser and Arbitrary Waveform Generator (AWG) are used to measure the bandwidth's gain. We measure the SNSPD pulse gain over a temperature range of 1 K up until 300 K.

The properties of the three amplifiers can be viewed in Table.5.1. They are set up to be in thermal contact with the 1 K sample stage of the DRYICE1K system. We use thermal Apizon grease and clamps. This provides maximum surface area in contact with the sample stages. The amplifiers' packaging design allowed them to be electrically grounded through the contact between the cryostat stage and the amplifier electrically conductive casing. The cryostat provides an electrically conductive path between the amplifier and the earth. Electrical grounding is a back-up pathway that provides an alternating route for the current to flow back to the ground if there is a fault in the wiring.

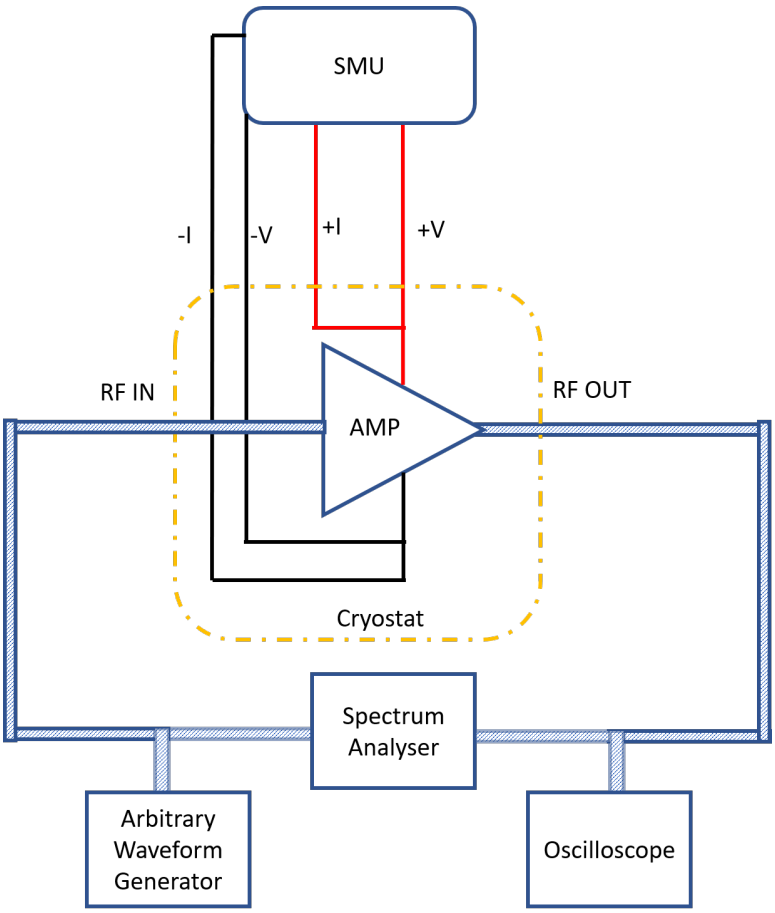

Figure 5.2: Amplifier test circuit. With the faded RF lines representing the changing of device dependent on measurement

Four-wire measurements are used to power the amplifiers using a SMU to provide constant voltage. The varying current allows the operation to be maintained at different temperature ranges. Also called Four-terminal sensing or the Kelvin method, this measurement method avoids errors caused by wire resistance. In low voltage and high current applications, we commonly find measuring instruments capable of four-wire sensing to minimise the effects of resistance between connections to avoid inducing a significant voltage drop on those paths. We use this technique to isolate the electrical power draw of the amplifiers and avoid measuring the resistance of the cryostat's internal wiring.

The connections break out (split out from the connector into separate I/O lines) from a 24 pin micro-D connector that breaks out through the top of the DRYICE1K. A calibrated RTD Cernox temperature sensor is in thermal contact with the base plate to monitor temperature.

The SNSPD pulse for these results is produced using a Tektronix AWG70000B Arbitrary Waveform Generator to allow for a full temperature range of amplifier characterisation with an SNSPD pulse. The SNSPD and amplifiers cannot share the sample stage as the temperature

Name	Gain (dB)	BW (GHz)	Material	V (V)	P (W)	Input	Op. Temp. (°C)
GVA-123+	16.9	0.05-12	GaAs	12	0.34	28dBm	-40 to 85
ZX60-6013E+	13.0	0.02-6	GaAs	12.5	0.65	15dBm	-45 to 85
ADL5611	22.2	0.03-6	GaAs	6.5	0.8	20dBm	-45 to 105
LNA-580T	23	0.01-0.58	Si	12	0.84	15dBm	-45 to 85
LNA-1000	33	0.01-1	Si	12	0.42	13dBm	-45 to 85

Table 5.1: Manufacture specifications of the amplifiers used in the signal gain from SNSPD pulses. With BW: Bandwidth, V: Voltage, P: Power and Op. Temp.: Operating temperature. [218–222]

rise from the heat of the amplifiers would increase over the T_c on the SNSPDs [223], resulting in inconsistent SNSPD pulse size and trigger rates, not giving a consistent pulse to compare against different temperatures. As the simulated pulse does not change decay time or rising edge gradient, the only contribution to any changes is in the amplifiers' performance.

The waveform generated pulse is made up of many frequencies to form the end pulse shape. This pulse can be tailored to match the amplitude, frequency, length and geometries of a voltage pulse generated from an SNSPD. The signals can be considered indistinguishable after noise and amplification.

5.3.3 Results

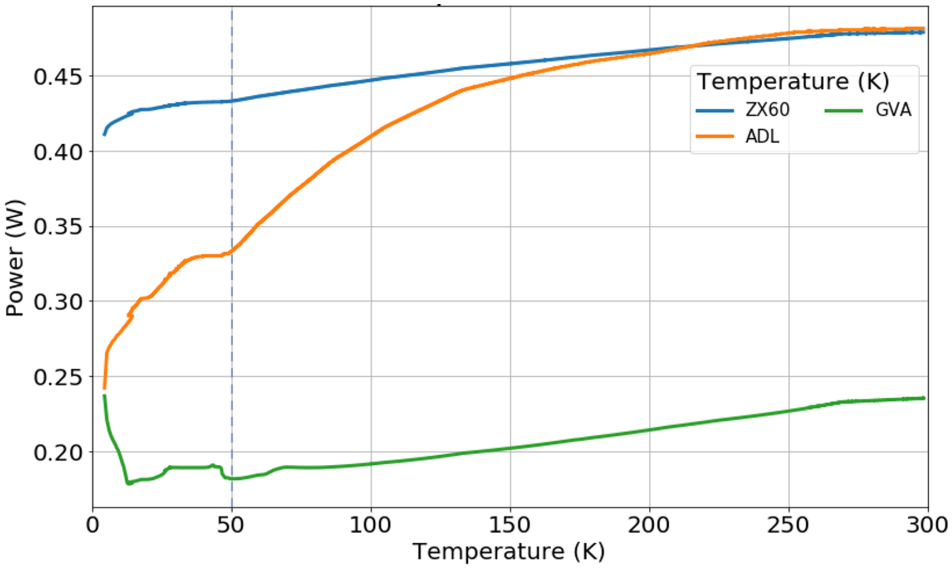

Figure 5.3: The power draw of the GaAs amplifiers showing linear change in power with temperature, until a cooling limit is reached. All of the amplifiers reach a temperature where this break down point occurs where the model begins to reach freeze out at around 50 K.

At all of the temperatures measured the amplifiers remained operational, there is an uncorrelated range in the difference in gain over the entire bandwidth. The gain varies by 3 dB in all

the amplifiers, demonstrating that their performance, and different components' performance within the amplifiers, are susceptible to cryogenic temperatures. The pulses of the SNSPDs amplification remain unchanged over the temperature range, as viewed in Figure.5.5. A 125 mV peak simulated pulse with 13 dB attenuation is shown in Figure.5.5 and the formula described in Section 5.2 is injected into each of the amplifiers. The amplitude and shape of the pulse remain consistent for all temperatures, except a slight increase in amplitude at lower temperatures over all amplifiers.

Two Si-based amplifiers from RF-Bay (LNA 580 and LNA 1000) are also tested, but due to carrier freeze-out [200], they stop drawing current at 120 K, and therefore cannot amplify any pulses. These are not characterised further.

All three amplifiers are successfully activated after thermal equilibrium is reached at 1 K with no reduction in their performance before and after activation at 1 K. In Figure.5.3 the power draw from each amplifier from 1.3 K to 300 K shows that none fail.

While all amplifiers are active, the temperature does not fall below 13 K from the combined dissipated 900 mW of heat energy from the amplifiers overpowering the 300 mW of cooling power regulated sample stage.

The gain spectra of the GaAs based amplifiers measured from 300 K to 1 K from 0.2 GHz to 6 GHz frequency range is shown in Figure.5.4. The bandwidths of the amplifiers are shown in TABLE.5.1. Figure.5.4 shows a range up to 1 GHz for all amplifiers, the frequency range dominant in an SNSPD pulse. The SNR values are measured for all of the detectors by using the average values of the peaks' ratio to the noise floor. We measured the noise the amplifiers had by splitting the input signal injected into the amplifiers into two and measuring the noise floor on both. When we inject the SNSPD pulse, the noise floor is higher than simulated pulses from the waveform generator and spectrum analysers. The dominant noise contribution is from the SNSPD pulse, and the signal is two magnitudes above the noise floor, therefore considered negligible. To measure the noise, we measured the difference between the error in the 0 voltage and the voltage size of the SNSPD signal pulse.

Figure.5.5 highlights the increase in signal for the SNR ratio for lower temperatures. This is from the decrease in thermal noise at these temperatures. By measuring the difference between the amplitude of the SNSPD pulse and the ground signal's noise, we can determine an SNR average of 4:1 across all the amplifiers.

The gain spectra of the amplifiers change less than 3 dB with temperature in each case, with the ADL5611 showing the greatest gain over all frequencies, as well as the most consistent gain over the 1 GHz range, after 200 MHz. The decrease in gain at 100 MHz is evident in the trailing edge of the SNSPD pulses measured from the ADL5611, as a dip can be seen in the trailing edge (exponential decay of voltage after the sharp rising) shown in Figure. 5.5, but does not affect the trigger (rise edge). All of the amplifiers show a higher trigger voltage at lower temperatures, inferring that higher frequencies are increased, or higher frequencies are reached. Consideration

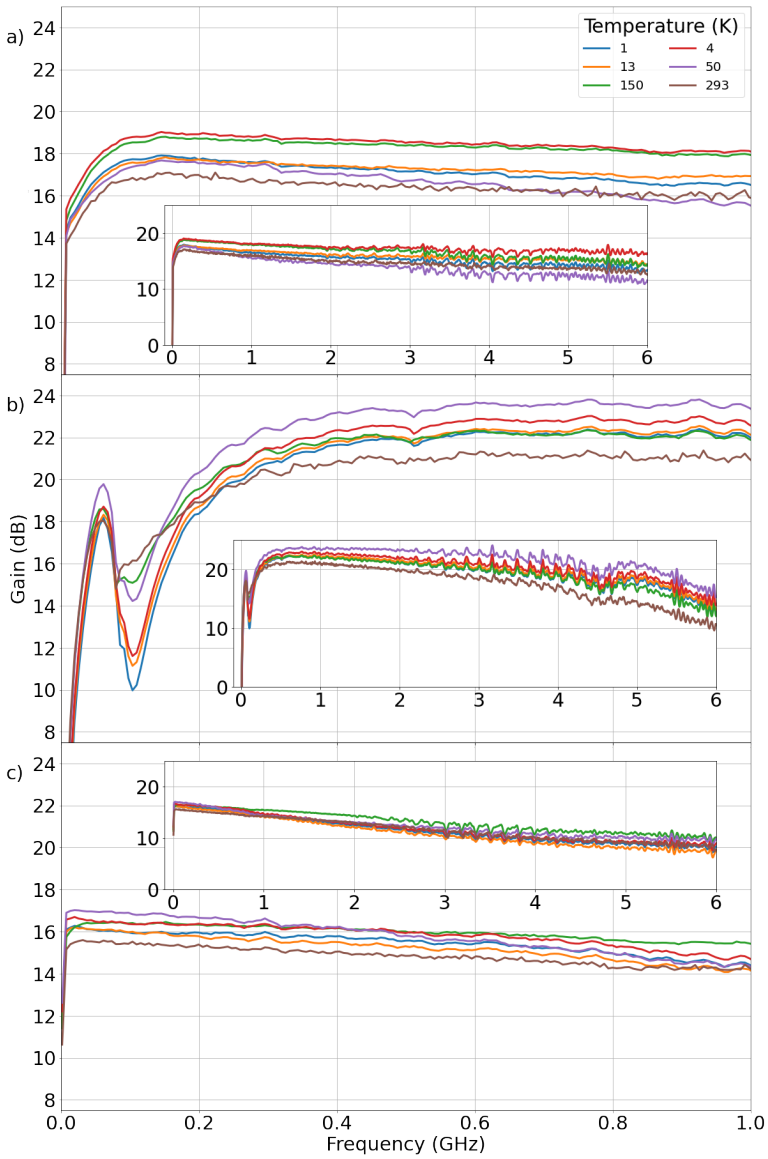

Figure 5.4: The gain against frequency between 0-1 GHz of a) GVA 123+, b) ADL5611 and c) ZX60-6013E+, with the insets showing a broader spectrum from 0 to 6 GHz. The frequency range shown illustrates the frequencies that make up an SNSPD pulse. Variance in gain of different frequencies hence changes the pulse shape.

is the power draw to gain ratio to maximise the amount of gain without losing cooling power, allowing for the most efficient use of cooling power to ensure the greatest number of detectors.

An SNSPD signal is in the frequency range between 200 MHz and 1.5 GHz [224]. We chose 500 MHz as this falls within this range and is a dominant frequency defining the pulse shape. At 500 MHz, ADL5611 has the highest gain to power ratio of 92.83 dB/W, followed by GVA-123 with 77.68 dB/W and ZX60 with 38.77 dB/W with the lowest power efficiency. ZX60 provides the smallest amount of gain in general, with the highest decay in gain for higher frequencies. This is

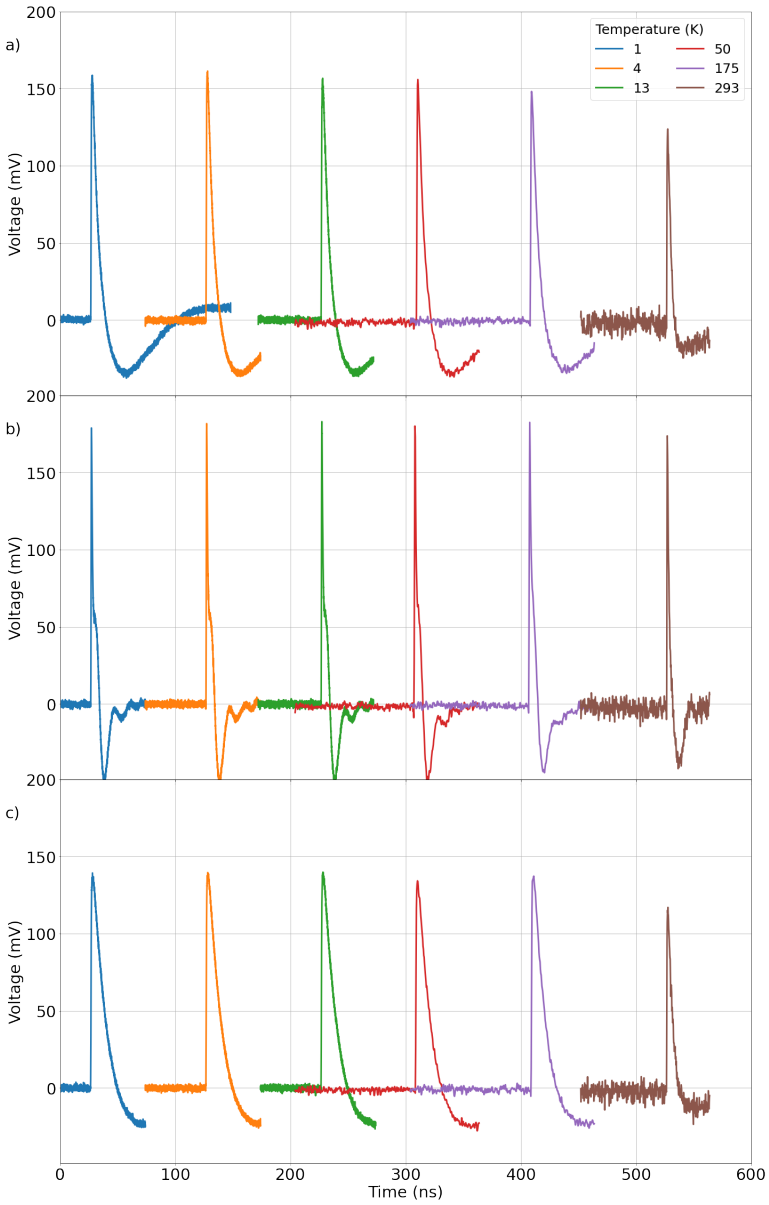

Figure 5.5: Simulated SNSPD pulse using an AWG, amplified from a) GVA 123+, b) ADL5611 and c) ZX60-6013E+, individually. The different pulses at temperatures are offset to show clear waveform shape difference between different temperatures.

comparable to previous research [213–215].

We can measure a decrease in the rising edge time across all the amplifiers from 300 K to 1 K by measuring the time difference between the minimum point before generating the pulse and the pulse's maximum. Using Figure. 5.5 we took the first part of the peak and measured the gradient to determine GVA-123 and ADL5611 rise time is 8 ± 1 ns at 300K. At 1 K, their rise times drop to 900±10 ps and 700±10 ps respectively.

The decay time gives an estimation of the dead time the amplifier induces and, therefore, the limit on the count rate of the SNSPD. ADL5611 has a dead-time of 27 ns, providing a 37 MHz count rate, with GVA-123 and ZX60 reporting lower max count rates of 13.7 MHz and 18.9 MHz, respectively.

5.3.4 Discussion

The GaAs amplifiers showed performance improvements and were able to operate at temperatures of 1 K. The devices remained in operation and could switch from inactivated to activated at 1 K, similarly to the CMOS devices researched in [214]. The devices' operational speed increased, while their signal to noise ratio decreased with temperature. This effect is expected as thermal noise from the devices is reduced. These effects are also addressed in [215]. The devices have been previously used in the amplification of SNSPD pulses, and their performance matches that of similar amplifiers used [225].

The amplifiers emit heat from the electronics because of the inefficiency of the electricity-conducting components inside, expelling heat out into the system. The cryostat is required to dedicate a larger portion of its cooling power to the amplifiers that could be used to host SNSPDs. Therefore if amplifiers are placed close to the SNSPDs, this would break the superconductivity by pushing the temperate above T_C. Hence, a warmer 4 K sample stage with greater cooling power (3 W over the 300 mW sample stage) is sufficient during the end-user system operation. A temperature of 1 K is reached when the amplifiers are deactivated. They are then powered individually to provide measurements from 1.3 K. The cooling power of the 1 K stage is limited, as the helium boil-off rate is greater than the helium feed rate. Once the He pot is empty, the stage temperature depends on the 4 K cold head.

The amplifiers tested here have shown that they can amplify an SNSPD electrical signal pulse. None of the detectors has enough gain to amplify an SNSPD pulse in isolation. When each is paired with another device, they are expected to amplify the pulse to be measurable by a time tagger. Their gains range from 16 to 24 dB between 200 MHz and 6 GHz. They amplified the pulse sufficiently, and the recognisable pulse shape shown in Figure. 5.5. The devices operated collectively at 13 K, a temperature close enough to the SNSPD operating temperatures to make them candidates to exist in the same cryostat. Their power output is also sufficiently low. Hence, the devices vary in performance but can be used as cryogenic amplifiers for SNSPDs. The investigation shown here is not a fully comprehensive list of all the possible commercial amplifiers available for SNSPD amplification. A handful of other devices are the subject of present and future studies and may prove superior candidates. An SNSPD pulse varies in noise, amplitude and shape, between SNSPDs. Future investigations are required to show that the amplifiers still have the same performance metrics when used to amplify other SNSPDs.

The results also focused on amplifying one signal inside the cryostat. Comparing the system's performance by expanding this to multiple SNSPDs and amplifiers will yield scaling possibilities.

The commercially packaged amplifiers discussed are currently not optimised for space or dissipating thermal energy. Integrating amplifiers onto the same electronic circuit boards as a time tagger with condense the design. Packing the device is its challenge, and testing amplifiers on a time tagger will require investigation.

5.3.5 Conclusion

The GaAs amplifiers tested are all candidates for amplifying SNSPD electrical signal pulse while within the same cryostat as the detectors. The Si amplifiers tested showed a failure to operate below 130 K and are therefore unsuitable to operate close to SNSPDs in the cryostat. The ADL5611 showed the highest gain to power ratio of 92.83dB/W. The gain to power efficiency is above the GVA-123 and the ZX60 by 20 % and 139 %, respectively. The ADL5611 was also shown to operate after a temperature cycle from 300 K to 1 K while inactive. The device showed improvement at operation when operating at 13 K than 300 K. The rise time is 700 ps, one-tenth of the value at room temperatures. This rise time is the smallest compared to the other amplifiers in this comparison. After amplification, the dead SNSPD pulse tail is 27 ns, again around half of the other two amplifiers' performances. This amplifier showed a bandwidth from 200 MHz to 6 GHz of operation, with less than 1 dB in gain difference between these frequencies. We amplify an SNSPD signal to voltage typically measured by a time tagger, two of the ADL5611 amplifiers would be needed, with them amplifying the same signal. 300 mW of power is required to operate the amplifiers at 13 K. The total of these amplifiers is below the cooling power at the 4 K stage of DRYICE1K. The results presented show that ADL5611 is the optimal amplification device for SNSPD pulse readout amplification, at cryogenic temperatures, for this comparison.

5.4 TDC on FPGA Cryogenic Temperatures

5.4.1 Design

The proposed TDC implementation is based on a 256 - staged delay line, which is implemented by using Xilinx's Artix-7 carry chain primitives, CARRY4. Each CARRY4 block consists of 4-bit adders; therefore, 256 - bins utilise 64 CARRY4 blocks. The 256 bins subdivide an external clock running at around 200 MHz by propagating the input trigger (SNSPD pulse) through the carry-in and out pins connecting the blocks. At the clock signal's rising edge, the output bins' values are captured to record how far the trigger signal propagated through the CARRY4 blocks by using the D-type flip-flops, providing a digital “snapshot" of the trigger's location to the clock edge. Figure.2.21 in chapter 2 demonstrates a TDC. In this Figure, the start signal would be a SNSPD signal, the stop is the clock, and each square block represents a CARRY4 block, with four adders within.

The output of the carry chain is a thermometer code, a code consisting of a trailing list of 1s and then 0s, with the last 1 being the position of the detection of the clock rising edge. Hence, the

output will be N number of 1s and 256 - N number of 0s. There will be 256 1s and 0s in total, with the change's position indicating the delay.

The protocol for the detection method is shown in Figure. 5.6. The T_{in} signal provided by an SNSPD pulse begins the carry chain, measured by the interception of the clock signal. This thermometer signal is passed to the input filter, ensuring it does not allow another restart of the delay chain within the same carry chain. This thermometer code is then decoded into an eight-bit data-frame long UART signal sent out of the FPGA to a UART to USB converter to be logged by the operator PC. There is also a coarse counter: this counts the number of clock cycles to differentiate SNSPD pulses for times large than the delay line time.

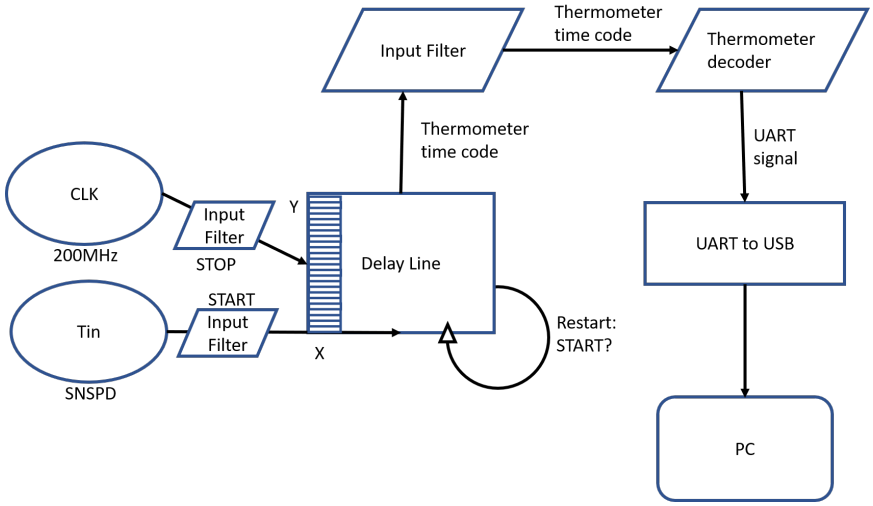

Figure 5.6: Schematic representation of the readout circuit used to detect SNSPD signals.

Details of a UART protocol can be found in Section 2.8.7 in Chapter 2. The UART code package at this point leaves the cryostat system. The UART to USB converter transforms the signal for the PC to decode to present the time tag.

5.4.2 Instruments

Two different FPGAs are used; their model numbers are XC7A35T and XC7A50T. They are tested in this chapter and are from the same FPGAs family: the Xilinx Artix-7 [226]. Their specifications are described in TABLE.5.3 and [227]. The XC7A35T is on a Basys 3 development board, shown in Figure.5.7, and the XC7A50T is on a custom-built PCB displayed in Figure.5.8, which is designed by Andrew Hart.

This family by Xilinx provide a low-cost solution with the highest DSP bandwidth available. A high DSP bandwidth is desirable for SNSPD rising edge detection. Both are implemented with the TDC program with the state machines illustrated in Figure.5.6. For simplicity, the XC7A35T

Connection	MK I				MK II			
	Type	$f(MHz)$	$V(V)$	$I(A)$	Type	$f(MHz)$	$V(V)$	$I(A)$
I/O P	DC A	0	3.3	1.5	DC A	0	3.3	1.5
Program P	DC A	0	1.8	1.3	DC A	0	1.8	1.3
Core P	DC A	0	1.0	0.15	DC A	0	1.0	0.15
CLK	DC D	0.01	3	0.01	RF D	200	3	0.01
Tin	DC A	0.01	0.8	0.01	RF A	50	0.8	0.01
UART	DC D	0.1	3.3	-	DC D	0.1	3.3	-
J-TAG	DC D	0	5	1.5	DC D	30	5	0.05
Amps Power	-	-	-	-	DC A	0	5	0.3
RTD Sensor	-	-	-	-	DC A	0	0.01	0.1
DXP & DXN	-	-	-	-	DC A	0	3.3	0.1

Table 5.2: FPGA PCB boards inputs' and outputs properties. f is frequency, V is voltage, I is current and the type represents a DC or RF connection hosting Digital (D) or Analogue (A) signal. (-) signifies that it is not available.

on the Basys 3 [228] will be referred to as the MK I as this is to test the concept and is then improved. The custom made PCB with the XC7A50T is now referred to as the MK II.

This consists of three power rails for the FPGAs: core power, programming power and input/output power. Another power line for the amplifiers added to the PCB. This uses a J-tag programming system and places for the RTD temperature sensor for calibration to be hosted. The RTD sensor is placed in thermal contact with the FPGA chip itself in the centre.

The Artix-7 is the lowest power of Xilinx's 7-series FPGAs. The family has 45 to 740 digital signal processing (DSP) slices, each with a 25 × 18-bit multiplier and 0.9 to 13.1 Mb of on-chip block random access memory. DSP configuration options include pre-and post-adders and a 48-bit accumulator. Different variants available are (-3,-2,-1) representing speed grades and power consumptions, with lower numbers for lower power (-L) and lower speeds. They are also rated to different environmental temperatures for Industry (-I), and Commercial (-C) purposes. One of the specific devices used in the instrument is an XC7A50T-2FGG484C, which has 50 k logic elements, 2.7 Mb of block RAM and 120 DSP slices, and comes from the common '-2' speed-grade bin in the commercial temperature range (0-85°C). Their power difference are identified in Table. 5.2.

The MK I and the MK II difference is that the MK I only had low-frequency connections for the clock and T_{in} signals. Therefore the START and STOP frequency could not match the period of the delay lines in MK I. These problems are overcome for characterisation of the TDC, but not practical, or entire SNSPD systems that can provide MHz of signals [223].

5.4.3 Experimental Setup

The set-up for the experiments involving the TDC is illustrated in Figure.5.9. Here we, an overview of the equipment used outside the cryogenic environment to control and operate the

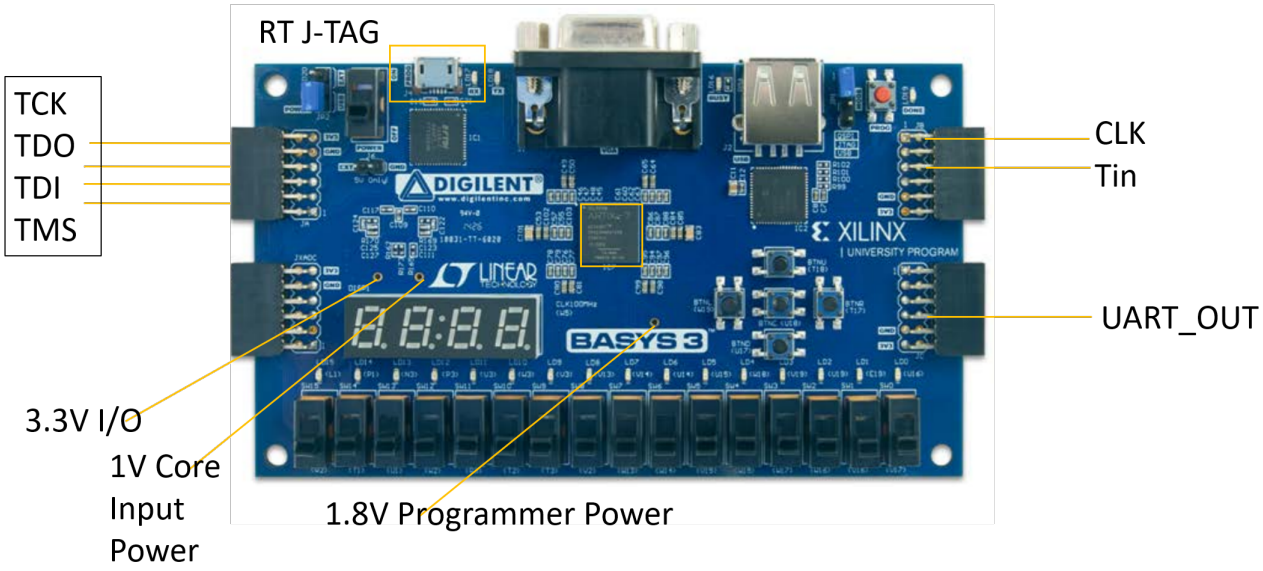

FIGURE 5.7. Basys 3 [229] development board used to test the Artix-7 family cryogenic capabilities, first version of TDC code. Key components mounted on the board and inputs and outputs are highlighted and then presented in text. The images are taken from the Basys 3 manual.

Name	Logic Cells	DSP Slices	Memory (kb)	I/O Pins	Speed Grade	Package
XC7A35T	33,280	90	1,800	250	-1	CPG236
XC7A50T	52,160	120	2,700	250	-2	FGG484

Table 5.3: Artix-7 FPGAs specifications used mounted on the Basys 3 development and the custom made time tagger readout system. The speed grade represents the overall logic connection speed capable, with design specific implementations varying. The speed grade also represents the power consumption type, with higher powers required for faster models. The package represents the size and connection architectures for interface, with the XC7A50 allowing for 100 more of inputs and 12 DSP over the 90 DSP on the XC7A35T.

FPGA, amplifiers and SNSPD. The ground is not indicated but is common for all equipment and the PCB. The photons are attenuated down to a single photon per dead time or less level. This is the full system, but the SNSPD pulse can come from the options of the SNSPDs themselves after amplification, a pulse pattern generator for sync with the clock pulses, or the AWG for a fully modelled SNSPD pulse. The SMU supplies power to FPGA power lines, using four-wire measurements to measure each line's power difference at lower temperatures and maintaining constant voltage during cool down to keep the FPGA active. If deactivated, the MK II will have the TDC program wiped.

To realise a full quantum photonics readout system that allows for the detection and readout of multiple qubit detection signals from within a single system [198], a combination of the

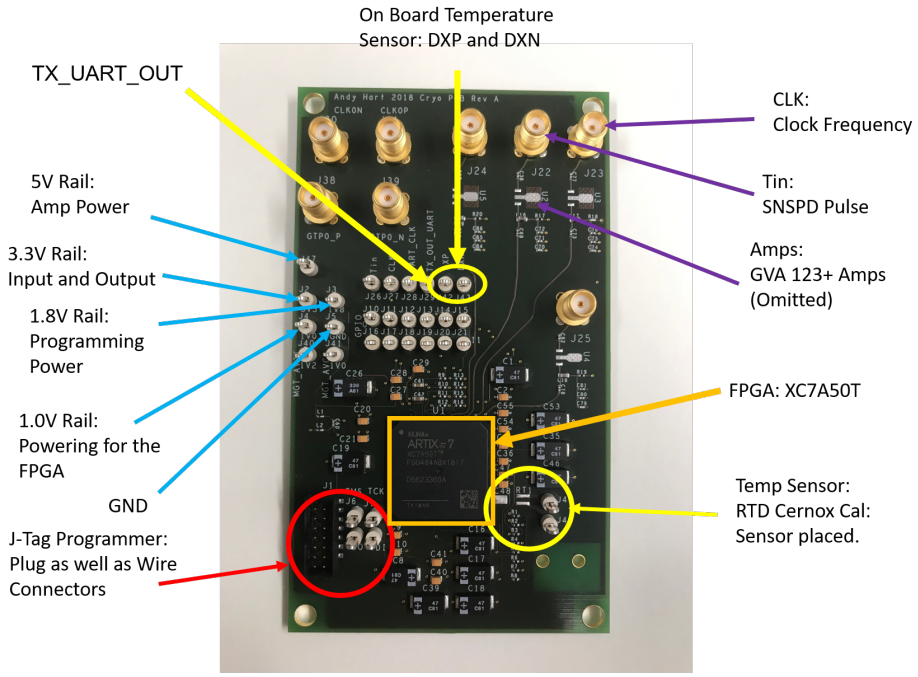

FIGURE 5.8. The custom designed cryogenic FPGA PCB (70 × 120 mm) with the inputs and outputs highlighted.

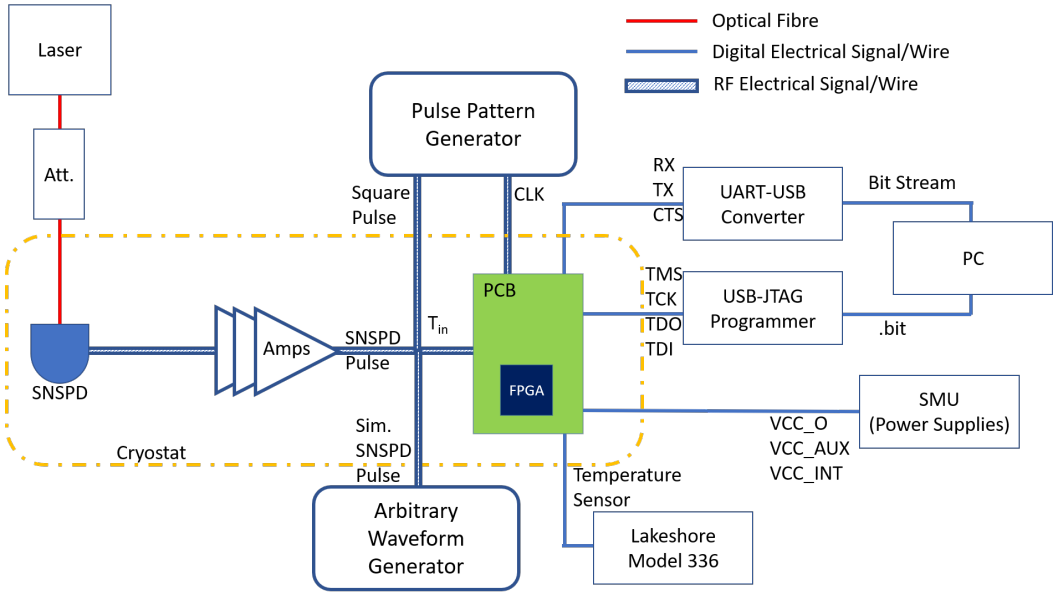

FIGURE 5.9. Schematic Diagram of the SNSPD readout equipment.

components tested in this chapter are networked together. We use the SNSPD of the system at the 1 K sample base stage to provide conversion of photonic qubits to the electrical micro voltage input signals. This micro voltage input signal is transferred via RF cables to a 4 K plate. The

amplifiers are situated to amplify the signal to over 3.3 V. The amplified signal is then read to the TDC, also in thermal contact with the 4 K stage. The TDC signal is then converted to a UART signal communicated to the computer that logs and presents the qubits state. The described system was constructed, as shown in Figure.5.9

For each of the following experiments, the equipment used will be highlighted. Here we provide their possible uses in each experiment. The pulse pattern generator is used as an external clock to adjust the timing to match the different carry delay lines periods that will occur for different temperatures, FPGAs and slices within the FPGAs measured throughout the chapter. We use a Teledyne Lecroy waveform generator that provides a 6 ns wide pulse, with peak-to-peak voltage V_{pp} of 3.3 V. The Tektronix AWG70000B Arbitrary Waveform Generator also provides a second signal for the Tin pulse. This is where the SNSPD pulse will be.

The SMU is the same Keysight B2901A as described in the chapter. 4. The SNSPDs and amplifiers are the same as in the Chapter. 4.

The set-up is the same schematic for room temperature and cryogenic temperatures, as the FPGA is housed in the cryostat to mitigate the difference in electronic connections. For the experiments described, the FPGAs are housed on a copper mounting plate that provides a custom-built design to mate the 1 K sample stage and the FPGA together, improving the thermal conductivity. The mounts from the FPGA to the copper plate are thermally coupled to the plate by copper wire and bobbins.

Figure. 5.9 also shows how we plan to connect an SNSPD to the FPGA using amplifiers and control the number of the rate of the number of pulses it produces using lasers and controlled attenuation. We can also control the count rate using just the DCR, which was characterised in Chapter. 4. We use DCR over pulse instead of Count rate as the current the determines the DCR can be synchronised with the captures of detection events. As the current source can be driven within the same system as the detection capture, but attenuates to determine count rate could not be. This would reduce the reproducibility of measurements. Hence DCR is used. It shows that the outputs of the FPGA go to the UART-USB converter and the inputs of the program is through a JTAG, that are both interacted through a PC. We also connect the Lakeshore Model 226, to monitor the temperatures of the Cernox RTDs.

The following description is of the available connections for both TDC systems. Stainless steel RF cables provide information communication during operation between the cryogenically operated FPGA and the room temperature instruments with SMA connectors at 50Ω. The clock signal and T_{in} signal use the RF lines to communicate to and from the environment as they are all high-frequency signals. Manganin quad twist wires carry the power and the UART readout data to a converter to USB signals, which can be read out via a PC. The converter was designed by Andrew Hart and utilises an Amega micro-controller. The digital pulses are then transformed into dynamic differential voltage signals, which are used by USBs. The quad twist also has a ground signal and one of the lines to reduce noise from the wiring. These pass through the 24-pin

Micro-D connector on the cryostat that leads it through to the environment. Six voltages lines drive the three different power lines needed to operate the FPGA. They are paired in parallel, allowing for power adjustment during cooling as the voltages change from room temperature to cryogenic temperatures. This allows for the resistances of the connection to be taken into account when driving the FPGAs. The Micro-D connector is represented in Figure. 5.9 by the blue lines representing DC electrical signals/wires.

Some of the experiment use simulated SNSPD pulses to provide consistent frequency, amplitude and signal shape, to allow for comparison between results, as the amplitude and frequency of SNSPDs signals fluctuate with temperature and current. Once this pulse crosses the voltage threshold, the FPGA clocks a hit (hit meaning a signal has been detected), this Look-Up Table (LUT) process time can be used as our smallest increment of measurable time on the FPGA, as there is a delay in the signal for every LUT passed through to represent the resolution of our clock. This time depends on the FPGA and the properties of the LUTs within it.

In this experiment, the two pulses (CLK and T_{in}) came from the same waveform generator, allowing them to be in sync. We drive the waveform generator at 100 mV_{pp} (peak-to-peak voltage), which is amplified with the on-chip GVA-123+ amplifiers to 3.3 V. This is the threshold of measurement by the I/O on the FPGA. The CLK is a 200 MHz sin wave, and the T_{in} is a 10 kHz pulse. The CLK frequency matches the delay line frequency and T_{in} to be below the UART communication frequency threshold. By changing the phase/delay time between the arrival of the pulses and measuring this value, we can sweep the full carry chain range and determine the full carry chain's size. By knowing the distance in time to enter bin "0" and bin "255" and dividing by the total number of bins, we can provide the average bin size in ps.

5.4.4 Temperature Sensor on FPGA

The Basys 3 (MKI) development board is not designed to allow access to in-built temperature sensors on the FPGA. Therefore the sensor in the FPGA is not calibrated, and a Cernox RTD sensor we glued in thermal contact with the FPGA is used to measure the device's temperature. This provides a more accurate temperature reading due to the sensor's proximity compared to the other sensors within the cryostat. On the MKII a calibrated RTD temperature sensor is mounted onto the FPGA to calibrate the on-board FPGA sensor. Quad twist magnium wires are used with the temperature sensors, using four-wire measurements to subtract the measurement wires' resistance. A small measurement unit device supplies a low steady current to the sensor for resistance measurement during calibration.

A Virtex device temperature-sensing diode is integrated into the FPGA centre and is accessible through the DXP (Anode) and DXN (Cathode) pins, as shown in Figure. 5.8. The DXP and DXN pins are connected to a diode-connected transistor, which creates a remote sensor. The DXP/DXN pins are dedicated pins and cannot be accessed from program interfaces. These pins are attached to the substrate/die itself.

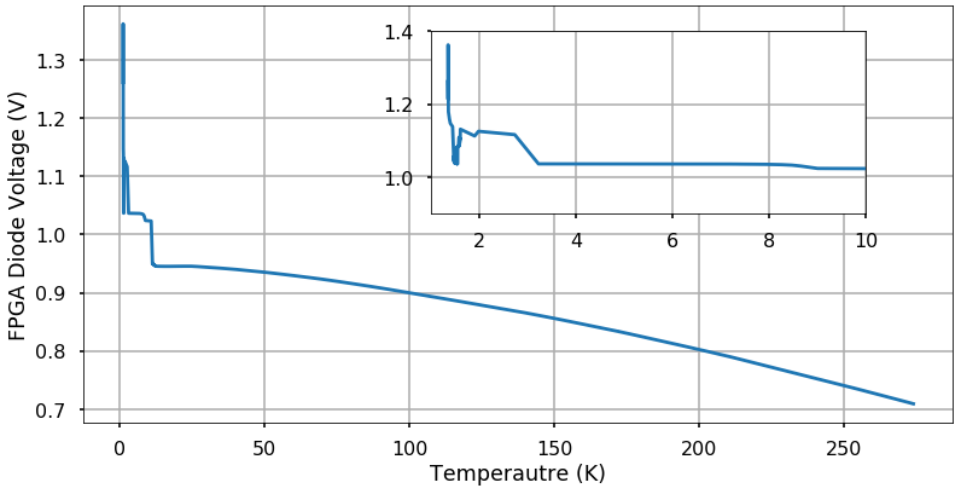

Figure 5.10: FPGA temperature diode calibration against external reference diode, while the FPGA diode is biased with 10 μA. As a hysteresis effect was presented in the measurement, the data is averaged between the two cycles. Several thousand points are used for the curve. Inset: zoomed focus for a low range to highlight the change in gradient.

The accuracy relies upon the temperature sensor device, which translates the IV vs temperature curves into a temperature reading.

The result of this calibration is shown in Figure. 5.10 and was obtained during both the warm-up and cool-down cycle and the FPGA switch off, while measuring both the diode and RTD sensor at changing intervals, with smaller intervals for lower temperatures.

The Si diode characteristics change at low temperatures due to carrier freeze-out. Between 3 K and 1.5 K, the resistance rises rapidly, providing a near discontinuity in resistance as seen in the inset on Figure. 5.10. Most of the TDC experiments on the MK II device are tested above this break down.

5.5 Results

5.5.1 FPGA utilisation

An FPGA has a limited amount of logic. This section describes the amount of logic utilised, showing the complexity of the system on the device and indicating how much more logic can be used. The power consumption is reflected in the amount of logic utilised, with the power directly proportional to the current draw. This also indicates how many TDCs can be hosted on one device. The logic utilisation of the system on the XC7A35T is recorded as 1037 registers (2%), 151 LUTs (1%) and 4 I/Os (4%). The logic utilisation of the system on the XC7A50T is recorded as 1690 registers (3%), 568 LUTs (2%) and 3 I/Os (1%). Hence, as one TDC utilised 3% of registers, the device can theoretically hold 33 TDCs. Vivado Lab is the software used to fabricate a simulation,

test and upload the logic program onto FPGAs. The software downloads the specifications of an FPGA and loads the configuration programme onto the simulated device. The device simulates each component's speed, critical paths, and logical process to test the program can work on the device. After this, the program can be uploaded to the device. The simulations predict a 0.117 W of total power on the chip, less than the 0.3 W of cooling power at the 1 K sample stage of the cryostat quoted by ICE Oxford.

5.5.2 TDC single-shot

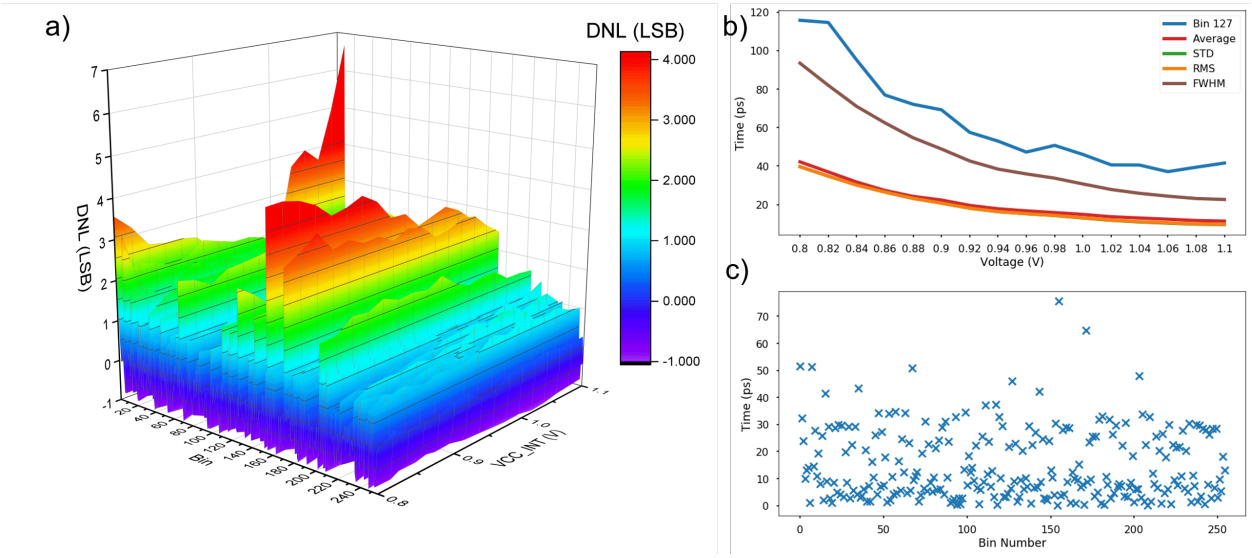

Figure 5.11: a) DNL values for a carry chain TDC implemented on MK I at room temperature. b) Statistical measurements on different parameters and metrics on bin size and jitter amount at room temperature. c) At 1 V VCC_{INT} the bin sizes measured at RT.

We performed a single-shot sweep of the two implemented TDCs to calibrate the device for low temperatures and record the non-equal distribution in the device. This is the error in the form of jitter on each event detection.

For this test, a 200 MHz clock frequency from the 81130A Pulse Pattern Generator and a 10 kHz simulated SNSPD pulse from the AWG70001A from Tektronix, asynchronous to one another, filled the 256 bins randomly. This provides an even probability that all bins would be filled equally if the bin sizes are the same. Therefore deviations away from this value provide the size of the bin and the DNL. The results obtained from the tests can be seen from Figure.5.12, where Figure.5.12 a) is the non-calibrated DNL values of all the bins, at the range of voltages, the FPGA is functional. Figure.5.12 b) is the average timing jitter plot errors for different voltages of the uncalibrated chosen carry chain slice comparable to [230]. For higher core voltages, the smaller all measures of the bins' error, therefore driving higher voltages, provides a consistent bin size.

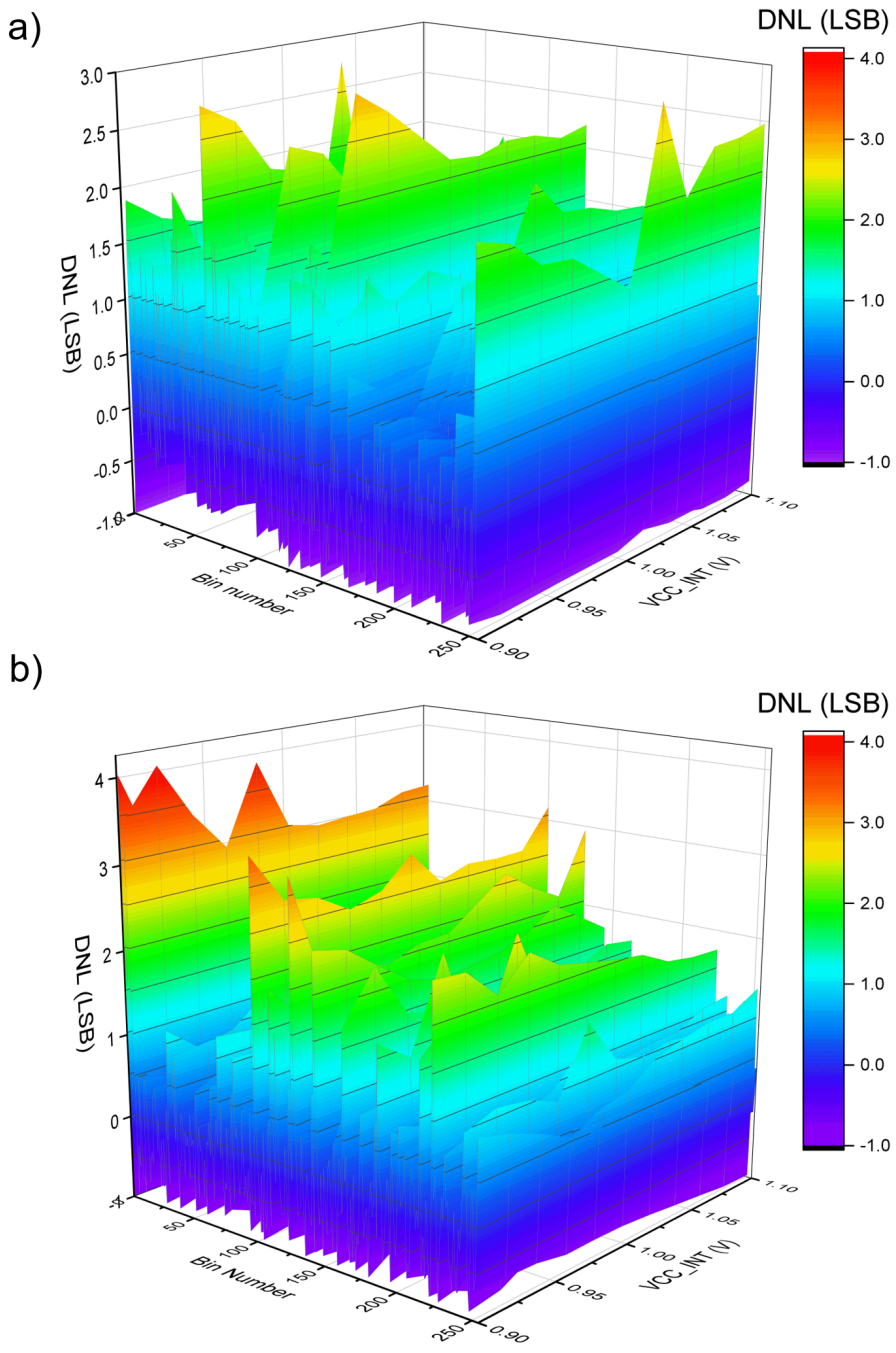

Figure 5.12: DNL values for a carry chain TDC implemented on MK II. a) The device at room temperature. b) The device at 11 K during operations. VCC_{INT} is the core voltage of the FPGA.

Figure.5.11 a) and Figure.5.12 show the collected counts into the 256 separate bins available on the FPGA and collected 500,000 SNSPD simulated pulses to find the distribution average between the bins. The average frequency between bins remained consistent, with < 500 counts

for a standard deviation. VCC_INT is the input core voltage of the FPGA that affects the time to complete a delay line, affecting the bin size in time. The bin sizes also change by different amounts relative to one another. Hence, to mitigate errors, we characterise the delay line for each voltage.

5.5.3 DNL and INL

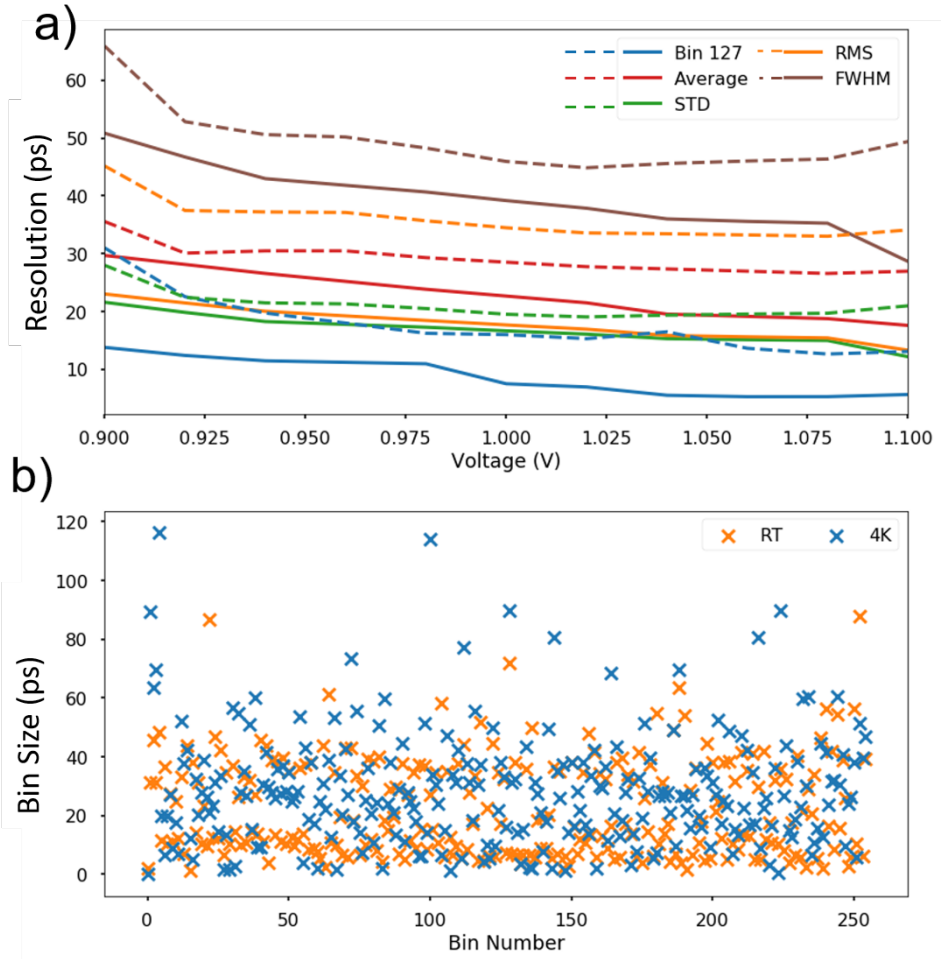

Figure 5.13: a) Statistical measurements on different parameters and metrics on bin size and jitter amount, with the dashed lines representing the RT measurements and solid lines 11 K. b) Bin sizes are measured at 1 V VCC_{INT} at RT and 11 K.

The TDC's non-linearity is mainly caused by unevenly spaced delays in the carry chain and non-perfect clock distribution [198]. The variability in the bins for the FPGAs DNL and INL are shown in the Figures. 5.12 & 5.14. This occurrence can happen anywhere in the device and is unavoidable in practice, but care cannot be chosen, particularly bad physical locations for the CARRY4 chains [198]. The difference between the different error metrics of the TDC at cryogenic

and RT is shown in Figure. 5.13 a), with all the metrics showing an increase in their parameters. The average of their differences can be viewed in Table. 5.4.

By using both Figure.5.13 a) and Figure.5.12 a rise in the DNL error average for each bin can be seen, leading to an overall error increase in the INL as well. The average of 50 ps per bin is a resolution roughly ten times less than the jitter on an SNSPD pulse. Hence, this device's resolution captures an SNSPD pulse with accuracy far beyond that on an SNSPD and near future SNSPD designs with shorter rise times down to 50 ps. We can determine that the errors measured in INL and DNL (see Chapter.2 for explanation on INL and DNL) are not important factor when using the device for time tagging.

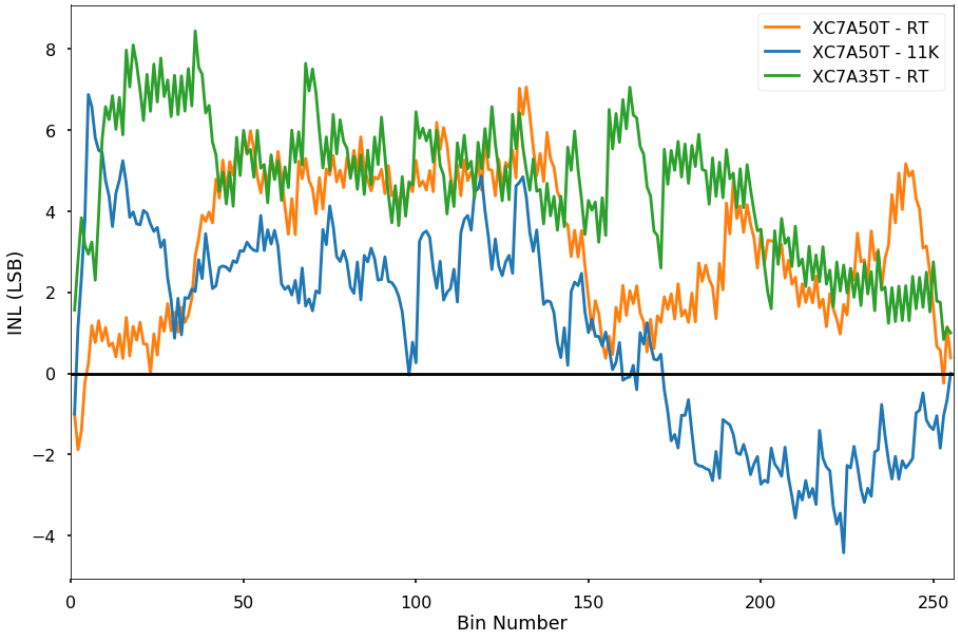

Figure 5.14: INL of the MKI room temperature and the MK II at room temperature and 11 K, measured using the sum of the INL from Figures. 5.11 and 5.12.

This increase in the error metrics is caused by the jitter increase of the IO delay, by the significant decrease in decoupling capacitance at cryogenic temperatures [195]. The decrease in total decoupling capacitance causes greater degradation at higher input frequencies as the current supplied to the FPGA switches with higher frequency. Some bins are more sensitive to temperature changes than other bins due to local variations in doping concentrations, so the relative delays between the bins increase.

The comparison of the INLs for RT and 11 K for the MK II and the RT of the MK I is seen in Figure.5.14. We can see that the MK I with the 35T model Artix-7 deviates the most, showing a maximum INL error of 8.2 LSB. The XC7A50T in the MK II before the max error is 6 LSB, with the 11 K readings presenting a greater deviation from the ideal INL value of 0, similar to the results in [198]. The worst error we can get is acceptable. 8.2 LSBs $\approx 8\times$ 30 ps = 240 ps. We only

Statistic	Values
Capture Rate	<29.5%
Standard Deviation	<27.5%
RMS	<103.8%

Table 5.4: The change in error under different metrics between room temperature and 4 K measurements for the MK II.

need to discriminate ≈ 600 ps for state of the art Gbit QKD as this is the time difference between bins in time-based encoded QKD [198, 231, 232]

5.5.4 Carry Delay

Figure.5.15 shows the average delay per carrying block versus the FPGA voltage for 300 K and 4 K. For both MK I and MK II the delay change is larger over the voltage range than over-temperature, emphasising the performance stability over temperature. However, it also shows that the voltage must be stable with ± 0.02V to achieve TDCs and ADCs that can be re-calibrated. A second observation is that the voltage range in which the FPGA operates changes over temperature. For MK I the range is significantly wider at RT (0.7 V – 1.5 V) than the specified range (0.95 V–1.05 V). At low temperature, it reduces significantly at both ends (0.7 V–1.15 V). Similar is for the MK II the range is significantly wider at RT (0.8 V – 1.2 V) and at low temperature, it reduces significantly at both ends (0.9 V–1.1 V). The higher voltages provide a shorter carry chain time, providing an increased resolution in detection time, therefore decreasing the jitter. These results are comparable to [233]. The voltage variation at cold temperatures is reduced. Using FPGAs at low temperatures is not only feasible but beneficial to the operational performance. The shaded regions in Figure. 5.15 represent the voltage range at which the FPGA no longer returns measurement results, as the voltage is too low or too high.

The carry delay is directly linked to the dead time of the TDC, as there must be at least one full carry chain's worth of delay between incoming pulses for them to be registered. Therefore, running the system above the recommend 1.0 V decreases the system's dead time, allowing for increased capture of hits. This property is named the capture rate and is defined by:

$$C_{rate} = \frac{C_{counts}}{TotalNumberofT}$$

$_{in}$ = T$_{TDC}$ $\frac{}{T_{CLK} = \frac{f_{CLK}}{f_{TDC}}}$ (5.3)

With T_{TDC} defined as period of the TDC, T_{CLK} period of the clock, f_{CLK} frequency of the CLK and f_{TDC} frequency of the TDC line.

The following results compare the difference in operations' performance between RT and cryogenic operation by performing a code density testing calibration. With the use of a multi-phase clock, calibrations can be performed on the TDC to increases resolution at the controlled temperatures and voltages. The multi-phase clock uses multiple phase-shifted clocks to generate

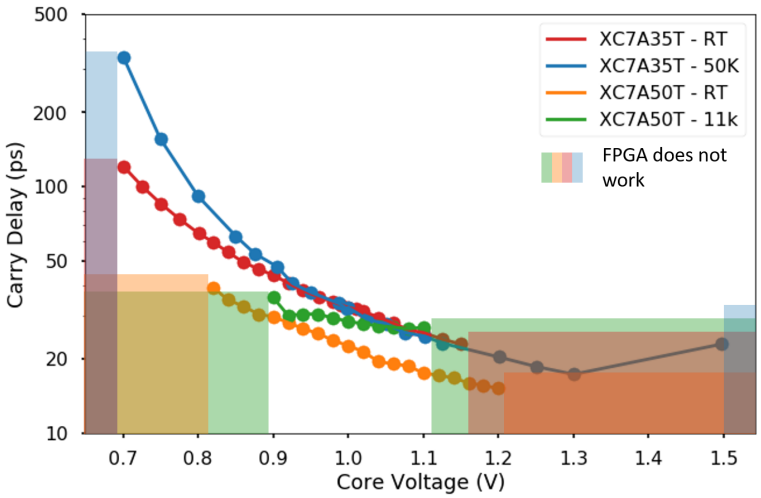

Figure 5.15: Delay of the carry elements in the carry chain versus FPGA voltage (VCC_INT) for multiple temperatures and FPGAs.

different counters. This increases resolutions at the cost of reasonably high logic utilisation. The calibration is done by measuring the carry chain delay, syncing the CLK and T_{in} pulse, and then sweeping and measuring the time difference between these pulses over the full range. The carry delay chain is measured, and the CLK changed to match the carry chain time. The FPGA die temperature during operation runs slightly above 4 K at 13 K.

Fixing the voltage supplied to initialise the delay line also fixes the system's clock speed for a fixed temperature. This can be calculated from Figure.5.15; by knowing that the length of the carry chain is 256 bits, and the inverse of the carry delay time provides frequency, we can calculate the clock frequency for each voltage and temperature using:

$$f_{CLK} = \frac{1}{T_{bin} \times 256}. \tag{5.4}$$

Hence, the clock frequency pulse supplied to the device can be tuned to match the device's clock speed. This tuning to match will minimise the dead time of the device between delay time initialisation. This ensures maximum capture of the TDC when the pulse frequency of the SNSPD is less than the clock frequency.

A clock frequency higher than the device's clock speed misses out on full-scale range bits; therefore, needlessly running a higher frequency places constraints on cabling requirements, making the system less resilient to clock jitter and noise. A clock frequency lower than the clock speed will mean that we miss some SNSPD pulses as we cannot tag longer than the internal delay line. Therefore the clock period needs to be slightly shorter than the delay line delay, with some margin to accommodate voltage supply/temperature fluctuations.

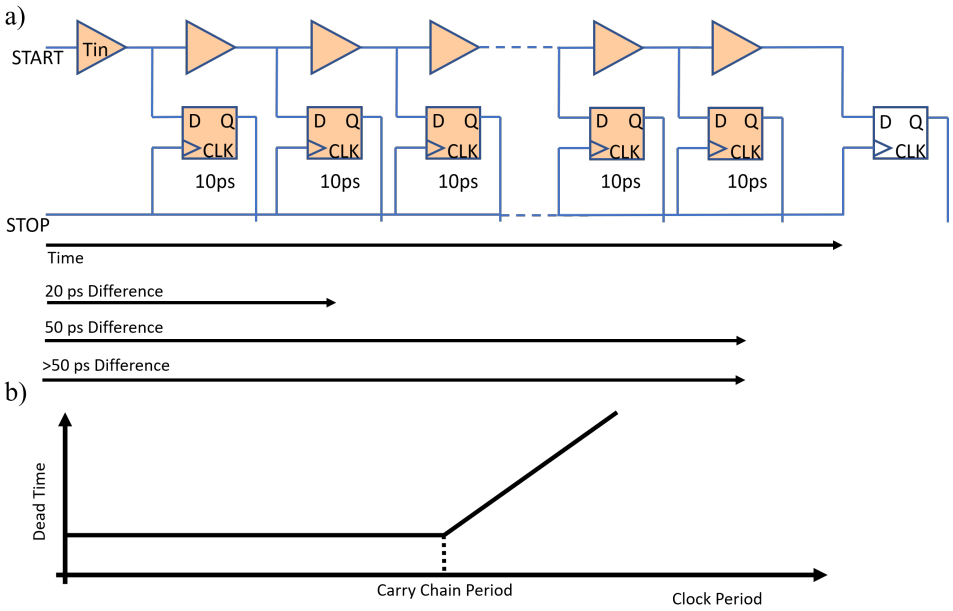

Figure 5.16: a) Schematic of carry chain that is 50 ps long, with different timing captured on the TDC shown by the arrows below the schematic. b) Graph of the dead-time gain in a TDC.

A clock period longer than the carry chain delay time increases the dead time of the system in between clock cycles, leading to lost signals between cycles. If the delay line is left with all the CARRY4 elements switched on in the carry chain delay line, this signifies that any T_{in} signal will be logged to be in the last bin, as shown in Figure. 5.16 a). A misrepresentation of the final bin will occur, tagging T_{in} pulses with the incorrect time. As when the STOP signal from the clock signal activates the recording of the bin position, any time after the last bin will be captured within the last bin and show a disproportionate representation of the last bin's frequency of hits.

To avoid this, a filter is also programmed into the device to discharge the carry chain and not capture any T_{in} signals after the last bin. In other words, the TDC resets itself immediately after the last element (bin) is activated, the carry chain discharges and pulses between the clock period and the TDC period are lost. Hence, we do not log delays longer than the last bin, as this could be due to no T_{in} signal. This code is open source and originally generated by Harald Homulle at TU Deflt [234]. As mentioned, the pulse's true timing will be lost as no bin represents its place in time. The large the difference between the clock period and the TDC period, the larger the dead time, as shown in Figure. 5.16 b).

The bin time width delays are the shortest measurable time by the TDC, and therefore the resolution is directly related to this. The delay elements are unchangeable and therefore lock this resolution. However, mathematically calibration and linearisation techniques can be applied to reduce further the resolution using multiple line TDCs. An example is that each delay line will have a unique sequence of bin periods. Every 256 bins in each delay line will have different bin sizes, so when used in conjunction with one another provided increased resolution, as covered in

Chapter 2, Section 2.8.6.

5.5.5 FPGA Power

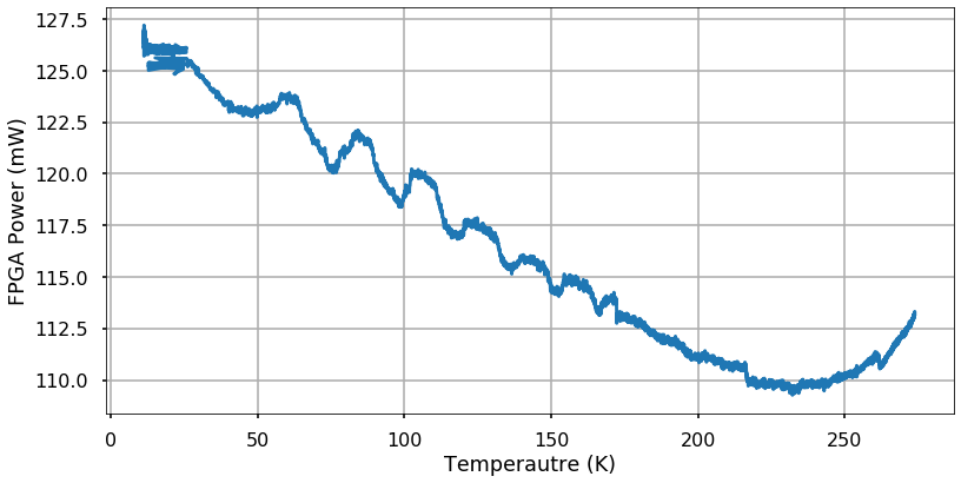

Figure 5.17: FPGA MK II power consumption measured using 4-wire measurements versus the temperature measured with the FPGA on board diode. The VCC_{INT}, VCC_{AUX} and $VCC_{I/O}$ are kept constant at 1, 1.8 and 3.3. respectively, while driving the current to keep the core voltage constant.

To study the self-heating effects of the FPGA, firstly, the internal FPGA diode was calibrated against a cernox RTD CX-SD previously calibrated. With the diode calibration obtained, the FPGA's self-heating was studied using a circuit capable of sweeping the power consumption of the FPGA, which is found in Figure.5.9, with the TDC configuration program active on the FPGA. The results of the sweep are shown in Figure. 5.17. A minor difference is observed in the response at different temperatures, increasing from 110 mW until 125 mW. This power consumption is smaller than the 1 K sample stage's cooling power and is still in operating temperature with SNSPD. Hence, kept on an isolated stage from SNSPD, on a warmer stage, radiation from FPGA to not affect SNSPD DCR.

5.5.6 Linearisation

5.5.6.1 Direct Calibration

A Single Shot Resolution (SSR) variation over time while we measure a constant input value. We measure this by accumulating samples with a constant input over repeated measurements. As the accuracy depends on the position in the full range, the performance over the complete range can be studied. A specific bin can be targeted by changing the time difference between the clock and the input trigger pulse. They have an average of 33.4 ps standard deviation with a 33.3 ps RMS. Figure.5.18 represents a direct calibration result of 7 different delay times space 534 ps

apart and the spread each pulse generates. The resolution is always better than 3 LSB (1σ) and, on average, 1.69 LSB. In Figure. 5.18 a) we see the raw number of pulses collected in each bin, with each different colour pulse being a different timing delay and 100'000 pulses are sent at the same time delay. We then extract the jitter from Figure. 5.18 a) to create Figure. 5.18 b) showing the jitter for each target bin.

These results were obtained using two-time synchronised pulses, with the clock pulse running at 200 MHz and the T_{in} pulse running at 100 kHz, making sure the UART buffer to not overload. A one second spacing between measurements as a latency issue was discovered, as the buffer in the FPGA for the UART code could provide results data from a previous time difference measurement. This time difference can be measured from the difference between the pulse is measured on the FPGA and the communication of the signal to the UART to USB converter. We are using an oscilloscope to measure the time difference between the SNSPD pulse and the UART pulse.

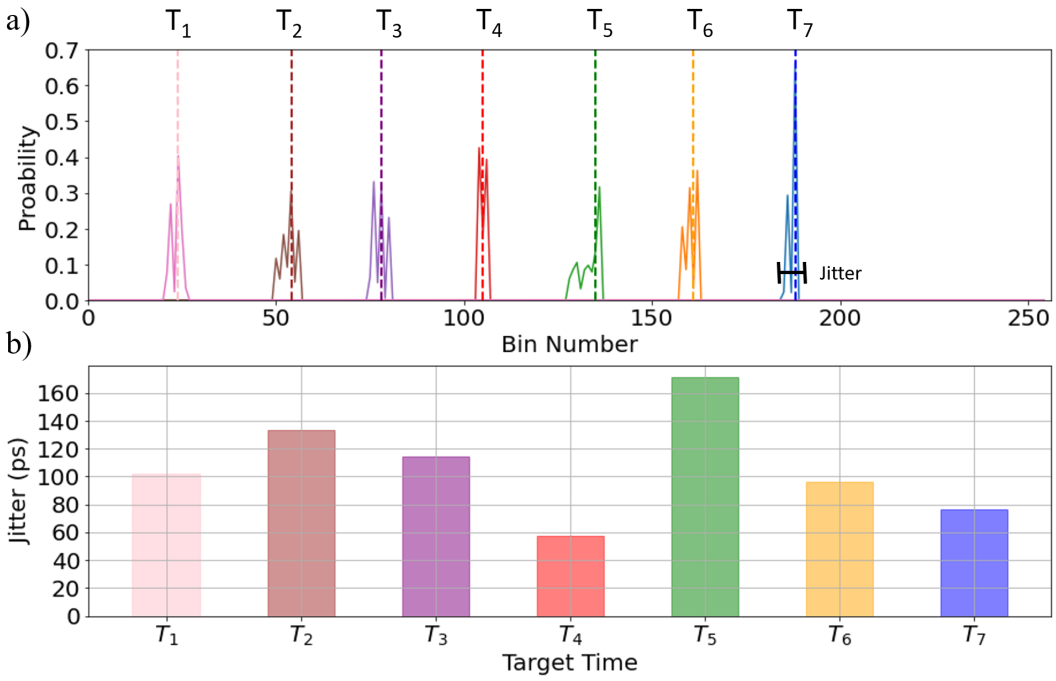

Figure 5.18: Direct calibration via single shot measurements of seven different time period of pulses, with each colour representing a different histogram from a different delay time between the START and STOP times, measured at room temperature.

5.5.6.2 9 Bit code

Implementing a 9 bit, TDC increases the total bin size to 512 per clock cycle. The larger number of delay elements leads to a longer carry chain. As each delay element has a certain delay time, the clock period needed to run this carry chain is now doubled, leading to a nominal 100 MHz

clock frequency. This longer carry chain can only capture one trigger per cycle; therefore, the dead time per cycle is doubled from 5 ns to 10 ns. The length of the maximum dead time is still on the scale of current commercial SNSPDs, and the SNSPD used to generate a trigger in this work.

The set-up is a benchtop experiment at room temperature supplying 1.0 V to VCC_{INT}, with a 1 MHz input frequency from the simulated SNSPD pulse on the Tektronix AWG3000. We used 500,000 counts to fill the bins, with a 10 ns clock period, with each count represented by a 0.02 ps time width. By multiplying the time with the number of counts of each bin, we can determine the bin size as seen in Figure. 5.19 a).

The increased number of delay elements statistically increases the confidence factor. The 8 bit 256 elements carry chains bin width histogram spread is comparable to the 9 bit 512 spread as seen in Figure. 5.19 b). The results measured contradict this as the standard deviation, and the RMS increases from 18.2 ps to 31.4 ps and the FWHM from 30.9 ps to 53.3 ps. This is from the carry chain used for the 9-bit implementation, consisting of wider varying bin sizes. The bin time width of each of the 512 bins is shown in Figure. 5.19 a). The difference in the bin size width spread compared to the 8-bit carry chain is presented in Figure.5.19 b). This indicates that doubling the delay line's size increases the variance of each bin as it becomes more challenging to find CARRY4 locations with similar delay parameters.

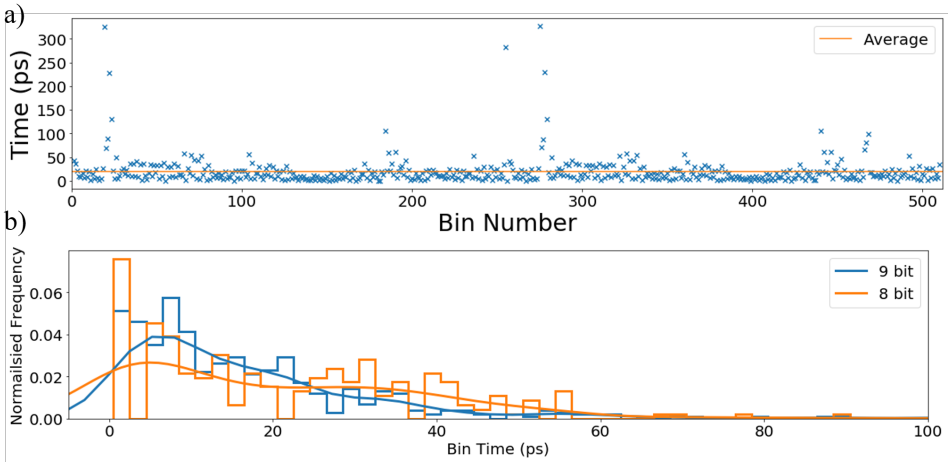

Figure 5.19: a) The bin time width of a 9 bit code length (512 bins) at room temperature b) Histogram spread of the bin time for both the 9bit code and the 8 bit code at room temperature.

5.5.6.3 Average delay lines

The DNL and INL improvements are reflected on the empty bin numbers in the code since averaging methods effectively split bins into how many bins used to average. The change in the spread in the bin size times for the 256 bins is shown in Figure. 5.20. Using the same 256 bins, four different carry chains were measured using a Code Density calibration, which we then proceeded to average over the bins. Though the INL value for a single delay line over the four

averaged remained unchanged, the σ in the DNL was reduced from 18.1 ps to 15.9 ps. However, this method takes up nearly four times the amount of logic resources to perform.

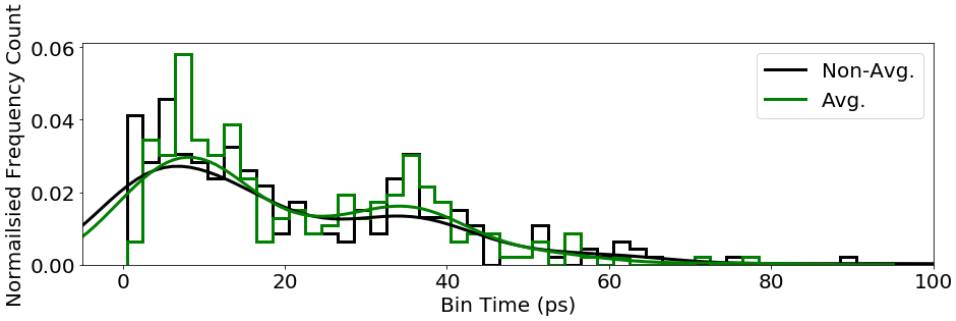

Figure 5.20: Histogram spread of bin times, averaging over multiple delay lines.

It is possible the average over further number of delay lines, with diminishing returns on the improvement in the precision of the DNL value. Nevertheless, we have showed that this is a viable method to improve the TDC accuracy.

A combination of the linearisation techniques discussed can be combined. Using multiple 9 bit codes and averaging over them all after direction calibration can provide further reducing the DNL value.

5.6 Summary and Outlook

Components of a quantum photonic readout system have been presented, showing that the capabilities to realise a closed cryogenic readout system can be achieved. The SNSPD, amplifiers and FPGA TDC can operate enclosed in a single cryostat, achieving 300 mW of cooling power at 1 K that has vibrations of between 8.50 μm and 9.11 μm in the device plane on the scale possible to couple to grating couplers. Allowing for fabricated waveguide integrated SNSPDs on-chip can be used to perform network QKD protocols. We may soon have future devices with waveguide integrated SNSPDs and passive optical components that will allow for a fully integrated MDI-QKD system self-contained within one system. This also motivates to ensure grating coupled SNSPDs are feasible.

Off-the-shelf amplifiers provide a 56 dB gain to the SNSPD signal for the TDC to register single shot activity and operation at 1 K and continuous operations of around 4 K. The performance of the device in gain, bandwidth in the range and SNSPDs signals are improved or have a minor hindrance in performance, depending on the amplifier. The power efficiency of the ADL5611 amplifier nearly doubles, providing the highest gain to power consumption ratio providing an obvious cryogenic SNSPD amplifier choice.

The Artix-7 FPGA TDC operates over a large range, from 4 K up to 300K, without significant performance loss, using the calibrated voltage diode built into the FPGA. In contrast, the system

FPGA's total power increases from 110 mW to 125 mW, which is easily achievable cooling power at 4.2 K with modern cryostats. The experiments presented also showed a halving over the resolution of a 256 bin carries chain from 38 ps to 17 ps per bin. The wide voltage supply from 0.8 to 1.2 V with low-performance sensitivity to input voltage noise shows system resilience to real-world operation. Besides, the bit rate error in the form of standard deviation also reduced from 22 ps to 17 ps. The 11 K operation temperature of the device shows up to 30% degradation in precision, but still on photon coincidences measurements on the scale of ns comparable to [204, 235]. We have shown the capability to calibrate further, linearise using longer and multiple delay lines and add more channels at low logic cost. The FPGA is ideal for implementing a low-cost TDC, with the capabilities to scale up to multiple readout channels.

Constructing a complex system containing within it subsystems capable of operating at very aggressive operating parameters such as multi GHz bandwidth, >50 dB gain high output power amplification, with high-speed digital time discrimination down to 10's of ps would be very challenging in a standard laboratory operating conditions. Constructing such a system to work at mK inside a sealed cryostat, inaccessible for debugging whilst running, is beyond a challenge. However, we have proposed, built and tested such a system that is not only feasible but also has clear advantages over alternative multi-channel high data-rate QKD systems.

5.6.1 Outlook

Future experiments are designed involving simultaneous readout of multiple SNSPD channels on the same TDC to allow for coincidence count measurements. The Intel "Horse Ridge" [236] uses multiplexing of channels, and SNSPD research has shown RSFQ circuits [193] that multiplex signals, minimising the number of channels through the cryostat and therefore reducing the number of amplifiers needed per SNSPD signal. FPGAs have been shown to have de-multiplexing capabilities. Other research has presented coincidence counts implemented on FPGAs; therefore, testing the performance at cryogenic temperatures is a good technological step. It will be necessary to look into the power issues that we would need to overcome when multiple amplifiers and SNSPDs, readout channel and more complex logic push the power budget of the cryostat. To achieve this, designing a PCB with inbuilt low-power amplifiers and larger logic capacity FPGAs may be necessary.

UART readout speeds are at kHz frequencies. Higher speed digital readout, such as an 8b/10b based encoding scheme, would solve this issue. A protocol called 8b/10b is a line code which maps 8-bit strings on to 10-bit strings to achieve DC-balance. This bounds disparity yet provides enough state changes to allow reasonable clock recovery. This means the difference between the counts of '1' and '0' in a string of at least 20 bits is no more than two. This reduces the demand for the lower bandwidth limit of the channel necessary to transfer the signal. Another consideration is changing the digital communication readout system to an Ethernet system or something bespoke.

5.7 Acknowledgements

The author's contributions consisted of mounting and characterising the device and the experimental set-up, designing and performing the experiments, and analysing the data. Andy Hart designed the development board for the MK II and programmed the code on the FPGA. Andy Hart also consulted on the engineering of the TDC on the FPGA. Providing experience in the RF electronics. Andy Hart also provide some of the code used to measure the results, and built the UART to USB converter.

CHAPTER 6

MODELLING CAVITY-ENHANCED SUPER CONDUCTING NANOWIRE SINGLE PHOTON DETECTORS >2μM

Silicon photonics is currently performed dominantly at the 1.55 μm telecommunications wavelength [237]. The indirect bandgap of Si is around 1.2 eV. TPA occurs when two photons of energy over half the bandgap (>E_g/2), being 0.6 eV, promote an electron from the valence to the conduction band [238]. This corresponds to a wavelength of 2.05 μm. Using photons with wavelength higher than 2.05 μm inhibits the TPA affect. TPA lowers the flux limit of light through Si waveguides [239–241], by increasing the attenuation of silicon with the power of these wavelengths. Using light in the Short Wave Infrared Range (SWIR) 2000nm-3000 nm, this effect can be minimised as shown in [242–244]. Quantum photonics for wavelengths longer than 1.55 μm has been impeded by the low-efficiency capabilities available in Single Photon Detectors (SPDs) [245]. Si is a suitable medium that can compliment SPD detection efficiencies in integrated photonics due to its high mode confinement in waveguides [93]. One of the ultimate goals for quantum communications, computing and other applications is to have a fully integrated system on a single device.

These integrated quantum photonics systems consist of photon sources, networks of active and passive integrated optic components and detectors. Si already exists as a technology platform to manipulate light in quantum photonics, and it is integrable with other non-semiconductor devices (CMOS and superconductors) [246, 247]. SNSPDs are one of the best candidates for achieving all the goals mentioned. Their properties of high detection efficiencies [248], low dark count rate [249], low jitter [250] and compatibility with Si photonics [175] make them an ideal technology to exploit.

SNSPDs function at cryogenic temperatures [92]. At these temperatures in Si, the indirect bandgap becomes unavailable as phonon interactions that come from thermal vibrations in the

crystal are of insufficient energy to be part of the promotion of the electron process. The direct bandgap in Si becomes the smallest energy gap to cross [251]. An electron cannot absorb sufficient energy through TPA to cross the direct bandgap with 2 μm light.

The most popular and well-studied superconducting material for SNSPDs is NbN. Its crystalline structure allows for spatial inhomogeneities and defects that can give low fabrication yields [252, 253]. Fabrication yields are also lowered as the longer the nanowire is, the lower the fabrication yields are as the probability of defects impedes the wire from reaching a superconducting state [254]. Therefore future chips fabricated with multiple working NbN detectors would prove difficult for current fabrication techniques. Other superconducting materials such as amorphous materials have boasted higher detection efficiencies and fabrication yield [184] than NbN [174]. This study focuses on four SNSPD material candidates, comparing crystalline (i.e. NbN, NbTiN) to amorphous superconductors (i.e. WSi, MoSi), with WSi being used as the leading example throughout. These four materials as a whole will be referred to as the SNSPD "candidate materials". Recent research into these materials at 1.55 μm shows competitive results compared to the most commercially used material, NbN, in relation to detection efficiencies and fabrication yields [242, 243]. NbN material is included in this study as a comparison.

Single-photon avalanche detectors, photomultiplier tubes and transition edge detectors are used for detecting photons at SWIR with the best efficiency of 1 % [255]. State of the art waveguide integrated SNSPDs at SWIR have efficiencies of 5.5 %, jitter of 150 ps and dead-times of 10 ns [248]. Other non-waveguide integrated SWIR SNSPDs have been demonstrated in 64 x 64-pixel array [256]. However, they do not focus on quantum computational requirements/applications such as high detection efficiency and low-jitter.

This chapter presents simulations and designs for waveguide SNSPDs with optimised performance tailored for photons at SWIR wavelengths.

Firstly, ellipsometry measurements are conducted on the SNSPD material candidates to measure dielectric constants for wavelengths 1 - 2.5 μm. Secondly, a waveguide integrated SNSPD based on previous research is optimised for the 2.1 μm wavelength, with simulations varying geometry of the structures to compensate for the photons' wavelength. The wavelength affects the confinement difference from the silicon and the energy encapsulated in the waveguide centre. Thirdly, we introduce an MMI crosser design to allow nanowires to enter a ring resonator structure while minimising disruption to the fundamental TE mode. This also includes limitations from fabrication tolerances. This leads to the racetrack ring design structure to trap light inside a cavity. The cavity can select specific wavelengths to allow for repeated detection events on non-detected photons. This looks to tackle the practicality problems mentioned in the paper by N. Tyler *et al.* [257]. Lastly, varying waveguide bend geometries with Euler and multimode parameterisations are investigated within the cavity to further reduce bending losses for maximisation of detection efficiencies.

6.1 Ellipsometry measurements of WSi, NbN, NbTiN and MoSi for SWIR

This section uses ellipsometry measurements to estimate the optical dielectric constants of the candidate materials and their thicknesses. This provides the values of refractive index and absorption used through numerical and analytical simulations of SNSPDs for the rest of the chapter. Ellipsometry is a two-step process: measuring the parameters, and fitting a model to the measured data to estimate the optical values.

6.1.1 Ellipsometry

Ellipsometry is an optical technique used to measure thin films' thickness and optical properties that vary with wavelength [258]. By measuring the change in polarisation from the reflection of multiple light beams at different wavelengths and comparing the transmissions, we can construct a model to interpret the samples' optical properties.

A schematic of RC2 Spectroscopic Ellipsometer optics, presented in Figure. 6.1 [259], has been used to support the data obtained by ellipsometry in the visible and NIR (210-2500nm). This is a dual rotating compensate ellipsometer that operates on reflectance data. The spectrometer and source lamps pivot around the sample to collect the specularly reflected light, with a varying incidence angle range from 20° to 90°. The light sources are lamps emitting at different wavelengths' spectra: a 30 W Deuterium lamp, a 20 W Quartz Tungsten Halogen lamp and a 75 W Xenon Arc light source for NIR. The spectrometer contains two diode arrays to detect at different wavelengths: a Si diode array to detect at 200 nm-1100 nm and an InGaAs diode array to the detector from 1100 nm-2500 nm.

Collimated light from the sources first passes through an α- Barium borate (BBO) linear polariser crystal, followed by an achromatic rotating compensator. The compensator is a waveplate that rotates to create a periodic change between linear and elliptical polarisations. The beam then reflects off the sample's surface before entering the compensator, another polariser, and, finally, the spectrometer on the other side of the device. The compensators rotate at different speeds to provide different combinations of input and output polarisations measured.

Si and SOI wafers with extensive measurements and minimal fluctuations indifference are used to calibrate and as a substrate for samples.

Ellipsometry measures the complex reflectance ratio ϕ of the system, which is parameterised by the amplitude Ψ and the phase difference Δ. The amplitude Ψ is broken into the s and p components, where the s component is oscillating perpendicular to the incidence plane. The p component is oscillating in the plane of incidence [258]. To find the maximum difference between these two components, light incidence should be close to the Brewster angle [260]. $\phi = \frac{r_p}{r_s} = tan\Psi e^{i\Delta}$, describes this relationship. This relationship only remains true at angles close

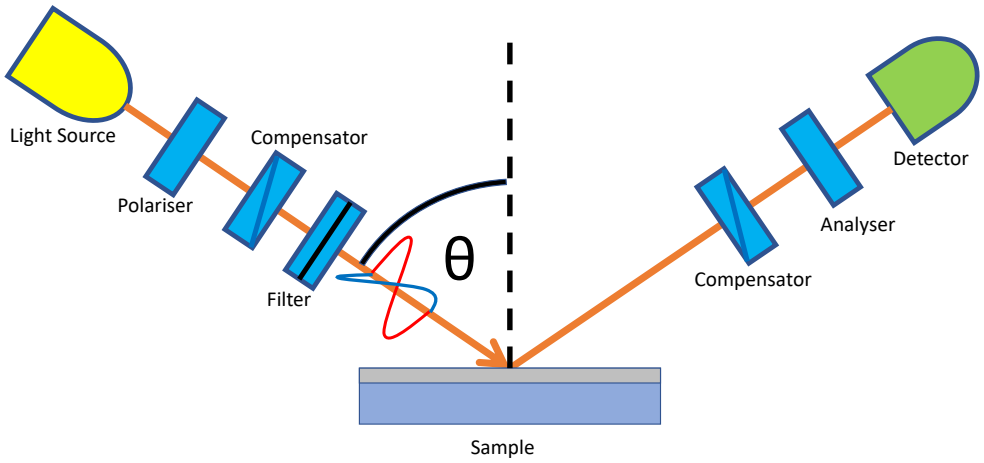

Figure 6.1: Schematic of the dual rotating compensator ellipsometer

to the Brewster angle. Several angles are measured around this angle to provide multiple path length changes through the sample, providing more information than a single measurement.

In this case, absorbing materials' optical constants can be derived using a Basis sum of functions (B-Spline) model. This is possible as the metal is ultra-thin (below 10 nm). B-Spline is an interpolation function that uses polynomials. They are smooth and continuous functions whose minimum features size is defined by the node spacing. The spacing of the nodes determines the fit shape's sensitivity; for metals/absorbing materials, 0.3 eV is the suggested spacing. This allows for a vast range of optical properties to be captured instead of real spectral shapes. B-splines are a double-edged sword as there is no direct relation to the physical parameters.

6.1.2 Elipsometry measurement setup

Ellipsometry measurements of SNSPD candidate materials are measured at wavelengths between 1 μm - 2.5 μm. The dielectric constants of the candidate materials in this study have not been explored in detail for film thicknesses below 10nm. RC2 J Woollam ellipsometer is used, with "CompleteEase" software to extract the thin film samples' optical constants. WSi films are purchased from Photon Spot, NbN & NbTiN are from by StarCryo, and the MoSi is grown by the QET Labs research group at the University of Bristol.

Ψ and Δ are measured at 5°, intervals between 50° and 70°. Using the optical constants data of the refractive index (n) and absorption coefficient (κ) from[261], models are parameterised using B-splines to the wavelengths ranges covered by the previous models. The models are fitted and extrapolated to the wavelength ranges previously beyond the model to include the new measured ranges. The substrate is an SOI that has the same thickness and optical properties across all samples. The SOI wafers the thin films sit on are modelled as Si substrate of infinite

thickness, with a layer of 2000 nm of SiO_2 and a 220 nm Si player on top. These layers are fitted with a J.A. Woollam company provided material models to provide our substrate's optical constants. During the fit, the thickness of Si ranged between 215 and 225 nm, with SiO_2 ranging from 1950 to 2050nm.

The dielectric constants use the difference of reflection and refraction of the two components of polarisation. Near the Brewster angle, the path difference between the light reflecting off the two material layers and angles of the reflectance provides different intensity at different wavelengths. From these values, optical constants or thickness can be extracted. We learn the thickness first by fitting the range we have a model for, and then by knowing the thickness, we extrapolate the model to the longer wavelengths.

There is also an oxide layer on top of the superconducting films in the models, which occurs naturally when the films are exposed to the atmosphere. Roughness on the surface is taken into account and compensated for when calculating the material properties [262]. A final aspect included in the model is "grading material", which allows the SOI layers to have a non-finite boundary layer between them from the diffusion of atoms that occur naturally.

6.1.3 Results

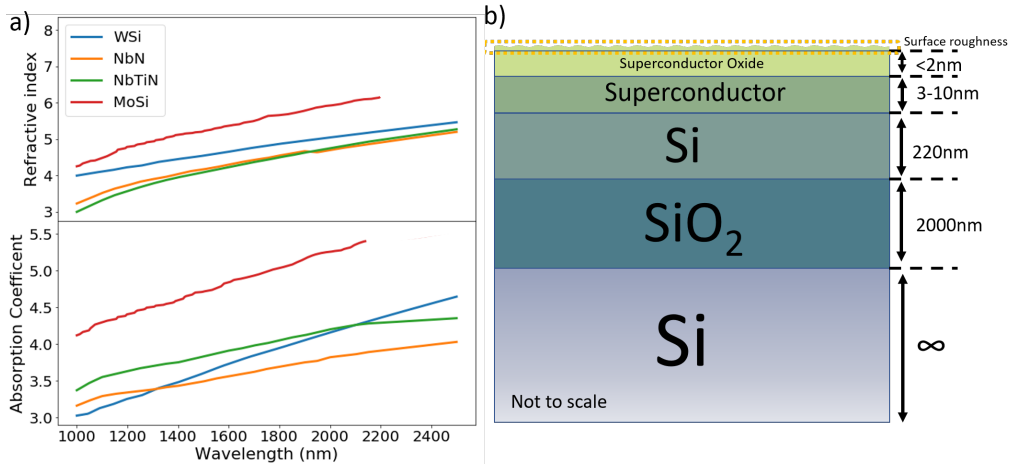

FIGURE 6.2. a) Optical properties of the candidate materials used for SNSPDs measured using ellipsometery and analysed in CompleteEase J Wollam software. The top is the refractive index (n) and the bottom is the absorption values (κ). The thickness of materials is calculated by using the models up to 2.2 μm, these values can be found in Table6.1 (b) Schematic of the layers modelled by ellipsometry of the superconducting thin films.

The optical constants were evaluated with VASE measurements for nominally 7nm-thick WSi film, 100nm-thick MoSi film, 8 nm-thick NbN and a 6nm-thick NbTiN film as presented in Figure.6.2. We note that the MoSi films are 100 nm thick and constitute a bulk material, so

Material	n	n_{eff}	Loss (dB/cm)	Thickness (nm)	Literature
WSi	5.1322 + i4.2567	2.4700 + i0.01067	2773.6	7.68	[264]
NbN	4.80801 + i3.8592	2.4694 + i0.009204	2391.9	8.38	[263]
NbTiN	4.8676 + i4.2588	2.4691 + i0.01041	2705.8	6.00	[261]
MoSi	6.0623 + i5.3522	2.4721 + i0.01500	3899.3	103.33	[263]
Si	3.4490	2.0037	2	≈220	
Si MMI		2.4677			

Table 6.1: Material property constants for the fundamental TE mode. The effective index and the loss is extracted using the Lumerical mode eigensolver with NW dimensions of 100 nm wide, 4 nm thick hair pin nanowire, laying on top of Si 1.67μm wide and 220 nm thick MMI waveguide. The Si value is for a single-mode waveguide of 650 x 220 nm. The refractive index and its imaginary part (i, the absorption) is the value for wavelengths at 2.1 μm. The material thickness is taken using the samples on the J Woollam ellipsometer. The Si refractive index and thickness are taken from the manufactures provided values, while n_{eff} and loss is also calculated from the eigenmode solver.

the surface physics considered during ellipsometry does not apply here, yet the models fitted when considering the material thickness match previous results [263]. NbTiN has a higher absorption coefficient than that of NbN, for all measured wavelengths, this agrees with [261]. This enhancement may be explained due to the Ti in NbTiN. The MoSi film is shown to have a much higher extinction coefficient than the whole spectral range. MoSi has a turning point at 2.2 μm, where the refractive index abruptly deviates. The refractive index values used (at 2.1 μm) in the simulations are taken, before the model's breakdown from [261]. This model is considered to break down as the refractive index does not follow the model's trend. The thickness difference grew, and the thickness taken into consideration for their model are different by at least 90nm. Therefore the MoSi values used (shown in Table.6.1) in the simulations are based on previous research [261].

WSi optical constants have not been previously measured above 2.0 μm. Interestingly it shows a higher gradient in absorption coefficient compared to NbN and NbTiN materials. Therefore at longer wavelengths from 2.1μm, WSi has a greater absorption. This suggests that longer wavelengths could use shorter nanowire wires in integrated waveguide SNSPDs to achieve the same absorption found at shorter wavelengths $\alpha = 4\pi k/\lambda$.

The measured n and κ values are then used in the rest of the simulations produced in this chapter. The values taken at 2.1 μm are shown in Table. 6.1.

6.2 Waveguide-Integrated SNSPD

The first design used for a SWIR Waveguide-Integrated SNSPD is viewed in Figure. 6.3. Superconducting nanowires sit on top of a straight Si waveguide. The waveguide sits on top of a 2 μm thick SiO_2 layer, with air cladding on the top and side walls. This set-up is used for numerical

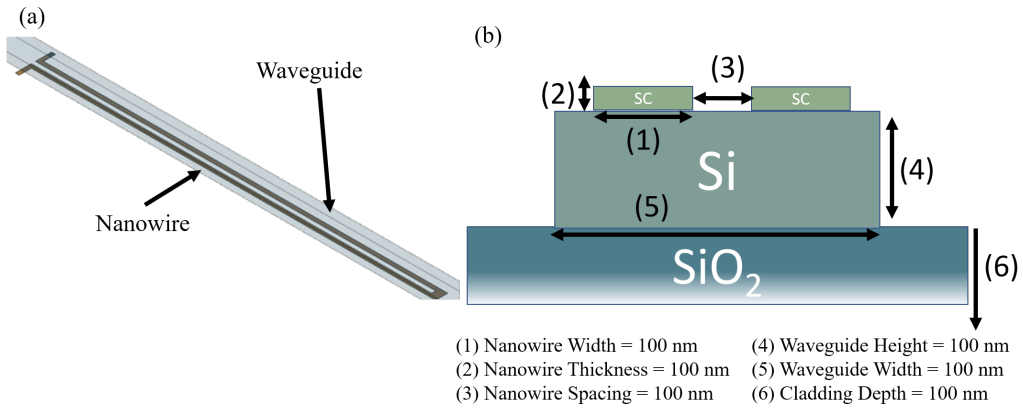

FIGURE 6.3. (a) Schematic of SNSPD length integrated on a Si waveguide, contact pads omitted. (b) Schematic of the dimensions varied in the simulations reported in this chapter. The designs are adapted from highly efficient, successfully fabricated SNSPDs by [183], with adaptations for SWIR modes [243], provided by internal collaborators. SC: SuperConductor

simulations using varFDTD. This is commonly left exposed to air to allow access by RF probes and wire bonds to the contact pads. The waveguide's cross-section is 650 x 220 nm as 650 nm width waveguides are simulated to have a lower loss for 2.1 μm photons [242]. The height is a standard thickness provided by Si foundries. The nanowire is 100 nm wide, 4 nm thick with 100 nm spacing between the two parallel wires [93]. A 100 nm bend in the nanowire is included in numerical simulations but not analytical, and this has a negligible difference in absorption. We used a 10 μm in length nanowire on 650 × 220 nm waveguide. For the following results, these dimensions are the dimensions used in simulations, unless otherwise explicitly stated.

6.2.1 Waveguide integrated SNSPD Simulation Method

The structure in Figure. 6.3 is simulated using an eigenmode solver provided by Lumerical [265]. The varFDTD method is a 2.5D version of the 3D FDTD solver. It allows for the broadband modelling of linear and non-linear phenomena in planar waveguide systems without making any assumptions about an optical axis, device geometry, or materials. The temperature within the numerical simulations area is set to 4 K. A temperature near the materials would operate as SNSPDs. The variance in temperature from 4 K to their actual operating temperature is assumed to be negligible. The candidate materials' optical properties as a function of temperature are not known at the wavelengths used in this study. The simulations are performed with optical properties of Si and SiO_2 at 4 K. Hence; we use the room temperature values from TABLE. 6.1 to perform the simulations. This is done for all future numerical simulations in this chapter. This study observes the changes in absorption of the device from contributions of the nanowire (width, thickness, displacement and length), waveguide (width and thickness) and SiO_2 or air cladding

layer on top. Lastly, the depth of over-etching is swept, where Si not covered by the nanowires is etched away, which may decrease the height of the waveguide. Nanowires during fabrication have a capping resist layer on top to protect from etching that can be modelled as SiO_2. Etching into the SiO_2 below the Si can also occur, but this effect is negligible compared to the waveguide's over-etching.

6.2.2 Results

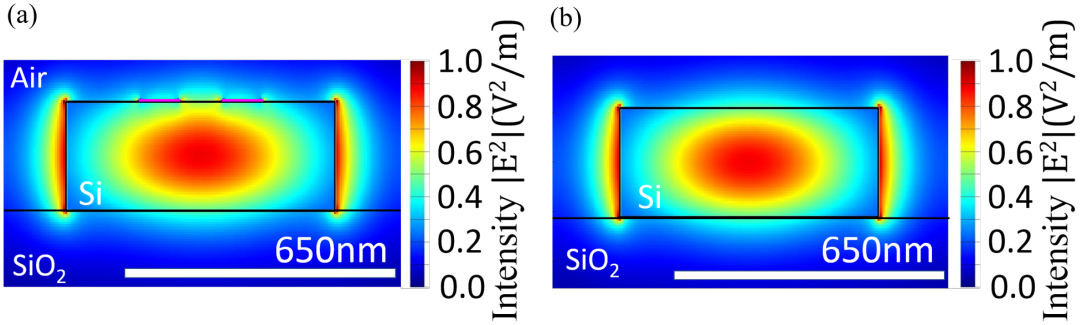

FIGURE 6.4. (a) 650 x 220 nm^2 waveguide with two WSi 100 x 4 nm^2 nanowires on top (in pink), (b) is the same except no nanowires. The fundamental TE polarised electric field mode is seen in both images. The fundamental mode shape between the two images in minimal. The effective index measured in (a) is 2.0186 + i0.0235 and an absorption of 6112.2 dB/cm, compared to (b) with effective index 2.0105 + i3.690E-10 with a loss of 9.59E-5 dB/cm. The scales are the normalised electric field values.

Figure. 6.4 a) show the fundamental quasi-Transverse Electric (TE) polarised mode in a 650 x 220 nm^2 waveguide [53] and with two WSi 100 x 4 nm^2 nanowires on top. The waveguide mode overlaps with the nanowire, allowing for the light to be absorbed by the nanowire. The two comparison results show that the nanowire's presence minimally changes the fundamental mode shaper.

The absorption within the waveguide can be described with the Beer-Lambert law of absorption for a solid [266],

$$I = I_0 e^{-\alpha L} \tag{6.1}$$

where I is intensity, I_0 is initial intensity, α is absorption dB per unit length, and L is the length over the absorption. The Beer-Lambert law is used to describe the absorption of the waveguide integrated nanowire on the light intensity.

The simulated transmissions of the TE mode through Si waveguides with WSi nanowires on top using Lumerical MODE. The values in each of the figures are the gradient of when a linear

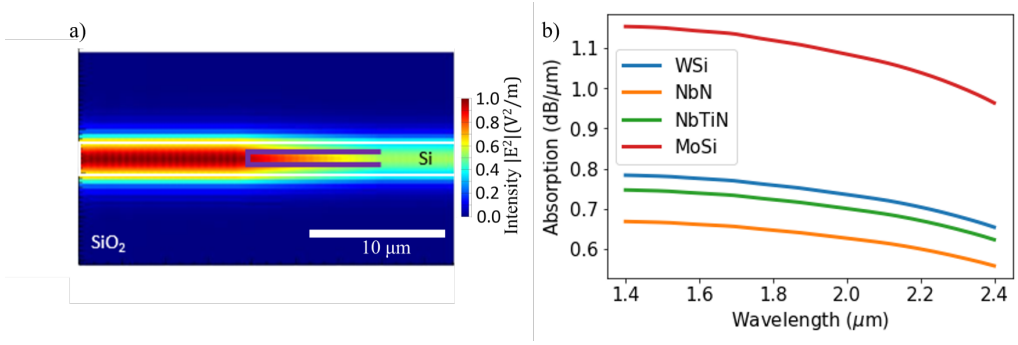

FIGURE 6.5. (a) Top view of the same waveguides in Figure.6.4, with the nanowire 10 μm long and depicted in purple. Light is injected into the waveguide from the left, attention is seen through the detection region. (b) Absorption over length values from FDTD simulations of integrated waveguide detector from (a) over different wavelengths and multiple materials.

fit is applied, giving fabrication sensitivity of absorption for each dimension. The previously mentioned standards in the chapter are used while changing only one parameter in each as stated.

All other variables were kept at constants unless stated otherwise. NW length: 10 μm, etch depth: 0, waveguide width: 650 nm, waveguide height: 220 nm, NW thickness: 4 nm, NW width: 100 nm, NW spacing: 100 nm, photon wavelength: 2.1μm.

The photon model is confined within the waveguide with a constant intensity until the nanowire detection region, where the intensity decreases as shown graphically in Figure. 6.5 a) and numerically in Figures. 6.6, 6.7, 6.8

The measured dielectric constants of all the candidate materials from 1400 to 2400 nm were entered into the varFDTD simulations to measure the wavelength's difference with the nanowires' absorption. The attenuation of the electric field increases inside the waveguide from a WSi nanowire is shown in Figure. 6.5 a). In Figure. 6.5 b), the absorption of the nanowire decreases for longer wavelengths, despite the absorption coefficient for these materials increasing for longer wavelengths. This effect is outweighed by the reduction in evanescent coupling due to relatively bigger changes in optical confinement of the mode. Using $\Delta(\lambda) = n_{si}(\lambda) - n_{SiO2}(\lambda)$ in the ranges 1.4 μm to 2.4 μm we calculate the difference between these effective indices. $\Delta(\lambda)$ values have a larger difference for shorter wavelengths than longer wavelengths. The dominant effect, therefore, is the mode shape of the photon. The shorter the wavelength, the smaller the trailing tail of the evanescence of the mode. This means that the electric field is concentrated within the waveguide along the nanowires. The dominant effect is the sum of the total E-field interacting with the nanowire rather than the material's absorption coefficient.

Simulated absorptions of the TE mode in the nanowire region are investigated while varying the nanowires' geometries and the waveguides for fabrication tolerance effects. Electron Beam

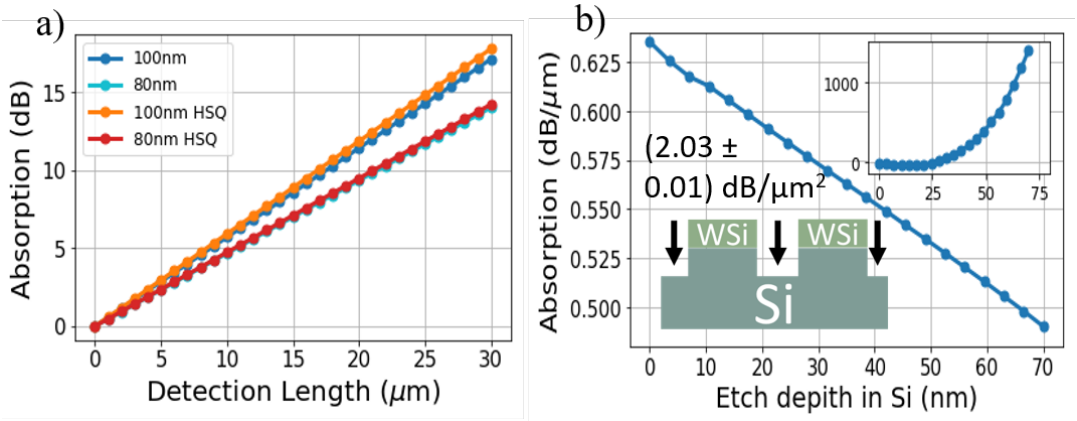

FIGURE 6.6. The simulated transmissions of the TE mode through Si waveguides with WSi nanowires on top using Lumerical MODE. a) Absorption at different width nanowires with an HSQ cladding of 1 μm on top simulated as SiO_2. b) Absorption when varying Si depth between nanowires still on top of the waveguide. The inset is without nanowires.

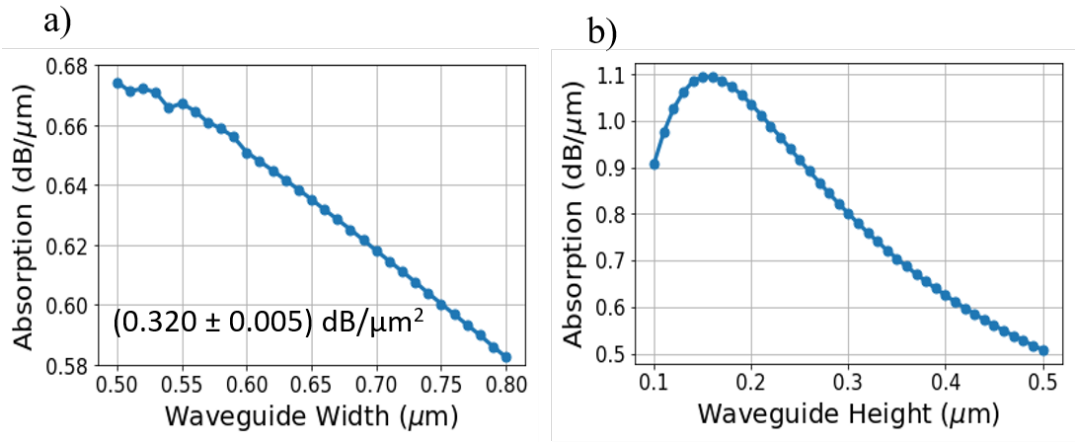

FIGURE 6.7. The simulated transmissions of the TE mode through Si waveguides with WSi nanowires on top using Lumerical MODE. a) and b) are changes in the width and height of the waveguide, respectively.

lithography can reliably provide structures with nanometre resolutions. The geometries of the parameters that are kept constant are stated in Figure.6.6 a). A reduced volume of nanowire decreases the total sum of E-field interacting with superconducting material. This figure shows nanowires of width 80 nm compared to 100 nm. The extra SiO_2 cladding on top and sides slightly increases absorption for both 80 and 100 nm wide nanowires. 1 μm cladding is of sufficient depth for the mode's evanescent tail to reach a small value to have no effects on the mode confinement. The smaller the difference of the refractive index between waveguide and cladding, reduces

the mode confinement. Therefore, the evanescent field of the mode increases, increasing the fundamental mode's size allowing for a higher E-field to overlap with the nanowire.

Figure. 6.6 b) shows the effect of over-etching into a silicon waveguide to absorption due to RIE. A cartoon representation of what this results in can be viewed in the inset. The chosen ranges covered are typical over-etching values for SNSPDs on silicon. This causes pits between and around the nanowires. The nanowires sit on the remains of the Si waveguide. The over-etch depth is given on the x-axis in the Figure. The absorption decreases as the mode confinement occur at greater distances away from the nanowires. The graph in the inset is without nanowires and shows a decrease in transmission as the mode is disturbed due to the higher confinement, which is a secondary effect experienced.

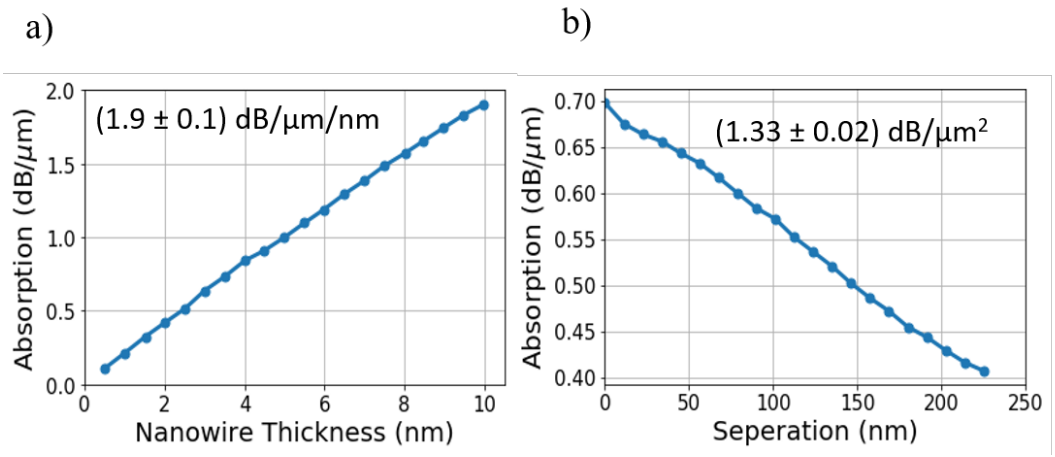

FIGURE 6.8. The simulated transmissions of the TE mode through Si waveguides with WSi a) is the nanowire thickness, and b) the spacing between the two nanowires measured from their inner edges.

Figure.6.7 a) and b) are the results of sweeping waveguide width and height, respectively. The absorption decreases with the increase in width as the mode is allowed to relax, giving less overlap with nanowires. The height shows peak absorption at 200 nm. Taller waveguides display reduced mode overlap. Figure.6.8 a) sweeps the thickness of the nanowire. The thicker the nanowire wire, the greater the absorption coefficient in the effective index. Figure.6.8 b) is the spacing between the two parallel nanowires. The mode intensity is concentrated in the centre of the waveguide. Nanowires further from the centre of the waveguide have reduced absorption. Fabrication tolerances and electrical current crowding limits the minimal size between nanowires. Current crowding on SNSPDs occur in bend regions and limits the critical current of the device. Generally, bends become tighter when the gap between the nanowire is reduced. The effect of current crowding increases with the increased angle gradient of the bend. Another factor is to keep above the fabrication tolerances of the E-beam Lithography as a gap size close to the tolerance range may not fabricate a gap, causing the nanowire to be short and decreasing the

yield of successfully operational devices.

The gradients measured via linear fits provide a fabrication sensitivity of each dimension fluctuation. If all waveguides' geometries are misaligned, the gain in loss inflicted is 0.033 dB/μm, including the nanowire separation, calculated by summing up the errors of all the gradients shown.

6.2.3 Conclusion

In summary, the simulations have shown that WSi nanowires absorb 2.1 μm photons. Ellipsometry measurements provide absorption coefficients as a function of wavelength, indicating the limitations of detection efficiencies by finding the absorption coefficients of the materials as shown in Figure. 6.5 b) [245]. The simulations' results of the absorption are comparable to previous research simulations done on NbN at 1550 nm [175], showing the potential to use WSi to make the first waveguide integrated SNSPD designed for SWIR with 0.61 dB/μm. The ellipsometry measurements are useful guidance for material parameters to be included in future SNSPD design and modelling.

The simulations have been used to estimate the effect fabrication limits have on absorption. The Raith Voyager EBL has tolerances of 8 nm for fabricating nanowires and waveguides. However, the alignment of multiple fabrication layers (such as WSi nanowires on top of Si waveguides) we increase the compensation for tolerances to 10 nm for the simulations.

To reach efficiencies of 99 % (equating to the 20 dB absorption at 30 μm long nanowires) comes with drawbacks—the device's footprint increases, reducing the number of detectors on a device. Larger devices increase the probability of fabrication defects, reducing the yield. Longer nanowires have a larger surface area, increasing the dark count rate and the detection jitter. Absorption efficiencies are at their highest when the nanowires are as close to the centre of the confined mode to maximise overlap.

6.3 Multi-mode Interference region for SNSPDs

The nanowire's material absorption can be engineered to offset the decrease confinement properties at longer wavelengths to maintain an overall even-absorption profile over a large bandwidth. Thicker and broader nanowires increase the amount of photon energy needed to break the superconductivity in the wire. Therefore having a thinner nanowire is more desirable for lower energy photons. One cavity structure that is readily used in quantum photonics are ring resonators. Following from [257] simulations of ring cavity structures with superconducting nanowires have shown potential higher detection efficiencies for shorter nanowire geometries. Here we proceed to build upon this use of a single crossing arm design in a ring cavity detector for 2.1 μm.

The paper by N. Tyler [257] does not address the nanowires injection into the ring cavity while maintaining the cavity.

Currently, waveguide integrated SNSPDs are designed such that photons travel through the waveguide, first interacting with the nanowire bend, then the two straight parallel wires, and lastly, where the nanowires taper out to their associated contact pads [74]. If the nanowires do not absorb the photon in the detection region, the photon can no longer be detected and is lost [267]. A path for the nanowires needs to be available from the contact pads to the detection region. The nanowires run on top of Si waveguides for ease of fabrication and connect to contact pads that require free access.

This section discusses a way to overcome the loss of a photon via different waveguide geometries. MMI crossers allow photons travelling in perpendicular directions to cross paths, with limited loss and interference, by relaxing the mode confinement during the crossing point [74, 268]. The MMI allows for a single-mode waveguide to taper into a wider waveguide where multiple modes can exist, as explained in Chapter 2. Both ends of the MMI are used for the photon to travel along, while the other channel acts as a path for the nanowires into the MMI structure centre as shown in Figure. 6.9 a). A single waveguide can be used as a conduit for the nanowires from the circuit. Therefore an intersection of three waveguides is also investigated. For clarity, the waveguide crossing arm is named the nanowire transfer arm. Furthermore, this waveguide does not require tapering as no mode is projected towards the crossing waveguide.

6.3.1 Design and Simulation of MMI region SNSPD

This study examines an SNSPD in a Multimode interference (MMI) waveguide crossing as previously studied in [74]. This structure has been chosen to allow for the insertion and exiting of nanowires for detection while minimising loss due to the structure of the waveguides confining. The proposed design and variables were chosen to investigate for the simulations shown in Figure. 6.9 a).

All of this sits on SOI with the same configurations as detailed in the previous section, with an air (simulated vacuum) being the top and side cladding. The design is optimised for the fundamental TE polarised mode. The eigenmode solver provides the refractive indices used for the Si (3.449) and the SiO_2 (1.43722) for 2.1 μm. The SNSPD consists of a nanowire, 4 nm thick, 100 nm wide parallel wires, separated by 100 nm spacing as before. Differences occur by the meandering bend around at either end to form two U-shapes and the centre of the top nanowires, being the exit path of the nanowire to contact pads as shown in Figure. 6.9 (a). The detection length (the distance between the two hairpin bends as shown in Figure. 6.9) of the loop is the overall length of this wire (except the arms to the transfer waveguide). The width of the transfer arm (Ch2) is investigated, while the width of Ch1 is kept constant at 650 nm, using the results of the previous section.

The SNSPD's nanowire detection section refers to the length of the region that the photon will be interacting with the nanowire. The nanowire is looped around in this area. Therefore it is twice as long as the detection region plus the two 100 nm bends for the spacing, minus the

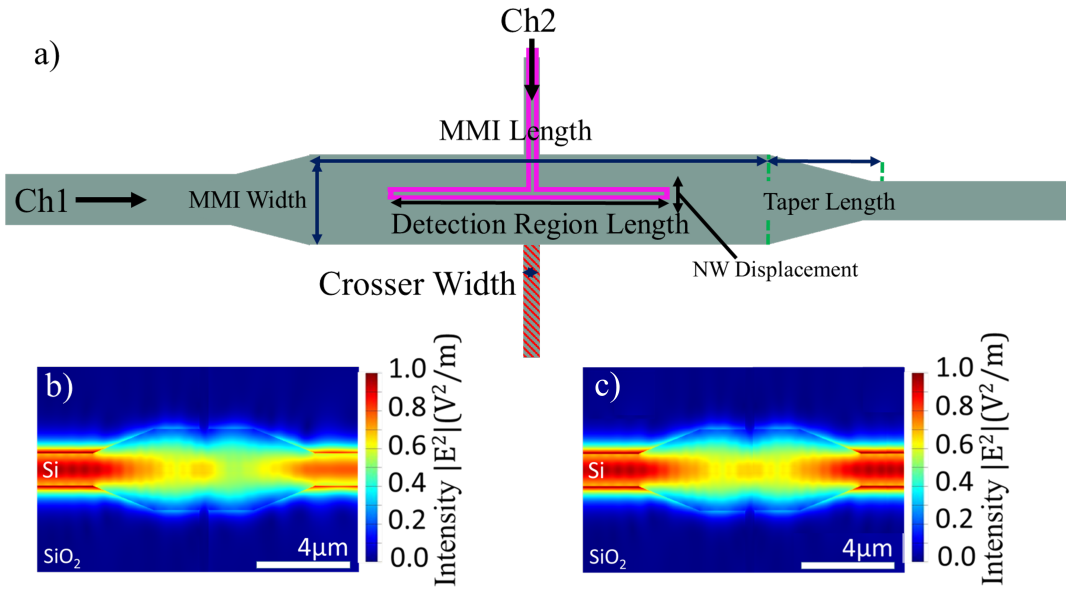

FIGURE 6.9. MMI crosser region with the nanowire placed in the centre. a) Demonstrates the variables adjusted to optimise the absorption through the detection region via just the nanowire and minimising the photon from other loss methods by the Si. Ch1 is the path of the photon, and Ch2 is the path from the contact pads. b) The electric-field mode through the MMI crosser, with light injected from the left, showing a clear absorption of the nanowire as intensity decreases. A 4 μm long nanowire is placed in the centre but is omitted for clarity. c) Is the same figure as b), but with no nanowire on top.

100 nm gap in the arms. The refractive index of the WSi nanowires used is in TABLE.6.1. A single-mode with a waveguide crosser would have scattering losses at the intersection.

6.3.2 Results

The reflection transmission from a 4 μm nanowire is 0.045%; henceforth, this is considered negligible and therefore omitted from further consideration. The MMI waveguide's effective indices with and without the different nanowire candidate materials on top are measured using the eigenmode solver and found in TABLE.6.1. The loss from a single-mode Si straight waveguide is considered to be around 2 dB/cm [269], therefore negligible at the distances considered in these simulations (<20 μm) and compared to losses from the nanowire region. A 4 μm nanowire was chosen after initial simulations to give a balance between short length, to keep fabrication yield high and Q factor low, but also having the wire long enough to ensure that during each pass through this component, the dominant loss mechanism is via absorption of the photon by the nanowire.

To find the minimal loss through this MMI region, the nanowire was omitted for most of the

simulations to find the crosser's optimal geometric properties to maximise transmission through the region. Hence we account loss only to the nanowire when added later.

Simulated transmissions through a Si MMI crosser with and without WSi nanowires on top using varFDTD. The geometries are as previously described unless stated otherwise. Unless stated otherwise the dimensions of the MMI crosser are: Width: 1.67 μm, Length 4.25 μm, taper length: 2.7 μm, transfer arm width: 400 nm

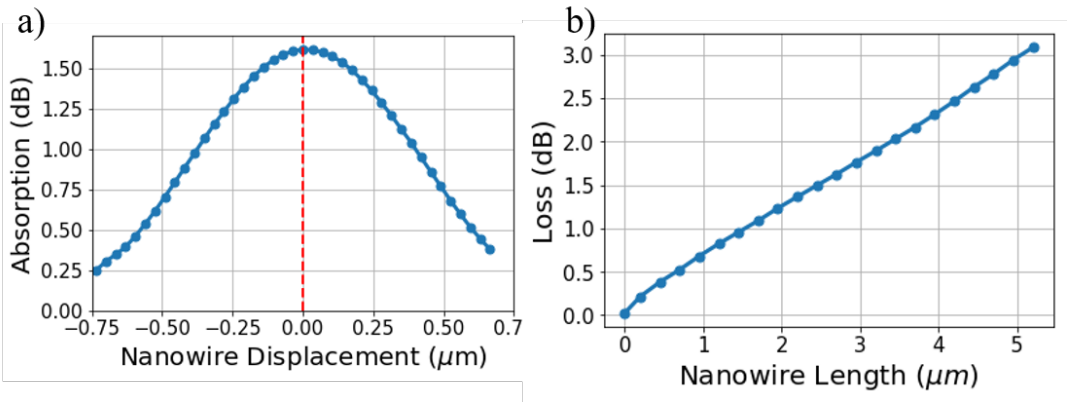

FIGURE 6.10. Simulated transmissions through a Si MMI crosser with and without WSi nanowires on top using varFDTD. Plots a), b) have nanowires on top of the waveguide in their simulations. a) Provides the absorption dependence on the displacement of the nanowire wires from the MMI waveguide region centre, halfway along the MMI width. b) Shows the absorption within the MMI region, with varying lengths of nanowire placed in the centre, lengthening from the centre outwards along the MMI length. The detection area length is half the length of the nanowire.

Figure.6.10 a) shows the absorption by the nanowires dependent on their displacement from the centre line, moving along the MMI waveguide width. The maximum absorption occurs when the two paths of the nanowire are evenly distanced away from the centre line of the MMI., the centre line of the MMI being the line of the photon path. Initial predictions expected two maximum points. We expected that if either long dimension of the nanowire is placed in the MMI mid-line, maximum absorption would occur at this displacement. This result suggests that the nanowire placement has a tolerance of hundreds of nanometers in either direction. Electron Beam Lithography (EBL) is a fabrication tool that scans a focused beam of electrons to draw custom shapes onto a surface covered with an electron-sensitive film called a resist. This has nanoscale precision, and multiple numbers of EBL steps can create the complex photonic structures designed here. EBL errors in the placement of nanowires on waveguides are on the scale of tens of nanometers. Hence, fabrication tolerance is not an issue when considering this parameter. This result is for photons of wavelength 2.1 μm. At wavelengths shorter than this, the initial prediction of two maximums on the figure may occur. As discussed earlier, the reason

is that the evanescence of the modes is confined to a small area at shorter wavelengths.

All MMI structure simulations with a nanowire use a 4 μm detection length unless stated otherwise. Here we show investigations in exploring the length of different nanowires in this region. Figure.6.10 b) shows the absorption of the nanowire within the MMI region. Optimised transmission for the MMI will allow the primary absorption mechanism to be dominated by the presence of a nanowire, as the E-field intensity gradient decreases exponentially with the long edges of the nanowire overlapping a small intensity part of the field.

The crossers arm lengths are set at 400nm width, with one (loss = 0.0284 dB) and two (loss = 0.0152 dB) arms have a negligible difference in losses. The loss is slightly lower for two arms as the mode is still confined in the centre. While one arm can shift the arm's mode for that shorter distance, the modes experience the MMI arm as the confinement mechanism. One arm can be chosen to simplify fabrication, but the simulations will use two arms for simplification.

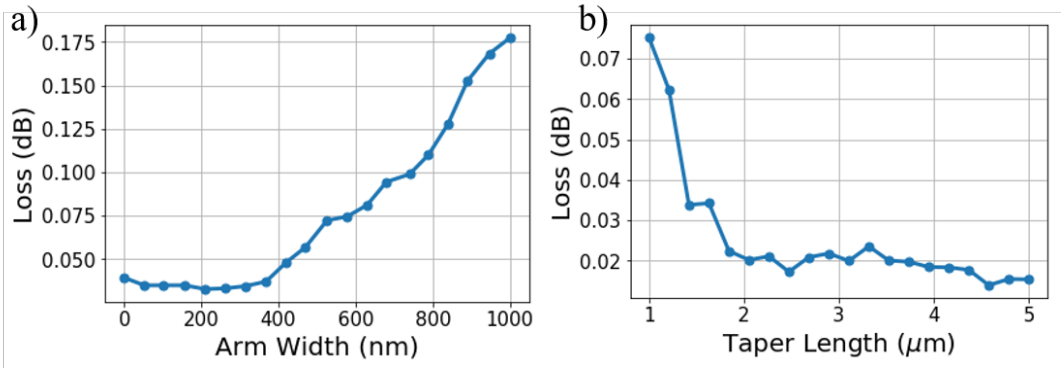

FIGURE 6.11. Simulated transmissions through a Si MMI crosser with and without WSi nanowires on top using varFDTD. The geometries are as previously described unless stated otherwise. a) Shows loss through crosser increase with the width of the NW transfer arm. This is simulated without nanowires. b) Shows loss against the taper region's length, from the single-mode to multimode waveguide. The angle changes with the length to meet the multimode and single-mode. The width of the MMI region is kept constant.

The losses are calculated as transmission through the MMI, with one and two arms intersecting, as shown in Figure.6.9(a). The arm width has no difference in transmission between 400 nm wide. In Figure.6.11 a), the 400 nm width is chosen to host the nanowires transfer arm. We also simulated how the length of the transfer arm affects loss. The length is measured from the edge of the waveguide. When the transfer arm has a length greater than 400 nm there is no change in loss. Allowing the transfer arm to be as short as possible will also shorten the nanowire's length before it expands out into contact pads. Minimising the nanowire's length within the transfer arm will minimise accidental photon detection, reducing dark counts.

In Figure.6.11 b), we simulate different lengths of the taper region (the region between the MMI waveguide and single-mode waveguide). We found that at 2.7 μm, there is no further

reduction in the loss. The adiabatic taper and the MMI length both contribute to the position the E-field maximas. This point is also chosen as a concentration of the mode occurs in the centre of the MMI region displayed in Figure.6.9 (b). A longer taper of lengths described in Eq.2.44 would produce an adiabatic change to the mode with no concentration in the centre of the MMI region, reducing the overall absorption potential by nanowires.

Lastly, in Figure.6.12 a) and b), we sweep across the MMI region's length and width. The loss oscillates from multiple modes forming in the MMI region. Multiple points of maximum intensity occur from self-imaging. A shortened MMI region will reduce the scatter loss, therefore to optimise, we chose to design our MMI crosser at the first maxima point. The effective index change from nanowire's introduction has an immeasurable effect on disrupting the MMI structure's modes. This can be seen as the peaks in the figures occur at the same MMI lengths. We analyse the MMI width in Figure.6.12 b), in which we can see a sharp loss from 3 μm onwards. At the inspection of the inset in Figure.6.12 b), we can see minima occur at 1.67 μm. A 4 μm long WSi nanowire is added to the simulation to see the absorption through the detection region. This region's absorption is 0.4 dB/μm, a third lower than the single-mode SWIR waveguide integrated nanowire of 0.61dB/μm. Hence, a longer detection region or multiple interactions with the detection region achieve the same absorption. The fundamental TE in the MMI is spread out much more broadly in space, which reduces the amplitude in the centre relative to the single-mode 650nm wide waveguide.

A multimode waveguide is tapered out from a single-mode waveguide, with 400 nm wide waveguides protruding out of the MMI region, perpendicular to the photon path. The single-mode waveguide is 650 × 220 nm. The MMI region has a 1.67 μm wide spacing while maintaining the same 220 nm height. The length of the taper region is 2.7 μm.

The effective indices for the measured cross-sections of the MMI regions with the nanowires for each material are shown in Table.6.1. The results demonstrate that the MMI region's effective index with nanowires on top undergoes a relatively small change depending on the material. The change in the effective index from changing these dimensions is also shown to be small compared to the effective index changes that can be introduced from fabrication imperfections such as over-etching, rough sidewalls, and errors in dimensions.

The MMI self-imaging at the centre of the multimode region focuses the light and avoids losses that occur from diffraction when the light reaches the crossing. This mode is set up to minimise E-field bleed into the transfer arm. The nanowire's lengths, which lay along the transfer arm and project into the MMI region and are perpendicular to the path of the photon, have little interaction with the photon. This was seen during the analysis of the results when looking at the E-field, and the absorption results when this section of the nanowire is removed from simulations.

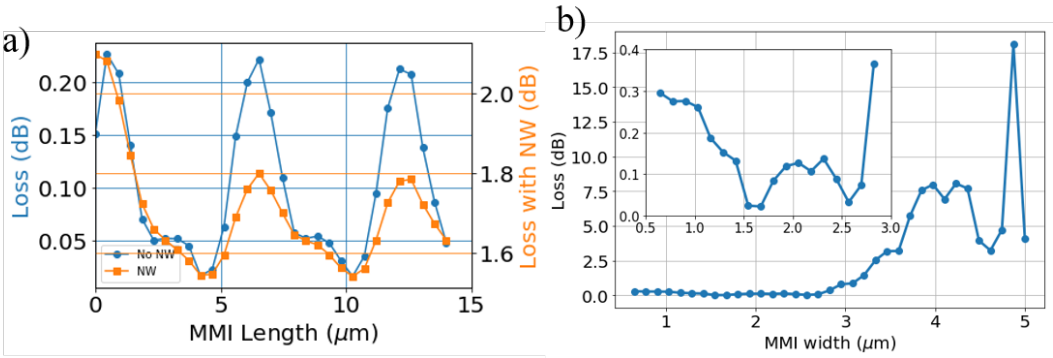

FIGURE 6.12. Simulated transmissions through a Si MMI crosser with and without WSi nanowires on top using varFDTD. The geometries are as previously described unless stated otherwise. Plots a) has nanowires on top of the waveguide in their simulations. a) Presents the MMI regions' length with and without a nanowire, showing how the change in effective refractive index can shift the maximum mode. The length of the nanowire used is 4 μm. The decrease in the loss over increased lengths is not considerable. b) Shows the MMI region's width sweep and inset zooms into the trend at lower values.

6.3.3 Conclusion

The dimensions chosen for the MMI crosser are used inside the RCD to allow a nanowire to enter the cavity. The MMI shows a minimal loss but maximum absorption contribution from a nanowire. The results are comparable to studies in [74, 270, 271]. The dimensions used for the MMI crosser in the RCD is in 6.2.

MMI (μm)			Transfer Arm (nm)		Nanowire	
Width	Length	Taper Length	Width	Length	Offset (nm)	Length (μm)
1.67	4.25	2.6	400	400	0	4

Table 6.2: The dimensions of the MMI region used throughout the rest of the chapters results. The nanowire offset is the displacement of the nanowire from the centre of the waveguide.

The structure is placed opposite the coupling region within the racetrack cavity, as shown in the next section.

6.4 Ring Resonator Detectors

This section examines an SNSPD in a cavity for SWIR and an MMI crosser for nanowire insertion. A ring resonator structure is chosen because of its well-established fabrication methods, well-understood theory and wavelength filtering potential. A cavity is provided by the ring geometries critically coupling photons of specific wavelength values. The proposed Racetrack Cavity Detector

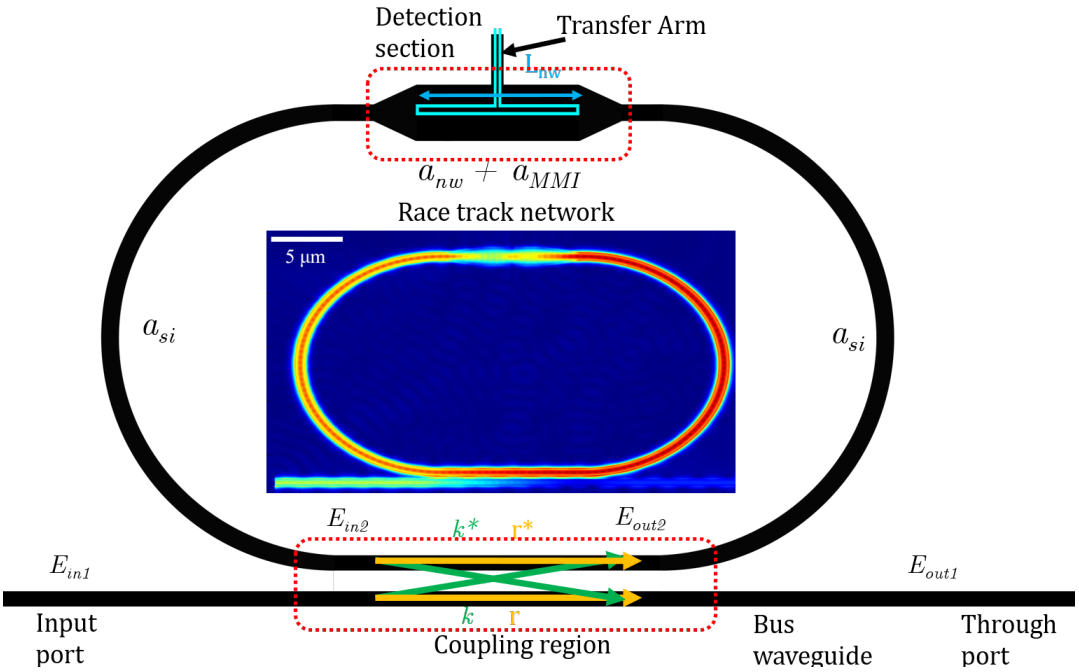

FIGURE 6.13. Schematic of the racetrack detector, broken into four different sections; bus waveguide, racetrack, coupling region and finally, the detection section. Light is inserted into the bus waveguide via E_{in1} and leaves via E_{out1}. The light coupled out of the bus into the ring is E_{out2}, while light into the bus from the ring is E_{in2}. k and r are the coupling and reflection coefficients from bus to ring, with their complex components k* and r* being the coefficients for the ring to bus coupling. The complex components are equal to their real counterparts. a is the Si, MMI's absorption coefficient, and the nanowire L_{nw} is the length of the detection section. The racetrack's E-mode is in the centre, with light coupling from the bus into the ring and small absorption at the detection section. NW is in light blue.

(RCD) design can be viewed in Figure.6.13. It consists of a bus waveguide coupling to a waveguide racetrack resonator containing an MMI region with an integrated SNSPD. The detection efficiency reaches its peak at critical coupling [272]. The dominating effect is nanowire absorption, giving a theoretically near-unity detection at resonance frequencies.

The ring is constructed from Si 650 nm x 220 nm cross-section waveguides on 2 μm thick SiO_2 slab. The design is optimised for the fundamental TE polarisation mode. This is the only mode considered. All the refractive indices used are taken from the ellipsometry and eigenmode solvers values, in Table.6.1, with 4 nm thick SNSPD and 100 nm wide parallel wires with 100 nm separation. The wavelength range is swept to find resonances at wavelengths closest to 2.1μm, and assumed refractive indices values remain unchanged. The RCD has a racetrack structure that uses a directional coupler as its coupling mechanism [273]. The structure is studied both analytically as well as numerically, and these results are compared.

The analytical model is implemented using Python to estimate the efficiencies of the detector

cavity. Both the numerical and analytical methods use the schematic Figure.6.13. First, concepts of Ring Resonators theory are presented in Chapter.2 Sec. 2.2.5.4. Here we continue the explanation of the theory specific to this section. Light is injected into the input port E_{in1}, where it reaches the coupling region where a fraction of the light can couple into the ring E_{out2}, or continue along the bus waveguide E_{out1}. The light after one round trip after passing through the detector region E_{in2} can be injected back into the bus waveguide or maintained inside the ring cavity.

The output light through the port can be expressed by the following:

$$E_{out1}(\lambda) = \left(\frac{r - \alpha e^{i\theta(\lambda)}}{1 - r\alpha e^{i\theta(\lambda)}}\right) E_{in1} = \left(\frac{r - \alpha e^{i\theta(\lambda)}}{1 - r\alpha e^{i\theta(\lambda)}}\right) E_0 e^{-0.5(\frac{2\pi c}{\lambda\sigma})^2} \tag{6.2}$$

For simplicity we normalise the electric field injected amplitude E_0 into the bus waveguide to 1. $\sigma = FWHM/(2\sqrt{2ln2})$, a CW pulse is used as the input and modelled with a Gaussian distribution. α is the transmission coefficient that is described by $\alpha = 10^{a_{nw}L_{nw} + a_{si}L_{si}}$, with a_{nw} and a_{si} as the transmission coefficients with units dB per unit length, inside the detector region and the rest of the ring, respectively. L_{nw} is the length of the nanowire section and L is the length of the entire ring. L_{si} = L - L_{nw} is the length of the Si waveguide of the rest of the racetrack cavity, minus the detection region. The phase has expression $\theta(\lambda) = 2\pi(n_{effsi}(L - L_{nw}) + n_{effnw}L_{nw})/\lambda$. Where n_{effsi} is the scatter probability inside the silicon and n_{effnw} is the scattering probability for the nanowire region. $E_{out2} = rE_{in1} - \kappa^* E_{out1}$ is the light that exits the racetrack. The transmission T is calculated by comparing the input to the output power in the bus waveguide and is described by:

$$T = \left(\frac{E_{out}(\lambda)}{E_{in}(\lambda)}\right)^2 = \left(\frac{r - \alpha e^{i\theta(\lambda)}}{1 - r\alpha e^{i\theta(\lambda)}}\right)^2. \tag{6.3}$$

1-T is the total probability of absorption by the detector.

The efficiency is maximised when the light leaving the cavity E_{in2} is minimised, and E_{out2} is maximised. This occurs when the system is critically coupled (r=α) and phase-matched ($e^{i\theta(\lambda)}$)=1, which is represented by η_{cc} and η_{pm} respectively and η_{pmcc} when both occur. The following equations describe these;

$$\eta_{pm,cc} = \frac{(1 - \eta_{si,beg})\eta_{nw}}{1 - (1 - \eta_{nw})(1 - \eta_{si})}, \tag{6.4}$$

$$\eta_{pm} = \left(1 - \left(\frac{r - \alpha}{1 - r\alpha}\right)^2\right)\eta_{pm,cc}, \tag{6.5}$$

$$\eta_{cc} = \left(1 - \left(\frac{\alpha(1 - e^{i\theta(\lambda_{CW})}}{(1 - \alpha^2 e^{i\theta(\lambda_{CW})}}\right)^2\right)\eta_{pm,cc}. \tag{6.6}$$

$\eta_{si,beg}$, η_{nw} and η_{si} are the scattering probability in the Si waveguide between first coupling into the ring until the detection section and the silicon for one round trip. A 100% quantum efficiency of the nanowires is assumed, so the absorption probabilities equal the detection efficiency.

Trapping a photon inside a cavity with no detection event reduces the timing resolution. Shorter nanowires absorb less, allowing the photon to remain in the cavity longer, taking more trips before detection. Jitter is a common measure of timing resolution, usually calculated by the FWHM of the laser pulse. Jitter can also be determined at the voltage pulse from the SNSPD. The jitter that the cavity structure can control is the geometrical jitter; that is, the jitter formed from the cavity's dimensions and shape trapping the photon. Jitter, in this case, will be the lifetime of the photon inside the ring cavity until there is a 95% chance the nanowires absorb it. At the time of writing, the electronics readout measures are the limiting factor on timing resolution. Comparing the increased jitter to electrical resolution is the baseline chosen to overcome. Setting the number of round trips until the 95% chance the photon is absorbed is the threshold set, as currently, SNSPDs do not perform better than 93% efficiency. By using the group index and lengths within the cavity network, the following equations describe the timing jitter:

$$t_{jitter} = \frac{R}{c} \sum_{x=Si}^{det} L_x n_{g,x} = \frac{R}{c} \left(L_{Si} n_{g,si} + L_{det} n_{g,det} \right), \tag{6.7}$$

where $n_{g,si}$ and $n_{g,det}$ are the group indices of the silicon ring and the detection section respectively. R is the number of round trips taken until 95% absorption (α_{eff} = 0.95), which is expressed using:

$$R > \frac{ln(1-\alpha_{eff})}{ln(\eta_{nw})}. \tag{6.8}$$

For the time the photon takes to complete a round trip, we use the photon's speed at different sections of the ring that are summed. This is multiplied by the number of nanowire photon interactions are needed to give a 95% absorption probability.

6.4.1 Design and Simulations

Previous models presented in this chapter, including research by [225, 269] show that photons can be captured and absorbed by nanowires. A racetrack design over ring design allows for the insertion of an MMI crosser into the racetrack without impacting ease of fabrication and simulations, allowing for a larger coupling region between bus and ring to increase fabrication tolerances. This also allows space for nanowire placement. The output transmission is dependent on r and k values, as phase difference is taken into account as the mechanism coupling the racetrack cavity to the bus waveguide is the same as a directional coupler covered in Chapter.2.

They already use an interface that has been heavily researched [273–275] of a bus waveguide coupling photons in the ring. Here we also use the NbTiN, NbN [276] and MoSi materials and the WSi in the simulations to compare performance. Properties from TABLE. 6.1 are used.

The length of the cavity is determined by the length of the coupling region (10μm) times 2, for both sides and the radius of the bends is 10μm [173]. The length of the ring is the bend length $L_{bend} = \pi 10\mu$m plus the straight waveguides (20), giving 83μm in length [257].

We use the MMI structure presented in the last section as the structure for the detection area. This area is known from now on as the detection area. Nanowires above this length have been simulated before. It was concluded that short nanowires ($\approx 1\mu m$) are desirable, as they increase yields and decrease intrinsic jitter and the design of the rings giving narrower filters bands for increase filtering. The analytical simulations produce results for the 4μm long detection region. These cases are shown for completeness, but the model degrades beyond this point.

6.4.2 Analytical Results

Figure.6.14 presents the detection efficiency response during critical coupling for a CW input for the four candidate materials which is calculated using Eq.6.6. As we can see in the figure.6.14 a), critical coupling occurs at a specific wavelength. There are multiple wavelengths at which critical coupling can occur but are omitted in this figure to present the spectrum that shows critical coupling and is closet to 2.1 μm. We can see that the length of the nanowire defines the FWHM. The FWHM also depends on the material, as we see can see for the same nanowire lengths, the difference in FWHM being shown in Figure.6.14 b). These effects can be seen in Eq.6.6: as the nanowire length increases, n_{nw} increases.

We can also see that this equation is periodic, depending on the phase of the incoming wave $e^{i\theta(\lambda_{CW})}$. Therefore hand-picking the length depending on material is necessary. The shorter the nanowires, the smaller the FWHM of the bandwidth, making the detector desirable for single-photon sensitive spectrometer applications and tailoring filtering with nanowire material length. The peak wavelength is dependent on the round trip time of the photon. The ring length is kept constant in this test; hence, an effective index is the only metric determining photon speed. The peak wavelength does not measurably shift as the detection area's effective index between materials and wavelengths is small.

Figure.6.15(a) and (b) shows the phase-matched detection efficiency using Eq.6.5 for different coupler transmissivity, over several different nanowire lengths. Near unity efficiency can be achieved for shorter nanowires inside the cavity, then for nanowires without a cavity as shown in ref [257]. This is achieved through multiple path interactions of the photon with the nanowire, giving a longer absorption time. For a smaller coupler transmissivity, shorter nanowires are desirable to achieve near-unity efficiencies. For each nanowire length, there is an optimal coupler transmissivity to achieve their maximum efficiency. This satisfies the critical coupling condition (r=α) [272].

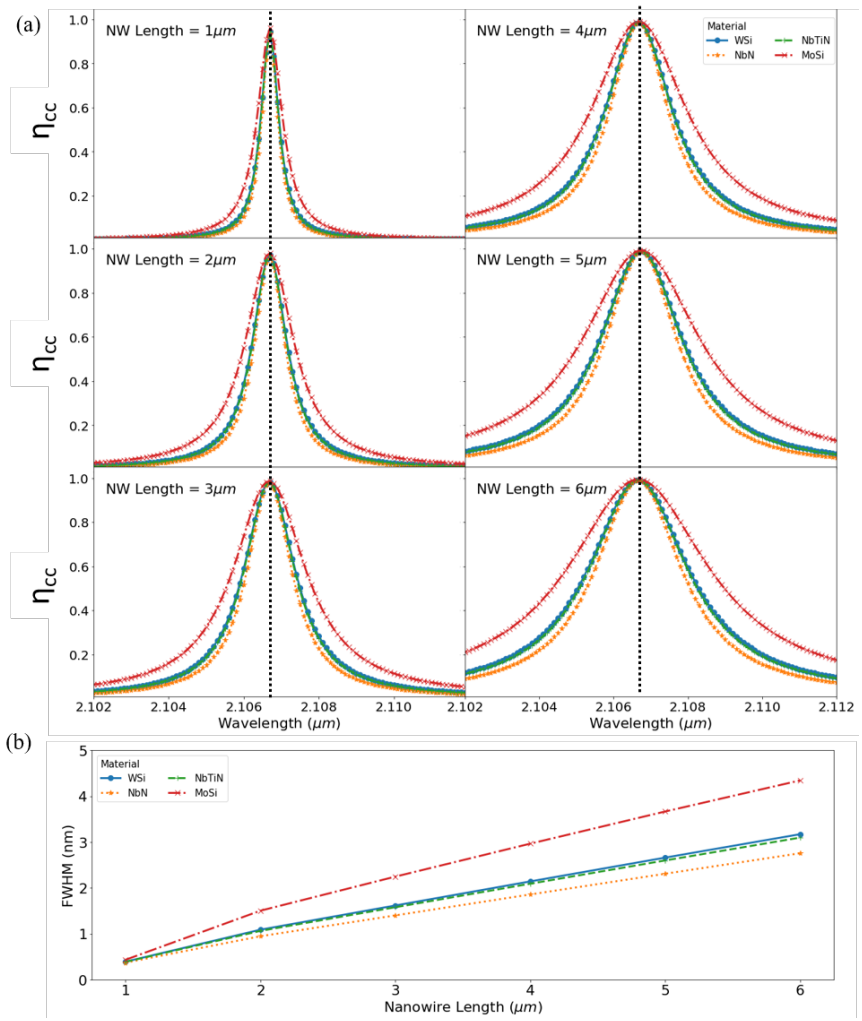

FIGURE 6.14. (a) Efficiency of absorption for different lengths of nanowire, swept over a range of wavelengths around 2.1μm. (b) FWHM of the peaks presented in (a). Ring length 83 μm for all candidate materials. The dimensions of MMI found in Table.6.2

In the insets critically coupled and phase-matched ring detectors display, longer nanowires give higher efficiencies as they provide more absorption probabilities ratio than the waveguide scatter but saturates around $2\mu m$. When changing the effective index of the detection region by swapping out SNSPD materials, minor differences can be seen in inefficiencies, as shown in Figure.6.15. The curves are shown in comparison to a nanowire region on a straight waveguide with the same dimensions but without a cavity. Detection efficiencies near to unity can be achieved with shorter nanowires than for a nanowire region along a straight waveguide with no cavity. These high efficiencies can be reached from the increased interaction time between the photon and the nanowires.

Detection efficiencies for a critically coupled and phase-matched detector's efficiency decrease

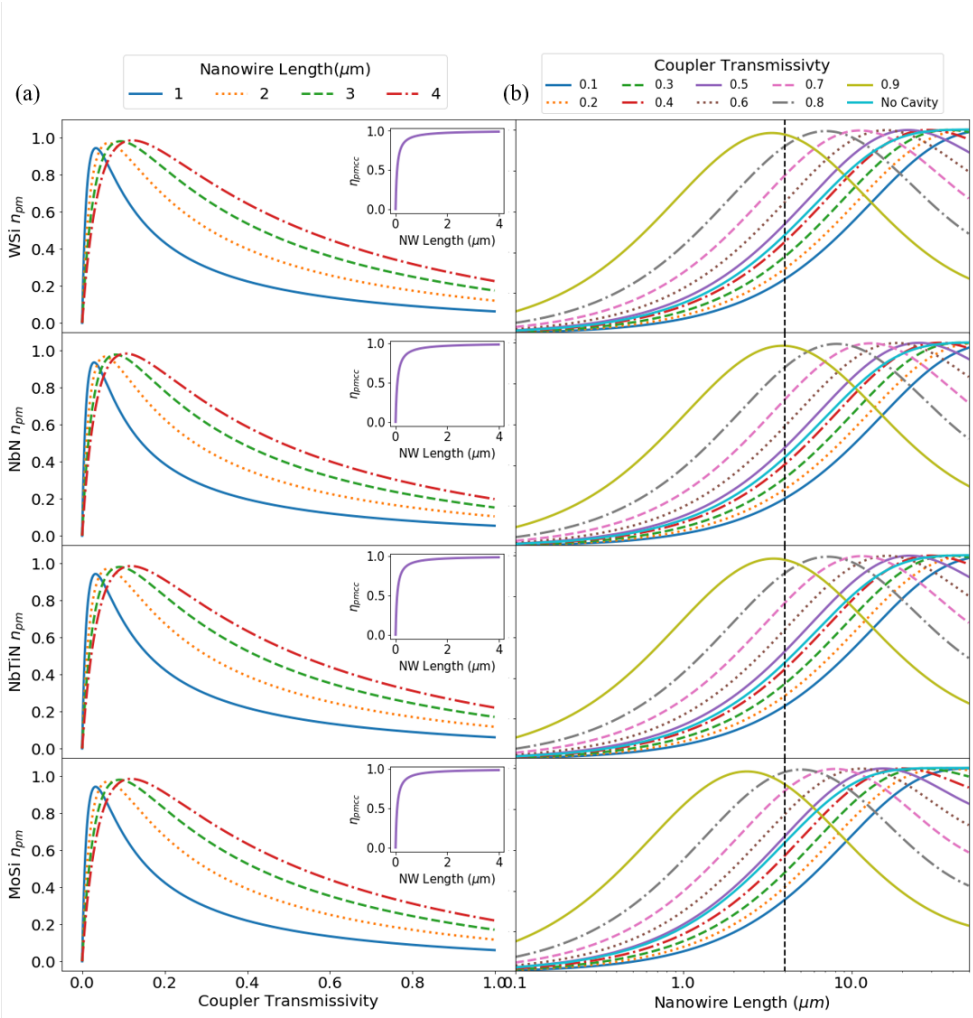

FIGURE 6.15. Detection efficiencies in the phase-matched regime. Going down, WSi, NbN, NbTiN and MoSi. (a) Phase matched Efficiencies as a function of coupler transmissivity. Insert: Efficiencies for different nanowire lengths, with coupler transmissivities optimised for critical coupling and phase matching [272]. (b) The efficiency with varying nanowire length, with different lines representing different coupling transmissivities in the coupling region. The light blue line represents the absorption with no cavity of the same nanowire on top of 650 × 220nm cross-section waveguide. The points of maxima can be found in Figure.6.16

with increased waveguide loss as presented in Figure.6.16 (a), for an 83μm long racetrack and 4μm long detection section. Increasing the track size shows an increased scatter probability from the Si. If the bend radius is decreased to below a certain threshold, scattering also increases. Even at higher waveguides losses (4dB/cm), at least 97% detection efficiencies for any candidate material is achieved. Currently, standard losses are at 2 dB/cm, but the art state has shown lower at 1.2 dB/m [277]. The higher the absorption coefficient of the detector material, the shallower

the gradient. Higher absorption gives higher efficiency for higher loss waveguides fabricated. The MoSi demonstrates the highest waveguide loss tolerance as the absorption coefficient of MoSi is the highest, therefore requiring fewer round trips until detection. This limits the probability of scattering by minimising the interaction time with Si waveguides while in the ring.

The maximum phase-matched detection efficiency achievable from each material is shown in Figure.6.16 (b). They all obtain their maximum efficiencies for each nanowire length at similar coupler transmissivities. The nanowire length is the more dominating factor in absorption than the nanowire material. The similarity of efficiencies at the same lengths supports the notion that the materials complex indices of refraction are insignificant relative to other considerations, such as waveguide parameters.

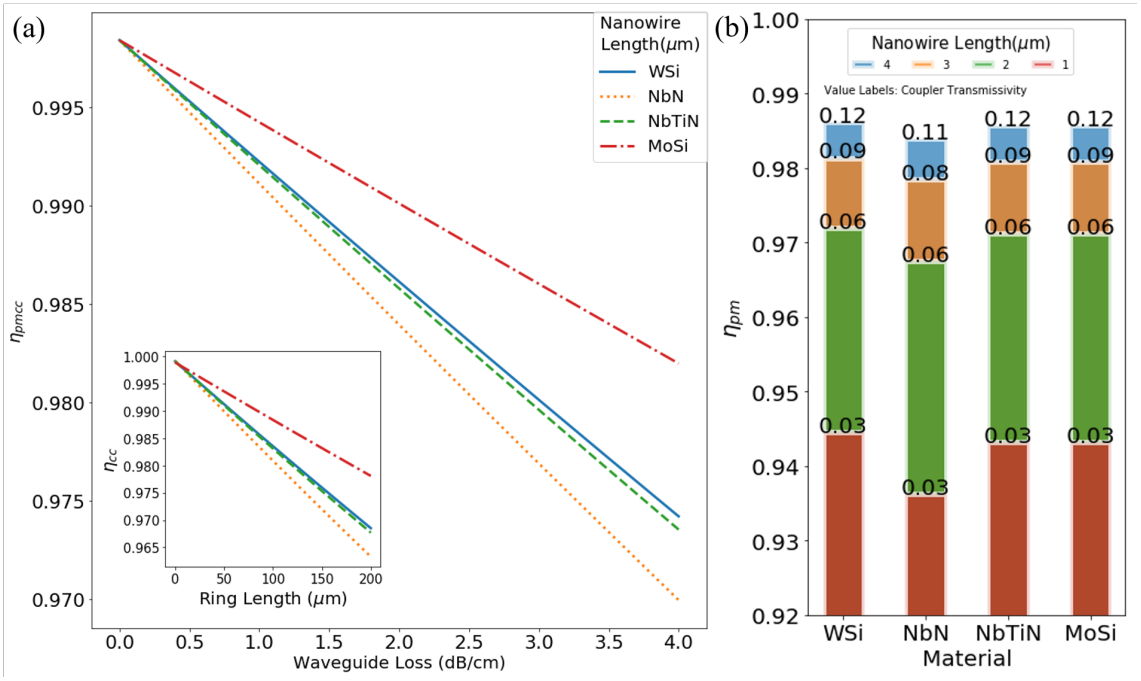

FIGURE 6.16. (a) The efficiency for a critically coupled and phase-matched racetrack detector, with varying waveguide loss, for a 4μm long detector region and 83μm long ring. Inset: The waveguide loss is 2 dB/cm. (b) The maximum efficiency of detection for a phase-matched ring, taken from Figure.6.15. The labels are the coupler transmissivity values used to reach the maximum detection efficiency for the specific nanowire length and SNSPD material at 2.1μm

When the cavity captures a photon, there is a period before the nanowire absorbs the photon. The photon may take several round trips around the cavity before absorption. An example of this is that the photon can be absorbed on the first interaction (round trip) with the nanowire or the seventh. As each round trip takes a specific amount of time to perform, the same photon may be measured at slightly different times depending on how many round trips are taken. This error in

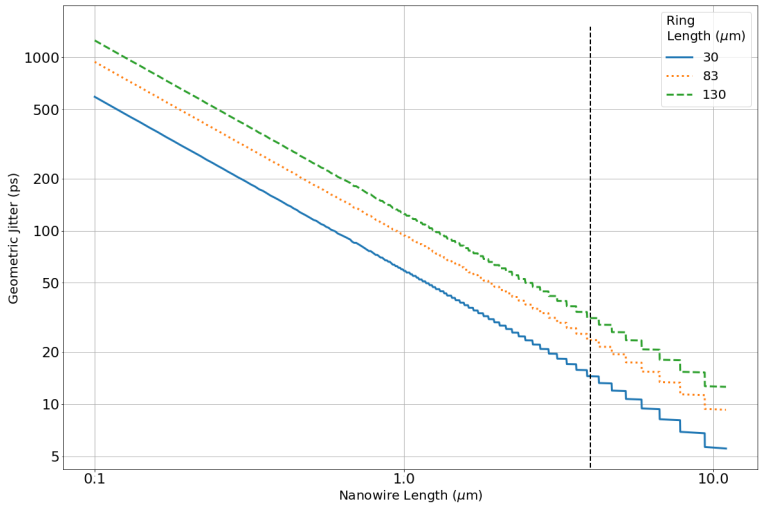

FIGURE 6.17. time between the photon's first interaction with the detection region and 95% absorption by the nanowires. This is measured for varying nanowire lengths and varying materials across different ring sizes. The dashed black line is at 4μm, where longer nanowires have a change in the effective index. The different candidate materials produce nearly identical jitter results; therefore, a single line is shown for all the materials

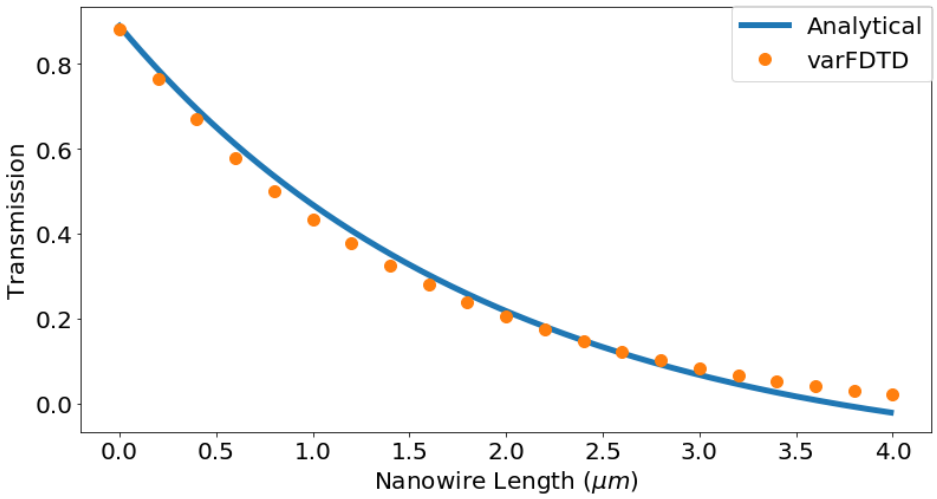

FIGURE 6.18. Comparison of results produced by varFDTD simulations and the analytical calculations. Different transmission values for different nanowire lengths. Calculation parameters: WSi nanowire, 83μm ring length, 4μm nanowire length, reflectively coefficient of 0.66.

the timing of the photons capture can be named as geometrical jitter and is measurable.

We simulate this for different racetrack cavity lengths, and it is shown in Figure.6.17. In this figure, an effective group index of 4.3 is used for the entire ring's entirety except for the detection

Material/Property	WSi	NbN	NbTiN	MoSi
FSR(nm)	57	57	57	57
FWHM(nm)	13.0	12.1	12.7	15.8
Max absorption	99.5	99.1	99.4	99.9
Q Factor	350.6	378.0	360.3	289.2
Filtering (dB)	23.0	20.5	22.2	30

Table 6.3: Numerically simulated values for the metrics that define a ring resonator detector at 2.10μm. Equations to describe metrics found in Chapter 2. For a 83 μm long cavity with a 4 μm nanowire length and using the MMI structure discussed in the previous section. The filtering is the extinction ratio between maximum and minimum transmission found. 6.19.

region with a value of 3.6, defined by the eigenmode solver. This is repeated using different ring cavity lengths. It is assumed that the cavity is critically coupled, and the photon is trapped inside the cavity before the detection event. Shorter path lengths decrease round trip time and increase the ratio of time of interaction with nanowire to Si waveguide: the longer the nanowire, the shorter the geometric jitter time. The geometric jitter is less than 10 ps for nanowire lengths longer than 1μm. After measuring all candidate materials, the difference between the n_g of the candidate materials range is 0.0005. This small value difference leads to a nearly immeasurable time difference in their jitter. We have chosen to present wSi in this figure.

6.4.3 Simulation Results

Figure.6.18 presents the racetrack detector's results as simulated numerically using a varFDTD solver. The simulation is completed for nanowires 0 to 4 μm long. For each simulation the transmission through the port is recorded and compared to analytical results calculated using Eq.6.3. There is a high agreement between the two methods, with a minimum transmission occurring at critical coupling close to a 4 μm long nanowire at 2.1 μm.

Transmission results from a varFDTD solver are presented in Figure.6.19 for a 4μm long nanowire, with all four different SNSPD candidate materials represented. The figures of merit for the ring detector have been extracted and presented in TABLE.6.3. For all materials, the FSR has no difference as the effective index change is minimal. Simultaneously, the FWHM are similar, except for MoSi, having a higher FWHM due to its higher absorption. All metrics presented in Table. 6.3 depend on the effective index of the detection region. We can then see that FSR remains unaffected by the effective index while other factors such as FWHM increase with increasing effective index. In turn, the higher the absorption coefficient of the material, the higher the potential efficiencies coefficients are achieved. The ring cavities provide a 95% extinction ratio for any material, therefore increasing the filtering of other wavelengths in the waveguides. An example is rejected pump wavelength light source, only to accept idler and signal frequencies. The simulations show between 99.1 to 99.9% efficiency, which is comparable to the analytical simulations.

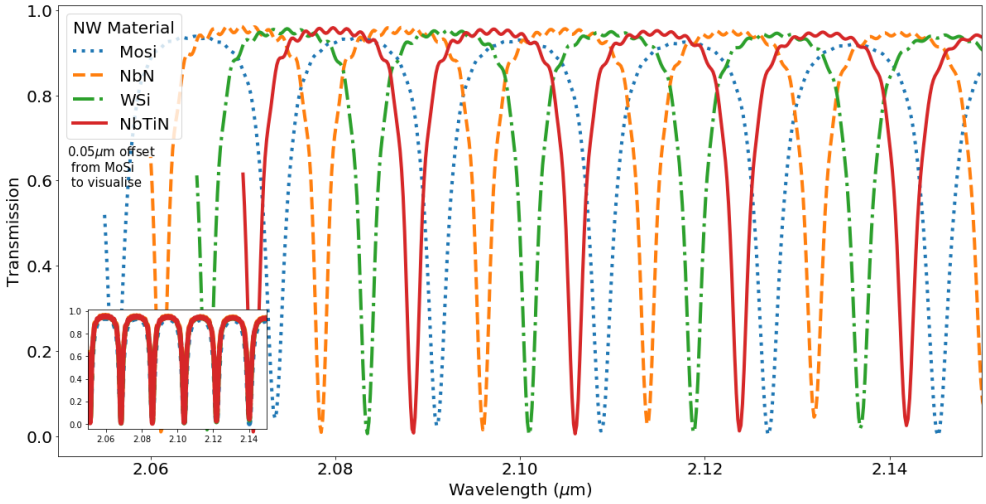

FIGURE 6.19. FSR spectrum of wavelength sweep around the 2.1μm range for multiple materials. The peaks are offset from one another for clarity. The inset shows the true values.

6.4.4 Conclusion

Simulation results describing the performance of an SNSPD embedded within the racetrack cavities are presented in this section. These results present the capabilities of cavity-enhanced photon detectors, in particular waveguide-coupled SNSPDs. This detector's spectral properties match the response of the cavity they are integrated with, allowing for bespoke-designed spectrometers. The racetrack design suggested in this work benefits from using standard fabrication methods and common use within silicon photonics. For a highly wavelength selective detector with the greatest detection efficiencies, a MoSi, 1μm detector, with a ring length of 83μm is the optimal option 2.1μm wavelengths.

6.5 Non-Uniform Ring Detector (NURD)

Such extreme light confinement in sub-micron SOI strip waveguides significantly enhanced propagation losses due to increased interaction of the waveguiding mode with the sidewall surface roughness [278]. Extensive experimental studies have shown that surface roughness is responsible for high propagation losses [279, 280], which can become prohibitive for building dense integrated circuits. High bend loss can also be a product of surface wall roughness, typically up to 1 dB per 90^O bend [269, 281]. Minimising the scattering loss contribution from the Si in the RCD will increase the detection region's absorption to the Si scattering loss ratio. We propose two solutions: using Euler curves to bend that single-mode and multiple mode waveguide bends.

6.5.1 Multi mode bends

Bending light in a multi-mode waveguide compared to single-mode guides has been heavily researched [282]. It shows that multimode waveguides have a lower loss due to reduced mode confinement relaxing the modes and effects from wall surface roughness hindered. Therefore an RCD with multi-mode bends can have reduced loss over a single-mode bend RCD. The bend's width increases linearly at the point of curvature until into 90°, where it reaches 3μm wide. After this point, it decreases linearly over the other 90° until single-mode waveguide width of 650nm. This geometry change occurs on both sides of the detector. An artist's impression is shown in Figure.6.20 (a). The difference between the single-mode structure and the multimode structure can be seen between figures.6.13 and figure.6.20. Using varFDTD, simulation of transmission through an Euler bend of path length $10\pi\mu m$ multimode bend and single-mode is carried out. Losses in single-mode is (0.00042dB) and multimode is (0.0026dB). The higher loss in the multimode is from the non-adiabatic change in the waveguide width, with the bend curvature, therefore giving more loss for each round trip. An adiabatic change in the mode requires a shallower angle of the waveguide taper, which requires a longer taper region.

The time difference in the geometric jitter of the ring is inspected. The group index in Si waveguides is smaller for wider waveguides. The group index at the bend's maximum width is 3.8, measured with an eigenmode solver, compared to the 4.2 value measured for 650 nm wide waveguides. The effective index change is assumed linear with the change in the width of the waveguide. This, therefore, decreases the jitter time when compared to single-mode, bends can be seen in Figure.6.20 (b).

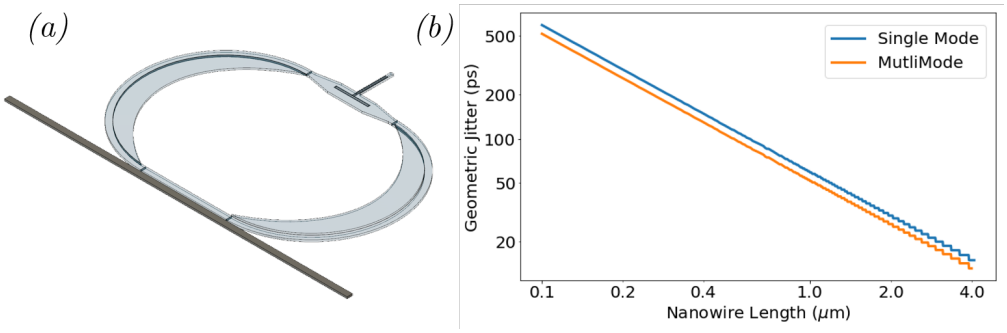

FIGURE 6.20. (a) Schematic of the non-uniform ring cavity detector design with linearly increasing waveguide widths around the bends up to 3μm, with the nanowire in the MMI region and the bus waveguide in dark grey. (b) Geometric jitter results of a WSi, nanowire in both single and multimode designs of at 83μm in length.

6.5.2 Euler Bend

An Euler bend has been shown to reduce higher-order modes' excitation and successfully demonstrated for single and multimode optical waveguides [283]. An Euler bend combats two major loss components, namely radiative losses inherent to a bend waveguide mode and transition losses from changing curvature. An Euler spiral is created via a linear increase of the bend's curvature along the path length. This results in a continuous transition from a straight waveguide to a bent one, allowing for an adiabatic change in the modes paths. A comparison between a 90° circular and Euler bend is visualised geometrically in Figure.6.21 (a), where the equations within the figure parameterise the Euler bend. Figure.6.21 (b)is simulated with the varFDTD solver and has the losses for a 180 $^{\circ}$ bend, similar to that in the proposed cavity structure for different bend geometries. The Euler bend is calculated to match the length of a 10 or 15μm radius bend, to provide comparable dB/μm for the whole bend. The transmissions of the single-mode circular bends show a higher loss then the Euler bends. The 15μm radius circular bend shows a lower loss from the shallower curvature angle experienced by the mode. The difference between the two Euler bend losses is minimal, but both have much lower losses than the circular bends.

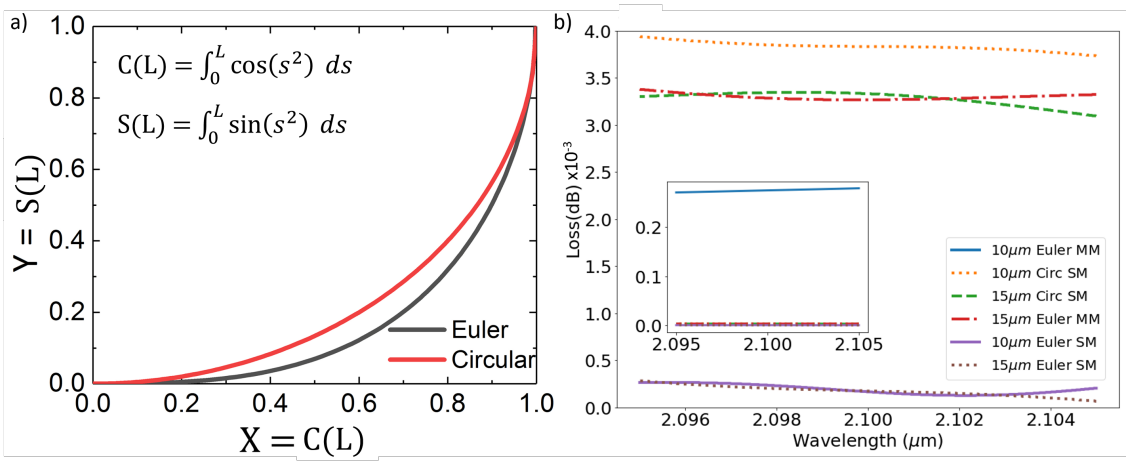

FIGURE 6.21. (a) Drawn 90° bend of a circular and an Euler bend, with Euler bend drawn using the equations displayed. Where s is an arbitrary parameter, L is the length along the curve, and C(L) and S(L) are the coordinates to describe the curve in the X-Y plane. (b) VarFDTD transmission of different configurations of circular and Euler waveguide bends, with multimode Euler, bends also presented at 10 or 15 μm radius. The inset is a zoomed out version of (b) to include the 10 μm Euler MM bend, which has significantly higher losses than the rest.

6.5.3 Conclusions

Euler bends provide a nearly immeasurable lower loss than circular bends at large ring radius'. This is due to their smooth adiabatic transition when implemented in single-mode waveguides.

The bending region's length is too short of introducing multimode waveguides as they would not be adiabatic. Further research at longer ring lengths may allow a multimode bend to be utilised in the cavity. A longer bend region would also change the ring properties, FSR and Q factors, and introduce more losses and jitter through longer path lengths. The MMI region is the dominant loss mechanism besides the ring's nanowire absorption, as shown by the relatively small losses from the ring bends presented. The large bend radius does increase the footprint size of the component: using a 15 μm radius racetrack structure increases the footprint area of the component by 50% for $448\mu m^2$

6.6 Discussion

These are the first data sets comparing these SNSPD materials' optical properties using numerical and analytical simulations for straight waveguide and ring cavity designs. From the results presented above, it can be concluded that the refractive index of SNSPD candidate materials WSi, NbN, and NbTiN, at thickness comparable to SNSPD thicknesses ($\approx$ 4nm), have roughly linearly increasing refractive and absorption coefficients for wavelengths up to 2.5μm.

The integrated waveguide structure shown to have the capability to allow wavelength demultiplexing of target wavelength light and highest detection efficiencies is a ring cavity structure, with multimode capable Euler bends, with a $4\mu m$ long MoSi nanowire area, using the MMI structure confused in the previous section as the detection region.

The new values given show higher absorptions at longer wavelengths, potentially increasing detection efficiencies at longer wavelengths with the correct designs. At the longer wavelengths, mode confinement within the waveguide decreases as the evanescence tales extend out of the waveguide and the mode's intensity is spread over a larger distance. Hence, using a wider nanowire will increase the area overlap between the electric field and the nanowire. The wider a nanowire, the greater the energy (the shorter the wavelength) of the photon needs to be recorded as a detection event by breaking the superconductivity. Therefore an optimal balance must be found in the nanowire's width and the wavelength to ensure maximum absorption probability and detection event occurrence. It is noted that longer wavelength photons have lower energies and affect the ability to break the superconductivity due to a lack of energy to create a "hotspot" in the nanowire. Nevertheless, this can be overcome with smaller nanowire widths of 80nm [179]. The narrower width allows photons with smaller energies to break the Cooper pairs, with enough energy to create a large enough "hotspot" to cover the nanowire's entire width.

The MoSi has ten times more thickness than the other materials measured, giving a higher refractive index than previously measured by other papers [261, 284].

For a straight waveguide integrated detector, the absorption of WSi surpasses that of the NbN and NbTiN. Absorption of the photon can be 6112.2 dB/cm at 2.1μm compared to 5490.2 dB/cm for 1.55μm. For smaller waveguides, the nanowire's absorption increases as TE mode

extends further to overlap with the nanowire increasing total absorption. Thicker nanowires also provide larger absorption, but thicker nanowire increases the photon energy needed to break superconductivity as mentioned in the last paragraph. Also, to conclude IWS, efficiency is dominated by the fabrication method, meaning that more precise fabrication methods would reduce absorption loss.

Using an MMI crosser to introduce the nanowires causes negligible loss of the photon into the Si, proving a viable method. With the correct MMI dimensions, a non-adiabatic taper, concentrating confinement in the centre, allows for dictated nanowire placement to maximise power absorption. Minimising the crosser arm width and keeping the nanowires central in the MMI also maximise the efficiency. Therefore an MMI with a crosser width below 400nm, 2.6 μm longer tapers, 4.25μm longer MMI region and 1.67μm wide gives the greatest transmission through the region. There is a trade-off between transmission loss and component footprint size. Longer MMI regions have shown lower transmission losses [285], but this increases the component footprint size. One of the claimed advantages of ring resonators is their small footprint size, which we aimed to keep. Lengthening of the MMI region would also increase length in other parts of the ring, leading to more Si scatter losses. Therefore a compromise is found with a shorter MMI, optimised around these lengths to minimise losses.

The ring cavity structure based on a ring resonator with an MMI waveguide-crossing inserted for nanowire transfer was presented. That trapped the photon in a cavity via a directional coupler until absorbed by the nanowires opposite side of the ring to the coupling region. The smaller ring cavity detector will provide the smallest detection jitter. However, the jitter in a single-mode waveguide detection region, as stated in [257] is much lower than the results provided here. The lower absorption of the detection region, leading to more round trips, is what pushes the geometric jitter up. This is necessary to keep the high detection efficiencies. Fabrication limitations only allow bends down to a few microns in radius and have higher losses. Longer nanowires are more sensitive to fabrication imperfections as the coupling coefficient is sensitive to changes in the width of waveguides, length or region and spacing between coupling waveguides. Longer nanowires provide a broader filtering peak but may lead to higher dark counts from photons that are not coupled within the waveguide. The materials chosen in the simulations have little effect on the absorption as the effective index change is smaller, depending on the geometries of the nanowires chosen. However, higher refractive index materials show slightly greater efficiencies, with finer filtering bandwidths. A shorter ring gives higher efficiencies up to a point, smaller jitter and broader bandwidth. In contrast, shorter nanowires increase jitter, decrease efficiencies, give higher bandwidth filtering, and are more sensitive to fabrication intolerances.

The RCD provides narrow ring filtering, allowing critical coupling of the photons for higher detection efficiencies. This can be broadened without affecting the nanowire or ring length by using a 2 × 2 MMI as the coupling mechanism into the racetrack over a directional coupler, as shown by [286].

A multimode bend reduces jitter but increases loss. It is also more sensitive to fabrication. It can change the electric field maximum in the MMI if it does not return to single-mode waveguide width before the detection region. Euler bends are only beneficial for longer ring cavities, which are not desirable due to footprints and efficiency.

6.7 Summary

Simulations results have been reported, detailing the performance of different superconducting materials in a ring cavity structure for SWIR light and an MMI entry region for the nanowire for different optimising considerations. The results illustrate the capability of using an MMI waveguide within a ring resonator, allowing the nanowire to enter the ring while minimising the loss. It has been shown that the impact of the difference between materials on the chance to detect photons at the SWIR is negligible. High efficiencies of absorption of the photons, showing potential to fabricate SWIR SNNPD, that can well surpass the previous reported 5.5% efficiencies are shown. The ring cavity allows for keeping nanowires at a shorter length below 4μm for reducing fabrication yield problems and increase wavelength filtering. However, if a detector with smaller jitter and larger bandwidth is desired, we can push to longer nanowire lengths within the cavity. These results help in understanding the tailoring of the component to detection specification requirements per application. The spectral characteristics shown for this type of detector are comparable to previously published results [257].

6.8 Future work

Multiple maxima of the fundamental TE mode occur along longer MMI lengths, as shown in Figure. 6.9 (c). With nanowires placed at each of these points, multiple photons coupled into the ring can be detected at once. While the one SNSPD is latched, the other nanowires may absorb and detect the photons counting for that pulse. Figure. 6.22. gives a design concept for a photon number resolving ring cavity detector.

6.9 Acknowledgements

The author's contributions consisted of mounting and characterising the device and the experimental set-up, designing and performing the experiments, and analysing the data. Dr. Mack Johnson helped with the theory and simulation guidance of the ring resonators. Dondu Sahin came up with the initial designs that are then built on and overlooked the project and end results. Dr. Nicola Tyler provided the initial theory and proof-of-concept the work is based on.

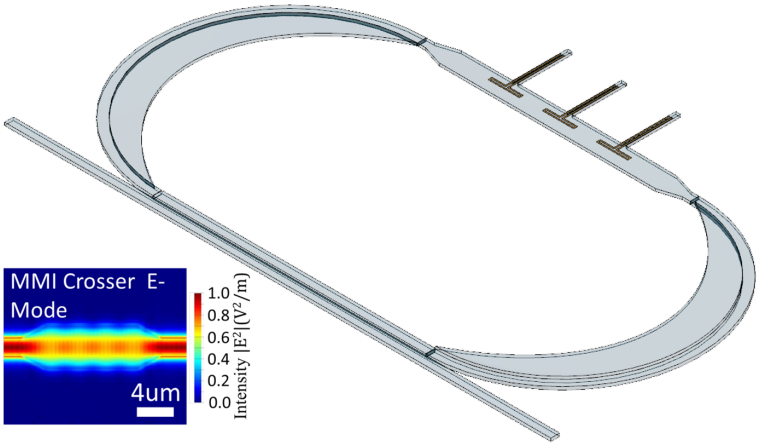

FIGURE 6.22. Artist's representation of a photon number resolving ring cavity detector. Multiple nanowires placed at points of maximum intensity along the MMI region. *Inset*: Electric field strength in the MMI region, showing three points of highest intensity to position the nanowires over the top. The simulation is without SNSPDs.

CHAPTER 7

CONCLUSION

This thesis reports on scientific and engineering tools for realising quantum communication networks and computations systems. It relies on the fundamental quantum physics and addresses practical challenges, cryogenic engineering feats, electronic signal processing at low temperatures and the fundamental physics limitations of the optical materials involved.

7.1 Summary

We first reported on the characterisation of three Si devices that we used to form a testing for a three device QKD network. To test the devices are suitable for QKD, we projected into sets of MUBs and measured their fidelity. We set a bench mark using a single device and measuring the computational $\hat{Z}$, Hadamard $\hat{H}$ and Y-basis $\hat{Y}$. Finding on average a 83% fidelity far above the 50% classical threshold and comparable to current Quantum measurements. When providing into 4D between two devices, we stabilise the spatial mode by using constantly adjusting the phase of the incoming states into the receive devices. We proved this was sufficient for some measures between two modes, by preforming a quantum interference measurement with high visibility ($> 90\%$). Using this result we test 4D Hadamard between two devices and measured 73% fidelity, well above the classical limit. Finally connecting a third device we performed 2D QKD, by measuring the computational and Hadamard basis and obtained 96% fidelity, that is on-par with current QKD research [132, 136]. Finally we test the communication of the 4D computational Z-Basis between three silicon devices. We reached a fidelity of 85 %. Using active phase stabilisation can minimise the phase drift between different spatial modes between integrated devices. We showed the potential for QKD using high dimensional entanglement distribution is possible.

We characterised the performance of the DRYICE1K system, by calibrating temperature sensors, testing its cooling performance and measuring the vibrations of the system. The system

provides 300 mW of cooling power at 1.3 K. We found that the system had over 60 μm of vibrational travel during operation, that allowed the system to not be suitable to couple into integrated photonic devices. We are able to damped the system vibrations from cold heads that power the cryogenic station to be reduced by 75 %, to 8.50 μm of displacement travel. This is at the threshold to maintain coupling between fibres and grating couplers.

With this system characterised we provided a suitable environment to test electronic devices in the systems such as the FPGA, SNSPD and amplifiers. We tested the performance of the SNSPD within the system. We found that comparable room temperature systems with the SNSPD used in the characterisation of the readout electronics system operating below 6.5 K, with a 20 ns dead-time, 66 MHZ max count rate, with at least 10 % detection efficiency at 1.55 μm. These results allow for the designing of an optimal NODE for QKD applications.

SNSPD signals were amplified by off-the-shelf GaAs amplifiers. We tested three devices all GaAs based, with different gain and power consumption's quoted. We chose the ADL5611, as it provides the highest gain to power ratio. The SNSPD signal must be amplified from the μV pulses it provides to single units of V to be measured by a time tagging system. The amplifier provided total of 28 dB gain at 1 GHz while operating at a single shot temperature of 1 K and resting temperature at 4 K. Using two in conjunction, is typical for SNSPD readout provides sufficient voltage for recording detections. With a minimal latency of 700 ps the lag time difference between detection and measurement is minimal and power efficiency doubling to 92.83 dB/W at this temperature. This allows for up to ten ADL5611 amplifiers to be hosted at the 4 K stage before the system cannot provide sufficient cooling power to the rest of the system. Allowing for five SNSPDs to be hosted at the sample stage. These results show the amplifiers can survive cryogenic temperatures and can be used, while the time tagger is also hosted within the cryostat.

The FPGA readout board operates at 4 K, surviving cooling cycles down to 1 K. The Artix-7 captures photon arrival times via SNSPD pulse signal conversion to digital readout via a Time to Digital Converter (TDC) reading in chain length to 17 ps per a bin and still showing operation between 0.8 and 1.2 V, allowing for tailoring of bin resolution size. The precision demonstrated is still comparable to the jitter found in SNSPD pulses. Proof of further calibrations and timing systems implementable on the FPGA to provide a reduced error in the readout is also provided. We showed that the FPGA chosen provides a sufficient TDC system for SNSPD readout at cryogenic temperatures and the power output allows for multiple SNSPDs to be hosted in the future in the same system. The results here are consistent with other TDCs [194, 195, 200] implemented at cryogenic temperatures and shows they can be hosted with an SNSPD.

The racetrack cavity Short Wave Infrared (SWIR) SNSPD simulations showed that out of our sample of WSi, NbN, NbTiN and MoSi, that detectors using MoSi as the material for the nanowire out performed the rest for longer wavelength photons. Firstly, using ellipsometry measurements to calculate the absorption coefficients at SWIR, MoSi is shown to have the highest efficiency in this study as the theoretical study goes on to present, in several different parts. We are

presenting first as simulations results of an SNSPD designed with a straight waveguide of varying dimensions to consider fabrication tolerances. We test a custom anisotropic MMI crosser structure implemented into the ring cavity structure, testing dimension to provide the highest confinement and lowest loss. We chose the shortest nanowires needed in the ring cavity, allowing for small footprints and high fabrication yields at 4 μm. We show that detection efficiencies of 99.9 % are theoretically achievable, with wavelength selectivity of 12.1 nm and filtering from over wavelengths to 30 dB. An MMI waveguide crossing structure is a suitable technology to allow for nanowire insertion into the cavity. The cavity itself can be tailored for FSR peaks, FWHM, and peak value.

The technological advancements presented here provide accessibility paths to provide the increased scaling needed to provide full commercial quantum systems, allowing for a network of the fully integrated detection system and with state-of-the-art SNSPDs.

7.2 Outlook

This thesis demonstrated the development of technologies to scale quantum communication and computation systems to multi-user systems. Here we discuss some potential ideas for further work.

7.2.1 High-Dimensional QKD

Expanding the MUBs measurements while stabilising the phase is proof required to create a high-dimensional QKD protocol. We demonstrated 4D Z-Basis measurements as a potential basis to be used in a QKD protocol between 3 separate devices; further basis measurements are required to allow for a QKD protocol to be established. As two MUB are required for QKD as explained in Chapter 2 and only one is measured in 4D across 3 devices. For example, the Hadamard basis which has the required interference between the spatial modes, requiring phase stabilisation between devices of four modes simultaneously.

7.2.2 Quantum Communication readout system

We expanded the system to host multiple detectors to show further that the system's engineering cooling capacity can handle the additional heat load. With the increasing number of detectors, the PCB would be redesigned to host as many input signals as possible until the FPGA or the UART communication bandwidth reaches capacity. We would then investigate using multiple time taggers within one system. Previously developed commercial time taggers have inbuilt logic operations to create virtual channels that reads out coincidence counts, multipliers and other counting metric tools. We would look to include this in our system, to adjust the data delivered to budget for the bandwidth.

7.2.3 Ring cavity SNSPD

This project's results are for SWIR photon detection but show that this design can be tailored for different wavelengths. Current research by [53, 242] show the SWIR photon detectors are becoming more desirable as the capabilities of SWIR for quantum information is proven. Further research in SWIR for quantum information showing it can out perform current operations and over come the limitations will provide further worth the SWIR SNSPDs. This research also has obvious progress in moving towards the fabrication of the devices and testing detector efficiency for devices in a live environment. The simulations also showed that in the multimode area of the ring cavity SNSPD multiple "hot spots" could lend to multiple nanowires being in the ring to detect multiple coupled photons, testing proof of a ring cavity photon number resolving detectors.

APPENDIX A

FABRICATION OF WAVEGUIDE INTERGRATED SNSPD WITH PASSIVE OPTICAL COMPONENTS

In this appendix we provide a detailed overview of the fabrication steps taken to produce a waveguide intergrated detector on SOI. The intention of this appendix is to demonstrate the capabilities needed to produce the designs laid out in Chapter.6. First, covering the theory and specific fabrication tools and techniques required to produce the device. This is followed by a recipe used to fabricate the device, with the end being subject to theory. Along the way we present any results demonstrating the quality of components fabricated.

A.1 Method

There are usually multiple components to the device and the entire fabrication process used in making each component needs to be tested to ensure the sufficient quality of that component [287]. Additionally cross fabrication, where another component/building block is used to make the fill device, affects the quality of other components on the device. Each of these different components can also overlap in fabrication producers. To separate the fabrication step, a system of layers is implemented, that guides the design flow. This ensures that each fabrication step gives clear information on how components may interact with other fabrication processes. An example of some components are the superconducting nanowire hair pin structure, Si optical waveguide and Au electrical contact pads. Where the Si layer is used to form optical waveguides, you can also etch the superconducting layer if the nanowire is not properly protected or the system is calibrated.

The substrate used for these fabrication methods is Silicon on Insulate (SOI) with a 220n m of Si on top of a 2 μm Burried Oxide (BOX) SiO_2 layer, that sits on a Si substrate base. In the thesis

SOI wafers are already supplied in this format, therefore their fabrication is not covered. They usually come with a protective photo-resist layer, which protects the Si from contamination. This layer is removed through chemical etching. The sample is washed in an acetone solution for up to 2 minutes. Acetone can leave a residual layer, therefore isopropylalcohol (IPA) is used to wash any residual off before it is rinsed with water and blown dry with a nitrogen gun. This is all performed in a vacuum hood. The vacuum hood has a positive flow coefficient, to minimise contamination on samples and to avoid chemical vapour building up, providing protective shielding for the users. You may also use this to remove contaminates to prepare new samples for processing and between fabrication steps, where the samples might have been exposed to multiple potentially damaging environments.

A.2 Fabrication Techniques

A.2.1 Spin Coating and baking

To perform lithography [288], a layer of resist needs to be applied to the sample to provide a platform to determine what material of the Si layer needs to be kept to create the optical components. The depth of the resist is a thin layer allowing for penetration of the light or electrons that chemically alter the resist. Resist is applied through a spin coater and then baking this to harden. The thickness can limit the resolution of features that can be defined with lithography processes and etching.

The spin coat allows us to produce a uniform thin layer of resist on top of the substrate. The sample sits on a chuck and is held in place with a vacuum. This chuck spins at a speed which determines the thickness, depending on the viscosity of the resist pipetted on top. Resists come with a data sheet explaining the thickness of the resist layer produced depending on the speed, which typically follows this relation:

$$h \propto \omega^{-m} \tag{A.1}$$

where h is the height of the resist layer, ω is the spin speed in revolution per minute (RPM) and m is a constant depending on the material viscosity. This theory explains that generally the faster the spin speed, the thinner the resist layer. As the resist layer also depends on the viscosity of the resist, diluting the solution can also decrease the thickness of the layer. After spin coating, the resist is usually baked at 200 °C on a hot plate, to allow the resist to cure in order to maintain the thickness.

A.2.2 Lithography

Lithography [289] is the chemical process to print an image onto a 2D surface. We can consider the surface to be 2D as the thickness of the print layer is negligibly thin compared to the plane

of the material. This process is heavily used in printing quantum optics circuits, as it defines the geometries of the structures on the device. There are two different types of resist in the form of positive and negative resists. Positive resist is already insoluble and the lithography process defines areas through the reactive lithography process the areas to become soluble. Negative resist is vice-versa. The distinction is found when you perform lithography with light or electrons: turning the structures that the photons or electrons are incident on soluble. Poly-Methyl Methacrylate (PMMA) and ZEP520A are examples of positive resists, whereas Hydrogen Silsesquioane (HSD) and LOR 7B are negative resists. They each provide benefits depending on the structures being made and can provide different resolutions when combined with the resist. As well, you have optical and E-beam type resists that are designed to be reactive with the different lithography methods.

A.2.2.1 Optical Lithography

Optical Lithography [290] is a process used for larger structures on quantum optical devices, due to the wavelength of the light used. Ultra-violet (UV) lights is used in the development process for the contact pads structures. Projecting light on-top the surface turns the resists insoluble to the developer. Allowing for a mask to determine geometry of the structures on the device, by blocking and allowing UV light through in the areas defined.

A.2.2.2 Electron Beam Lithography

Electron Beam Lithography (EBL) [291] is use to write high resolution components on to photonics devices. This process uses electrons as the source over light, as the smaller wavelength of electrons allows for a sharper definition. The method of generating the electrons is the same as a Scanning Electron Microscopy (SEM) device, using a thermionic emission source in the form of a heated filament lamp, therefore EBL devices are usually also used as SEMs. SEMs are key for the calibrations and sample preparation required to preform EBL to a high standard. The electrons are guided through an aperture that is one of the components in controlling the resolution. The area the EBL can cover without having to re-position mechanically is called the write field. A write field is on the scale of hundreds of micrometers. The EBL is deflected within the write field area, to write out the components. Components such as waveguides connect over multiple write fields, therefore re-positioning is required, that can lead to stitching errors, or misalignment between write fields. During calibration, this is corrected with markers on the sample to calibrate the write field.

The resolution of the EBL is defined by the following parameters:

Electron Acceleration Voltage

The accelerating voltage within an E-beam system determines the amount of momentum that the electrons have. A higher momentum allows for deeper penetration into the resist to ensure that the entire thickness is reacted with. Higher momentum reduces the beam size as the high

momentum reduces side scatter, also increasing the resolution of the components. Changing the amount of time the beam is incident is also key as high energy in one location can cause an overreaction, distorting the features.

Resist type and thickness

As mentioned earlier, these can affect resolution as the molecular size and their structures determine the scattering magnitude. The resists chosen to be used in E-beam are PMMA [292], HSQ [293] and ZEP520A [294]. PMMA and HSQ provide high resolution EBL results with pattern features down to 10 nm, while ZEP520A shows high resistance to etching techniques, providing greater selectivity.

Step Size

The distance between each e-beam pulse: the smaller pulses overlap and create less roughing on structures, but also the write time increases.

Aperture mode

The size of the aperture, determined by the number of electrons flowing through and therefore the beam current. Smaller beam current requires a longer dwell time to achieve the same dosing.

An important metric to keep control of is the dosage measured in μCcm^{-2}, and the requirement for each resist is dependent on the chemical and the thickness. Finding the correct dosage is key, as over-dosing creates over-size components and under-dosing can lead to the reverse. A correct dosage to allow for full penetration for the electrons is called the clearance dose. Using the clearance dose results in fully developed resist underneath the beam.

A.2.2.3 Dosage test of nanowires

E-beam Lithography using the Raith Voyager system was used to find the current per an area (which we will call the dosage) needed to give nanowires of consistent width to a resolution of a few nanometers. Si was used as a substrate depositing FOX-16 HSQ via spin-coating at 2000 RPM for 30 second, to give a thickness of 0.95 μm. Four different designs of nanowires were patterned to study how the U-bend from the E-beam differs. The designs are numbered 1-4 going left to right.

The SEM used an accelerating voltage of 5 kV. The higher the accelerating voltage, the greater the penetration depth of the electrons. The higher voltage gives better resolution, but due to the thickness of the HSQ and the transparency of the electrons, no nanowires could be imaged at this voltage.

As the substrate and HSQ are dielectrics, electric charge from the incoming electrons disperses on the surface, and causing reflection of incoming electrons, potentially reducing the quality of images. To overcome this a sputter system was used to deposit a Au/Pd metal layer of 10 nm, to provide a conductive surface for the charge to flow over. Au/Pd is used as its structure is relaxed and crystal structure fits well at thin thickness.

Even using this technique the resolution of the SEM system is stretched, going to several

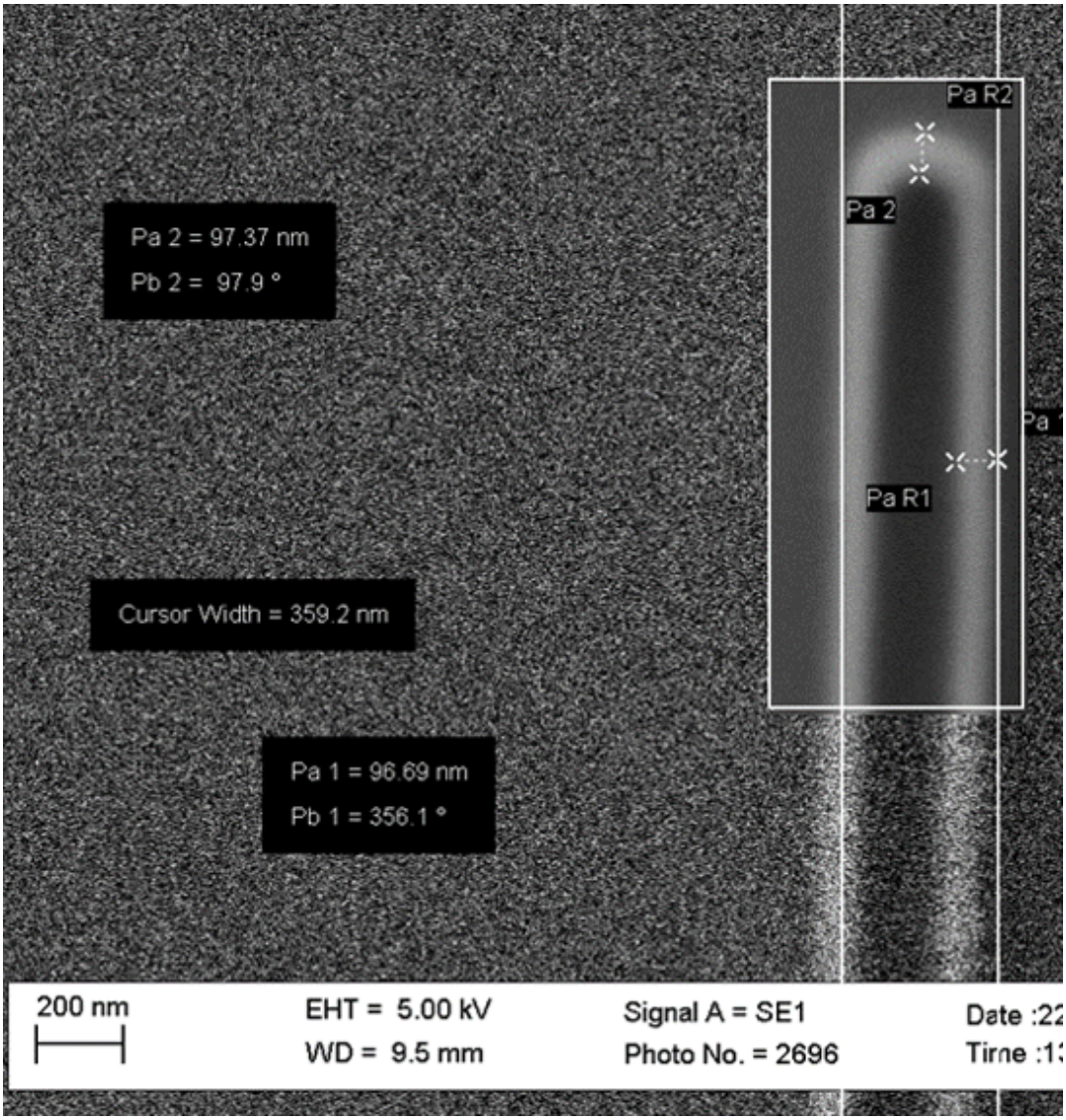

FIGURE A.1. SEM Images of nanowire E-beamed to have 80nm width with curved U-bend end at a dose of 4.6 times 250 $\mu mC/cm^2$.

nanometers. Figure.A.1 shows the nanowire of design 1 to have a quality of a recognisable structure, at the scales needed to produce usable nanowires. With a measured width of 9 6nm, this is within other nanowire designs that vary from 80-150 nm. As the design is made of separate polygons, misalignment areas can occur. As shown in the image there is a continuous wire with no visible signs of imperfections.

Design 2 in Figure.A.2a has a thicker design than the other two that can be seen compared to the other nanowires. All the nanowires in Figure. A.2 have a continuous structure. Designs 3 and 4 in Figure. A.2 b), c) have no visible difference in designs, even though one is made of 3 polygons and the other one continuous polygon. Therefore the alignment at this scale is considered to give

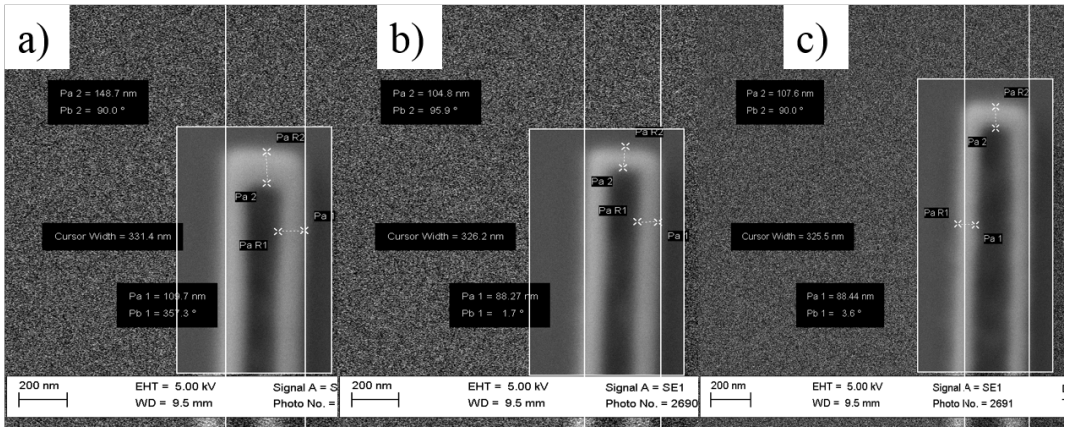

FIGURE A.2. SEM Images of nanowires E-beamed to have 80 nm width with curved different U-bend structures. Left to right: the left is made of 3 polygons, two for the nanowires and one 330 nm thick polygon for the U-bend. Next is one single polygon with a 160 nm thick U-bend, and the last is 3 polygons again with a 160nm thick U-bend. All are at a dose of 4.6 times 250 $\mu mC/cm^2$.

the performance needed to produce nanowires.

A.2.3 Reactive Ion Etching

Reactive Ion Etching (RIE) [295] is a technique used to remove material from a surface, ultimately allowing for patterns and components to be etched into the layers. The etching process forms the structure of waveguides, grating couplers and other passive optical components. The RIE mechanism is as follows: The sample to be etched is placed in a high vacuum chamber, which is then filled only with the gas to be used to etch the sample. An electric field is driven across the gas to form a plasma, creating ionised particles that are then accelerated towards the target. As two parallel capacitor plates sit either side of the sample, this allows for a single direction of etching, allowing for an an-isotropic etching method over chemical etching. Chemical etching involves dipping the sample in a liquid that erodes away the material. A feature of this is its an isotropic etching process eroding the material equally in all directions. The etching mechanisms are both physical and chemical, meaning the consideration of the momentum, the mass of the particles can affect etch rate as well as the charge and the electronegativity. Physically etching is when the momentum from the particle breaks the bond in the materials through transfer of kinetic energy from the etching material onto the surface. Chemical etching is a chemical reaction between the etching particles and the substrate particle, where this bond is stronger than the surface particles bonds.

Metrics for consideration while performing RIE are the etch rate, the selectivity and the anisotropy. The etch rate is the speed that etching through the layer of films occurs at, which is typically between 10 to 100 nm a minute. Selectivity is a ratio between the materials that

are being etched. Different materials will etch at different rates, so if etched simultaneously the difference between the height of structures may differ before and after the etching process. This is a key concept to understand and control, by using resists' thickness and composition to tailor the finished components dimensions. An example of this is determining the correct height of HSQ on top of Si, to protect the Si long enough to form a 220 nm deep waveguides. Knowing the ratio between their etch rates will determine the thickness of the HSQ needed. If the etch rate of HSQ is greater than Si, more than 220 nm of HSQ thickness is needed.

Anisotropy is when etching in one dimension occurs at a faster rate than another. In the case of RIE, etching only in the Z-direction perpendicular to the plane of the sample is typically desired. For the purpose of fabrication of waveguides and other photonic components, the aim is to have etching in only one dimension, so no slanted angle side walls on waveguide occur, or undercutting. Undercutting is where a material with a higher etching rate is under another, therefore forming an overhang if left to over-etch.

A.2.4 Deposition

A.2.4.1 Evaporation

This technique [296] is used to coat the electrical contact pads needed to apply a potential bias across the nanowire. Using optical lithography and spin coating, the area for metal deposition is left exposed. During the metal evaporation coating, the whole sample surface is coated by the resist, which allows for a technique called lift-off. The contact pads are made of a 20 nm thin layer of Cr followed by a 200 nm layer of Au. The Cr acts as a buffer layer, providing a phase matching between the Si substrate and the Au. It is not used entirely due to its high oxidation. Samples of each of the metal are placed into crucibles, and are connected to a high amperage (up to 20 A) DC power source. The sample is placed above them facing downwards, in the direction of the metal vapour path.

The evaporation process is performed in a bell jar, allowing for a high vacuum to be obtained, to minimise the number of containments on the sample that can nucleate from the atmosphere, due to the high temperature achieved in the bell jar. Using a roughing and diffusion pump, the system is evacuated. A high current is applied across the Cr first, and the deposition rate onto the sample is measured using a crystal next to the sample and the deposition rates onto both are assumed to be equal.

The crystal vibrates at a resonance frequency, and this frequency changes when matter is deposited. By calibrating the crystal, and knowing the rate of change of frequency from the material deposited onto, we can calculate and determine the rate of deposition and the total deposition of material onto the sample by the difference in the driving frequency applied to the crystal. This is a different rate for different materials and therefore the driving frequency and voltage is selected dependent on the material being deposited.

A.2.4.2 Magnetron Sputtering

This is a technique [297] to deposit ultra thin films of high evaporation point materials. Target samples are in a vacuum environment to reduce contamination. The target is heated to close to 1000 °C as the temperature allows for nucleation on the targets' substrate surface. Sources of the constituent materials are heated with RF or DC bias sources, depending on their magnetic properties. Ar gas is used inside the chamber and an electric field is used to create an Ar plasma. The Ar ions in the plasma are accelerated towards the sources using the magnetic field within the chamber. The sources emit material with an even probability distribution across the chamber. Source material that comes into contact with the target sample nucleate onto the substrate. Multiple sources can be used at once and their DC or RF voltages can be tailored to change their emission rates. The emissions rates and proximity to the target sample tailors the stoichiometry of the thin film formed. In the University of Bristol a Magnetron sputter device is used to produce MoSi films for SNSPDs, using Mo and Si sources. This is a key step required in the fabrication of the SNSPDs and the stoichiometry, thickness and material of the films all play an important part in the properties of a SNSPD. Film growth is a heavily researched topic in itself, that is not covered in this thesis but is referenced here to form a complete pictures of the fabrication process required to develop a waveguide integrated SNSPD.

A.2.4.3 Lift-off

After the metal contact layers have been deposited on the top layer, part of the layer is removed to leave a metal layer in the shape of the features designed. The bond between the metal layer and the Si layer will remain bonded, while the resist layer that sits between the other regions between the metal and Si will dissolve in a developer such as TMAH or acetone. Lifting-off the metal not needed, leaving the desired features.

The devices are placed in a bath of the developer and this then undergoes sonicfication to assist in the penetration of the developer of the resist, to remove all resist and leave only the metal layer.

A.3 SNSPD Fabrication Recipe

In this section we break down the step-by-step process of the fabrication method to create a waveguide integrated WSi SNSPD for SWIR. Figure.A.3 shows a cross-section of each steps' results.

Concept: Creating a waveguide integrated SNSPD, with a WSi nanowire on SOI and Au contact pads for probing. The idea is to have a hairpin nanowire 100 nm wide and 10s of micron long, laying on top of a 500 nm × 220 nm Si waveguide, with a grating coupler for 1550 nm at the end of it. The nanowire will be connected to Au contact pads.

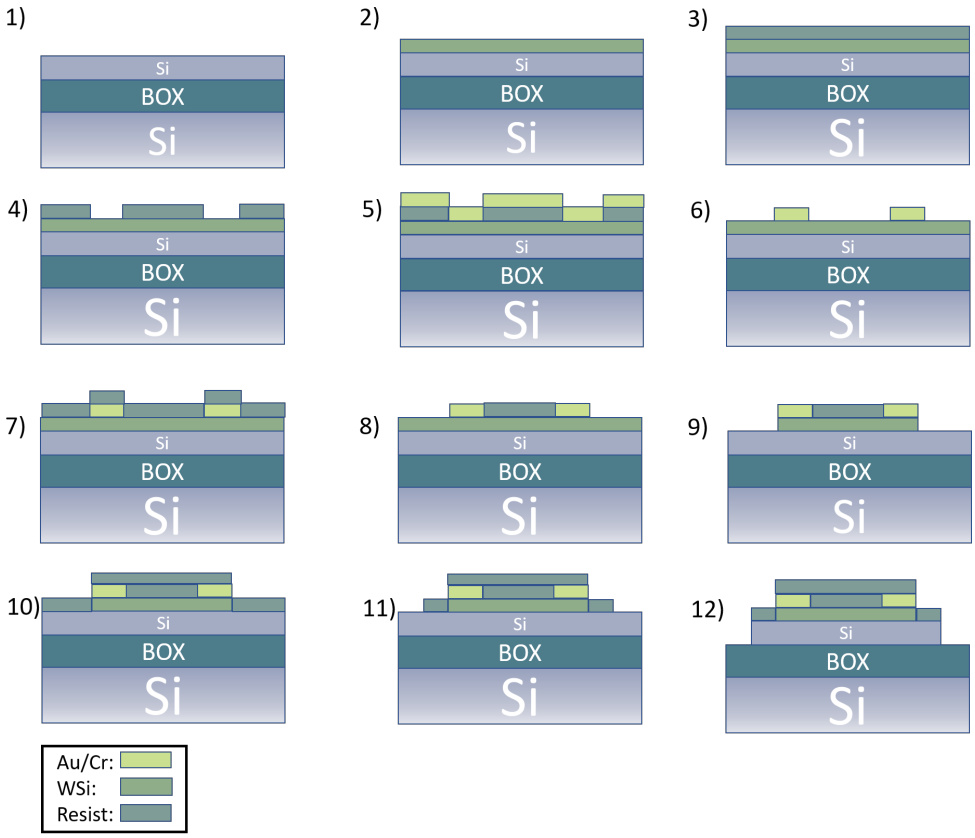

FIGURE A.3. Step-by-step guide to the fabrication of a waveguide integrated SNSPD. Each step is explained in the text in-depth, but here we list the techniques used. We assume that the method will start with a supplied SOI waffer, as this is a well-supplied material. 1)→2): Sputtering of WSi. **Deposition of contact pads** 2)→3): Spin coating and baking, 3)→4): Optical Lithography and development, 4)→5): Sputtering of Cr and Au, 5)→6): lift off. **Fabrication of SNSPD**: 6)→7): Spin coating and baking, 7)→ 8): EBL and development, 8)→ 9): RIE. **Fabrication of Waveguide**: 9)→10): Spin coat and bake, 10)→11): EBL and development, 11)→12): RIE

Listed below are tables of the settings used for different fabrication equipment listed in the fabrication recipe.

A.3.1 Contact Pads

A.3.1.1 Optical Spin Coating of Optical Resist and Development

This fabrication step covers parts 2) to 4) in Figure. A.3. The specification for the spin coating setting is found in Table. A.1.

1. The specification for the spin coating setting is found in Table. A.1.

Ref	Resist	Spin (RPM)	t (s)	α_s (RPM/s)	Developer	Dev t (s)	T (^OC)	Bake t	H (nm)
SC1	FOX-16	2000	30	2000	TMAH	120	150/200	120/120	80
SC2	950 PMMA A4	4000	60	4000	IPA:MIBK (3:1)	50	100	90	200
SC3	950 PMMA A9	4000	60	4000	IPA:MIBK (3:1)	90	100	90	1500
SC4	LOR 7B	2000	30	2000	MIF326	35	200	60	600
SC5	S1805	3000	10	3000	MIF326	35	110	60	200
SC6	FOX-14	5000	30	5000	TMAH	120	150/200	120/120	200

Table A.1: The spin coat settings required for each of the steps outlined in the fabrication recipe: T is the temperature, t is the time, α_s is the acceleration and H is the height.

Ref	Etcher	Material	Rate (nm/min)	Chemical	SCCM	RF (W)	Pressure (mTorr)
E1	JLS	WSi	8.4	CHF_3:SF_6	21:2	50	10
E2	ICP	Si	32	CHF_3:SF_6	14:56	30	10

Table A.2: The RIE settings for the above fabrication recipe.

Structure	Column Mode	Resist	Doseage ($\mu C/cm$)	Comments
Contacts Pads	HC_Ap70	PMMA A9	1000	Focus on sample
Nanowires	LC_Ap30	HSQ	1125	Burn Dots
Optical Components	LC_Ap30	HSQ	1100	Burn Dots
Neg Optical Components	LC-Ap30	PMMA A4	500	Burn Dots

Table A.3: The EBL settings used in the above fabrication steps

2. Dice the samples into 8 mm square slices using the dicing machine or the diamond pen cutter. Do this on a cleanroom tissue paper, using tweezers to hold down the sample and forming straight deep scratches onto the polished side. Then turn and place pressure with the pen on the other side of the sample until the force causes the sample to break, along a straight line down. You can measure using a ruler.

3. Sonicate the samples in acetone for 20 mins and then clean off in IPA and then DI water.

4. Turn on the mask aligner and allow for the system to warm up, for the emission source to reach temperature to emit the correct wavelength of light for the optical lithography.

5. Clean the spin coater, the hot plate, the pipette, the sample holder, and all equipment with IPA and tissue paper. This is to avoid contamination.

6. You will now perform the spin coating. You will need:
   Optical Resist: LOR7B
   Optical Resist: S1805 Yellow
   200μl Pipette
   Tissues Paper
   Optcail Resist dedicated spin Guard
   Tweezers

Spin Coater
IPA
Sample holder piece with small pillar on it (not Flat)
Test sample tubes
Hot Plate
Pipette Tip Head
Mask Aligner
Devoplper MF316
Di Water
Beakers

7. Take LOR 7B and S1805 out of the bottle into a small test sample tube and ensure that you label them correctly.

8. The program for the spin coater (Spinner 1) for LOR 7B is Prog 23: 2000 RPM, 30 seconds, 4000 RPM/s. and you bake for 1min at 200 degrees.

9. The program for S1805

10. Resolution: 3000 RPM, 10 seconds and 4000 RPM/s and then you bake for 1 min at 150 degrees. Cover the entire sample with Optical resist, ensure that the tip doesn't touch any surface, make sure there are no air bubbles in the deposited resist and spin up the spinner very shortly after depositing resist.

11. After spin coating the sample, ensure the back of the sample is clean or comes off after you bake, as it could just peel off then. Make sure you bake between each coating. Both coatings go onto the same sample, one after another after each other's baking.

12. Leave the sample space clean.

13. Take the optical mask and align with the design and overlap.

14. Ensure that the mask is cleaned with IPA and that it creates a tight vacuum seal around the optical mask holder on the optical mask. Ensure that the chrome side is facing down and line up the sample with the correct design. Ensure that the chip is touching the optical mask, by looking for absence of diffraction from the mask on the sample, by looking through the microscope. Make sure there is not too much pressure to break the mask, but enough to ensure good uniform contact.

15. Expose the mask to 75 seconds of UV light, timing it separately and ensuring that it ends, so as not to over expose. Remove sample and complete with the rest.

16. After this develop the sample in developer MF316 for 2 minutes and then use DI water to stop the development process. Ensure that the sample is dried with the Nitrogen gun on tissue paper.

A.3.1.2 Evaporation of Cr and Au contact pads

This fabrication step covers parts 4) to 5) in Figure. A.3.

1. Stick the samples to a glass slide, using Carbon tape, shiny side exposed.
2. Follow the evaporation procedure for the evaporator provided.
3. Use the Chromium rodes and the Au particles in the white crucible and ensure that the Cr rode is on the right side and the Au on the left side.
4. Once all is loaded and pumped down and you are ready to expose, use the evaporator instructions to evaporate the materials. Use previously logged voltages for Au and Cr as references. Ensure you meet and stay at this voltage, and only use the shutter to allow for deposition.
5. Allow the system to cool properly before removing the samples.

A.3.1.3 Lift-Off

This fabrication step covers parts 5) to 6) in Figure. A.3 .

1. Place the samples on a dish still attached to the glass slide and trap in a container along with acetone, so that the vapour for the acetone only penetrates the sample. Leave this for 24 hours, and there should be cracks where the Au should peel away.
2. Take the samples and place them into the white plastic sample holder in Dondus draw. Place the samples in here, and in a beaker of acetone and sonicate for up to 20minutes. All of the Au should peel away where the resist was left.
3. If the Au has not lifted off, you can squirt acetone directly onto the sample, while being held over a large container. The chemical and the force from the acetone will remove remaining Au. This is a last resort as it can damage the Au that you want to keep on the sample.
4. Ensure you clean the sample with IPA and DI Water after this step.
5. After this you must clean with MIF326 developer to remove the LOR 7B that does not come off with acetone and was underneath the S1805. The chip will be red in colour before this and become the original colour when started after cleaning.

A.3.2 Nanowire

A.3.2.1 Spin coating HSQ of NW E-Beam

This fabrication step covers parts 6) to 7) in Figure. A.3. The specification for the spin coating setting is found in Table. A.1.

1. Clean the spin coater, the hot plate, the pipette, the sample holder, and all equipment with IPA and Tissue Paper.

2. You will now perform the spin coating. You will need:
   Fox-16 HSQ
   Yellow 200μl Pipette
   Tissues Paper
   HSQ dedicated spin Guard
   Tweezers
   Spin Coater
   IPA
   Sample holder piece with small pillar on it (not Flat)
   Test sample tubes
   Hot Plate
   Pipette Tip Head

3. Take fresh HSQ out of the bottle into a small test sample tube and let it warm up for 20mins, by setting a timer. You can prepare the other equipment during this time.

4. The program for the spin coater (Spinner 2) is Prog 23: 2000RPM, 30seconds, 4000RPM/s

5. Cover the Sample completely with HSQ, ensure that the tip doesn't touch any surface, make sure there are no air bubbles in the deposited HSQ and spin up the spinner very shortly after depositing resist.

6. After spin coating the sample, ensure the back of the sample is clean or comes off after you bake, as it could just peel off then.

7. Bake for 2 mins at 150 degrees and then 2 mins at 200 degrees.

A.3.2.2 E-beam on nanowire and development

This fabrication step covers parts 7) to 8) in Figure. A.3. The specification for the spin coating setting is found in Table. A.3.

1. Following the designs provided by the GDS. E-beam the nanowire to match and expand onto the Au probe contact pads, to ensure a strong connection and that the impedance constraint is only in the detection area of the nanowire.

2. Use the alignment markers and auto-align the nanowire, using the Au crossers to match the nanowire onto the contact pads. Make sure that layer 61 and auto-alignment markers are placed and that they are e-beamed onto the sample.

3. Develop the sample in TMAH for 2 minutes and stop the development with DI water. You can etch for a longer time if needed.

A.3.2.3 Etching of WSi nanowire

This fabrication step covers parts 8) to 9) in Figure. A.3. The specification for the spin coating setting is found in Table. A.2

1. Using the JLS etcher, run the recipe through first for 5 minutes with our own dedicated Si sample wafer as a holder. The recipe to Etch WSi and is:

   7nm/s 21 CHF3 SCC : 2 SF6 SCCM 50 Watts Power RF 10mTorr Pressure 50 seconds

2. Afterwards, place the sample in the centre and allow the system to pump down and etch the sample for 50 seconds. Do each sample individually, allowing them to be in the centre to ensure a uniform RF electric field strength of the sample.

3. Remove the sample and check the current and etching with the 4-probe measurement and the AFM.

A.3.3 Optical Components

A.3.3.1 Spin coating on PMMA

This fabrication step covers parts 9) to 10) in Figure. A.3. The specification for the spin coating setting is found in Table. A.1.

1. Clean the spin coater, the hot plate, the pipette, the sample holder, and all equipment with IPA and Tissue Paper.

2. You will now perform the spin coating. You will need:
   PMMA A4
   Yellow 200μl Pipette
   Tissues Paper
   HSQ dedicated spin Guard
   Tweezers

Spin Coater
IPA
Sample holder piece with small pillar on it (not Flat)
Test sample tubes
Hot Plate
Pipette Tip Head

3. Take fresh HSQ out of the bottle into a small test sample tube and let it warm up for 20mins, by setting a timer. You can prepare the other equipment during this time.
4. Program the spin coater with settings to: 4000RPM, 60seconds, 10000RPM/s
5. Cover the Sample completely with HSQ, ensure that the tip doesn't touch any surface, make sure there are no air bubbles in the deposited HSQ and spin up the spinner very shortly after depositing resist.
6. After spin coating the sample, ensure the back of the sample is clean or comes off after you bake, as it could just peel off then.
7. Bake for 90 seconds at 100 degrees.
8. Add a second layer repeating the steps above. As one coat will make 200nm thick which is not enough, a second coat will give 400nm thickness, enough to safely etch.

A.3.3.2 E-Beaming Optical Structures

This fabrication step covers parts 10) to 11) in Figure. A.3. The specification for the spin coating setting is found in Table. A.3

1. Using the designs from Macks previous work and the designs provided, the structure will just be one GC connected to another making multiple structures.
2. Take the GDS structure from the designs and go through E-beam Calibration. Use a base dose of 250μC and a dose factor 1.8-1.93, on the structures for HSQ. Use a low column mode, Aperture size 30, ensuring that focus, stigma, write field alignment and dot burning has occurred.
3. After the samples have been E-beamed, they will be developed in TMAH for 2 minutes and then washed in DI water to stop the development process. Inspect under the optical microscope for further development.
4. In this circumstance is we are using PMMA here, which is a positive resist and the sample. Therefore the e-beaming will occur in the locations where the structures are not located.

There will be trenches around the waveguide and GC to allow them to be etched out. Positive resist is being used to cover the Au contact pads, to then be allow use in the ICP etcher.

A.3.3.3 Etching the Si for Passive Optical Components

This fabrication step covers parts 11) to 12) in Figure. A.3. The specification for the spin coating setting is found in Table. A.2

1. Place the Sample on a Si wafer and place into the load lock of the ICP and insert the sample into the system. Wait for pump down and select the recipe named: MackSi2018a

2. Etch the device in the ICP etcher with a recipe of: 56:14 SCCM, SF6:CHF3, 30W RIE Power, 32nm/min You will have to use the Interferometor to track the etching and stop at the moment you reach the end of the Si as the etch rate can vary slightly.

3. Stop the etching immediately and remove the sample to then be taken for SEM.

4. Inspect the devices with SEM, looking at the wall roughness and the etch depth, measuring the contrast and ensuring that a HSQ capping layer still exists.

5. After etching, clean off the remaining PMMA with Acetone.

A.3.4 Geometrical Dimensions of all layers

For each step different layers are fabricated. For each step we list here the materials that were added and their dimensions as a look-up reference.

1. 1): SOI Si: 220 nm, SiO_2: 2000 nm, Si Substrate: millimetres

2. 1)→2): Superconducting Materials (WSi) 7-10 nm

3. 2)→4): LOR 7B 700 nm, S1805 500 nm

4. 4)→6): Cr 20 nm, Au 200 nm

5. 6)→8): HSQ 90 nm

6. 8)→12): HSQ 400 nm

A.4 Summary

In this appendices we have covered the techniques necessary to develop a waveguide integrated SNSPD, using the recipe defined. We described how to use E-beam Lithography, Sputters, Optical Lithography, RIE, and spin coating to perform the recipe. We provided a step through step guide of the tools needed and the processed used at each step. With these techniques it would be possible to continue on the research presented in Chapter 6, to fabricate the design to test the performance for comparison to simulations.

BIBLIOGRAPHY

[1] H.-K. K. Lo, M. Curty, and K. Tamaki, "Secure quantum key distribution," *Nature Photonics*, vol. 8, pp. 595–604, 7 2014.

[2] S. Wehner, D. Elkouss, and R. Hanson, "Quantum internet: A vision for the road ahead," *Science*, vol. 362, 10 2018.

[3] H.-K. K. Lo, M. Curty, and B. Qi, "Measurement-Device-Independent Quantum Key Distribution," *Physical Review Letters*, vol. 108, p. 130503, 3 2012.

[4] R. Shankar, *Principles of Quantum Mechanics*.
Springer US, 1994.

[5] B. G. Streetman, *Solid State Electronic Devices: Global Edition*.
2015.

[6] A. Kohnle, "Quantum Mechanics: A Paradigms Approach. Quantum Mechanics: A Paradigms Approach.David H.McIntyrewith contributions from Corinne A. Manogue, Janet Tate and thegroup at Oregon State University. 592 pp. Addison-Wesley, San Francisco, 2012," *American Journal of Physics*, vol. 80, pp. 650–651, 7 2012.

[7] P. C. Humphreys, B. J. Metcalf, J. B. Spring, M. Moore, X. M. Jin, M. B. Kolthammer, and I. A. Walmsley, "Linear optical quantum computing in a single spatial mode," in *Optics InfoBase Conference Papers*, p. QTh2A.4, Optical Society of America (OSA), 3 2014.

[8] C. Lupo, C. Ottaviani, D. Bunandar, D. Englund, G. Vallone, J. S. Shaari, J. L. Pereira, L. Banchi, M. Berta, M. Razavi, M. Tomamichel, P. Villoresi, P. Wallden, R. Colbeck, S. Pirandola, T. Gehring, U. L. Andersen, V. C. Usenko, G. Vallone, P. Villoresi, and P. Wallden, "Advances in quantum cryptography," *Advances in Optics and Photonics, Vol. 12, Issue 4, pp. 1012-1236*, vol. 12, pp. 1012–1236, 12 2020.

[9] V. Giovannetti, S. Lloyd, and L. MacCone, "Advances in quantum metrology," *Nature Photonics*, vol. 5, pp. 222–229, 4 2011.

[10] I. M. Georgescu, S. Ashhab, and F. Nori, "Quantum simulation," *Reviews of Modern Physics*, vol. 86, p. 153, 3 2014.

[11] M. A. Sepiol, A. C. Hughes, J. E. Tarlton, D. P. Nadlinger, T. G. Ballance, C. J. Ballance, T. P. Harty, A. M. Steane, J. F. Goodwin, and D. M. Lucas, "Probing qubit memory errors at the part-per-million level," *Physical Review Letters*, vol. 123, p. 110503, 9 2019.

[12] D. Loss and D. P. DiVincenzo, "Quantum Computation with Quantum Dots," *Physical Review A - Atomic, Molecular, and Optical Physics*, vol. 57, pp. 120–126, 1 1997.

[13] A. Imamoglu, "Are quantum dots useful for quantum computation?," in *Physica E: Low-Dimensional Systems and Nanostructures*, vol. 16, pp. 47–50, North-Holland, 1 2003.

[14] F. Arute, K. Arya, R. Babbush, D. Bacon, J. C. Bardin, R. Barends, R. Biswas, S. Boixo, F. G. Brandao, D. A. Buell, B. Burkett, Y. Chen, Z. Chen, B. Chiaro, R. Collins, W. Courtney, A. Dunsworth, E. Farhi, B. Foxen, A. Fowler, C. Gidney, M. Giustina, R. Graff, K. Guerin, S. Habegger, M. P. Harrigan, M. J. Hartmann, A. Ho, M. Hoffmann, T. Huang, T. S. Humble, S. V. Isakov, E. Jeffrey, Z. Jiang, D. Kafri, K. Kechedzhi, J. Kelly, P. V. Klimov, S. Knysh, A. Korotkov, F. Kostritsa, D. Landhuis, M. Lindmark, E. Lucero, D. Lyakh, S. Mandrà, J. R. McClean, M. McEwen, A. Megrant, X. Mi, K. Michielsen, M. Mohseni, J. Mutus, O. Naaman, M. Neeley, C. Neill, M. Y. Niu, E. Ostby, A. Petukhov, J. C. Platt, C. Quintana, E. G. Rieffel, P. Roushan, N. C. Rubin, D. Sank, K. J. Satzinger, V. Smelyanskiy, K. J. Sung, M. D. Trevithick, A. Vainsencher, B. Villalonga, T. White, Z. J. Yao, P. Yeh, A. Zalcman, H. Neven, and J. M. Martinis, "Quantum supremacy using a programmable superconducting processor," *Nature*, vol. 574, pp. 505–510, 10 2019.

[15] J. R. Weber, W. F. Koehl, J. B. Varley, A. Janotti, B. B. Buckley, C. G. Van De Walle, and D. D. Awschalom, "Quantum computing with defects," *Proceedings of the National Academy of Sciences of the United States of America*, vol. 107, pp. 8513–8518, 5 2010.

[16] J. W. Silverstone, D. Bonneau, K. Ohira, N. Suzuki, H. Yoshida, N. Iizuka, M. Ezaki, C. M. Natarajan, M. G. Tanner, R. H. Hadfield, V. Zwiller, G. D. Marshall, J. G. Rarity, J. L. O 'brien, and M. G. Thompson, "On-chip quantum interference between silicon photon-pair sources," 2014.

[17] B. M. Terhal, "Quantum supremacy, here we come," *Nature Physics*, vol. 14, pp. 530–531, 6 2018.

[18] A. B. Arons and M. B. Peppard, "Einstein's Proposal of the Photon Concept—a Translation of the Annalen der Physik Paper of 1905," *American Journal of Physics*, vol. 33, pp. 367–374, 5 1965.

[19] V. Scarani, H. Bechmann-Pasquinucci, N. J. Cerf, M. Dušek, N. Lütkenhaus, and M. Peev, "The security of practical quantum key distribution," *Reviews of Modern Physics*, vol. 81, pp. 1301–1350, 9 2009.

[20] P. Chaiwongkhot, S. Sajeed, L. Lydersen, and V. Makarov, "Finite-key-size effect in a commercial plug-and-play QKD system," *Quantum Science and Technology*, vol. 2, p. 044003, 12 2017.

[21] N. Gisin and R. Thew, "Quantum communication," *Nature Photonics*, vol. 1, pp. 165–171, 3 2007.

[22] A. Politi, J. C. F. Matthews, M. G. Thompson, and J. L. O'Brien, "Integrated quantum photonics," *IEEE Journal on Selected Topics in Quantum Electronics*, vol. 15, pp. 1673–1684, 11 2009.

[23] X. Qiang, X. Zhou, J. Wang, C. M. Wilkes, T. Loke, S. O'Gara, L. Kling, G. D. Marshall, R. Santagati, T. C. Ralph, J. B. Wang, J. L. O'Brien, M. G. Thompson, and J. C. F. Matthews, "Large-scale silicon quantum photonics implementing arbitrary two-qubit processing," *Nature Photonics*, vol. 12, pp. 534–539, 9 2018.

[24] H.-S. Zhong, H. Wang, Y.-H. Deng, M.-C. Chen, L.-C. Peng, Y.-H. Luo, J. Qin, D. Wu, X. Ding, Y. Hu, P. Hu, X.-Y. Yang, W.-J. Zhang, H. Li, Y. Li, X. Jiang, L. Gan, G. Yang, L. You, Z. Wang, L. Li, N.-L. Liu, C.-Y. Lu, and J.-W. Pan, "Quantum computational advantage using photons," *Science*, vol. 370, pp. 1460–1463, 12 2020.

[25] J. P. Dowling and G. J. Milburn, "Quantum technology: the second quantum revolution," *Philosophical Transactions of the Royal Society of London. Series A: Mathematical, Physical and Engineering Sciences*, vol. 361, pp. 1655–1674, 8 2003.

[26] Stephen Barnett, *Quantum Information*.
Oxford: Oxford University Press, oxford mas ed., 2009.

[27] M. A. Nielsen and I. L. Chuang, *Quantum Computation and Quantum Information*.
Cambridge University Press, 2004.

[28] G. Lindblad, "A general no-cloning theorem," *Letters in Mathematical Physics*, vol. 47, pp. 189–196, 1 1999.

[29] J. M. Lukens and P. Lougovski, "Frequency-encoded photonic qubits for scalable quantum information processing," *Optica*, vol. 4, p. 8, 12 2016.

[30] A. Crespi, R. Ramponi, R. Osellame, L. Sansoni, I. Bongioanni, F. Sciarrino, G. Vallone, and P. Mataloni, "Integrated photonic quantum gates for polarization qubits," *Nature Communications*, vol. 2, pp. 1–6, 11 2011.

[31] Y. Wang, Z. Hu, B. C. Sanders, and S. Kais, "Qudits and high-dimensional quantum computing," *Frontiers in Physics*, vol. 8, 7 2020.

[32] G. Cañas, N. Vera, J. Cariñe, P. González, J. Cardenas, P. W. R. Connolly, A. Przysiezna, E. S. Gómez, M. Figueroa, G. Vallone, P. Villoresi, T. F. da Silva, G. B. Xavier, and G. Lima, "High-dimensional decoy-state quantum key distribution over 0.3 km of multicore telecommunication optical fibers," *Physical Review A*, vol. 96, 10 2016.

[33] A. Einstein, B. Podolsky, and N. Rosen, "Can quantum-mechanical description of physical reality be considered complete?," *Physical Review*, vol. 47, pp. 777–780, 5 1935.

[34] R. Santagati, J. W. Silverstone, M. J. Strain, M. Sorel, S. Miki, T. Yamashita, M. Fujiwara, M. Sasaki, H. Terai, M. G. Tanner, C. M. Natarajan, R. H. Hadfield, J. L. O'Brien, and M. G. Thompson, "Silicon photonic processor of two-qubit entangling quantum logic," *Journal of Optics (United Kingdom)*, vol. 19, p. 114006, 10 2017.

[35] J. Wang, S. Paesani, Y. Ding, R. Santagati, P. Skrzypczyk, A. Salavrakos, J. Tura, R. Augusiak, L. Mančinska, D. Bacco, D. Bonneau, J. W. Silverstone, Q. Gong, A. Acín, K. Rottwitt, L. K. Oxenløwe, J. L. O'Brien, A. Laing, and M. G. Thompson, "Multidimensional quantum entanglement with large-scale integrated optics," *Science*, vol. 360, pp. 285–291, 4 2018.

[36] S. Wang, C. X. Liu, J. Li, and Q. Wang, "Research on the Hong-Ou-Mandel interference with two independent sources," *Scientific Reports*, vol. 9, pp. 1–7, 12 2019.

[37] K. I. Harada, H. Takesue, H. Fukuda, T. Tsuchizawa, T. Watanabe, K. Yamada, Y. Tokura, and S. I. Itabashi, "Indistinguishable photon pair generation using two independent silicon wire waveguides," *New Journal of Physics*, vol. 13, p. 065005, 6 2011.

[38] P. Kok, H. Lee, and J. P. Dowling, "Creation of large-photon-number path entanglement conditioned on photodetection," *Physical Review A - Atomic, Molecular, and Optical Physics*, vol. 65, p. 5, 4 2002.

[39] L. Zhang and K. W. C. Chan, "Scalable Generation of Multi-mode NOON States for Quantum Multiple-phase Estimation," *Scientific Reports*, vol. 8, p. 11440, 12 2018.

[40] M. Wieśniak, T. Paterek, and A. Zeilinger, "Entanglement in mutually unbiased bases," *New Journal of Physics*, vol. 13, p. 053047, 5 2011.

[41] R. L. Rivest, A. Shamir, and L. Adleman, "A Method for Obtaining Digital Signatures and Public-Key Cryptosystems," *Communications of the ACM*, vol. 21, pp. 120–126, 2 1978.

[42] V. Scarani, H. Bechmann-Pasquinucci, N. J. Cerf, M. Dusek, N. Lutkenhaus, and M. Peev, "The Security of Practical Quantum Key Distribution," 2 2008.

[43] P. Shor, "Algorithms for quantum computation: discrete logarithms and factoring," pp. 124–134, Institute of Electrical and Electronics Engineers (IEEE), 12 2002.

[44] C. H. Bennett and G. Brassard, "Quantum cryptography: Public key distribution and coin tossing," *Theoretical Computer Science*, vol. 560, pp. 7–11, 3 2014.

[45] H. F. Chau, "Practical scheme to share a secret key through a quantum channel with a 27.6% bit error rate," *Physical Review A*, vol. 66, no. 6, p. 4, 2002.

[46] N. Jain, E. Anisimova, I. Khan, V. Makarov, C. Marquardt, and G. Leuchs, "Trojan-horse attacks threaten the security of practical quantum cryptography," *New Journal of Physics*, vol. 16, p. 123030, 12 2014.

[47] F. Xu, M. Curty, B. Qi, and H.-K. Lo, "Practical aspects of measurement-device-independent quantum key distribution," *New Journal of Physics*, vol. 15, p. 11, 5 2013.

[48] Y. Liu, T.-Y. Chen, J.-H. J. Wang, W.-Q. Cai, X. Wan, L.-K. Chen, J.-H. J. Wang, S.-B. Liu, H. Liang, L. Yang, C.-Z. Peng, K. Chen, Z.-B. Chen, and J.-W. Pan, "Decoy-state quantum key distribution with polarized photons over 200 km," *Optics Express*, vol. 18, p. 8587, 4 2010.

[49] J. Leuthold, C. Koos, and W. Freude, "Nonlinear silicon photonics," *Nature Photonics*, vol. 4, pp. 535–544, 8 2010.

[50] J. W. Silverstone, D. Bonneau, J. L. O'Brien, and M. G. Thompson, "Silicon Quantum Photonics," *IEEE Journal of Selected Topics in Quantum Electronics*, vol. 22, pp. 390–402, 11 2016.

[51] M. Azadeh, "Fiber Optic Communications: A Review," pp. 1–27, Springer, Boston, MA, 2009.

[52] M. Lemmens, "Lidar," *GIM International*, vol. 21, p. 11, 2 2007.

[53] L. M. Rosenfeld, D. A. Sulway, G. F. Sinclair, V. Anant, M. G. Thompson, J. G. Rarity, and J. W. Silverstone, "Mid-infrared quantum optics in silicon," *Optics Express 28*, vol. 25, pp. 37092 – 37102, 6 2019.

[54] M. Poot, C. Schuck, X.-s. Ma, X. Guo, and H. X. Tang, "Design and characterization of integrated components for SiN photonic quantum circuits," *Optics Express*, vol. 24, p. 6843, 4 2016.

[55] A. D. Greentree, M. R. Henderson, B. C. Gibson, H. Ebendorff-Heidepriem, K. Kuan, V. S. Afshar, J. O. Orwa, I. Aharonovich, T. J. Karle, S. Tomljenovic-Hanic, S. Prawer, and T. M. Monro, "Diamond in glass, a new platform for quantum photonics," in *Optics InfoBase Conference Papers*, Optical Society of America (OSA), 2012.

[56] D. Marris-Morini, V. Vakarin, J. M. Ramirez, Q. Liu, A. Ballabio, J. Frigerio, M. Montesinos, C. Alonso-Ramos, X. Le Roux, S. Serna, D. Benedikovic, D. Chrastina, L. Vivien, and G. Isella, "Germanium-based integrated photonics from near- to mid-infrared applications," *Nanophotonics*, vol. 7, pp. 1781–1793, 11 2018.

[57] T. K. Sharma, M. Zorn, F. Bugge, R. Hülsewede, G. Erbert, and M. Weyers, "High-power highly strained InGaAs quantum-well lasers operating at 1.2 μm," *IEEE Photonics Technology Letters*, vol. 14, pp. 887–889, 7 2002.

[58] J. C. Adcock, C. Vigliar, R. Santagati, J. W. Silverstone, and M. G. Thompson, "Programmable four-photon graph states on a silicon chip," *Nature Communications*, vol. 10, p. 3528 (2019), 12 2019.

[59] J. Carolan, C. Harrold, C. Sparrow, E. Martín-López, N. J. Russell, J. W. Silverstone, P. J. Shadbolt, N. Matsuda, M. Oguma, M. Itoh, G. D. Marshall, M. G. Thompson, J. C. F. Matthews, T. Hashimoto, J. L. O'Brien, and A. Laing, "Universal linear optics," *Science*, vol. 349, pp. 711–716, 8 2015.

[60] C. M. Hessel, E. J. Henderson, and J. G. Veinot, "Hydrogen silsesquioxane: A molecular precursor for nanocrystalline Si-SiO2 composites and freestanding hydride-surface-terminated silicon nanoparticles," *Chemistry of Materials*, vol. 18, pp. 6139–6146, 12 2006.

[61] D. E. Hagan and A. P. Knights, "Mechanisms for optical loss in SOI waveguides for mid-infrared wavelengths around 2 μm," *Journal of Optics (United Kingdom)*, vol. 19, 2 2017.

[62] F. P. Payne and J. P. Lacey, "A theoretical analysis of scattering loss from planar optical waveguides," *Optical and Quantum Electronics*, vol. 26, pp. 977–986, 10 1994.

[63] M. Gnan, S. Thoms, D. S. MacIntyre, R. M. De La Rue, and M. Sorel, "Fabrication of low-loss photonic wires in silicon-on-insulator using hydrogen silsesquioxane electron-beam resist," *Electronics Letters*, vol. 44, no. 2, pp. 115–116, 2008.

[64] T. Horikawa, D. Shimura, and T. Mogami, "Low-loss silicon wire waveguides for optical integrated circuits," *MRS Communications*, vol. 6, pp. 9–15, 3 2016.

[65] S. Suzuki, M. Yanagisawa, Y. Hibino, and K. Oda, "High-Density Integrated Planar Lightwave Circuits Using SiO2-GeO2 Waveguides with a High Refractive Index Difference," *Journal of Lightwave Technology*, vol. 12, no. 5, pp. 790–796, 1994.

[66] O. Salehzadeh, M. Vachon, N. Sabourin, S. Janz, and A. J. SpringThorpe, "Vertically tapered waveguide spot size converters fabricated via a linewidth controlled grey tone

lithography for InP-based photonic integrated circuits," *Optics Express*, vol. 28, p. 23523, 8 2020.

[67] R. Marchetti, C. Lacava, A. Khokhar, X. Chen, I. Cristiani, D. J. Richardson, G. T. Reed, P. Petropoulos, and P. Minzioni, "High-efficiency grating-couplers: Demonstration of a new design strategy," *Scientific Reports*, vol. 7, pp. 1–8, 12 2017.

[68] N. Hoppe, W. S. Zaoui, L. Rathgeber, Y. Wang, R. H. Klenk, W. Vogel, M. Kaschel, S. L. Portalupi, J. Burghartz, and M. Berroth, "Ultra-Efficient Silicon-on-Insulator Grating Couplers with Backside Metal Mirrors," *IEEE Journal of Selected Topics in Quantum Electronics*, vol. 26, 3 2020.

[69] Y. Luo, Y. Yu, M. Ye, C. Sun, and X. Zhang, "Integrated dual-mode 3 dB power coupler based on tapered directional coupler," *Scientific Reports*, vol. 6, 3 2016.

[70] A. P. Foster, B. Royall, C. Bentham, E. Clarke, L. R. Wilson, M. S. Skolnick, and Z. K. Bishop, "Electro-mechanical control of an on-chip optical beam splitter containing an embedded quantum emitter," *Optics Letters, Vol. 43, Issue 9, pp. 2142-2145*, vol. 43, pp. 2142–2145, 5 2018.

[71] L. Chrostowski and M. E. Hochberg, *Silicon photonics design*.
Cambridge: Cambridge University Press, 2015.

[72] A. Yariv, "Coupled-Mode theory for guided-wave optics," *IEEE Journal of Quantum Electronics*, vol. 9, no. 9, pp. 919–933, 1973.

[73] M. Johnson, M. G. Thompson, and D. Sahin, "Low-loss, low-crosstalk waveguide crossing for scalable integrated silicon photonics applications," *Optics Express*, vol. 28, p. 12498, 4 2020.

[74] M. Johnson, M. G. Thompson, and D. Sahin, "Low-loss, low-crosstalk waveguide crossing for scalable integrated silicon photonics applications," *Optics Express*, vol. 28, p. 12498, 4 2020.

[75] L. Chen and Y.-k. Chen, "Compact, low-loss and low-power 8×8 broadband silicon optical switch," *Optics Express*, vol. 20, p. 18977, 8 2012.

[76] S. Han, T. J. Seok, N. Quack, B.-W. Yoo, and M. C. Wu, "Large-scale silicon photonic switches with movable directional couplers," *Optica*, vol. 2, p. 370, 4 2015.

[77] P. J. Bock, P. Cheben, J. H. Schmid, J. Lapointe, A. Delâge, D.-X. Xu, S. Janz, A. Densmore, and T. J. Hall, "Subwavelength grating crossings for silicon wire waveguides," *Optics Express*, vol. 18, p. 16146, 7 2010.

[78] E. A. J. Marcatili, "Dielectric Rectangular Waveguide and Directional Coupler for Integrated Optics," *Bell System Technical Journal*, vol. 48, pp. 2071–2102, 9 1969.

[79] Y. Tan and D. Dai, "Silicon microring resonators," *Journal of Optics (United Kingdom)*, vol. 20, p. 054004, 5 2018.

[80] M. Jacques, A. Samani, E. El-Fiky, D. Patel, Z. Xing, and D. V. Plant, "Optimization of thermo-optic phase-shifter design and mitigation of thermal crosstalk on the SOI platform," *Optics Express*, vol. 27, p. 10456, 4 2019.

[81] B. J. Frey, D. B. Leviton, and T. J. Madison, "Temperature-dependent refractive index of silicon and germanium," in *Optomechanical Technologies for Astronomy* (E. Atad-Ettedgui, J. Antebi, and D. Lemke, eds.), vol. 6273, p. 62732J, SPIE, 6 2006.

[82] D. Mishra and R. K. Sonkar, "2D modeling of silicon optical PN phase shifter," *Applied Optics*, vol. 59, p. 998, 2 2020.

[83] R. Foord, R. Jones, C. J. Oliver, and E. R. Pike, "The Use of Photomultiplier Tubes for Photon Counting," *Applied Optics*, vol. 8, p. 1975, 10 1969.

[84] S. Cova, A. Longoni, and A. Andreoni, "Towards picosecond resolution with single-photon avalanche diodes," *Review of Scientific Instruments*, vol. 52, pp. 408–412, 3 1981.

[85] M. D. Eisaman, J. Fan, A. Migdall, and S. V. Polyakov, "Invited Review Article: Single-photon sources and detectors," *Review of Scientific Instruments*, vol. 82, 7 2011.

[86] S. Cova, A. Lacaita, M. Ghioni, G. Ripamonti, and T. A. Louis, "20-ps timing resolution with single-photon avalanche diodes," *Review of Scientific Instruments*, vol. 60, pp. 1104–1110, 6 1989.

[87] B. T. Matthias, T. H. Geballe, and V. B. Compton, "Superconductivity," *Reviews of Modern Physics*, vol. 35, pp. 1–22, 1 1963.

[88] J. Bardeen, L. N. Cooper, and J. R. Schrieffer, "Theory of superconductivity," *Physical Review*, vol. 108, pp. 1175–1204, 12 1957.

[89] A. Peacock, P. Verhoeve, N. Rando, A. Van Dordrecht, B. G. Taylor, C. Erd, M. A. Perryman, R. Venn, J. Howlett, D. J. Goldie, J. Lumley, and M. Wallis, "Single optical photon detection with a superconducting tunnel junction," *Nature*, vol. 381, pp. 135–137, 5 1996.

[90] T. Gerrits, N. Thomas-Peter, J. C. Gates, A. E. Lita, B. J. Metcalf, B. Calkins, N. A. Tomlin, A. E. Fox, A. L. Linares, J. B. Spring, N. K. Langford, R. P. Mirin, P. G. R. Smith, I. A. Walmsley, and S. W. Nam, "On-chip, photon-number-resolving, telecom-band detectors for scalable photonic information processing," 7 2011.

[91] C. Zhang, P. A. R. Ade, Z. Ahmed, M. Amiri, D. Barkats, R. B. Thakur, C. A. Bischoff, J. J. Bock, H. Boenish, E. Bullock, V. Buza, J. Cheshire, J. Connors, J. Cornelison, M. Crumrine, A. Cukierman, M. Dierickx, L. Duband, S. Fatigoni, J. P. Filippini, G. Hall, M. Halpern, S. Harrison, S. Henderson, S. R. Hildebrandt, G. C. Hilton, H. Hui, K. D. Irwin, J. Kang, K. S. Karkare, E. Karpel, S. Kefeli, J. M. Kovac, C. L. Kuo, K. Lau, K. G. Megerian, L. Moncelsi, T. Namikawa, H. T. Nguyen, R. O'Brient, S. Palladino, N. Precup, T. Prouvé, C. Pryke, B. Racine, C. D. Reintsema, S. Richter, A. Schillaci, B. Schmitt, R. Schwarz, C. D. Sheehy, A. Soliman, T. S. Germaine, B. Steinbach, R. V. Sudiwala, K. L. Thompson, C. Tucker, A. D. Turner, C. Umiltà, A. G. Vieregg, A. Wandui, A. C. Weber, D. V. Wiebe, J. Willmert, W. L. K. Wu, E. Yang, K. W. Yoon, E. Young, and C. Yu, "Characterizing the Sensitivity of 40 GHz TES Bolometers for BICEP Array," *Journal of Low Temperature Physics*, vol. 199, pp. 968–975, 2 2020.

[92] G. Gol'Tsman, O. Okunev, G. Chulkova, A. Lipatov, A. Dzardanov, K. Smirnov, A. Semenov, B. Voronov, C. Williams, and R. Sobolewski, "Fabrication and properties of an ultrafast NbN hot-electron single-photon detector," in *IEEE Transactions on Applied Superconductivity*, vol. 11, pp. 574–577, 3 2001.

[93] W. H. Pernice, C. Schuck, O. Minaeva, M. Li, G. N. Goltsman, A. V. Sergienko, and H. X. Tang, "High-speed and high-efficiency travelling wave single-photon detectors embedded in nanophotonic circuits," *Nature Communications*, vol. 3, pp. 1–10, 12 2012.

[94] J. P. Allmaras, A. G. Kozorezov, A. D. Beyer, F. Marsili, R. M. Briggs, and M. D. Shaw, "Thin-Film Thermal Conductivity Measurements Using Superconducting Nanowires," *Journal of Low Temperature Physics*, pp. 1–7, 7 2018.

[95] Y. Ivry, J. J. Surick, M. Barzilay, C.-S. Kim, F. Najafi, E. Kalfon-Cohen, A. D. Dane, and K. K. Berggren, "Superconductor–superconductor bilayers for enhancing single-photon detection," *Nanotechnology*, vol. 28, p. 435205, 10 2017.

[96] A. V. Antipov, V. A. Seleznev, Y. B. Vakhtomin, P. V. Morozov, D. D. Vasilev, E. I. Malevannaya, K. M. Moiseev, and K. Smirnov, "Investigation of WSi and NbN superconducting single-photon detectors in mid-IR range," in *IOP Conference Series: Materials Science and Engineering*, vol. 781, Institute of Physics Publishing, 4 2020.

[97] A. Vetter, S. Ferrari, P. Rath, R. Alaee, O. Kahl, V. Kovalyuk, S. Diewald, G. N. Goltsman, A. Korneev, C. Rockstuhl, and W. H. P Pernice, "Cavity-Enhanced and Ultrafast Superconducting Single-Photon Detectors," *Nano Letters*, vol. 16, no. 11, pp. 7085 – 7092, 2016.

[98] E. Schmidt, K. Ilin, and M. Siegel, "AlN-Buffered Superconducting NbN Nanowire Single-Photon Detector on GaAs," *IEEE Transactions on Applied Superconductivity*, vol. 27, pp. 1–5, 6 2016.

[99] S. Khasminskaya, F. Pyatkov, K. Słowik, S. Ferrari, O. Kahl, V. Kovalyuk, P. Rath, A. Vetter, F. Hennrich, M. M. Kappes, G. Gol'tsman, A. Korneev, C. Rockstuhl, R. Krupke, and W. H. P. Pernice, "Fully integrated quantum photonic circuit with an electrically driven light source," *Nature Photonics*, vol. 10, pp. 727–732, 11 2016.

[100] S. Miki, T. Yamashita, M. Fujiwara, M. Sasaki, and Z. Wang, "Multichannel SNSPD system with high detection efficiency at telecommunication wavelength," *Optics Letters*, vol. 35, p. 2133, 7 2010.

[101] H. Zhang, L. Xiao, B. Luo, J. Guo, L. Zhang, and J. Xie, "The potential and challenges of time-resolved single-photon detection based on current-carrying superconducting nanowires," *Journal of Physics D: Applied Physics*, vol. 53, p. 013001, 1 2020.

[102] K. Jousten, ed., *Handbook of Vacuum Technology*.
Weinheim, Germany: Wiley-VCH Verlag GmbH & Co. KGaA, 6 2016.

[103] J. F. Allen and A. D. Misener, *Flow of liquid helium II*, vol. 141.
Nature Publishing Group, 1 1938.

[104] D. SHOENBERG, "Low Temperature Physics," *Nature*, vol. 162, pp. 510–510, 10 1948.

[105] H. O. McMahon and W. E. Gifford, "A New Low-Temperature Gas Expansion Cycle," in *Advances in Cryogenic Engineering*, pp. 354–367, Springer US, 1960.

[106] I. Urieli and D. M. Berchowitz, *Stirling cycle engine analysis*.
1984.

[107] F. Li, D. Chen, L. He, and J. Cong, "Architecture evaluation for power-efficient FPGAs," in *Proceedings of the 2003 ACM/SIGDA eleventh international symposium on Field programmable gate arrays - FPGA '03*, (New York, New York, USA), p. 175, Association for Computing Machinery (ACM), 2003.

[108] G. Smith, *FPGAs 101*.
Elsevier, 2010.

[109] R. Mueller, J. Teubner, and G. Alonso, "Data processing on FPGAs," *Proceedings of the VLDB Endowment*, vol. 2, pp. 910–921, 8 2009.

[110] S. Hauck, "The roles of FPGA's in reprogrammable systems," *Proceedings of the IEEE*, vol. 86, no. 4, pp. 615–638, 1998.

[111] J. J. Rodriguez-Andina, M. J. Moure, and M. D. Valdes, "Features, design tools, and application domains of FPGAs," *IEEE Transactions on Industrial Electronics*, vol. 54, pp. 1810–1823, 8 2007.

[112] I. Kuon and J. Rose, *Quantifying and exploring the gap between FPGAs and ASICs: Measuring and exploring*.
Springer US, 2010.

[113] F. M. Zhu, S. C. Hsieh, W. W. Yen, and H. P. Chou, "A digital coincidence measurement system using FPGA techniques," in *Nuclear Instruments and Methods in Physics Research, Section A: Accelerators, Spectrometers, Detectors and Associated Equipment*, vol. 652, pp. 454–457, North-Holland, 10 2011.

[114] E. Engin, D. Bonneau, C. M. Natarajan, A. S. Clark, M. G. Tanner, R. H. Hadfield, S. N. Dorenbos, V. Zwiller, K. Ohira, N. Suzuki, H. Yoshida, N. Iizuka, M. Ezaki, J. L. O'Brien, and M. G. Thompson, "Photon pair generation in a silicon micro-ring resonator with reverse bias enhancement," *Optics Express*, vol. 21, p. 27826, 11 2013.

[115] S. Tancock, E. Arabul, and N. Dahnoun, "A Review of New Time-To-Digital Conversion Techniques," *IEEE Transactions on Instrumentation and Measurement*, vol. 68, pp. 3406–3417, 10 2019.

[116] C. Wang, H. Li, Y. Zhang, H. Baghaei, R. Ramirez, S. Liu, S. An, and W. H. Wong, "A real time coincidence system for high count-rate TOF or non-TOF PET cameras using hybrid method combining AND-logic and Time-mark technology," in *2009 16th IEEE-NPSS Real Time Conference - Conference Record*, pp. 321–325, 2009.

[117] R. Nock, N. Dahnoun, and J. Rarity, "Low cost timing interval analyzers for quantum key distribution," in *Conference Record - IEEE Instrumentation and Measurement Technology Conference*, pp. 475–479, 2011.

[118] X. Hu, L. Zhao, S. Liu, J. Wang, and Q. An, "A stepped-up tree encoder for the 10-ps wave union TDC," *IEEE Transactions on Nuclear Science*, vol. 60, no. 5, pp. 3544–3549, 2013.

[119] A. Samarah and A. C. Carusone, "A digital phase-locked loop with calibrated coarse and stochastic fine TDC," *IEEE Journal of Solid-State Circuits*, vol. 48, no. 8, pp. 1829–1841, 2013.

[120] J. Kalisz, "Review of methods for time interval measurements with picosecond resolution," *Metrologia*, vol. 41, pp. 17–32, 2 2004.

[121] H. Zhou and J. Bruck, "A Universal Scheme for Transforming Binary Algorithms to Generate Random Bits from Loaded Dice," *arXiv preprint arXiv:1209.0726*, 9 2012.

[122] B. K. Swann, B. J. Blalock, L. G. Clonts, D. M. Binkley, J. M. Rochelle, E. Breeding, and K. M. Baldwin, "A 100-ps time-resolution CMOS time-to-digital converter for positron emission tomography imaging applications," *IEEE Journal of Solid-State Circuits*, vol. 39, pp. 1839–1852, 11 2004.

[123] J. Kostamovaara and R. Myllylä, "Time-to-digital converter with an analog interpolation circuit," *Review of Scientific Instruments*, vol. 57, pp. 2880–2885, 11 1986.

[124] S. Mandai and E. Charbon, "A 128-channel, 9ps column-parallel two-stage TDC based on time difference amplification for time-resolved imaging," in *European Solid-State Circuits Conference*, pp. 119–122, 2011.

[125] A. Elkholy, T. Anand, W. S. Choi, A. Elshazly, and P. K. Hanumolu, "A 3.7 mW Low-Noise Wide-Bandwidth 4.5 GHz Digital Fractional-N PLL Using Time Amplifier-Based TDC," *IEEE Journal of Solid-State Circuits*, vol. 50, pp. 867–881, 4 2015.

[126] A. S. Yousif and J. W. Haslett, "A fine resolution TDC architecture for next generation PET imaging," *IEEE Transactions on Nuclear Science*, vol. 54, pp. 1574–1582, 10 2007.

[127] J. P. Jansson, P. Keranen, S. Jahromi, and J. Kostamovaara, "Enhancing Nutt-Based Time-to-Digital Converter Performance with Internal Systematic Averaging," *IEEE Transactions on Instrumentation and Measurement*, vol. 69, pp. 3928–3935, 6 2020.

[128] Zaworski, D. Chaberski, M. Kowalski, and M. Zieliński, "Quantization Error in Time-to-Digital Converters," *Metrology and Measurement Systems*, vol. 19, pp. 115–122, 1 2012.

[129] S. Friedrichs, M. Fugger, and C. Lenzen, "Metastability-Containing Circuits," *IEEE Transactions on Computers*, vol. 67, pp. 1167–1183, 8 2018.

[130] C. Lenzen and M. Medina, "Efficient metastability-containing gray code 2-sort," in *Proceedings - International Symposium on Asynchronous Circuits and Systems*, vol. 2016-Octob, pp. 49–56, IEEE Computer Society, 10 2016.

[131] K. Katoh and K. Namba, "A low area calibration technique of TDC using variable clock generator for accurate on-line delay measurement," in *Proceedings - International Symposium on Quality Electronic Design, ISQED*, vol. 2015-April, pp. 430–434, IEEE Computer Society, 4 2015.

[132] Y. Ding, D. Bacco, K. Dalgaard, X. Cai, X. Zhou, K. Rottwitt, and L. K. Oxenløwe, "High-Dimensional Quantum Key Distribution based on Multicore Fiber using Silicon Photonic Integrated Circuits," *npj Quantum Information*, vol. 3, p. 25, 10 2016.

[133] B. Da Lio, L. K. Oxenløwe, D. Bacco, D. Cozzolino, N. Biagi, T. N. Arge, E. Larsen, K. Rottwitt, Y. Ding, and A. Zavatta, "Stable Transmission of High-Dimensional Quantum States over a 2-km Multicore Fiber," *IEEE Journal of Selected Topics in Quantum Electronics*, vol. 26, 7 2020.

[134] Y. Jo, H. Park, S.-W. Lee, and W. Son, "Efficient High-Dimensional Quantum Key Distribution with Hybrid Encoding," *Entropy*, vol. 21, p. 80, 1 2019.

[135] D.-S. Ding, W. Zhang, S. Shi, Z.-Y. Zhou, Y. Li, B.-S. Shi, and G.-C. Guo, "High-dimensional entanglement between distant atomic ensemble memories," *Light: Science & Applications 5*, vol. 10, pp. e16157–e16157, 12 2016.

[136] M. Erhard, M. Krenn, and A. Zeilinger, "Advances in High Dimensional Quantum Entanglement," *Nature Reviews Physics*, vol. 2, pp. 365–381, 11 2019.

[137] M. Kues, C. Reimer, P. Roztocki, L. R. Cortés, S. Sciara, B. Wetzel, Y. Zhang, A. Cino, S. T. Chu, B. E. Little, D. J. Moss, L. Caspani, J. Azaña, and R. Morandotti, "On-chip generation of high-dimensional entangled quantum states and their coherent control," *Nature*, vol. 546, pp. 622–626, 6 2017.

[138] M. Malik, M. Erhard, M. Huber, M. Krenn, R. Fickler, and A. Zeilinger, "Multi-photon entanglement in high dimensions," *Nature Photonics*, vol. 10, pp. 248–252, 4 2016.

[139] S. K. Joshi, D. Aktas, S. Wengerowsky, M. Loncaric, S. P. Neumann, B. Liu, T. Scheidl, G. C. Lorenzo, Samec, L. Kling, A. Qiu, M. Razavi, M. Stipcevic, J. G. Rarity, and R. Ursin, "A trusted node-free eight-user metropolitan quantum communication network," *Science Advances*, vol. 6, p. eaba0959, 9 2020.

[140] J. Wang, S. Paesani, Y. Ding, R. Santagati, P. Skrzypczyk, A. Salavrakos, J. Tura, R. Augusiak, L. Mancinska, D. Bacco, D. Bonneau, J. W. Silverstone, Q. Gong, A. Acin, K. Rottwitt, L. K. Oxenlowe, J. L. O'Brien, A. Laing, M. G. Thompson, A. Laing, and M. Thompson, "Large-scale Integration of Multidimensional Quantum Photonics Circuits on Silicon," in *Conference on Lasers and Electro-Optics*, (Washington, D.C.), p. JTh5B.4, OSA, 5 2018.

[141] N. J. Cerf, M. Bourennane, A. Karlsson, and N. Gisin, "Security of quantum key distribution using d-level systems," *Physical Review Letters*, vol. 88, p. 4, 7 2001.

[142] D. Mayers and A. Yao, "Quantum cryptography with imperfect apparatus," in *Annual Symposium on Foundations of Computer Science - Proceedings*, pp. 503–509, IEEE Comp Soc, 1998.

[143] C. Branciard, E. G. Cavalcanti, S. P. Walborn, V. Scarani, and H. M. Wiseman, "One-sided Device-Independent Quantum Key Distribution: Security, feasibility, and the connection with steering," *Physical Review A - Atomic, Molecular, and Optical Physics*, vol. 85, 9 2011.

[144] S. Ristic, A. Bhardwaj, M. J. Rodwell, L. A. Johansson, and L. A. Coldren, "An Optical Phase-Locked Loop Photonic Integrated Circuit," *Journal of Lightwave Technology*, vol. 28, pp. 526–538, 2 2010.

[145] J. Y. Liu, H. J. Ding, C. M. Zhang, S. P. Xie, and Q. Wang, "Practical Phase-Modulation Stabilization in Quantum Key Distribution via Machine Learning," *Physical Review Applied*, vol. 12, p. 014059, 7 2019.

[146] H. J. Lee, S. K. Choi, and H. S. Park, "Experimental Demonstration of Four-Dimensional Photonic Spatial Entanglement between Multi-core Optical Fibres," *Scientific Reports*, vol. 7, pp. 1–8, 12 2017.

[147] Y. Ding, C. Peucheret, H. Ou, and K. Yvind, "Fully etched apodized grating coupler on the SOI platform with 058 dB coupling efficiency," *Optics Letters*, vol. 39, p. 5348, 9 2014.

[148] N. C. Harris, Y. Ma, J. Mower, T. Baehr-Jones, D. Englund, M. Hochberg, C. Galland, J. Sun, E. Timurdogan, A. Yaacobi, E. S. Hosseini, M. R. Watts, D. Kwong, A. Hosseini, J. Covey, Y. Zhang, X. Xu, H. Subbaraman, and R. T. Chen, "Large-scale nanophotonic phased array," *Nature*, vol. 493, pp. 195–199, 2013.

[149] D. Gross, Y. K. Liu, S. T. Flammia, S. Becker, and J. Eisert, "Quantum state tomography via compressed sensing," *Physical Review Letters*, vol. 105, p. 150401, 10 2010.

[150] D. Llewellyn, *Quantum Information Processing by Programming Optical Nano-Circuits in Silicon*.
PhD thesis, University of Bristol, 2020.

[151] J. Wang, D. Bonneau, M. Villa, J. W. Silverstone, R. Santagati, S. Miki, T. Yamashita, M. Fujiwara, M. Sasaki, H. Terai, M. G. Tanner, C. M. Natarajan, R. H. Hadfield, J. L. O'Brien, and M. G. Thompson, "Chip-to-chip quantum photonic interconnect by path-polarization interconversion," *Optica*, vol. 3, p. 407, 4 2016.

[152] M. Peev, T. Langer, T. Lorunser, A. Happe, O. Maurhart, A. Poppe, and T. Theme, "The SECOQC Quantum-Key-Distribution network in Vienna," in *Conference on Optical Fiber Communication, Technical Digest Series*, p. OThL2, Institute of Electrical and Electronics Engineers Inc., 3 2009.

[153] M. Sasaki, M. Fujiwara, H. Ishizuka, W. Klaus, K. Wakui, M. Takeoka, S. Miki, T. Yamashita, Z. Wang, A. Tanaka, K. Yoshino, Y. Nambu, S. Takahashi, A. Tajima, A. Tomita, T. Domeki, T. Hasegawa, Y. Sakai, H. Kobayashi, T. Asai, K. Shimizu, T. Tokura, T. Tsurumaru, M. Matsui, T. Honjo, K. Tamaki, H. Takesue, Y. Tokura, J. F. Dynes, A. R. Dixon, A. W. Sharpe, Z. L. Yuan, A. J. Shields, S. Uchikoga, M. Legré, S. Robyr, P. Trinkler, L. Monat, J.-B. J.-B. Page, G. Ribordy, A. Poppe, A. Allacher, O. Maurhart, T. Länger, M. Peev, and A. Zeilinger, "Field test of quantum key distribution in the Tokyo QKD Network," *Optics Express*, vol. 19, p. 10387, 5 2011.

[154] S. K. Liao, W. Q. Cai, W. Y. Liu, L. Zhang, Y. Li, J. G. Ren, J. Yin, Q. Shen, Y. Cao, Z. P. Li, F. Z. Li, X. W. Chen, L. H. Sun, J. J. Jia, J. C. Wu, X. J. Jiang, J. F. Wang, Y. M. Huang, Q. Wang, Y. L. Zhou, L. Deng, T. Xi, L. Ma, T. Hu, Q. Zhang, Y. A. Chen, N. L. Liu, X. B. Wang, Z. C. Zhu, C. Y. Lu, R. Shu, C. Z. Peng, J. Y. Wang, and J. W. Pan, "Satellite-to-ground quantum key distribution," *Nature*, vol. 549, pp. 43–47, 9 2017.

[155] B. M. Leiner, V. G. Cerf, D. D. Clark, R. E. Kahn, L. Kleinrock, D. C. Lynch, J. Postel, L. G. Roberts, and S. Wolff, "A brief history of the internet," *ACM SIGCOMM Computer Communication Review*, vol. 39, pp. 22–31, 10 2009.

[156] Andrew Dugan, "Intelligent network," tech. rep., 10 1999.

[157] Y. L. Tang, H. L. Yin, S. J. Chen, Y. Liu, W. J. Zhang, X. Jiang, L. Zhang, J. Wang, L. X. You, J. Y. Guan, D. X. Yang, Z. Wang, H. Liang, Z. Zhang, N. Zhou, X. Ma, T. Y. Chen, Q. Zhang, and J. W. Pan, "Measurement-device-independent quantum key distribution over 200 km," *Physical Review Letters*, vol. 113, p. 190501, 11 2014.

[158] L. You, X. Yang, Y. He, W. Zhang, D. Liu, W. Zhang, L. Zhang, L. Zhang, X. Liu, S. Chen, Z. Wang, and X. Xie, "Jitter analysis of a superconducting nanowire single photon detector," *AIP Advances*, vol. 3, no. 7, 2013.

[159] P. Hu, H. Li, L. You, H. Wang, Y. Xiao, J. Huang, X. Yang, W. Zhang, Z. Wang, and X. Xie, "Detecting single infrared photons toward optimal system detection efficiency," *Optics Express 28*, vol. 24, pp. 36884 – 36891, 9 2020.

[160] K. M. Svore, A. V. Aho, A. W. Cross, I. Chuang, and I. L. Markov, "A layered software architecture for quantum computing design tools," *Computer*, vol. 39, pp. 74–83, 1 2006.

[161] L. Schweickert, K. D. Jöns, K. D. Zeuner, S. F. Covre Da Silva, H. Huang, T. Lettner, M. Reindl, J. Zichi, R. Trotta, A. Rastelli, and V. Zwiller, "On-demand generation of background-free single photons from a solid-state source," *Applied Physics Letters*, vol. 112, p. 093106, 2 2018.

[162] "Photon Spot, 2021. [Online]. Available: https://www.photonspot.com/ [Accessed: 24- Mar-2021].."

[163] "ICEoxford - Innovative Cryogenic Engineering [Online] https://www.iceoxford.com/, [2020-12-05]."

[164] "shicryogenics, 'www.shicryogenics.com', [2020-12-05]," tech. rep.

[165] C. D. Hodgman and S. C. Lind, "Handbook of Chemistry and Physics.," *The Journal of Physical and Colloid Chemistry*, vol. 53, pp. 1139–1139, 7 1949.

[166] T. Tomaru, T. Suzuki, T. Haruyama, T. Shintomi, A. Yamamoto, T. Koyama, and R. Li, "Vibration analysis of cryocoolers," *Cryogenics*, vol. 44, pp. 309–317, 5 2004.

[167] X. P. Qing, S. J. Beard, A. Kumar, K. Sullivan, R. Aguilar, M. Merchant, and M. Taniguchi, "The performance of a piezoelectric-sensor-based SHM system under a combined cryogenic temperature and vibration environment," *Smart Materials and Structures*, vol. 17, p. 055010, 10 2008.

[168] Y. Ikushima, R. Li, T. Tomaru, N. Sato, T. Suzuki, T. Haruyama, T. Shintomi, and A. Yamamoto, "Ultra-low-vibration pulse-tube cryocooler system - cooling capacity and vibration," *Cryogenics*, vol. 48, pp. 406–412, 9 2008.

[169] C. Wang and J. G. Hartnett, "A vibration free cryostat using pulse tube cryocooler," *Cryogenics*, vol. 50, pp. 336–341, 5 2010.

[170] M. Hasibuzzaman, A. Shufian, R. K. Shefa, R. Raihan, J. Ghosh, and A. Sarker, "Vibration Measurement Analysis Using Arduino Based Accelerometer," in *2020 IEEE Region 10 Symposium, TENSYMP 2020*, pp. 508–512, Institute of Electrical and Electronics Engineers Inc., 6 2020.

[171] "Anti-vibration [Online] 'https://www.iceoxford.com/Technologies/Anti-vibration.htm', [2020-12-05]."

[172] J. Luo, K. Ying, and J. Bai, "Savitzky-Golay smoothing and differentiation filter for even number data," *Signal Processing*, vol. 85, pp. 1429–1434, 7 2005.

[173] M. K. Akhlaghi, H. Atikian, A. Eftekharian, M. Loncar, and A. Hamed Majedi, "Reduced Dark Counts in Optimized Geometries for Superconducting Nanowire Single photon Detectors," *Optics Express 20*, vol. 21, pp. 23610 – 23616, 2012.

[174] V. B. Verma, B. Korzh, F. Bussières, R. D. Horansky, S. D. Dyer, A. E. Lita, I. Vayshenker, F. Marsili, M. D. Shaw, H. Zbinden, R. P. Mirin, and S. W. Nam, "High-efficiency superconducting nanowire single-photon detectors fabricated from MoSi thin-films," *Optics Express*, vol. 23, p. 33792, 12 2015.

[175] R. H. Hadfield, "Single-photon detectors for optical quantum information applications," *Nature Photonics*, vol. 3, pp. 696–705, 12 2009.

[176] K. Il'in, D. Rall, M. Siegel, A. Engel, A. Schilling, A. Semenov, and H. W. Huebers, "Influence of thickness, width and temperature on critical current density of Nb thin film structures," *Physica C: Superconductivity*, vol. 470, pp. 953–956, 10 2010.

[177] A. Engel, K. Inderbitzin, A. Schilling, R. Lusche, A. Semenov, H. W. Hübers, D. Henrich, M. Hofherr, K. Il'In, and M. Siegel, "Temperature-dependence of detection efficiency in NbN and tan SNSPD," *IEEE Transactions on Applied Superconductivity*, vol. 23, no. 3, 2013.

[178] H. Nyquist, "Thermal agitation of electric charge in conductors," *Physical Review*, vol. 32, pp. 110–113, 7 1928.

[179] A. Engel, J. Lonsky, X. Zhang, and A. Schilling, "Detection mechanism in SNSPD: Numerical results of a conceptually simple, yet powerful detection model," *IEEE Transactions on Applied Superconductivity*, vol. 25, 6 2015.

[180] W. J. Skocpol, M. R. Beasley, and M. Tinkham, "Self-heating hotspots in superconducting thin-film microbridges," *Journal of Applied Physics*, vol. 45, p. 4054, 10 2003.

[181] D. K. Liu, L. X. You, S. J. Chen, X. Y. Yang, Z. Wang, Y. L. Wang, X. M. Xie, and M. H. Jiang, "Electrical characteristics of superconducting nanowire single photon detector," *IEEE Transactions on Applied Superconductivity*, vol. 23, no. 3, 2013.

[182] C.-M. Zhang, J.-R. Zhu, and Q. Wang, "Practical decoy-state reference-frame-independent measurement-device-independent quantum key distribution," *PHYSICAL REVIEW A*, vol. 95, 2017.

[183] W. Pernice, C. Schuck, O. Minaeva, M. Li, G. N. Goltsman, A. V. Sergienko, and H. X. Tang, "High Speed and High Efficiency Travelling Wave Single-Photon Detectors Embedded in Nanophotonic Circuits," *Nature Communications*, vol. 3, pp. 1 – 10, 8 2011.

[184] G. N. Gol'tsman, O. Okunev, G. Chulkova, A. Lipatov, A. Semenov, K. Smirnov, B. Voronov, A. Dzardanov, C. Williams, R. Sobolewski, G. N. Gol'tsman, O. Okunev, G. Chulkova, A. Lipatov, A. Semenov, K. Smirnov, B. Voronov, A. Dzardanov, C. Williams, R. Sobolewski, G. N. Gol'tsman, O. Okunev, G. Chulkova, A. Lipatov, A. Semenov, K. Smirnov, B. Voronov, A. Dzardanov, C. Williams, and R. Sobolewski, "Picosecond superconducting single-photon optical detector," *Applied Physics Letters*, vol. 79, pp. 705–707, 8 2001.

[185] D. Zhu, Q.-Y. Zhao, H. Choi, T.-J. Lu, A. E. Dane, D. R. Englund, and K. K. Berggren, "A scalable multi-photon coincidence detector based on superconducting nanowires," *Nature nanotechnology*, vol. 13, no. 7, pp. 596 – 601, 2018.

[186] G. Brennen, E. Giacobino, and C. Simon, "Focus on Quantum Memory," *New Journal of Physics*, vol. 17, p. 050201, 5 2015.

[187] M. Sidorova, A. Semenov, H. W. Hübers, I. Charaev, A. Kuzmin, S. Doerner, and M. Siegel, "Physical mechanisms of timing jitter in photon detection by current-carrying superconducting nanowires," *Physical Review B*, vol. 96, 11 2017.

[188] E. W. Bryerton, M. Morgan, and M. W. Pospieszalski, "Ultra low noise cryogenic amplifiers for radio astronomy," in *IEEE Radio and Wireless Symposium, RWS*, pp. 358–360, 2013.

[189] N. E. Booth, B. Cabrera, and E. Fiorini, "LOW-TEMPERATURE PARTICLE DETECTORS," *Annual Review of Nuclear and Particle Science*, vol. 46, pp. 471–532, 12 1996.

[190] P. Krantz, M. Kjaergaard, F. Yan, T. P. Orlando, S. Gustavsson, and W. D. Oliver, "A quantum engineer's guide to superconducting qubits," *Applied Physics Reviews*, vol. 6, p. 21318, 6 2019.

[191] R. K. Kirschman, "Low-Temperature Electronics," *IEEE Circuits and Devices Magazine*, vol. 6, no. 2, pp. 12–24, 1990.

[192] E. A. Gutiérrez-D, M. Jamal Deen, C. L. Claeys, and L. G. Rubin, "Low temperature electronics: Physics, devices, circuits, and applications," *Physics Today*, vol. 55, pp. 62–63, 5 2002.

[193] M. Hofherr, O. Wetzstein, S. Engert, T. Ortlepp, B. Berg, K. Ilin, D. Henrich, R. Stolz, H. Toepfer, H.-G. Meyer, and M. Siegel, "Orthogonal sequencing multiplexer for superconducting nanowire single-photon detectors with RSFQ electronics readout circuit," *Optics Express*, vol. 20, p. 28683, 12 2012.

[194] H. Homulle, *Cryogenic electronics for the read-out of quantum processors*. 2019.

[195] H. Homulle, S. Visser, B. Patra, G. Ferrari, E. Prati, F. Sebastiano, and E. Charbon, "A reconfigurable cryogenic platform for the classical control of quantum processors," *Review of Scientific Instruments*, vol. 88, p. 045103, 4 2017.

[196] P. Kok and B. W. Lovett, *Introduction to optical quantum information processing*. Cambridge University Press, 1 2013.

[197] J. I. Colless and D. J. Reilly, "Cryogenic High-Frequency Readout and Control Platform for Spin Qubits," *Review of Scientific Instruments*, vol. 83, no. 2, p. 023902, 2012.

[198] E. Arabul, S. Paesani, S. Tancock, J. G. Rarity, and N. Dahnoun, "A Precise High Count-Rate FPGA Based Multi-Channel Coincidence Counting System for Quantum Photonics Applications," *IEEE Photonics Journal*, vol. 12, pp. 1–1, 1 2020.

[199] B. Patra, J. P. G. van Dijk, S. Subramanian, A. Corna, X. Xue, C. Jeon, F. Sheikh, E. Juarez Hernandez, B. Perez Esparza, H. Rampurawala, B. Carlton, N. Samkharadze, S. Ravikumar, C. Nieva, S. Kim, H.-J. Lee, A. Sammak, G. Scappucci, M. Veldhorst, L. Vandersypen, M. Babaie, F. Sebastiano, E. Charbon, and S. Pellerano, "A Scalable Multi-Channel Cryogenic Controller for Spin Qubits/Transmons with Frequency Multiplexing Capability Implemented in Intel 22nm FinFET Technology," *Bulletin of the American Physical Society*, vol. Volume 65,, 2020.

[200] B. Patra, R. M. Incandela, J. P. Van Dijk, H. A. Homulle, L. Song, M. Shahmohammadi, R. B. Staszewski, A. Vladimirescu, M. Babaie, F. Sebastiano, and E. Charbon, "Cryo-CMOS Circuits and Systems for Quantum Computing Applications," *IEEE Journal of Solid-State Circuits*, vol. 53, pp. 309–321, 1 2018.

[201] J. D. Cressler and H. A. Mantooth, *Extreme environment electronics*. CRC Press, Taylor & Francis Group, 2013.

[202] J. Bieger and H. Seifert, "A Low-Noise CMOS Preamplifier Operating at 4.2 K," *IEEE Journal of Solid-State Circuits*, vol. 29, no. 8, pp. 921–926, 1994.

[203] C. Cahall, D. J. Gauthier, and J. Kim, "Scalable cryogenic readout circuit for a superconducting nanowire single-photon detector system," *Review of Scientific Instruments*, vol. 89, p. 063117, 6 2018.

[204] I. D. C. Lamb, J. I. Colless, J. M. Hornibrook, S. J. Pauka, S. J. Waddy, M. K. Frechtling, and D. J. Reilly, "An FPGA-based Instrumentation Platform for use at Deep Cryogenic Temperatures," *Review of Scientific Instruments*, vol. 87, no. 1, p. 014701, 2016.

[205] C. Wang, H. Li, R. A. Ramirez, Y. Zhang, H. Baghaei, S. Liu, S. An, and W. H. Wong, "A real time coincidence system for high count-rate TOF or non-TOF PET cameras using hybrid method combining AND-logic and time-mark technology," in *IEEE Transactions on Nuclear Science*, vol. 57, pp. 708–714, NIH Public Access, 4 2010.

[206] I. Kuon and J. Rose, "Measuring the gap between FPGAs and ASICs," in *IEEE Transactions on Computer-Aided Design of Integrated Circuits and Systems*, vol. 26, pp. 203–215, 2 2007.

[207] T. Arakawa, Y. Nishihara, M. Maeda, S. Norimoto, and K. Kobayashi, "Cryogenic amplifier for shot noise measurement at 20 mK," *Applied Physics Letters*, vol. 103, p. 172104, 10 2013.

[208] I. T. Vink, T. Nooitgedagt, R. N. Schouten, L. M. Vandersypen, and W. Wegscheider, "Cryogenic amplifier for fast real-time detection of single-electron tunneling," *Applied Physics Letters*, vol. 91, p. 123512, 9 2007.

[209] O. V. Dvornikov, N. N. Prokopenko, A. V. Bugakova, V. A. Tchekhovski, and I. V. Maliy, "Cryogenic Operational Amplifier on Complementary JFETs," in *Proceedings of 2018 IEEE East-West Design and Test Symposium, EWDTS 2018*, Institute of Electrical and Electronics Engineers Inc., 11 2018.

[210] Q. Y. Zhao, D. F. Santavicca, D. Zhu, B. Noble, and K. K. Berggren, "A distributed electrical model for superconducting nanowire single photon detectors," *Applied Physics Letters*, vol. 113, 8 2018.

[211] Q. Zhao, L. Zhang, T. Jia, L. Kang, W. Xu, J. Chen, and P. Wu, "Intrinsic timing jitter of superconducting nanowire single-photon detectors," *Applied Physics B: Lasers and Optics*, vol. 104, pp. 673–678, 9 2011.

[212] M. J. Deen, "Cryogenic temperature dependence of the voltage transfer characteristics of CMOS inverters," *Solid State Electronics*, vol. 31, pp. 1299–1308, 8 1988.

[213] F. Gago, J. J. Diaz, F. Garzón, and J. Patrón, "Characterization of the OPA350 Operational Amplifier at Cryogenic Temperatures," in *Scientific detectors for astronomy 2005*, pp. 645–650, Springer Netherlands, 9 2006.

[214] Z. Švindrych, Z. Janů, F. Soukup, and R. Tichý, "Operational amplifiers operating in temperature range from 300 to 4.2 K," *Cryogenics*, vol. 48, pp. 160–165, 3 2008.

[215] K. Hayashi, K. Saitoh, Y. Shibayama, and K. Shirahama, "A current to voltage converter for cryogenics using a CMOS operational amplifier," *Journal of Physics: Conference Series*, vol. 150, p. 012016, 2 2009.

[216] Q. Zhao, A. Mccaughan, A. Dane, F. Najafi, F. Bellei, D. De Fazio, K. Sunter, Y. Ivry, and K. K. Berggren, "Eight-fold signal amplification of a superconducting nanowire single-photon detector using a multiple-avalanche architecture," *Optics Express*, vol. 22, no. 20, pp. 24574 – 24581, 2014.

[217] S. Miki, T. Yamashita, H. Terai, and Z. Wang, "High performance fiber-coupled NbTiN superconducting nanowire single photon detectors with Gifford-McMahon cryocooler," *Optics Express*, vol. 21, p. 10208, 4 2013.

[218] "LNA-580 LNA Series 10-580MHz Low Noise Amplifier [Online], 'rfbay-inc.com/products_pdf/product_1_578.pdf', [2020-03-30]," tech. rep.

[219] "LNA-1000 LNA Series 10-1000MHz Low Noise Amplifier [Online], "rfbay-inc.com/products_pdf/product_2_76.pdf' [2020-03-03]," tech. rep.

[220] "Monolithic Amplifier GVA-123+ MiniCircuits, [Online], 'https://www.minicircuits.com/pdfs/GVA-123+.pdf' , [2020-03-30]," tech. rep.

[221] A. Devices, "30 MHz to 6 GHz RF/IF Gain Block, [Online], 'www.analog.com, [2020-03-30]," tech. rep.

[222] "ZX60-6013E-S+ Mini Circuits, 'www.minicircuits.com', '[2020-03-30]," tech. rep.

[223] L. You, "Superconducting nanowire single-photon detectors for quantum information," *Nanophotonics*, vol. 9, pp. 2673–2692, 9 2020.

[224] N. Calandri, Q.-Y. Zhao, D. Zhu, A. Dane, and K. K. Berggren, "Superconducting nanowire detector jitters limited by detector geometry," *Applied Physics Letters*, vol. 109, 7 2016.

[225] F. Mattioli, Z. Zhou, A. Gaggero, M. G. Tanner, L. San, E. Alvarez, W. Jiang, S. Subashchandran, R. Okamoto, L. Zhang, A. Engel, J. J. Renema, K. Il 'in, C. M. Natarajan, M. G. Tanner, and R. H. Hadfield, "Superconducting nanowire single-photon detectors: physics and applications Photon-number-resolving superconducting nanowire detectors A superconducting nanowire single photon detector on lithium niobate Investigation of the Performance of an Ultralow-Dark," *Supercond. Sci. Technol. Supercond. Sci. Technol*, vol. 25, no. 25, pp. 63001–16, 2012.

[226] "Artix-7 FPGA Family [Online], 'https://www.xilinx.com/products/silicon-devices/fpga/artix-7.html#productTable', [2020-12-04]."

[227] Xilinx, "Cost-Optimized Portfolio Product Tables and Product Selection Guide, [Online], 'https://www.xilinx.com/support/documentation/selection-guides/7-series-product-selection-guide.pdf', [2020-12-04]," tech. rep., 2015.

[228] "Basys 3 Development Board [Online], 'https://reference.digilentinc.com/_media/basys3:basys3_sch.pdf' ,[2020-01-22]."

[229] "Basys 3 Reference Manual [Online], 'https://reference.digilentinc.com/reference/programmable-logic/basys-3/reference-manual' ,[2020-12-04]."

[230] J. M. Hornibrook, J. I. Colless, I. D. Conway Lamb, S. J. Pauka, H. Lu, A. C. Gossard, J. D. Watson, G. C. Gardner, S. Fallahi, M. J. Manfra, and D. J. Reilly, "Cryogenic control architecture for large-scale quantum computing," *Physical Review Applied*, 2015.

[231] P. Sibson, C. Erven, M. Godfrey, S. Miki, T. Yamashita, M. Fujiwara, M. Sasaki, H. Terai, M. G. Tanner, C. M. Natarajan, R. H. Hadfield, J. L. O'Brien, and M. G. Thompson, "Chip-based quantum key distribution," *Nature Communications*, vol. 8, pp. 1–6, 2 2017.

[232] T. Kupko, M. von Helversen, L. Rickert, J. H. Schulze, A. Strittmatter, M. Gschrey, S. Rodt, S. Reitzenstein, and T. Heindel, "Tools for the performance optimization of single-photon quantum key distribution," *npj Quantum Information*, vol. 6, pp. 1–8, 12 2020.

[233] H. Homulle, S. Visser, B. Patra, G. Ferrari, E. Prati, F. Sebastiano, and E. Charbon, "A reconfigurable cryogenic platform for the classical control of quantum processors," *Review of Scientific Instruments*, vol. 88, no. 4, p. 045103, 2017.

[234] "FPGA designs for reconfigurable converters , H Homulle , [Online] 'https://cas.tudelft.nl/fpga_tdc/index.html' , [2021-03-02]."

[235] H. Homulle, S. Visser, B. Patra, and E. Charbon, "FPGA Design Techniques for Stable Cryogenic Operation," *arXiv preprint arXiv:1709.04190*, 2017.

[236] "Intel Introduces 'Horse Ridge' to Enable Commercially Viable Quantum Computers | Intel Newsroom [Online], https://newsroom.intel.com/news/intel-introduces-horse-ridge-enable-commercially-viable-quantum-computers/#gs.n6wzb2, [2020-12-04]."

[237] E. Knill, R. Laflamme, and G. J. Milburn, "A scheme for efficient quantum computation with linear optics," *Nature*, vol. 409, pp. 46–52, 1 2001.

[238] D. X. Xu, J. H. Schmid, G. T. Reed, G. Z. Mashanovich, D. J. Thomson, M. Nedeljkovic, X. Chen, D. Van Thourhout, S. Keyvaninia, and S. K. Selvaraja, "Silicon photonic integration platform-Have we found the sweet spot?," *IEEE Journal on Selected Topics in Quantum Electronics*, vol. 20, 7 2014.

[239] F. Gunning and B. Corbett, "Time to Open the 2-μm Window?," *Optics and Photonics News*, vol. 30, p. 42, 3 2019.

[240] R. Soref, "Group IV photonics: Enabling 2 μm communications," *Nature Photonics*, vol. 9, pp. 358–359, 6 2015.

[241] D. J. Richardson, "Filling the light pipe," *Science*, vol. 330, pp. 327–328, 10 2010.

[242] J. W. Silverstone, L. M. Rosenfeld, D. A. Sulway, B. D. Sayers, J. Biele, G. F. Sinclair, D. Sahin, L. Kling, J. C. Matthews, M. G. Thompson, and J. G. Rarity, "Silicon quantum photonics in the short-wave infrared: A new platform for big quantum optics," in *2019 Conference on Lasers and Electro-Optics Europe and European Quantum Electronics Conference, CLEO/Europe-EQEC 2019*, Institute of Electrical and Electronics Engineers Inc., 6 2019.

[243] S. Prabhakar, T. Shields, A. Dada, M. Ebrahim, G. G. Taylor, D. Morozov, K. Erotokritou, S. Miki, M. Yabuno, H. Terai, C. Gawith, M. Kues, L. Caspani, R. H. Hadfield, and M. Clerici, "Two-photon Quantum Interference and Entanglement at 2 μm," *Science Advances*, vol. 6, p. eaay5195, 6 2020.

[244] Y. Zou, S. Chakravarty, C.-J. Chung, X. Xu, and R. T. Chen, "Mid-infrared silicon photonic waveguides and devices [Invited]," *Photonics Research*, vol. 6, p. 254, 4 2018.

[245] "Efficient Single Photon Detection From 0.5 To 5 Micron Wavelength," in *Conference on Lasers and Electro-Optics 2012*, (Washington, D.C.), p. QTu1E.2, OSA, 2012.

[246] "Silicon photonics: CMOS going optical," *Proceedings of the IEEE*, vol. 97, pp. 1161–1165, 7 2009.

[247] M. Streshinsky, R. Ding, Y. Liu, A. Novack, C. Galland, A. E.-J. Lim, P. Guo-Qiang Lo, T. Baehr-Jones, and M. Hochberg, "The Road to Affordable, Large-Scale Silicon Photonics," *Optics and Photonics News*, vol. 24, p. 32, 9 2013.

[248] F. Marsili, V. B. Verma, J. A. Stern, S. Harrington, A. E. Lita, T. Gerrits, I. Vayshenker, B. Baek, M. D. Shaw, R. P. Mirin, and S. W. Nam, "Detecting single infrared photons with 93% system efficiency," *Nature Photonics*, vol. 7, pp. 210–214, 3 2013.

[249] H. Shibata, K. Fukao, N. Kirigane, S. Karimoto, and H. Yamamoto, "SNSPD With Ultimate Low System Dark Count Rate Using Various Cold Filters," *IEEE Transactions on Applied Superconductivity*, vol. 27, pp. 1–4, 6 2017.

[250] M. Caloz, M. Perrenoud, C. Autebert, B. Korzh, M. Weiss, C. Schönenberger, R. J. Warburton, H. Zbinden, F. Bussières, F. Eres, and F. Bussières, "High-detection efficiency and low-timing jitter with amorphous superconducting nanowire single-photon detectors," *Applied Physics Letters*, vol. 112, p. 061103, 2 2018.

[251] N. A. Tyler, G. F. Sinclair, G. E. Villarreal, G. Gough, J. Barreto, D. Sahin, and M. G. Thompson, "Determining the Optical Nonlinearity of Silicon at Cryogenic Temperatures for Applications in Integrated Photonics," in *Conference on Lasers and Electro-Optics*, p. JTh1E.5, Optical Society of America, 2017.

[252] K. M. Rosfjord, J. K. W. Yang, E. A. Dauler, A. J. Kerman, V. Anant, B. M. Voronov, G. N. Gol'tsman, and K. K. Berggren, "Nanowire single-photon detector with an integrated optical cavity and anti-reflection coating," *Optics Express*, vol. 14, p. 527, 1 2006.

[253] A. J. Kerman, E. A. Dauler, J. K. Yang, K. M. Rosfjord, V. Anant, K. K. Berggren, G. N. Gol'tsman, and B. M. Voronov, "Constriction-limited detection efficiency of superconducting nanowire single-photon detectors," *Applied Physics Letters*, vol. 90, p. 101110, 3 2007.

[254] F. Mattioli, Z. Zhou, A. Gaggero, R. Gaudio, S. Jahanmirinejad, D. Sahin, F. Marsili, R. Leoni, and A. Fiore, "Photon-number-resolving superconducting nanowire detectors," *Superconductor Science and Technology*, vol. 28, p. 104001, 8 2015.

[255] M. P. Hansen and D. S. Malchow, "Overview of SWIR detectors, cameras, and applications," p. 69390I, 3 2008.

[256] J. P. Allmaras, A. D. Beyer, R. M. Briggs, F. Marsili, M. D. Shaw, G. V. Resta, J. A. Stern, V. B. Verma, R. P. Mirin, S. W. Nam, and W. H. Farr, "Large-Area 64-pixel Array of WSi superconducting nanowire single photon detectors," in *2017 Conference on Lasers and Electro-Optics, CLEO 2017 - Proceedings*, vol. 2017-Janua, pp. 1–2, Institute of Electrical and Electronics Engineers Inc., 10 2017.

[257] N. A. Tyler, J. Barreto, G. E. Villarreal-Garcia, D. Bonneau, D. Sahin, J. L. O'Brien, and M. G. Thompson, "Modelling superconducting nanowire single photon detectors in a waveguide cavity," *Optics Express*, vol. 24, p. 8797, 4 2016.

[258] H. Fujiwara, "Spectroscopic Ellipsometry Principles and Applications," tech. rep., WILEY, 2007.

[259] "RC2 Ellipometer [Online], 'https://www.jawoollam.com/download/pdfs/rc2-brochure.pdf' [2020-12-04]."

[260] W. Emery and A. Camps, "Basic Electromagnetic Concepts and Applications to Optical Sensors," in *Introduction to Satellite Remote Sensing*, pp. 43–83, Elsevier, 1 2017.

[261] A. Banerjee, R. M. Heath, D. Morozov, D. Hemakumara, U. Nasti, I. Thayne, and R. H. Hadfield, "Optical properties of refractory metal based thin films," *Optical Materials Express*, vol. 8, p. 2072, 8 2018.

[262] C. A. Mack, "Uncertainty in roughness measurements: putting error bars on line-edge roughness," *Journal of Micro/Nanolithography, MEMS, and MOEMS*, vol. 16, p. 010501, 1 2017.

[263] A. Banerjee, L. J. Baker, A. Doye, M. Nord, R. M. Heath, K. Erotokritou, D. Bosworth, Z. H. Barber, I. MacLaren, and R. H. Hadfield, "Characterisation of amorphous molybdenum silicide (MoSi) superconducting thin films and nanowires," *Superconductor Science and Technology*, vol. 30, 7 2017.

[264] F. Marsili, F. Bellei, F. Najafi, A. E. Dane, E. A. Dauler, R. J. Molnar, and K. K. Berggren, "Efficient Single Photon Detection from 500 nm to 5 μm Wavelength," *Nano Letters*, vol. 12, pp. 4799–4804, 9 2012.

[265] "Optical Waveguide Design Software - Lumerical MODE."

[266] D. F. Swinehart, "The Beer-Lambert law," *Journal of Chemical Education*, vol. 39, no. 7, pp. 333–335, 1962.

[267] S. Ferrari, C. Schuck, and W. Pernice, "Waveguide-integrated superconducting nanowire single-photon detectors," *Nanophotonics*, vol. 0, 9 2018.

[268] J. Li, C. Xia, and X. Chen, "A benchmark dataset and saliency-guided stacked autoencoders for video-based salient object detection," *IEEE Transactions on Image Processing*, vol. 27, pp. 349–364, 1 2018.

[269] Y. A. Vlasov and S. J. McNab, "Losses in single-mode silicon-on-insulator strip waveguides and bends," *Optics Express*, vol. 12, p. 1622, 4 2004.

[270] W. Bogaerts, P. Dumon, D. V. Thourhout, and R. Baets, "Low-loss, low-cross-talk crossings for silicon-on-insulator nanophotonic waveguides," *Optics Letters*, vol. 32, p. 2801, 10 2007.

[271] D. Celo, D. J. Goodwill, P. Dumais, J. Jiang, and E. Bernier, "Low-loss waveguide crossings for photonic integrated circuits on SOI technology," in *IEEE International Conference on Group IV Photonics GFP*, pp. 189–190, IEEE Computer Society, 11 2014.

[272] A. Yariv, "Critical coupling and its control in optical waveguide-ring resonator systems," *IEEE Photonics Technology Letters*, vol. 14, pp. 483–485, 4 2002.

[273] D. G. Rabus, "Ring resonators: Theory and modeling," *Springer Series in Optical Sciences*, vol. 127, pp. 3–40, 2007.

[274] S. Azzini, D. Grassani, M. J. Strain, M. Sorel, L. G. Helt, J. E. Sipe, M. Liscidini, M. Galli, and D. Bajoni, "Ultra-low power generation of twin photons in a compact silicon ring resonator.," *Optics express*, vol. 20, pp. 23100–7, 10 2012.

[275] S. Clemmen, K. Phan Huy, W. Bogaerts, R. G. Baets, P. Emplit, and S. Massar, "Continuous wave photon pair generation in silicon-on-insulator waveguides and ring resonators.," *Optics express*, vol. 17, pp. 16558–70, 9 2009.

[276] V. Anant, A. J. Kerman, E. A. Dauler, J. K. W. Yang, K. M. Rosfjord, and K. K. Berggren, "Optical properties of superconducting nanowire single-photon detectors," *Optics Express*, vol. 16, p. 10750, 7 2008.

[277] J. F. Bauters, M. L. Davenport, M. J. R. Heck, J. K. Doylend, A. Chen, A. W. Fang, and J. E. Bowers, "Silicon on ultra-low-loss waveguide photonic integration platform," *Optics Express*, vol. 21, p. 544, 1 2013.

[278] X. Jiang, H. Wu, and D. Dai, "Low-loss and low-crosstalk multimode waveguide bend on silicon," *Optics Express*, vol. 26, p. 17680, 6 2018.

[279] K. K. Lee, D. R. Lim, H. C. Luan, A. Agarwal, J. Foresi, and L. C. Kimerling, "Effect of size and roughness on light transmission in a Si/SiO2 waveguide: Experiments and model," *Applied Physics Letters*, vol. 77, pp. 1617–1619, 9 2000.

[280] I. of Engineering, I. C. Technology., and G. C. Patil, "IET optoelectronics.," 2019.

[281] T. Fujisawa, S. Makino, T. Sato, and K. Saitoh, "Low-loss, compact, and fabrication-tolerant Si-wire 90° waveguide bend using clothoid and normal curves for large scale photonic integrated circuits," *Optics Express*, vol. 25, p. 9150, 4 2017.

[282] L. H. Gabrielli, D. Liu, S. G. Johnson, and M. Lipson, "On-chip transformation optics for multimode waveguide bends," *Nature Communications*, vol. 3, 2012.

[283] C. J. Oton, O. Lemonnier, M. Fournier, and C. Kopp, "Adiabatic bends in silicon multimode waveguides," in *IEEE International Conference on Group IV Photonics GFP*, vol. 2016-Novem, pp. 108–109, IEEE Computer Society, 11 2016.

[284] V. Anant, "Engineering the optical properties of subwavelength devices and materials," *PhD diss., Massachusetts Institute of Technology*, 2007.

[285] D. Celo, P. Dumais, W. Liu, C. Zhang, D. J. Goodwill, J. Jiang, and E. Bernier, "Optical proximity correction in geometry sensitive silicon photonics waveguide crossings," in *14th International Conference on Group IV Photonics, GFP 2017*, pp. 45–46, Institute of Electrical and Electronics Engineers Inc., 10 2017.

[286] D.-X. Xu, A. Densmore, P. Waldron, J. Lapointe, E. Post, A. Delâge, S. Janz, P. Cheben, J. H. Schmid, and B. Lamontagne, "High bandwidth SOI photonic wire ring resonators using MMI couplers," *Optics Express*, vol. 15, no. 6, p. 3149, 2007.

[287] Z. Cui, *Nanofabrication: Principles, Capabilities and Limits: Second Edition*. Springer International Publishing, 1 2017.

[288] N. Sahu, B. Parija, and S. Panigrahi, "Fundamental understanding and modeling of spin coating process: A review," in *Indian Journal of Physics*, vol. 83, pp. 493–502, Scientific Publishers, 4 2009.

[289] L. F. THOMPSON, "An Introduction to Lithography," pp. 1–13, 5 1983.

[290] F. H. Dill, "Optical Lithography," *IEEE Transactions on Electron Devices*, vol. 22, no. 7, pp. 440–444, 1975.

[291] A. A. Tseng, K. Chen, C. D. Chen, and K. J. Ma, "Electron beam lithography in nanoscale fabrication: Recent development," *IEEE Transactions on Electronics Packaging Manufacturing*, vol. 26, pp. 141–149, 4 2003.

[292] D. J. Carbaugh, J. T. Wright, R. Parthiban, and F. Rahman, "Photolithography with polymethyl methacrylate (PMMA)," *Semiconductor Science and Technology*, vol. 31, p. 025010, 12 2015.

[293] D. Lauvernier, J. P. Vilcot, M. François, and D. Decoster, "Optimization of HSQ resist e-beam processing technique on GaAs material," *Microelectronic Engineering*, vol. 75, pp. 177–182, 8 2004.

[294] R. Kirchner, V. A. Guzenko, I. Vartiainen, N. Chidambaram, and H. Schift, "ZEP520A - A resist for electron-beam grayscale lithography and thermal reflow," *Microelectronic Engineering*, vol. 153, pp. 71–76, 3 2016.

[295] G. C. Schwartz and P. M. Schaible, "Reactive Ion Etching of Silicon," *J Vac Sci Technol*, vol. 16, pp. 410–413, 3 1979.

[296] R. F. Bunshah, "High-rate Evapouration/Deposition processes of Metals, Alloys and Ceramics for Vacuum Metallurigcal Applications.," *J Vac Sci Technol*, vol. 11, pp. 814–819, 7 1974.

[297] S. Swann, "Magnetron sputtering," *Physics in Technology*, vol. 19, pp. 67–75, 3 1988.